Università degli Studi di Salerno

Dottorato di Ricerca in Informatica e Ingegneria dell'Informazione
Ciclo 31 – a.a 2017/2018

TESI DI DOTTORATO / PH.D. THESIS

Methods and Algorithms for Behavioral Modeling of Ferrite Power Inductors

KATERYNA STOYKA

SUPERVISOR: **PROF. NICOLA FEMIA**
CO-SUPERVISOR: **DR. GIULIA DI CAPUA**

PHD PROGRAM DIRECTOR: **PROF. PASQUALE CHIACCHIO**

Dipartimento di Ingegneria dell'Informazione ed Elettrica
e Matematica Applicata
Dipartimento di Informatica

To my grandparents

Contents

Introduction

Information technology allows solving numerous problems regarding all the aspects of everyday life, including technical activities related to the design of devices and systems. In the electronic field, different types of softwares are widely used to support designers in solving the problems of electronic circuit design, at device level and system level. Power electronics is one of the most important modern technologies, since power supply systems are used to feed any electric and electronic device and system in manifold applications (e.g. computers, automotive, aerospace, consumer electronics, *etc*). The features of power supplies affect the reliability and performances of the whole system in which they are used. Switching power supply design is mostly driven by high efficiency and high reliability requirements. The strong non linearity of switching power supplies and the difficulty of application of advanced design methodologies often push designers to adopt a conservative approach, based on simplified robust and reliable methods. This mostly result in sub-optimal design solutions characterized by components oversizing.

This dissertation discusses innovative applications of enhanced numerical techniques and intelligent algorithms to power supplies optimization and design. The impact of innovative modeling and computing techniques in the discovery of novel advanced solutions outperforming the traditional conservative designs is emphasized. A detailed introductory overview of major power electronics design issues is provided hereafter, to help the reader in better understanding of the technical foundations of the dissertation.

Power electronics is ever moving towards higher efficiency and higher power density solutions. Reduction in the size and weight of power electronics systems and increasing efficiency requirements are two main specifications in Switch-Mode Power Supply (SMPS) design [1]. Magnetic components — inductors and transformers — occupy a significant amount of space in today's power supplies, and furthermore, considerable losses occur in these components. In order to achieve a higher level of miniaturization, reduction in the size of these components is crucial. However, as higher power densities are also required, heat dissipation and temperature rise may become critical issues too. This is particularly accentuated in integrated System on Chip (SoC) applications. As in SoC as in discrete solutions, attention should be paid to the power losses and thermal analysis of magnetic parts.

Ferrite Power Inductors (FPIs) are usually the first choice for high-efficiency designs of SMPS, thanks to their resulting low losses [2] [3]. However, FPIs suffer of a pretty sharp inductance drop when their current exceeds a certain threshold, occurring due to the saturation of their magnetic core. For each FPI, the manufacturer typically provides the values of saturation currents $I_{10\%}$, $I_{20\%}$ and $I_{30\%}$, causing 10%, 20% and 30% drop of the inductance with respect to its nominal value L_{nom}. These parameters are normally used by SMPS designers to select FPIs: the higher the values $I_{10\%}$, $I_{20\%}$ required by a given application, the bigger the magnetic cores necessary to realize inductors having a desired nominal inductance [4]. In fact, the conventional design approach usually adopted by SMPS designers consists in ensuring that, even in the worst case conditions, the peak current flowing through the inductor does not exceed the $I_{10\%}$ or $I_{20\%}$ saturation current, keeping the inductor peak-to-peak current ripple Δi_{Lpp} close to 40% [5]. This limitation is partially motivated by the assumption that the inductor operating with a higher saturation degree may be subjected to a higher peak-to-peak current ripple and power losses. As a possible second reason, it looks difficult to predict the peak-to-peak current ripple when the inductor operates in the region where its inductance sharply rolls off. The

consequence of the adoption of such conventional design approach is that inductors are often oversized, thus requiring more space in SMPS and having, usually, a higher price.

In recent years, inductors saturation has been the subject of several scientific investigations [6–13]. Some authors have verified that smaller volume inductors working in moderate saturation help achieving more compact SMPSs with an acceptable amount of power losses [10–13]. In [10] it has been demonstrated that a saturable inductor is suitable for power factor correction applications, and can save considerable space (up to 65%) and cost over a conventional linear inductor. In [11] a saturable inductor has been adopted in the photovoltaic inverter application. It has been shown that the inductor can be designed with an adapted saturation characteristic, allowing a reduction of the inductor volume by about 15% compared to a constant inductance, over the whole current range of the inverter. In [12] a method has been presented on how to adjust the inductance curve of a saturable inductor with respect to a desired shape, showing that a highly efficient construction with low stray fields and maximum package density can be achieved, with 32% smaller size if compared to traditional non-saturated solutions. In [13] Milner *et al.* have demonstrated that a 3.3x3.3x1.0mm^3 (10.9mm^3) ferrite-core 1μH inductor rated for 1.6A can properly operate in a converter also past its saturation point up to 2.1A. The authors have also proved that the saturated inductors can reduce PCB area by 50% over competing non-saturated alternatives, while increasing total peak-power conduction losses by no more than 3%.

To effectively and safely exploit the benefits offered by the use of FPIs in moderate and controlled saturation, appropriate saturation models and power loss models are needed, reliably describing inductor behavior by including saturation effects. Generally, inductor models can be divided into two main categories: *physical* models and *behavioral* models [14]. The first category refers to numerical models based on the physical principles governing the device. Such models are obtained by constructing a system of physical equations using the geometry and material information

of inductor. The two most popular physical models for inductors are the Jiles-Atherton model [15] and the Preisach model [16], describing the hysteresis loop of the magnetic core material, starting from which both the magnetic permeability and core losses can be derived as a function of the DC bias magnetic field. However, most physical models require additional winding and core data well beyond what is typically available in manufacturers' datasheets. Such models are complicated and not practical for engineers. While physical modeling techniques can be effectively used during the inductor design stage, behavioral models are more suitable for system-level simulations. Such models are based on the use of empirical equations or equivalent circuits, by means of which the experimental inductor characteristic of interest can be fitted, e.g., saturation, power losses, hysteresis, *etc.* Such models are simpler compared to physical models, and easier to use for SMPS designers. Therefore, the behavioral model-based approach is adopted in this dissertation to reliably describe the main characteristics of ferrite inductors needed to analyze their behavior in saturation.

The key point is that the saturation and power loss models of FPIs have to be consistent with the large-signal square-wave voltage conditions imposed by SMPSs to inductors. As regards the saturation models, recently several inductor manufacturers have started providing more complete information about the inductance *vs* current (L *vs* i_L) curves for their magnetic parts at different temperatures [17–19]. To accurately describe such curves, an *arctangent-based* behavioral model has been recently proposed in [20], which can be used in combination with a developed numerical algorithm to reliably reconstruct the inductor current waveshape under SMPS conditions, including saturation. Such model and numerical algorithm have been verified only for positive inductor currents in Continuous Conduction Mode (CCM). However, certain applications may involve High Current Ripple (HCR) inductor operation, which represents the new trend in power converters using wide band-gap devices, such as Silicon Carbide (SiC) and Gallium Nitride (GaN) transistors [21]. HCR operation can result

in the occurrence of negative inductor currents in synchronous-rectification converter topologies, and Discontinuous Conduction Mode (DCM) in diode-rectification topologies. Hence the existing arctangent-based saturation model needs to be extended and the relative numerical algorithm adapted also to cases involving negative inductor currents and DCM operation, in order to develop a generalized saturation behavioral model for FPIs. However, to obtain realistic reconstructions of the inductor current waveforms in saturation, reliable L *vs* i_L data are needed. The datasheet L *vs* i_L curves of FPIs are typically characterized by high uncertainty levels (e.g., $\pm 20\%$), due to manufacturing tolerances on components. Moreover, such curves are measured under small-signal sinusoidal voltage test conditions, thus making the manufacturers' data not sufficiently reliable for a realistic determination of the peak-to-peak inductor current ripple in large-signal square-wave voltage conditions imposed by the SMPS operation. Therefore, the systematic procedures are needed for identification of the temperature-dependent L *vs* i_L curves in real SMPS conditions.

As regards the power loss models, FPIs total power losses are determined by winding losses and magnetic core losses. However, the core and winding losses cannot be easily measured as separate contributions in SMPS applications. FPIs total power losses can be alternatively evaluated as the sum of a DC term and an AC term. Since the DC losses can be easily estimated from the DC winding resistance and the DC current flowing through the winding, the major challenge still remains how to determine a compact behavioral model for the AC losses of FPIs, given as a function of the main operating conditions directly imposed to the inductor by the SMPS. Eventually, the saturation models and power loss models of FPIs need to be coherent between them. As discussed above, the saturation L *vs* i_L curves depend on the inductor temperature, which, in its turn, is dependent on the ambient temperature and inductor total power losses, through the device thermal resistance. Thus the temperature is not a real *input* to the inductor model, but rather an *output*, representing the response of the device to given ambient temperature and total power losses. Therefore the

inductor total power losses should be used as an input to the saturation model, instead of temperature. Once the saturation models and power loss models of FPIs have been identified, they can be adopted at system-level simulation of the converter, so as to discover and exploit the benefits offered by the use of FPIs operating in saturation.

Considering the above issues, the aim of this dissertation is to provide organic and systematic answers to the problems of the high-power-density SMPS design exploiting the use of FPIs operating in saturation. In particular, the specific objectives of this dissertation are:

a) development of numerical techniques and intelligent algorithms for generation and discovery of behavioral models for saturation and power losses of FPIs used in SMPS applications;

b) development of enhanced numerical algorithms, using the above models, able to reliably predict the FPIs behavior under given SMPS conditions;

c) development of enhanced numerical algorithms able to identify feasible inductor solutions, possibly operating in saturation, allowing to reduce the inductor size and increase the converter power density.

The dissertation is organized as follow:

In Chapter 1, a generalized *arctangent*-based behavioral model accurately fitting the L *vs* i_L curve of FPIs is presented. Such model can be used in combination with the proposed numerical algorithm to reliably predict the inductor current wave-shape in whatever operating condition, including saturation.

In Chapter 2, the Evolutionary Algorithm-based approach for the identification of the temperature-dependent L *vs* i_L curves of FPIs is discussed, based on the use of experimental inductor current waveforms and temperatures in real SMPS conditions. Then, an alternative approach is presented, based on the local and global approximations of the inductor saturation characteristic, obtained

under small-amplitude and large-amplitude current ripple conditions, respectively.

In Chapter 3, a non-linear modeling of ferrite inductors with a stepped air-gap is discussed. The arctangent-based L *vs* i_L model, proposed in Chapter 1 for fixed air-gap FPIs, is extended to a *double-arctangent model*. Such model accurately describes the saturation characteristic of stepped air-gap inductors and allows to reliably predict their current wave-shapes in saturation.

In Chapter 4, the Sustainable Saturation Operation (SSO) of FPIs is discussed, which is verified if the inductor current ripple, power losses and temperature rise are acceptable and reliable for both the device and the SMPS, despite the inductance drop determined by the core saturation. An algorithm is presented which identifies SSO-compliant FPIs with minimum size and volume, thus allowing to increase the SMPS power density, while preserving the overall converter efficiency.

In Chapter 5, behavioral modeling of the FPIs total power losses is presented, followed by the modeling of the sole AC loss contribution. Both approaches are based on the use of a Genetic Programming algorithm, which identifies the power loss model structure and the relevant parameters, starting from a set of experimental power loss data measured on a wide range of SMPS operating conditions.

In Chapter 6, a novel *power-loss-dependent* saturation model is presented, which provides the inductance as a function of inductor current, parameterized with respect to the component total power losses.

Chapter 1

Saturation Behavioral Modeling of Ferrite Inductors

This chapter discusses saturation behavioral modeling for Ferrite Power Inductors (FPIs) used in Switch-Mode Power Supply (SMPS) applications. First, a brief description of the main properties of ferrite materials is given, followed by some useful definitions of inductance. Then, an analytical model is presented accurately describing the inductance *versus* current saturation characteristic of FPIs. A numerical method is discussed for reliable prediction of the inductor current waveform, including possible operation in saturation. Such method and relative numerical algorithm are valid for both Continuous Conduction Mode (CCM) and Discontinuous Conduction Mode (DCM), as well as for both Synchronous Rectification (SR) and Diode Rectification (DR) converter topologies.

1.1 Magnetic Core Materials

In power electronics, there are two basic classes of the soft magnetic materials used for magnetic cores of transformers and inductors [22]. The first class of materials are alloys of iron containing

some amounts of other elements, such as silicon (Si), nickel (Ni), chrome (Cr), and cobalt (Co). These materials are referred to as *ferromagnetic materials*. The values of the saturation induction begin at 1.4 T, and for some of the materials the values are near 1.9 T. The electrical resistivity of these alloys is only slightly higher than that of good conductors, such as copper or aluminum. The second class of magnetic materials are *ferrimagnetic materials* (*ferrites*). Ferrites are ceramic materials, basically soft magnetic oxide mixtures of iron and other magnetic elements, such as manganese (Mn), zinc (Zn), nickel, and cobalt. They are characterized by a high resistivity. The order of magnitude of the resistivity is at least 10^6 higher than that of the first class.

Depending on the applications, the desirable properties of the magnetic materials are different. In most soft magnetic material applications, high permeability and saturation induction and low coercivity and power losses are preferable. Mechanical properties of the materials are also important. Generally, it is not possible to have all the desirable properties in a single material, so for a given application the choice of the material is usually a compromise. Currently ferrites are still the soft magnetic materials most widely used in power electronics. The most important characteristic of ferrites, as compared to other magnetic materials, is the high volume resistivity of the material. In high frequency applications eddy current losses are usually dominant and increase approximately with the square of the frequency. These losses are inversely proportional to the resistivity. Therefore, the high resistivity of the ferrites is the factor most contributing to their wide application in high frequency magnetic components. A brief description of the main properties of ferrites is presented next.

1.1.1 Ferrites: Main Properties

Ferrites are dark gray or black ceramic materials. They are chemically inert, brittle, very hard, and difficult to process, except with water-cooled diamond tools. Ferrites are derived from iron oxide mined from the earth. Metals such as nickel, zinc and manganese

are added to the iron oxide. Ferrite material is then pressed and fired to form a crystalline structure that gives ferrite cores their properties. The general chemical formula is $MeFe_2O_3$, where Me represents one or more divalent transition metals, such as manganese, zinc, nickel, cobalt, or magnesium. The most common combinations are manganese and zinc (MnZn) or nickel and zinc (NiZn). MnZn ferrites are characterized by a high permeability, high saturation induction levels and low eddy current losses, usually they are applicable up to a few MHz. NiZn have lower permeabilities with very low eddy current losses. They are, in general, used in higher frequency ranges (above 1 MHz) and are suitable for low induction levels.

Ferrite cores are gapped by creating a space in the magnetic flux path. These gaps are achieved by grinding the gap in a one-piece core or placing a non-magnetic spacer between halves of assembled cores. This explains the performance differences between them and the iron powder cores, in terms of magnetic saturation. Iron powder cores consist of small particles of pure iron, coated with a thin electrically insulating layer and pressed to a bulk material at high pressure. The small non-magnetic distances between the particles act as tiny air-gaps, which do not all saturate at exactly the same flux level (applied current), so a saturation happens in a gradual fashion. Ferrites, instead, saturate in a much more abrupt fashion. Fig. 1.1 depicts typical L *vs* i_L characteristics of power inductors realized with ferrite (red) and iron powder (blue) core, both having the same nominal inductance of 12 μH but different saturation behavior [17].

One of the effects of introducing an air-gap in a magnetic core results in a reduction of its effective permeability and, consequently, of the inductance. Another effect is a flattening (or *shearing*) of its hysteresis loop [23]. For this reason, the hysteresis is not taken into account hereinafter during the modeling of FPIs.

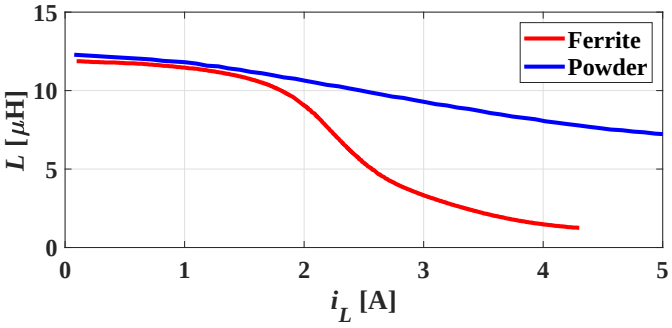

Figure 1.1: Typical L *vs* i_L curves of ferrite and iron powder core inductors.

1.2 Inductance: Definitions

The term inductance can be defined in different ways with respect to the non-linearity of the magnetic flux linkage Ψ *versus* the winding current i_L (or, Ψ *vs* i_L) dependence [22]. Let us note that the flux linkage Ψ represents the magnetic flux linked to all turns of the inductor winding, which is related to the average flux Φ of one turn according to: $\Psi = \Phi \cdot n$, where n is the winding turn number.

The slope of the chord in the Ψ *vs* i_L curve is called *chord inductance*, *amplitude inductance* or *static inductance* (see Fig. 1.2(a)), and is denoted as L_s:

$$L_s = \frac{\Psi}{i_L} \tag{1.1}$$

The derivative of the flux linkage $\Psi = \Psi(i_L)$ with respect to the current i_L is the *differential*, or *dynamic*, *inductance* L_d, which is observed when small signals are superimposed to the inductor current i_L:

$$L_d = \frac{d\Psi}{di_L} \tag{1.2}$$

For material presenting hysteresis (see Fig. 1.2(b)), a minor loop is observed resulting in a lower small-signal inductance, called

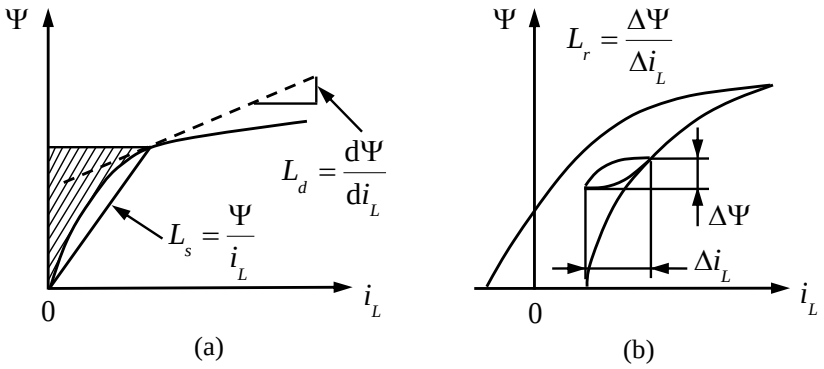

Figure 1.2: Flux linkage Ψ as a function of current i_L: (a) without hysteresis; (b) with hysteresis.

reversible inductance L_r, given by (1.3):

$$L_r = \frac{\Delta\Psi}{\Delta i_L} \tag{1.3}$$

Neglecting the hysteresis, the differential inductance equals the reversible one: $L_d = L_r$. The shaded area in Fig. 1.2(a) represents the stored inductive energy. Therefore an energetic inductance L_w can be defined as:

$$L_w = \frac{2\int_0^{\Psi} i_L d\Psi}{i_L^2} \tag{1.4}$$

The relation between the different definitions of inductance for a normal saturating curve (without hysteresis and with a negative second derivative) is: $L_d < L_w < L_s$.

Inductors are tested by manufacturers by using proper test conditions. Their characterization is often performed by applying a sinusoidal voltage of angular frequency ω to the inductor, which results in a non-sinusoidal inductor current. The inductance value is obtained as follows:

$$L_v = \frac{V_{rms}}{\omega I_{rms}} \tag{1.5}$$

where V_{rms} and I_{rms} are the measured RMS voltage and current values. The same measurement can be done feeding inductor with a sinusoidal current of angular frequency ω, and sensing the inductor voltage.

1.3 Inductance *vs* Current Behavioral Model for FPIs

Fig. 1.3 shows a typical curve of the dynamic inductance L *versus* the winding current i_L (or, L *vs* i_L) for a FPI. Fig. 1.3 highlights the inductance values L^{high} and L^{low} at the two curve extremes. For gapped-core inductors, the deep-saturation inductance L^{low} is about 10%-20% of the weak-saturation inductance L^{high}. Accordingly, three regions of operation can be identified:

- the *weak-saturation* region, wherein the inductance slightly decreases with respect to L^{high}, down to about 70%-80% of L^{high};
- the *deep-saturation* region, wherein the inductance is lower than about 20%-30% of L^{high} and approaches L^{low};
- the *roll-off* region, wherein the inductance is comprised between about 70%-80% of L^{high} and 20%-30% of L^{high}.

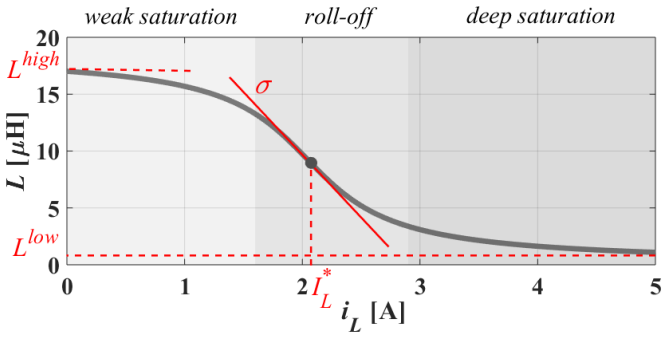

Figure 1.3: Typical L *vs* i_L curve of a FPI.

The L *vs* i_L curves of FPIs can be analytically described by means of an arctangent function, defined as follows:

$$L\left[i_L\left(t\right)\right]=L^{low}+\frac{L^{high}-L^{low}}{2}\left\{1-\frac{2}{\pi}\text{atan}\left\{\sigma\left[\left|i_L\left(t\right)\right|-I_L^*\right]\right\}\right\} \quad (1.6)$$

where parameters L^{high} and L^{low} are the horizontal asymptotes of the L *vs* i_L curve, I_L^* is its inflection point at which $L(I_L^*) = 1/2\left(L^{high}+L^{low}\right)$, and σ is proportional to the slope of the curve in I_L^* according to $dL/di_L\,|_{i_L=I_L^*} = -\sigma\left(L^{high}-L^{low}\right)/\pi$. The values of L^{high} and L^{low} can be taken from the inductance curves provided in the manufactures' datasheets. The values of σ and I_L^* are usually not directly available, but they can be obtained by applying (1.6) for two current values $i_L(t) = I_{\alpha\%}$ and $i_L(t) = I_{\beta\%}$, corresponding to the $\alpha\%$ drop and the $\beta\%$ drop of inductance with respect to L^{high}, namely $L_{\alpha\%}$ and $L_{\beta\%}$, respectively. Any couple of percent drops between 10% and 90% can be adopted, if the inductance curves are available on such a range. According to (1.6), given $\alpha\% = 30\%$ and $\beta\% = 70\%$, the values of σ and I_L^* can be calculated by using (1.7):

$$\sigma = \frac{\cot(\pi\Gamma_{30\%}) - \cot(\pi\Gamma_{70\%})}{I_{30\%} - I_{70\%}} \quad (1.7a)$$

$$I_L^* = \frac{I_{70\%}\cot(\pi\Gamma_{30\%}) - I_{30\%}\cot(\pi\Gamma_{70\%})}{\cot(\pi\Gamma_{30\%}) - \cot(\pi\Gamma_{70\%})} \quad (1.7b)$$

$$\Gamma_{30\%} = \frac{L_{30\%} - L^{low}}{L^{high} - L^{low}}, \qquad \Gamma_{70\%} = \frac{L_{70\%} - L^{low}}{L^{high} - L^{low}} \quad (1.7c)$$

where $L_{30\%}$ and $L_{70\%}$ are relative to the 30% drop and the 70% drop with respect to L^{high}, occurring in the correspondence of the currents $I_{30\%}$ and $I_{70\%}$ respectively. An example of comparison between the datasheet L *vs* i_L curve and the curve modeled by means of the arctangent function (1.6) is shown in Fig. 1.4.

Some power inductors manufacturers provide data describing the change of the L *vs* i_L curves with temperature. Mostly, the curves available in datasheets present a horizontal left-side drift with increasing temperature [17], as shown in Fig. 1.5. Starting

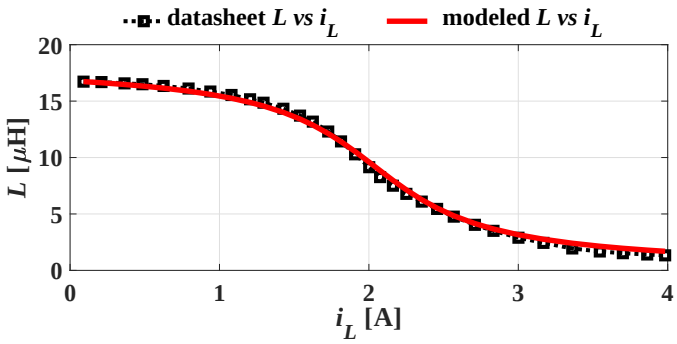

Figure 1.4: Datasheet and modeled L *vs* i_L curve of a FPI.

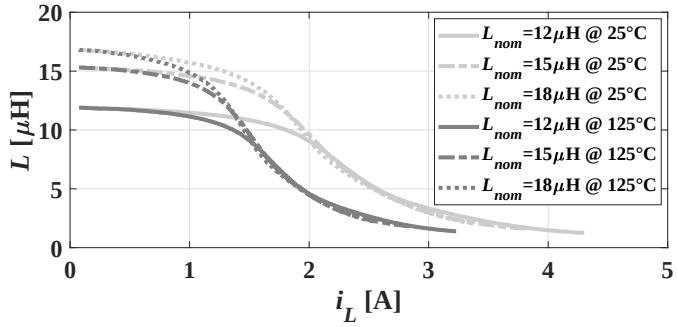

Figure 1.5: Temperature impact on datasheet L *vs* i_L curves.

from the L *vs* i_L curves relative to two different reference temperatures (namely, T_α and T_β), thermal coefficients $\partial_{30\%}$ and $\partial_{70\%}$ can be determined for the current values $I_{30\%}$ and $I_{70\%}$:

$$\partial_{30\%} = \frac{I_{30\%@T_\beta} - I_{30\%@T_\alpha}}{I_{30\%@T_\alpha}\,(T_\beta - T_\alpha)} \qquad \partial_{70\%} = \frac{I_{70\%@T_\beta} - I_{70\%@T_\alpha}}{I_{70\%@T_\alpha}\,(T_\beta - T_\alpha)} \tag{1.8}$$

From (1.8), the temperature impact on $I_{30\%}$ and $I_{70\%}$ can be evaluated through (1.9):

$$I_{30\%}(T) = I_{30\%@T_\alpha}\,[1 + \partial_{30\%}(T - T_\alpha)] \tag{1.9a}$$
$$I_{70\%}(T) = I_{70\%@T_\alpha}\,[1 + \partial_{70\%}(T - T_\alpha)] \tag{1.9b}$$

Therefore, from (1.9) the updated temperature-dependent values of σ and I_L^* can be determined by means of (1.7a) and (1.7b).

1.4 Method for Inductor Current Reconstruction

This Section discusses a generalized method for predicting FPIs behavior in SMPS applications, including possible inductor operation in saturation, with a reliable evaluation of the current ripple. Such method and relative numerical algorithm are valid for both Continuous Conduction Mode (CCM) and Discontinuous Conduction Mode (DCM) operation, as well as for both Synchronous Rectification (SR) and Diode Rectification (DR) topologies of SMPSs. Fig. 1.6 depicts the three basic converter topologies considered for the investigation. The main quantities of interest relevant to buck,

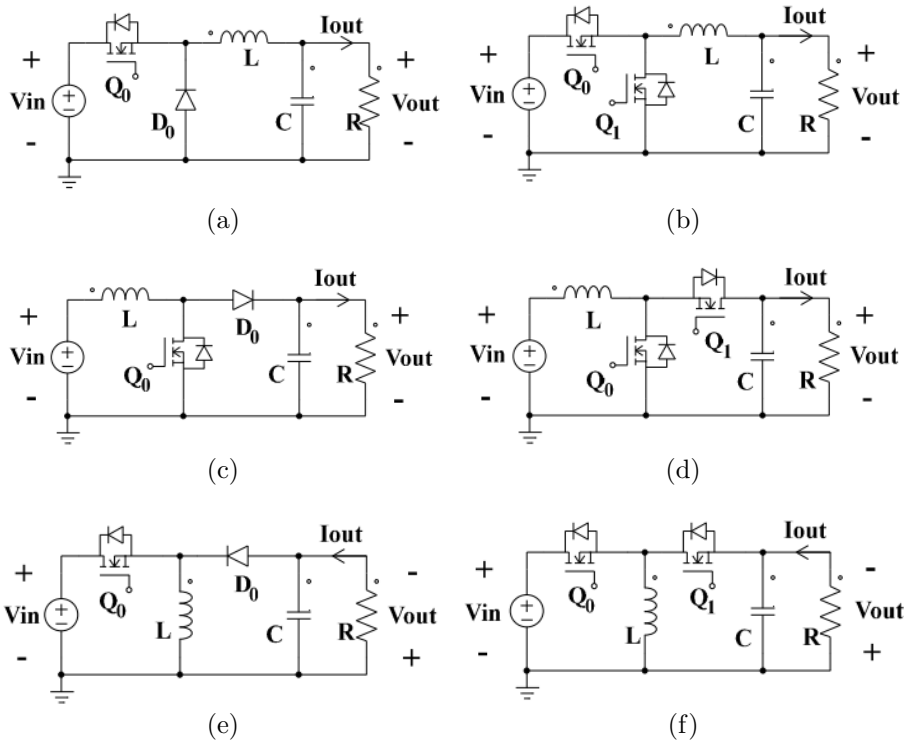

Figure 1.6: Converter topologies: (a) DR buck; (b) SR buck; (c) DR boost; (d) SR boost; (e) DR buck-boost; (f) SR buck-boost.

Table 1.1: Main quantities for buck, boost and buck-boost.

Topology	buck	boost	buck-boost
Average current in inductor [A]	I_{out}	$I_{out}/(1-D)$	$I_{out}/(1-D)$
Average current in diode D_0/ switch Q_1 [A]	$I_{out}(1-D)$	I_{out}	I_{out}
Average current in switch Q_0 [A]	$I_{out}D$	$I_{out}D/(1-D)$	$I_{out}D/(1-D)$
Average rise voltage in inductor [V]	$V_{in}-V_{out}$	V_{in}	V_{in}
Average fall voltage in inductor [V]	$-V_{out}$	$V_{in}-V_{out}$	$-V_{out}$
Switch Q_0 duty-cycle (in CCM)	V_{out}/V_{in}	$1-V_{in}/V_{out}$	$V_{out}/(V_{in}+V_{out})$

boost and buck-boost converters operating in CCM are listed in Table 1.1.

The converter achieves output voltage V_{out} regulation thanks to a controller, which adjusts the duty-cycle D until the difference of the output voltage with respect to the desired nominal value is nulled, or reduced below a certain acceptable accuracy threshold. Whatever control technique is implemented, the controller ensures the desired output voltage regulation in steady-state operation at the instant load current. Then, the output, input and inductor currents settle at their due average values, namely I_{out}, I_{in} and I_L respectively. In a buck converter, the energy continues to flow into the load (*via* the inductor) during the entire switching period T_s. Therefore, the average inductor current must be equal to the load current. In a boost or buck-boost converter, the energy flows

into the output (*via* the diode) only during the fall-time interval. Thus, the average diode current must be equal to the load current.

In CCM operation, the converter imposes a square-wave voltage of period T_s to the inductor: a constant positive voltage V_{Lr} is applied to the device during the rise-time interval $T_r = [0, DT_s)$, and a constant negative voltage V_{Lf} is applied to it during the fall-time interval $T_f = [DT_s, T_s]$, as shown in Fig. 1.7(a). If the inductor operates in the weak-saturation region of the L *vs* i_L curve, its inductance is almost equal to the nominal value L_{nom}, and its current presents a triangular wave-shape, as depicted in Fig. 1.7(b). A magnitude of the peak-to-peak current ripple $\Delta i_{Lpp} = I_{pk} - I_{vl}$ can be approximated by (1.10):

$$\Delta i_{Lpp} = \frac{V_{Lr} D}{f_s L_{nom}} \tag{1.10}$$

where $f_s = 1/T_s$ is the converter switching frequency.

If the inductor operates in the roll-off region, its inductance varies with the instantaneous inductor current $i_L(t)$ during the switching period, thus resulting in a cusp-like wave-shape of the ripple (see Fig. 1.7(c)), whose magnitude is not easy to estimate. The next Subsection discusses a method for predicting a wave-shape of such a distorted waveform and evaluating a magnitude of the peak-to-peak current ripple, by using the saturation behavioral model (1.6).

1.4.1 Inductor Saturation Modeling

From (1.6), the instantaneous inductor voltage $v_L(t)$ is related to the current $i_L(t)$ according to (1.11):

$$\begin{aligned} v_L(t) = L\left[i_L\left(t\right)\right]\frac{di_L(t)}{dt} = \frac{1}{2}\left(L^{high} + L^{low}\right)\frac{di_L(t)}{dt} + ... \\ -\frac{1}{\pi}\left(L^{high} - L^{low}\right)\operatorname{atan}\left\{\sigma\left[\left|i_L\left(t\right)\right| - I_L^*\right]\right\}\frac{di_L(t)}{dt} \end{aligned} \tag{1.11}$$

where v_L represents the inductance voltage drop only. Integrating (1.11) between 0 and $t \in T_r$ (within the rise-time interval) yields

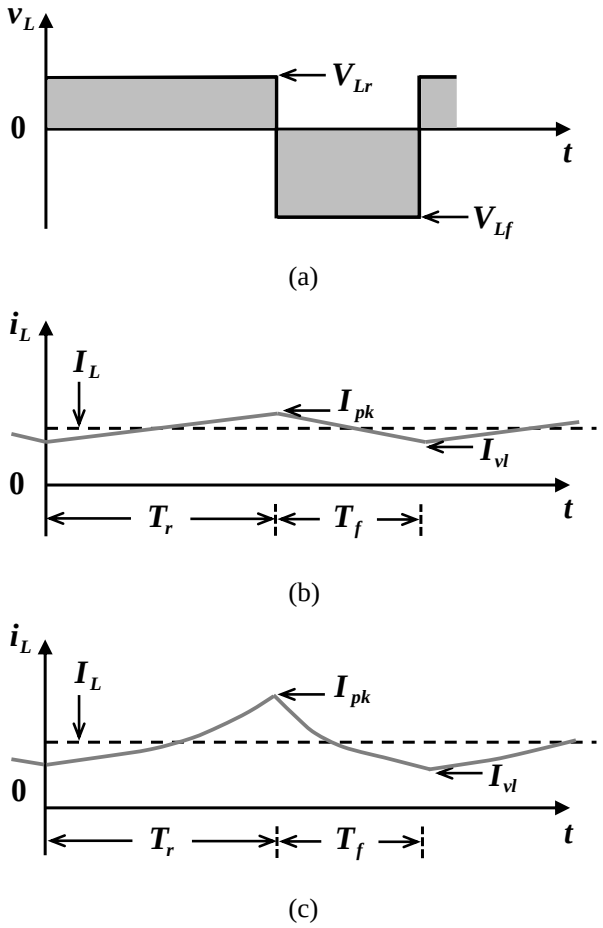

Figure 1.7: Inductor waveforms in CCM: (a) voltage, (b) current in weak-saturation operating condition, (c) current in roll-off operating condition.

(1.12), while integrating (1.11) between DT_s and $t \in T_f$ (within the fall-time interval) provides (1.13):

$$\int_0^t v_L(t)dt = V_{Lr} \cdot t = \int_0^t L\left[i_L(t)\right] \frac{di_L(t)}{dt} dt \qquad (1.12)$$

$$\int_{DT_s}^{t} v_L(t)dt = V_{Lf} \cdot (t - DT_s) = \int_{DT_s}^{t} L\left[i_L\left(t\right)\right] \frac{di_L(t)}{dt} dt \tag{1.13}$$

By solving integrals in (1.12) and (1.13), two main equations can be obtained, provided in (1.14) and (1.15) respectively:

$$\begin{aligned} -V_{Lr} \cdot t + \frac{1}{2}\left(L^{high} + L^{low}\right)\left[i_{Lr}(t) - i_{L0}\right] + ... \\ - \frac{1}{\pi}\left(L^{high} - L^{low}\right) \cdot z\big|_{i_{L0}}^{i_{Lr}(t)} = 0, \qquad for\ t \in T_r \end{aligned} \tag{1.14}$$

$$\begin{aligned} -V_{Lf} \cdot (t - DT_s) + \frac{1}{2}\left(L^{high} + L^{low}\right)\left[i_{Lf}(t) - i_{LD}\right] + ... \\ -\frac{1}{\pi}\left(L^{high} - L^{low}\right) \cdot z\big|_{i_{LD}}^{i_{Lf}(t)} = 0, \qquad for\ t \in T_f \end{aligned} \tag{1.15}$$

where $i_{L0} = i_L(0)$, $i_{LD} = i_L(DT_s)$, $i_{Lr}(t)$ and $i_{Lf}(t)$ are the unknown instantaneous values of the rising and falling inductor currents during T_r and T_f respectively, and z corresponds to the i_L-based indefinite integral given by (1.16):

$$z = z\left(i_L\right) = \int \operatorname{atan}\left[\sigma\left(|i_L| - I_L^*\right)\right] di_L \tag{1.16}$$

In particular, z is equal to z^+ for $i_L \geq 0$ and z^- for $i_L < 0$, given by (1.17a) and (1.17b) respectively:

$$z^+ = (i_L - I_L^*) \operatorname{atan}\left[\sigma\left(i_L - I_L^*\right)\right] - \frac{\log\left[1 + \sigma^2\left(i_L - I_L^*\right)^2\right]}{2\sigma} \tag{1.17a}$$

$$z^- = -\left(i_L + I_L^*\right) \operatorname{atan}\left[\sigma\left(i_L + I_L^*\right)\right] - \frac{\log\left[1 + \sigma^2\left(i_L + I_L^*\right)^2\right]}{2\sigma} \tag{1.17b}$$

According to (1.14), $z(i_L)$ has to be determined between i_{L0} and $i_{Lr}(t)$ during the interval T_r. If both such values are positive, the resulting inductor current waveform is above zero, and it follows

that:

$$z|_{i_{L0}}^{i_{Lr}(t)} = z^{+}|_{i_{L0}}^{i_{Lr}(t)} = ...$$
$$(i_{Lr}(t)-I_L^*)\,\mathrm{atan}\left[\sigma\left(i_{Lr}(t)-I_L^*\right)\right]-\frac{\log\left[1+\sigma^2\left(i_{Lr}(t)-I_L^*\right)^2\right]}{2\sigma}+...$$
$$-\left(i_{L0}-I_L^*\right)\mathrm{atan}\left[\sigma\left(i_{L0}-I_L^*\right)\right]+\frac{\log\left[1+\sigma^2\left(i_{L0}-I_L^*\right)^2\right]}{2\sigma} \tag{1.18}$$

Otherwise, if i_{L0} is negative and $i_{Lr}(t)$ is positive, it results:

$$z|_{i_{L0}}^{i_{Lr}(t)} = z^{-}|_{i_{L0}}^{0} + z^{+}|_{0}^{i_{Lr}(t)} = ...$$
$$(i_{Lr}(t)-I_L^*)\,\mathrm{atan}\left[\sigma\left(i_{Lr}(t)-I_L^*\right)\right]-\frac{\log\left[1+\sigma^2\left(i_{Lr}(t)-I_L^*\right)^2\right]}{2\sigma}+...$$
$$+\left(i_{L0}+I_L^*\right)\mathrm{atan}\left[\sigma\left(i_{L0}+I_L^*\right)\right]-\frac{\log\left[1+\sigma^2\left(i_{L0}+I_L^*\right)^2\right]}{2\sigma}+...$$
$$-2I_L^*\mathrm{atan}\left[\sigma I_L^*\right]+\frac{\log\left[1+\sigma^2\left(I_L^*\right)^2\right]}{2\sigma} \tag{1.19}$$

According to (1.15), $z(i_L)$ has to be determined between i_{LD} and $i_{Lf}(t)$ during the interval T_f. Similarly, if both such values are positive, it follows that:

$$z|_{i_{LD}}^{i_{Lf}(t)} = z^{+}|_{i_{LD}}^{i_{Lf}(t)} = ...$$
$$(i_{Lf}(t)-I_L^*)\,\mathrm{atan}\left[\sigma\left(i_{Lf}(t)-I_L^*\right)\right]-\frac{\log\left[1+\sigma^2\left(i_{Lf}(t)-I_L^*\right)^2\right]}{2\sigma}+...$$
$$-\left(i_{LD}-I_L^*\right)\mathrm{atan}\left[\sigma\left(i_{LD}-I_L^*\right)\right]+\frac{\log\left[1+\sigma^2\left(i_{LD}-I_L^*\right)^2\right]}{2\sigma} \tag{1.20}$$

Otherwise, if i_{LD} is positive and $i_{Lf}(t)$ is negative, it results:

$$
\begin{aligned}
z|_{i_{LD}}^{i_{Lf}(t)} &= z^{+}|_{i_{LD}}^{0} + z^{-}|_{0}^{i_{Lf}(t)} = ... \\
-\left(i_{Lf}(t)+I_L^*\right)\operatorname{atan}\left[\sigma\left(i_{Lf}(t)+I_L^*\right)\right] &+ \frac{\log\left[1+\sigma^2\left(i_{Lf}(t)+I_L^*\right)^2\right]}{2\sigma} + ... \\
-\left(i_{LD}-I_L^*\right)\operatorname{atan}\left[\sigma\left(i_{LD}-I_L^*\right)\right] &+ \frac{\log\left[1+\sigma^2\left(i_{LD}-I_L^*\right)^2\right]}{2\sigma} + ... \\
+2I_L^*\operatorname{atan}\left[\sigma I_L^*\right] &- \frac{\log\left[1+\sigma^2\left(I_L^*\right)^2\right]}{2\sigma}
\end{aligned}
\tag{1.21}
$$

Equations (1.14) and (1.15) can be solved with respect to the inductor current $i_{L,x}(t)$ ($x = \{r, f\}$) only in numerical form. However, the inductor currents in $t = 0$ and $t = DT_s$ are not known in advance, so an iterative procedure and guess values for i_{L0} and i_{LD} are needed. A possible guess value $i_{L0,guess}$ of the valley inductor current can be determined starting from the peak-to-peak current ripple evaluated in non-saturated condition for triangular inductor current wave-shape (see Eq. (1.10)), according to (1.22):

$$
i_{L0,guess} = I_L - \frac{V_{Lr}D}{2f_sL_{nom}} \tag{1.22}
$$

Given $i_{L0,guess}$, equation (1.14) can be solved in numerical form in $t = DT_s$ to find $i_{LD,guess}$. From these guess values, (1.14) and (1.15) must be solved within the intervals T_r and T_f to get the values of the inductor current in a given number of sampling points N_s for each interval. The following Subsections discuss a procedure for proper selection of sampling points over the switching period, and the resulting inductor current reconstruction in CCM and DCM.

1.4.2 Current Reconstruction in CCM

Inductor Operation with Positive Currents

If the inductor operates in CCM with a limited magnitude of the peak-to-peak current ripple and its resulting current waveform is

always above zero during the switching period, a good reconstruction of the current wave-shape within each time interval can be achieved by means of five time samples ($N_s = 5$) as shown in Fig. 1.8, corresponding to:

- the starting instant t_s;
- the ending instant t_e;
- the middle instant t_m, given by the intersection of the tangents in t_s and t_e;
- the left middle instant t_{lm}, given by the intersection of the tangents in t_s and t_m;
- the right middle instant t_{rm}, given by the intersection of the tangents in t_m and t_e.

Samples and corresponding time instants are shown for the rise-time interval T_r in Fig. 1.8, indicated with subscript "1". Samples and time instants relative to the fall-time interval T_f will be hereinafter indicated with subscript "2". The tangents to the current waveform in t_s, t_m and t_e instants are indicated as f_s, f_m

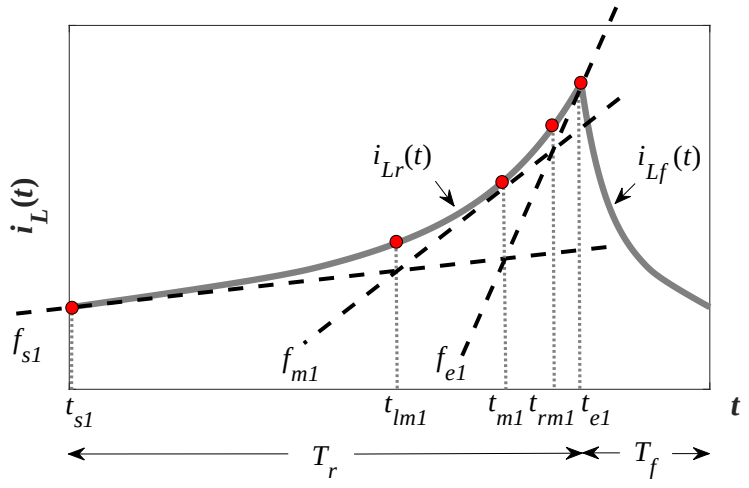

Figure 1.8: Typical saturated current waveform of a FPI in CCM.

and f_e, respectively. The flow diagrams given in Fig. 1.9 summarize the entire procedure to calculate the samples of the inductor current over the switching period. Let us refer to the rise-time interval $T_r = [0, DT_s]$. Thus, $t_{s1} = 0$ and $t_{e1} = DT_s$. Let us suppose that the inductor current $i_L(t_{s1}) = i_{L0}$ is known. Given i_{L0}, a root-finding algorithm can be applied to equation (1.14) to find the value $i_L(t_{e1}) = i_{LD}$: in this circumstance, it is $t = DT_s$ in (1.14) and $i_{Lr}(t) = i_{LD}$ is the unknown. Since the inductor current is never negative during the switching period in this particular case study, the integral solution for $z(i_L)$ refers to positive i_L values only. For both i_{L0} and i_{LD}, (1.6) provides the relevant dynamic inductance L and, for each sample, the ratio between the inductor voltage V_{Lr} and the inductance L allows to evaluate the inductor current slope di_L/dt, useful for the analytical expression of the tangents f_{s1} and f_{e1}, as highlighted in Fig. 1.9. The tangents to the inductor current in t_{s1} and t_{e1} intersect each other at the time instant t_{m1}. Given i_{L0}, a root-finding algorithm can be applied again to equation (1.14) to find the value of $i_L(t_{m1})$: in this circumstance, it is $t = t_{m1}$ in (1.14) and $i_{Lr}(t) = i_L(t_{m1})$ is the unknown. Then, the tangent to the inductor current in t_{m1} can be determined. It intersects the tangent in t_{s1} and the tangent in t_{e1} in correspondence of the time instants t_{lm1} and t_{rm1}, respectively. Finally, applying a root-finding algorithm to equation (1.14), $i_L(t_{lm1})$ and $i_L(t_{rm1})$ can be found. Thus, the five samples within T_r interval are obtained. A similar approach can be used to obtain the current samples and the corresponding time instants t_{s2}, t_{lm2}, t_{m2}, t_{rm2} and t_{e2} in the fall-time interval $T_f = [DT_s, T_s]$, by applying a root-finding algorithm to equation (1.15) and assuming $t_{s2} = t_{e1} = DT_s$, $t_{e2} = T_s$, $i_L(t_{s2}) = i_L(t_{e1}) = i_{LD}$. The number of samples N_s can influence the accuracy and reliability of the inductor current prediction. Under certain operating conditions yielding deeper inductor saturation levels, more samples could be needed to achieve a good reconstruction of the inductor current wave-shape, as shown hereinafter.

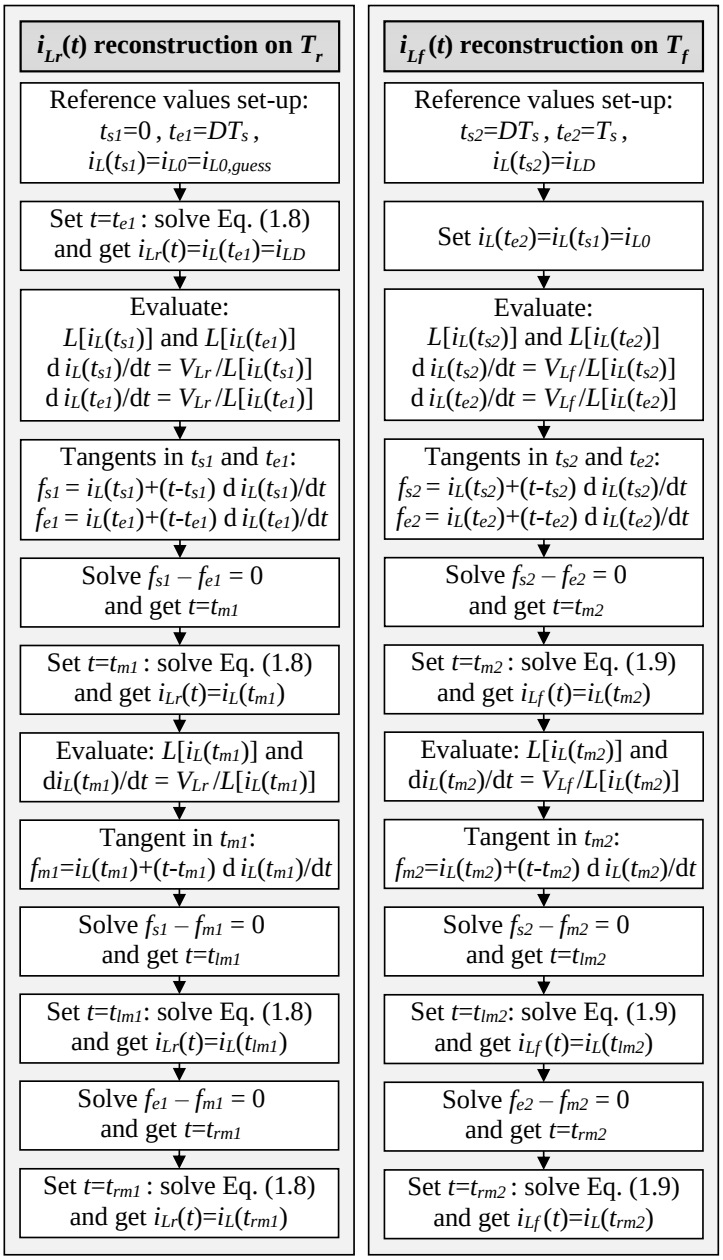

Figure 1.9: Algorithm for inductor current wave-shape reconstruction including positive current values.

Inductor Operation with Positive and Negative Currents

If the inductor operates in SR converters with a high magnitude of the peak-to-peak current ripple, its resulting current waveform may become negative for a certain portion of the switching period. In this case the tangents f_s and f_e, used to identify the sampling time instant t_m, may intersect each other outside the interval of reference, thus causing a failure of the inductor current reconstruction procedure discussed so far. This is due to the fact that the inductor current waveform is concave on a negative range and convex on a positive range, as depicted in Fig. 1.10. To avoid algorithm failures when both positive and negative inductor currents are present (or, equivalently, when i_{L0} and i_{LD} have opposite sign), the two middle instants t_{m1} and t_{m2} relative to the intervals T_r and T_f have to correspond to zero-crossings of the inductor current in the respective intervals. An example of the resulting samples in such operating conditions is given in Fig. 1.10, relative to the rise-time interval T_r. The flow diagram given in Fig. 1.11 summarizes the entire procedure to calculate

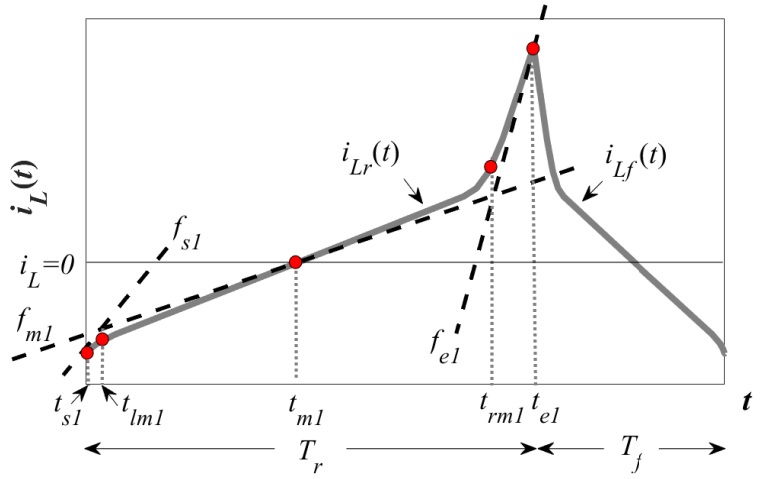

Figure 1.10: Typical saturated current waveform of a FPI in CCM including positive and negative current values.

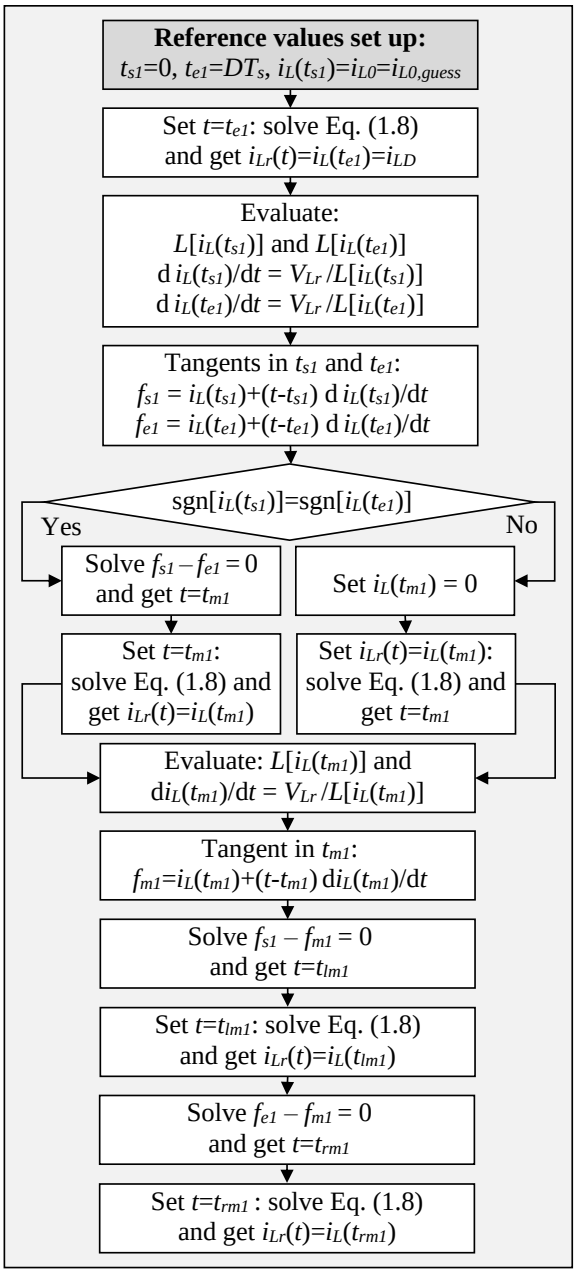

Figure 1.11: Algorithm for inductor current wave-shape reconstruction including positive and negative current values.

the five samples of the inductor current over the same interval. The unique difference with respect to the flow diagram of Fig. 1.9 is that, if i_{L0} and i_{LD} have opposite sign, the time instant t_{m1} has to be automatically fixed at $i_L = 0$: in this circumstance, it is $i_{Lr}(t_{m1}) = 0$ in (1.14) and $t = t_{m1}$ is the unknown. A similar approach can be used to obtain the current samples and the corresponding time instants in the fall-time interval T_f, by replacing subscript "1" with subscript "2", Eq. (1.14) with Eq. (1.15) and V_{Lr} with V_{Lf} (in the gray shaded block, consider $t_{s2} = t_{e1} = DT_s$, $t_{e2} = T_s$, $i_L(t_{s2}) = i_{LD} = i_L(t_{e1})$). Thus the flow diagram of Fig. 1.11, including the case of inductor current wave-shapes with both positive and negative values, generalizes the results of the flow diagram of Fig. 1.9, which is valid for inductor current wave-shape reconstruction when only positive current values are involved.

Inductor Current Ripple Evaluation

In the above procedure for inductor current reconstruction, all the samples have been calculated assuming that the value of i_{L0} is known. The calculation of i_{L0}, i_{LD} and of the resulting current ripple can be achieved by means of the flow diagram shown in Fig. 1.12, given the converter operating conditions $\{V_{in}, V_{out}, I_{out}, f_s\}$ and the inductors parameters $\left\{L^{high}, L^{low}, \sigma, I_L^*\right\}$. In particular, starting from the guess reference value $i_{L0,guess}$ (estimated by means of Eq. (1.22)), the inductor current wave-shape reconstruction is performed for the rise-time and the fall-time intervals by means of the generalized procedure given in the flow diagram of Fig. 1.11. Such reconstruction is iteratively updated, until the resulting average output current $\tilde{I}_{out}$ of the reconstructed wave-shape corresponds to the assigned load current I_{out}. In fact, by using the previous current samples, we can impose that:

$$I_{out} = f_s \int_0^{T_s} i_{out}(t)dt \cong f_s \left(\frac{\Psi_r + \Psi_f}{2} \right) = \tilde{I}_{out} \qquad (1.23)$$

where $1/2(\Psi_r + \Psi_f)$ is an approximation of the integral of $i_{out}(t)$ *via* the trapezoidal method, starting from the inductor current

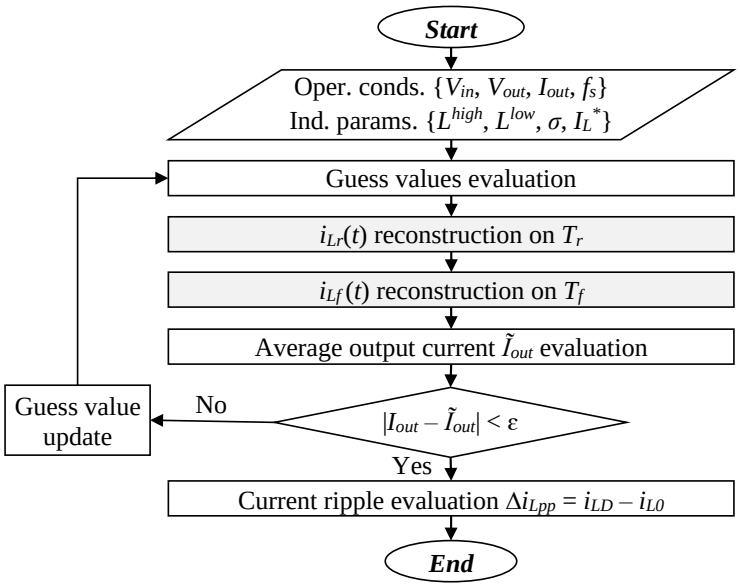

Figure 1.12: Generalized algorithm for inductor current reconstruction and ripple evaluation.

wave-shape reconstruction. In particular, $1/2\Psi_r$ and $1/2\Psi_f$ are the approximations of the integral over the rise-time and the fall-time interval, respectively. In a buck converter, the effective average inductor current I_L is equal to the average output current I_{out} (see Table 1.1), so that $\Psi_r \neq 0$ and $\Psi_f \neq 0$ are both needed to evaluate $\tilde{I}_{out}$. Such quantities are given by (1.24) and (1.25):

$$\begin{aligned}\Psi_r = &[i_L(t_{s1})+i_L(t_{lm1})](t_{lm1}-t_{s1})+[i_L(t_{lm1})+i_L(t_{m1})](t_{m1}-t_{lm1})+\ldots\\ &+[i_L(t_{m1})+i_L(t_{rm1})](t_{rm1}-t_{m1})+[i_L(t_{rm1})+i_L(t_{e1})](t_{e1}-t_{rm1})\end{aligned} \tag{1.24}$$

$$\begin{aligned}\Psi_f = &[i_L(t_{s2})+i_L(t_{lm2})](t_{lm2}-t_{s2})+[i_L(t_{lm2})+i_L(t_{m2})](t_{m2}-t_{lm2})+\ldots\\ &+[i_L(t_{m2})+i_L(t_{rm2})](t_{rm2}-t_{m2})+[i_L(t_{rm2})+i_L(t_{e2})](t_{e2}-t_{rm2})\end{aligned} \tag{1.25}$$

For a boost or buck-boost converter, the current of the diode D_0 (or the MOSFET Q_1 in SR converters) can instead be used

as a reference to evaluate $\tilde{I}_{out}$, since the average diode current I_D (or the average MOSFET current in SR topologies) is equal to the average output current I_{out} (see Table 1.1). In such conditions, $\Psi_r = 0$ and $\Psi_f \neq 0$ have to be adopted to evaluate $\tilde{I}_{out}$ in (1.23). For each iteration of the algorithm given in Fig. 1.12, the difference $|I_{out} - \tilde{I}_{out}|$ is determined: if it is lower than a minimum acceptable error ϵ (ϵ = 1e-5 in this study), then the loop is terminated, otherwise the reference guess value ($i_{L0,guess}$) is updated based on a linear law. In particular, the new value of $i_{L0,guess}$ is obtain as:

$$i_{L0,guess(new)} = i_{L0,guess} + \delta_i(I_{out} - \tilde{I}_{out}) \tag{1.26}$$

where the factor δ_i determines the convergence speed and the stability of the algorithm ($\delta_i = 0.1$ in this study).

1.4.3 Current Reconstruction in DCM

If the inductor operates in DR converters with a high magnitude of the peak-to-peak current ripple, its resulting current waveform may become zero for a certain portion of the switching period, thus causing inductor operation in DCM. Under these circumstances, a constant positive voltage V_{Lr} is applied to the inductor during the rise-time interval $T_r = [0, D_1T_s)$ and a constant negative voltage V_{Lf} is applied to it during the fall-time interval $T_f = [D_1T_s, (D_1 + D_2)T_s)$, while both inductor voltage and current are zero during the idle-time interval $T_i = [(D_1 + D_2)T_s, T_s]$, as depicted in Fig. 1.13, where the inductor current waveform is relative to operating conditions involving saturation.

Equations (1.14) and (1.15) are still valid in DCM. However, since the inductor current is never negative during the switching period, the integral solution for $z(i_L)$ refers to positive i_L values only. The inductor currents $i_{Lr}(t)$ for $t \in T_r$ and $i_{Lf}(t)$ for $t \in T_f$ are two unknowns of interest in (1.14) and (1.15), which can be numerically solved only if D_1 and D_2 are known. In fact, in this condition, $i_L(0) = i_L[(D_1 + D_2)T_s] = i_L(Ts) = 0$. Let us consider that for inductor operation in CCM, $D_1 = D$ and $D_2 = 1 - D$ are

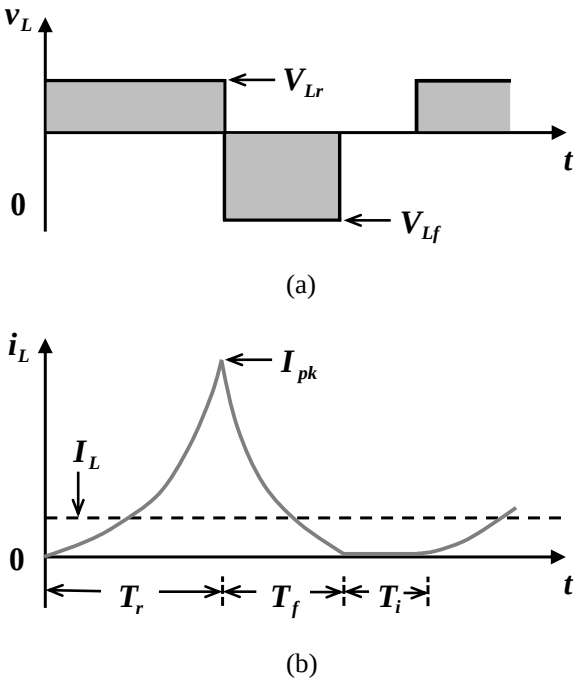

Figure 1.13: Inductor waveforms in DCM: (a) voltage, (b) current in roll-off operating condition.

known in advance because of the inductor volt-second balance [24], whereas i_{L0} is not. In such a case, an appropriate current guess value must be used and an iterative procedure adopted in order to find a correct i_{L0} value, giving a proper inductor current reconstruction with the desired average current value. Conversely, for inductor operation in DCM, the i_{L0} value is always zero and D_1 and D_2 must be iteratively evaluated, until the desired average inductor current is obtained. Guess values for D_1 and D_2 (namely, $D_{1,guess}$ and $D_{2,guess}$) can be obtained assuming the inductor operation in a non-saturated condition, with a triangular current wave-shape. From the inductor volt-second balance and output capacitor charge balance [24], $D_{1,guess}$ and $D_{2,guess}$ values can be estimated for each converter topology. From the inductor

volt-second balance over a switching period, it follows:

$$V_L = f_s \int_0^{T_s} v_L(t)dt = 0 \quad \Rightarrow \quad V_{Lr}D_1 + V_{Lf}D_2 = 0 \qquad (1.27)$$

From the output capacitor charge balance obtained for a triangular inductor current wave-shape, for buck topology it is:

$$I_C = I_L - I_{out} = 0 \quad \Rightarrow \quad I_{out} = \frac{1}{2}\frac{V_{Lr}D_1T_s}{L}(D_1+D2) \qquad (1.28)$$

whereas for boost and buck-boost topologies it follows:

$$I_C = I_D - I_{out} = 0 \quad \Rightarrow \quad I_{out} = \frac{1}{2}\frac{V_{Lr}D_1T_s}{L}D2 \qquad (1.29)$$

By solving (1.27) and (1.28) for $\{D_1, D_2\}$, the following guess values can be obtained for the buck converter:

$$D_{1,guess} = \sqrt{\frac{-2LV_{Lf}I_{out}}{V_{Lr}(V_{Lr}-V_{Lf})T_s}} \quad D_{2,guess} = -\frac{V_{Lr}}{V_{Lf}}D_{1,guess} \qquad (1.30)$$

By solving (1.27) and (1.29) for $\{D_1, D_2\}$, the following guess values can be obtained for the boost and buck-boost converters:

$$D_{1,guess} = \sqrt{\frac{-2LV_{Lf}I_{out}}{V_{Lr}^2T_s}} \qquad D_{2,guess} = -\frac{V_{Lr}}{V_{Lf}}D_{1,guess} \qquad (1.31)$$

Given $D_{1,guess}$ and $D_{2,guess}$, (1.14) and (1.15) must be solved within the time intervals T_r and T_f, in order to obtain the inductor current values in a given number of sampling points N_s for each interval. An example of the resulting samples in such operating condition is given in Fig. 1.14, where samples and corresponding time instants are shown for the time interval T_f. The procedure given in the flow diagram of Fig. 1.11 is valid also in DCM to calculate the five samples of the inductor current over the interval T_r. In particular, the following set-up can be adopted: $t_{s1} = 0$, $t_{e1} = D_{1,guess}T_s$, $i_L(t_{s1}) = i_{L0} = 0$, for the rise time interval T_r. If $D_{1,guess}$ is known, the root-finding algorithm can be applied to

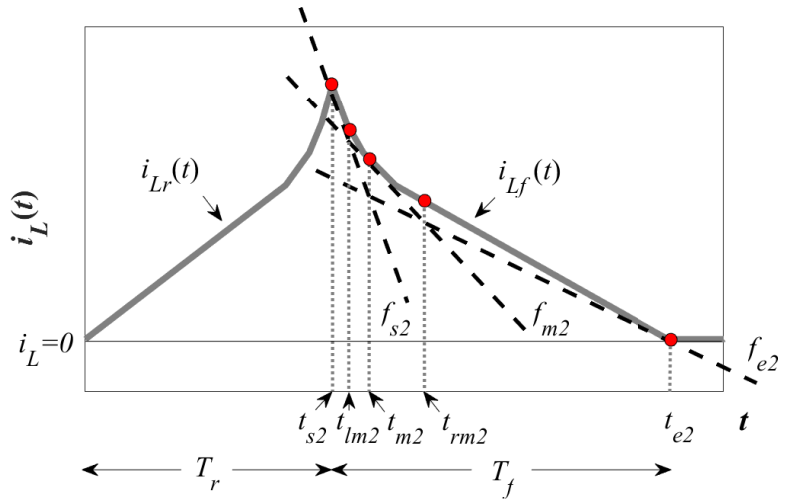

Figure 1.14: Typical saturated current waveform of a FPI in DCM.

(1.14) to find the value $i_L(t_{e1}) = i_{LD}$: in this circumstance, it is $t = D_{1,guess}T_s$ in (1.14) and $i_{Lr}(t) = i_{LD}$ is the unknown. Then, the tangents to the inductor current in t_{s1} and t_{e1} can be evaluated, which intersect within the time interval T_r in $t = t_{m1}$. Given $i_{L0} = 0$, the root-finding algorithm can be applied again to (1.14) to find the value of $i_L(t_{m1})$: in this circumstance, it is $t = t_{m1}$ in (1.14) and $i_{Lr}(t) = i_L(t_{m1})$ is the unknown. The intersections of the tangents to the inductor current in t_{s1} and t_{m1} and of the tangents to the inductor current in t_{m1} and t_{e1} can be determined. They intersect in $t = t_{lm1}$ and $t = t_{rm1}$, respectively. Finally, applying the root-finding algorithm to (1.14), $i_L(t_{lm1})$ and $i_L(t_{rm1})$ can be found. Thus, the five samples $\{t_{s1}, t_{lm1}, t_{m1}, t_{rm1}, t_{e1}\}$ within T_r are obtained. A similar approach can be used to obtain the current samples and the time instants $\{t_{s2}, t_{lm2}, t_{m2}, t_{rm2}, t_{e2}\}$ in the interval T_f by applying the root-finding algorithm to (1.15), assuming $t_{s2} = t_{e1} = D_{1,guess}T_s$, $t_{e2} = (D_{1,guess} + D_{2,guess})T_s$, $i_L(t_{s2}) = i_L(t_{e1}) = i_{LD}$ and $i_L(t_{e2}) = i_L(t_{s1}) = 0$, for the fall time interval T_f. Also in DCM, deeper inductor saturation levels may require more samples for reliable reconstruction of the inductor

current wave-shape.

The flow diagrams of Fig. 1.12 can be used for DCM as well, to analyze the current $i_L(t)$ over the whole switching period T_s, given the converter operating conditions and the inductor parameters. In particular, starting from the guess reference values $D_{1,guess}$ and $D_{2,guess}$, the inductor current wave-shape reconstruction is performed for the rise-time and the fall-time intervals by means of the generalized procedure given in the flow diagram of Fig. 1.11, also including the DCM idle-time interval T_i wherein the inductor current is zero. Such reconstruction is iteratively updated, until the resulting average output current $\tilde{I}_{out}$ of the reconstructed wave-shape corresponds to the assigned load current I_{out}. Regarding the convergence rule given in Fig. 1.12, the unique difference with respect to CCM is that $D_{1,guess}$ value has to be iteratively updated, instead of $i_{L0,guess}$ value, according to (1.32):

$$D_{1,guess(new)} = D_{1,guess} + \delta_i(I_{out} - \tilde{I}_{out}) \tag{1.32}$$

whereas $D_{2,guess(new)}$ is automatically determined as a function of this new value, according to (1.27).

1.5 Experimental Verification

A MATLAB code has been developed to implement the proposed numerical algorithm for inductor current reconstruction. The behavior of the Coilcraft MSS5131-472 inductor has been simulated and tested, both in CCM and in DCM. The method has been validated experimentally for the buck and boost converters, since the FPIs analysis for the buck-boost converter is based on formulas similar to the ones of the boost converter (see Table 1.1). In particular, the results of simulations have been validated through experimental tests realized by means of three Texas Instruments evaluation boards:

- the TPS54160EVM-230 [25], shown in Fig. 1.15(a) and implementing a DR buck, with nominal specifications: V_{in}=6-36V, V_{out}=3.3V, $I_{out,max}$=1.5A, f_s=465kHz;

- the TPS55340EVM-017 [26], shown in Fig. 1.15(b) and implementing a DR boost, with nominal specifications: V_{in}=5-12V, V_{out}=24V, $I_{out,max}$={0.8A@V_{in}=5V, 1.9A@V_{in}=12V}, f_s=600kHz;
- the LM5122EVM-1PH [27], shown in Fig. 1.15(c) and implementing a SR boost, with nominal specifications: V_{in}=9-20V, V_{out}=24V, $I_{out,max}$=4.5A, f_s=250kHz.

For current measurements, the MSS5131-472 part has been connected to each board through a pair of wires allowing to hang a current probe, as shown in Fig. 1.15(a)-(c). The experimental measurements set-up included a LeCroy WaveSurfer 3054 500MHz Oscilloscope, a LeCroy CP030 30A current probe, a Sorensen Electronic Load SLM-4 mainframe with SLM series electronic load modules 60V/60A/300W, a 30V/3A Key Tech DF1731SB dual out DC Power Supply, a Fluke 179 digital multimeter with a type K thermocouple, as shown in Fig. 1.15(d).

Since the inductor saturation curves provided in manufacturers' datasheets are typically subjected to about 20%-30% uncertainty, an identification procedure has been herein adopted to obtain more accurate L *vs* i_L curves at two different reference temperatures. The resulting saturation curves are depicted in Fig. 1.16 for 25°C and 75°C, while the relative identified parameters are given in Table 1.2. From such curves, the parameters {L^{high}, L^{low}, σ, I_L^*} of the arctangent model (1.6) and their thermal dependences have been evaluated according to (1.7)-(1.9). The saturation curves identification procedure is discussed in detail in Chapter 2.

Table 1.2: MSS5131-472 saturation curves parameters.

L^{high} $[\mu H]$	L^{low} $[\mu H]$	$I_{30\%,25^\circ C}$ $[A]$	$I_{70\%,25^\circ C}$ $[A]$	$I_{30\%,75^\circ C}$ $[A]$	$I_{70\%,75^\circ C}$ $[A]$
5.7	0.1	1.43	1.87	1.29	1.64

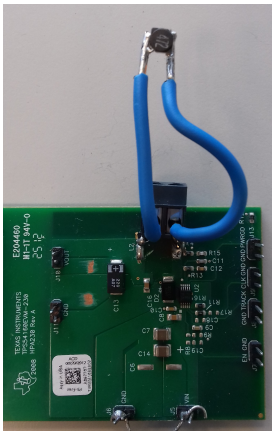

(a)

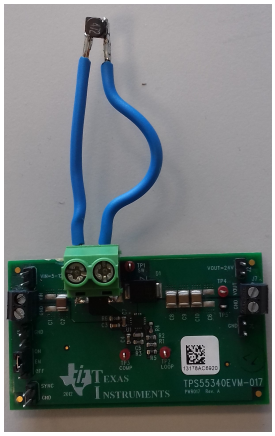

(b)

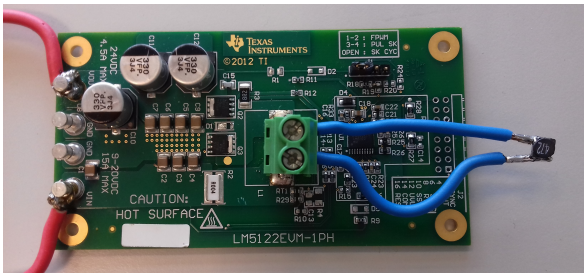

(c)

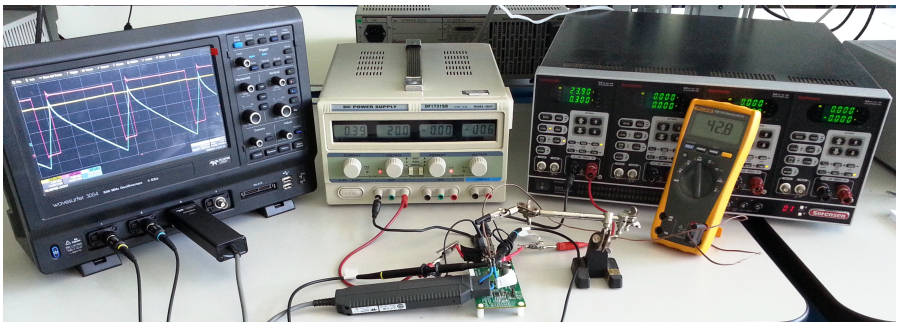

(d)

Figure 1.15: (a)-(c) Evaluation boards adopted for the experimental tests; (d) experimental set-up.

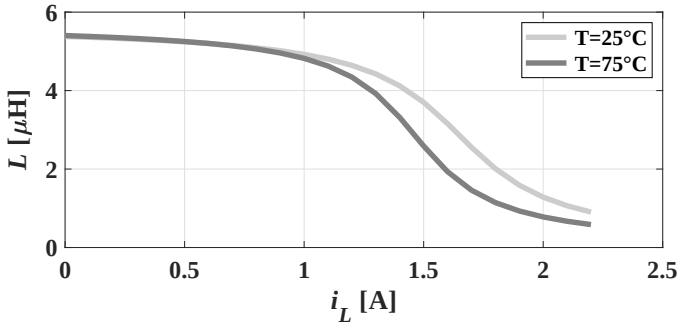

Figure 1.16: MSS5131-472 saturation curves.

Three groups of experimental tests have been performed by means of the evaluation boards of Fig. 1.15(a)-(c), to validate the proposed generalized numerical algorithm for inductor current reconstruction in saturation. First, the TPS54160EVM-230 DR buck board has been adopted to test the MSS5131-472 operation in CCM under conditions of limited current ripple, involving positive current values only, thus validating the inductor current reconstruction procedure described in Subsection 1.4.2 and summarized in the flow diagram of Fig. 1.9. Six different case studies have been considered, whose relative operating conditions are listed in the first part of Table 1.3. Second, the LM5122EVM-1PH SR boost board has been used to test the MSS5131-472 operation in CCM under conditions of high current ripple, involving positive and negative current values, thus validating the inductor current reconstruction procedure described in Subsection 1.4.2 and summarized in the flow diagram of Fig. 1.11. Six analyzed case studies and relative operating conditions are listed in the second part of Table 1.3. Eventually, the TPS55340EVM-017 DR boost board has been used to test the MSS5131-472 operation in DCM, thus validating the inductor current reconstruction procedure described in Subsection 1.4.3. Six analyzed case studies and relative operating conditions are listed in the third part of Table 1.3. For each case study, experimental inductor temperature has also been measured and used to determine the temperature-dependent values

Table 1.3: Case studies and relevant operating conditions.

Case studies		V_{out} $[V]$	f_s $[kHz]$	V_{in} $[V]$	I_{out} $[A]$	T_{exp} $[^{\circ}C]$
DR buck	#1	3.3	465	5	1.00	29.1
	#2			5	1.30	30.4
	#3			5	1.60	32.8
	#4			8	1.00	32.4
	#5			8	1.30	33.3
	#6			8	1.60	35.3
SR boost	#7	24.0	253	18	0.10	58.5
	#8			19	0.10	50.7
	#9			20	0.10	45.8
	#10			19	0.20	51.3
	#11			19	0.25	52.2
	#12			19	0.30	52.8
DR boost	#13	24.2	591	9	0.20	44.6
	#14			9	0.25	46.2
	#15			9	0.30	51.8
	#16			12	0.30	47.1
	#17			12	0.35	49.4
	#18			12	0.40	51.8

of σ and I_L^* of the arctangent model (1.6), adopted during the inductor current reconstruction for the relative case study.

Fig. 1.17(a)-(f), Fig. 1.18(a)-(f) and Fig. 1.19(a)-(f) show the inductor current measurements (green waveforms) and the simulation results (red lines with circle markers) obtained by using the proposed generalized algorithm for the case studies given in Table 1.3 and tested on the DR buck (#1 - #6), SR boost (#7 - #12) and DR boost (#13 - #18), respectively. For higher accuracy, the inductor current ripple prediction has been obtained by using $N_s \geq 5$, requiring MATLAB computing times up to 20 sec.

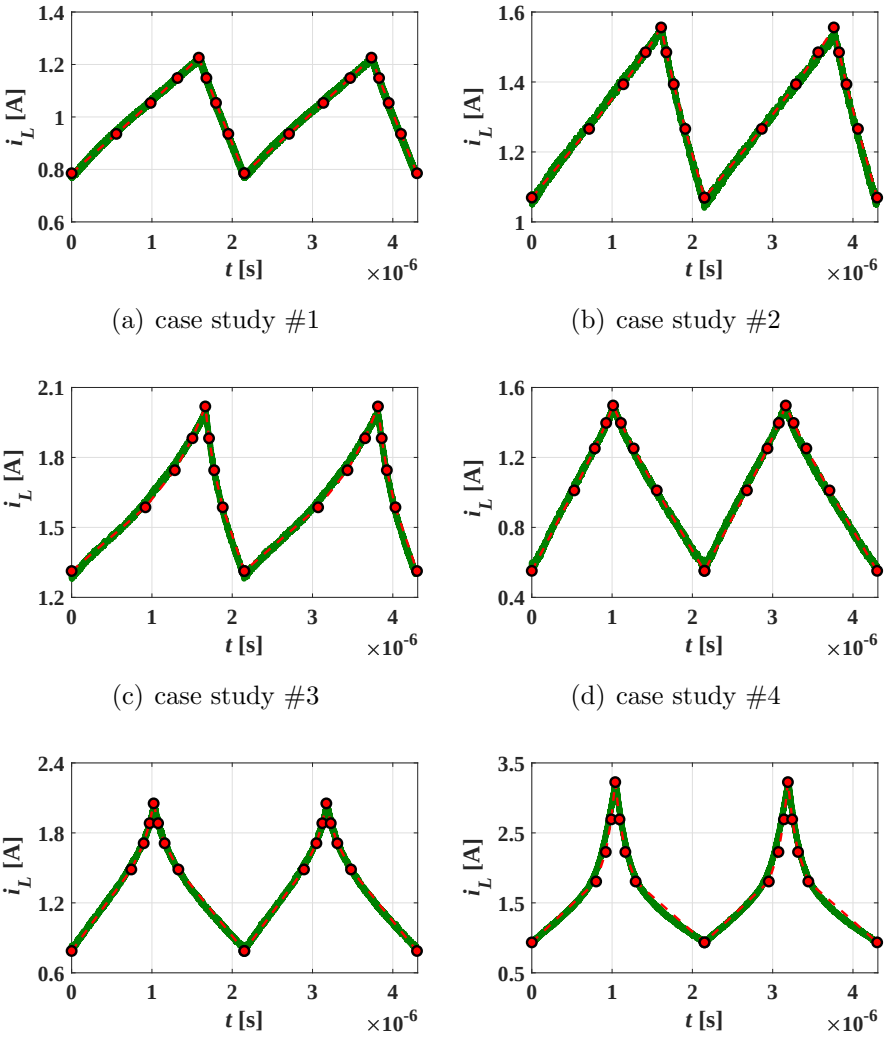

(a) case study #1 (b) case study #2

(c) case study #3 (d) case study #4

(e) case study #5 (f) case study #6

Figure 1.17: MSS5131-472 current waveforms in DR buck: experimental measurements (green waveforms) *vs* simulated reconstructions (red lines with circle markers).

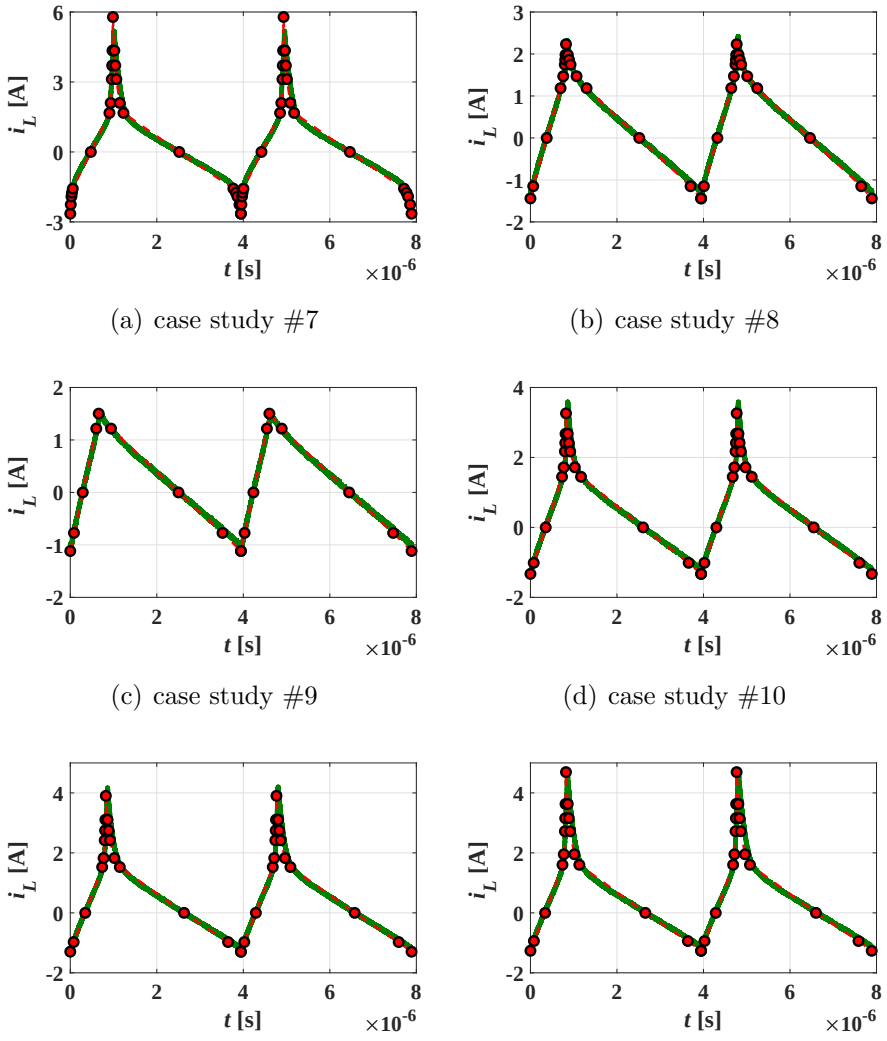

(a) case study #7

(b) case study #8

(c) case study #9

(d) case study #10

(e) case study #11

(f) case study #12

Figure 1.18: MSS5131-472 current waveforms in SR boost: experimental measurements (green waveforms) *vs* simulated reconstructions (red lines with circle markers).

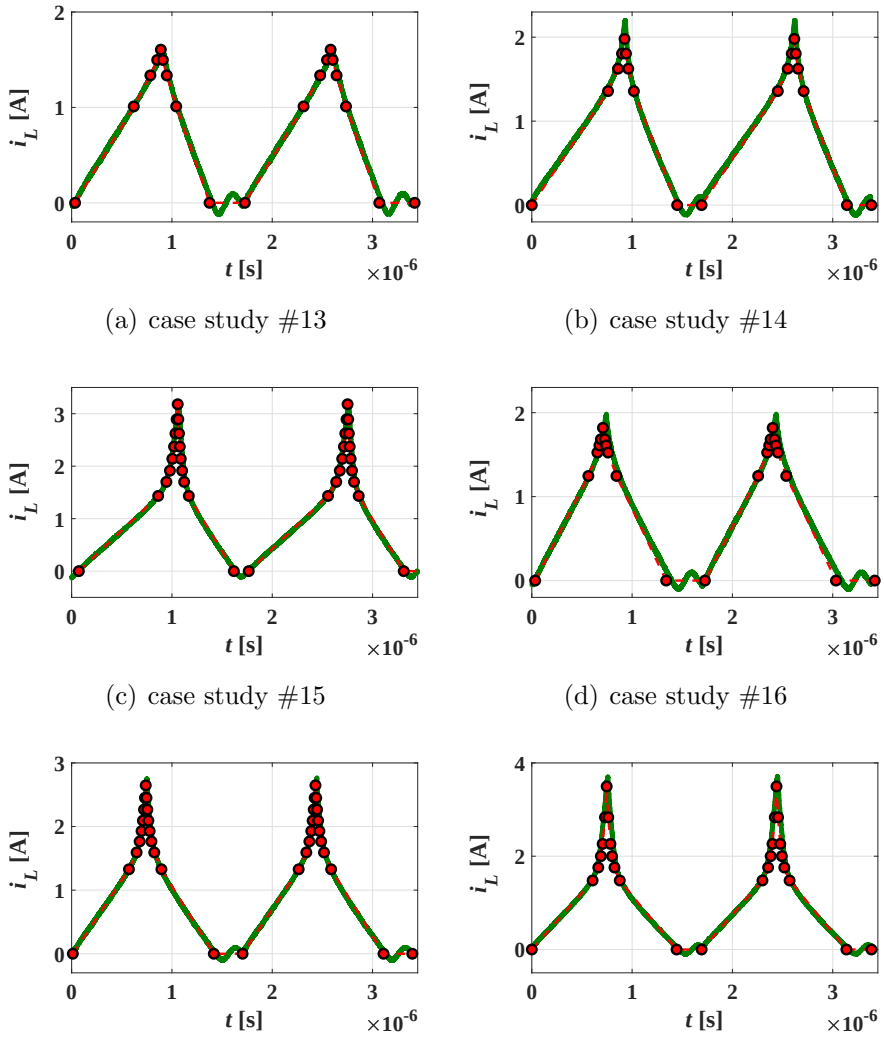

(a) case study #13 (b) case study #14

(c) case study #15 (d) case study #16

(e) case study #17 (f) case study #18

Figure 1.19: MSS5131-472 current waveforms in DR boost: experimental measurements (green waveforms) *vs* simulated reconstructions (red lines with circle markers).

First, a default value $N_s = 5$ has been adopted for each case study, thus obtaining 9 initial samples t_k per switching period, with $k = 1, ..., 9$ (the last sample of the rise-time interval T_r coincides with the first sample of the fall-time interval T_f). Then, a recursive procedure has been implemented to obtain additional current samples in the regions wherein the inductance is strongly variable, determined in the following way. For each couple of the contiguous initial samples t_k and t_{k+1}, an additional intermediate sample t_j has been generated if the percent difference between the respective inductor current slopes $di_L(t_k)/dt$ and $di_L(t_{k+1})/dt$ exceeded a certain threshold (50% in this study). Such sample t_j is given by the intersection of the two tangents to the inductor current waveform in t_k and t_{k+1}. Then, the same recursive procedure has been applied on subintervals $[t_k, t_j]$ and $[t_j, t_{k+1}]$, thus obtaining other additional samples, up to a maximum of N_{max} samples within the interval $[t_k, t_{k+1}]$ ($N_{max} = 2$ in this study).

Fig.s 1.17-1.19 show a very good agreement between the experimental results and simulated current wave-shapes, for all the considered case studies, both in CCM and in DCM. It is worth noting that the ringing of the inductor current waveforms in the DR boost converter (see Fig. 1.19) is due to the coupling of the inductance with the parasitic capacitances of the MOSFET and the diode during the idle-time interval of DCM operation. For each case study, the simulated and experimental peak-to-peak ripple and rms current values are given in Table 1.4. The simulated rms current I_{Lrms} has been estimated by adopting a piece-wise linear approximation of the inductor current waveform, starting from the samples of the current I_k and the respective time instants t_k provided by the proposed inductor current reconstruction algorithm, as given in (1.33):

$$I_{Lrms} \cong \sqrt{\frac{1}{T_s} \sum_{k=1}^{2(N_s-1)} \frac{\left(I_{k+1}^2 + I_{k+1} I_k + I_k^2\right)(t_{k+1} - t_k)}{3}} \qquad (1.33)$$

The results show that the errors on the peak-to-peak and rms values are all limited in the range of ±10% with respect to the

Table 1.4: Experimental *vs* simulated inductor current data.

Case studies		Δi_{Lpp} (exp.) $[A]$	Δi_{Lpp} (sim.) $[A]$	Δi_{Lpp} error $[\%]$	I_{Lrms} (exp.) $[A]$	I_{Lrms} (sim.) $[A]$	I_{Lrms} error $[\%]$
DR buck	#1	0.45	0.44	-2.1	1.01	1.01	∼0
	#2	0.50	0.49	-2.7	1.31	1.31	∼0
	#3	0.72	0.71	-2.0	1.61	1.60	-0.1
	#4	0.93	0.95	1.3	1.04	1.04	∼0
	#5	1.25	1.27	1.2	1.33	1.33	∼0
	#6	2.30	2.29	-0.4	1.69	1.67	-1.0
SR boost	#7	7.83	8.43	7.7	1.34	1.33	-0.9
	#8	3.63	3.68	1.2	0.88	0.93	5.3
	#9	2.53	2.62	3.4	0.72	0.76	5.6
	#10	4.80	4.59	-4.4	1.01	1.01	∼0
	#11	5.37	5.20	-3.1	1.10	1.07	-2.4
	#12	5.80	5.96	2.7	1.18	1.15	-2.4
DR boost	#13	1.60	1.61	0.3	0.79	0.78	-1.1
	#14	2.20	1.98	-9.9	0.94	0.91	-3.3
	#15	3.23	3.18	-1.6	1.14	1.11	-2.6
	#16	1.98	1.82	-8.3	0.86	0.83	-3.9
	#17	2.75	2.65	-3.7	0.10	0.99	-1.0
	#18	3.70	3.50	-5.5	1.19	1.11	-6.5

experimental data. It is worth remarking that case studies like #7 and #12, characterized by very high magnitudes of the peak-to-peak current ripple, have been considered to highlight the reliability of the discussed modeling approach. In real-world SPMS applications, such extreme conditions are avoided for safety and efficiency reasons. Indeed, they are prevented by current limit circuitry integrated in each SMPS. These simulations demonstrate the reliability of the proposed generalized algorithm for inductor current reconstruction in whatever operating conditions, including saturation.

The main outcome of the research activity presented in this Chapter resulted in the publication of the scientific papers:

- G. Di Capua, N. Femia, K. Stoyka, "A Generalized Numerical Method for Ferrite Inductors Analysis in High Current Ripple Operation", *Integration, the VLSI Journal*, vol. 54, pp. 473-484, June 2017.
- G. Di Capua, N. Femia, K. Stoyka, "An Improved Algorithm for the Analysis of Partially Saturated Ferrite Inductors in Switching Power Supplies", *13th Int. Conf. on Synthesis, Modeling, Analysis and Simulation Methods and Appl. to Circuit Design (SMACD)*, June 2016.

Chapter 2

Saturation Curves Identification of Ferrite Inductors

This chapter discusses the identification of the inductance *vs* current (L *vs* i_L) saturation curves for FPIs operating in SMPSs. The experimental L *vs* i_L curves provided in manufacturers' datasheets and on-line tools are typically characterized by high uncertainty levels (*e.g.*, $\pm 20\%$). Moreover, such curves are measured under small-signal sinusoidal voltage test conditions, whereas SMPSs impose large-signal square-wave voltages to the inductors, thus making the manufacturers' data not sufficiently reliable for a realistic determination of the peak-to-peak inductor current ripple in SMPS. The first part of this Chapter discusses the Evolutionary Algorithm-based approach for the L *vs* i_L curves identification starting from experimental measurements performed in real SMPS conditions. Then, an alternative approach is presented, based on the local and global approximations of the inductor saturation characteristic, obtained under small-amplitude and large-amplitude current ripple conditions, respectively.

2.1 Evolutionary Algorithm-based Approach

Evolutionary Algorithms (EAs), like Genetic Algorithm (GA) and Differential Evolution (DE), have been widely used for parameters identification and model parameters extraction of magnetic devices, such as inductors, transformers and magnetic cores. The GA has been adopted to identify the parameters of a π-based physical model for RF inductors in [9]. Immune algorithm and μ-GA have been adopted for topology optimization of inductor shapes in [11]. The geometric programming has been applied to the transformer design optimization problem in [14], to minimize the total mass (or cost) of the core and wire material, while ensuring proper transformer ratings and design constraints, like efficiency, voltage regulation, temperature rise and winding fill factor. In [15], the GA has been adopted to fit the magnetic permeability *vs* frequency characteristics of ferrite cores. The DE method has been used in [16] to extract the parameters of the Jiles-Atherton model for ferrites. Eventually, in [18] it has been proved that the DE ensures better and faster fitting than the GA. For this reason, the DE algorithm has been adopted hereinafter to identify the saturation curves of FPIs operated in SMPSs.

2.1.1 Differential Evolution

Differential Evolution (DE) was developed by Price and Storn in 1995. Like genetic algorithms, the DE repeatedly modifies a population of individual solutions. Each individual is represented by a vector of numeric parameters to be identified during the optimization process. Each vector is assigned a fitness value, which represents its goodness in the population. Like the GAs, the DE uses three typical operators to search the solution space: crossover, mutation and selection. Among these operators, mutation plays a key role in the performance of the DE algorithm [28]. Similarly to the other population-based algorithms, the DE generates new points that are perturbations of existing points; in particular, the

DE perturbs vectors with the scaled difference of two randomly selected population vectors - from here the name "differential" evolution.

To produce the mutant vector for each vector of the current population (target vector), the DE adds the scaled, random vector difference to a third randomly selected population vector (base vector). Then it recombines the obtained mutant vector with the target vector, so as to obtain a trial vector. In the selection stage, the trial vector competes against the population vector of the same index (target vector). The procedure repeats until all the population vectors have competed against a randomly generated trial vector. The survivors of such competitions become parents for the next generation in the evolutionary cycle [29]. The technical name for the described method is *"DE/rand/1/bin"*, because the base vector is randomly chosen, one vector difference is added to it and because the number of parameters donated by the mutant vector during the crossover closely follows a binomial distribution. There exist several DE strategies discussed in literature [28], which use different mutation operators. The above strategy is often referred to as "classic DE". In this study, such strategy has been adopted. A brief overview of key steps of the *"DE/rand/1/bin"* is next presented. A complete description of the DE principles and operation is available in [29].

Population Structure

DE maintains a pair of vector populations, both containing N_p D-dimensional vectors of real-valued parameters. The current population, symbolized by $P_{\mathbf{x}}$, is composed of the vectors $\mathbf{x}_{i,g}$ that have already been found to be acceptable in the previous comparisons:

$$\begin{aligned} &P_{\mathbf{x},g} = (\mathbf{x}_{i,g}), \quad i = 0, 1, ..., N_p - 1, \quad g = 0, 1, ..., g_{max}, \\ &\mathbf{x}_{i,g} = (x_{j,i,g}), \quad j = 0, 1, ..., D - 1 \end{aligned} \tag{2.1}$$

The index $g = 0, 1, ..., g_{max}$ indicates the generation to which a vector belongs. In addition, each vector is assigned a population index i, going from 0 to $N_p - 1$. Parameters within vectors are indexed with j, going from 0 to $D - 1$.

Mutation

Once initialized, the DE mutates randomly chosen vectors to produce an intermediary population $P_{\mathbf{v}}$ of N_p mutant vectors $\mathbf{v}_{i,g}$:

$$\begin{aligned} &P_{\mathbf{v},g} = (\mathbf{v}_{i,g}), \quad i = 0, 1, ..., N_p - 1, \quad g = 0, 1, ..., g_{max}, \\ &\mathbf{v}_{i,g} = (v_{j,i,g}), \quad j = 0, 1, ..., D - 1 \end{aligned} \tag{2.2}$$

In particular, *differential mutation* adds a scaled, randomly selected vector difference to a third vector. Eq. (2.3) shows how to combine three different, randomly chosen vectors to create a mutant vector $\mathbf{v}_{i,g}$:

$$\mathbf{v}_{i,g} = \mathbf{x}_{r0,g} + SF \cdot (\mathbf{x}_{r1,g} - \mathbf{x}_{r2,g}) \tag{2.3}$$

The scale factor $SF \in (0, 1+)$ is a positive real number that controls the rate at which the population evolves. While there is no upper limit on SF, effective values are seldom greater than 1.

The base vector index r_0 is a randomly chosen vector index that is different from the target vector index i. The difference vector indices r_1 and r_2 are also randomly selected, once per mutant, and have to be distinct from each other and from both the base and target vector indices. Such procedure is repeated N_p times, until the mutant population $P_{\mathbf{v}}$ is constructed, containing one mutant vector for every member of the current population $P_{\mathbf{x}}$.

Crossover

Once the mutant population has been generated, each vector in the current population is recombined with the respective mutant vector, to produce a trial population $P_{\mathbf{u}}$ of N_p trial vectors $\mathbf{u}_{i,g}$:

$$\begin{aligned} &P_{\mathbf{u},g} = (\mathbf{u}_{i,g}), \quad i = 0, 1, ..., N_p - 1, \quad g = 0, 1, ..., g_{max}, \\ &\mathbf{u}_{i,g} = (u_{j,i,g}), \quad j = 0, 1, ..., D - 1 \end{aligned} \tag{2.4}$$

In particular, the DE generates a trial vector according to a *uniform crossover* scheme:

$$\mathbf{u}_{i,g} = u_{j,i,g} = \begin{cases} v_{j,i,g}, & \text{if } (rand_j(0,1) \leq C_r \text{ or } j = j_{rand}) \\ x_{j,i,g}, & \text{otherwise} \end{cases} \tag{2.5}$$

The crossover probability $C_r \in [0, 1]$ is a user-defined value that controls the fraction of parameter values that are copied from the mutant. In addition, the trial parameter with randomly chosen index j_{rand} is taken from the mutant to ensure that the trial vector does not duplicate $\mathbf{x}_{i,g}$. During recombination, trial vectors overwrite the mutant population.

Selection

If the trial vector $\mathbf{u}_{i,g}$ has an equal or lower fitness function F value than that of its target vector $\mathbf{x}_{i,g}$, it replaces the target vector in the next generation; otherwise, the target retains its place in the population for at least one more generation:

$$\mathbf{x}_{i,g+1} = \begin{cases} \mathbf{u}_{i,g}, & \text{if } F(\mathbf{u}_{i,g}) \leq F(\mathbf{x}_{i,g}) \\ \mathbf{x}_{i,g}, & \text{otherwise} \end{cases} \tag{2.6}$$

Once the new population is created, the process of mutation, recombination and selection is repeated until the optimum is located, or a pre-specified termination criterion is satisfied, *e.g.*, the number of generations reaches a preset maximum g_{max}. Fig. 2.1 shows a detailed flow diagram of the DE algorithm, proposed by Price and Storn in [29].

2.1.2 Saturation Curves Identification by DE

The L *vs* i_L curves identification has been formulated as an optimization problem and solved by means of the DE, as discussed in [30]. For a given FPI, the goal has been to identify the parameters of the behavioral model (1.6) at two different reference temperatures (namely, T_α and T_β), starting from the experimental measurements of the inductor current and temperature. Once the curves relative to T_α and T_β have been obtained, the curve at whatever temperature T (comprised between T_α and T_β) can be derived by using formulas (1.7)-(1.9).

The DE individual has been composed of the following parameters to be identified $\{L^{high}, L^{low}, I_{30\%@T_\alpha}, I_{70\%@T_\alpha}, I_{30\%@T_\beta}, I_{70\%@T_\beta}\}$,

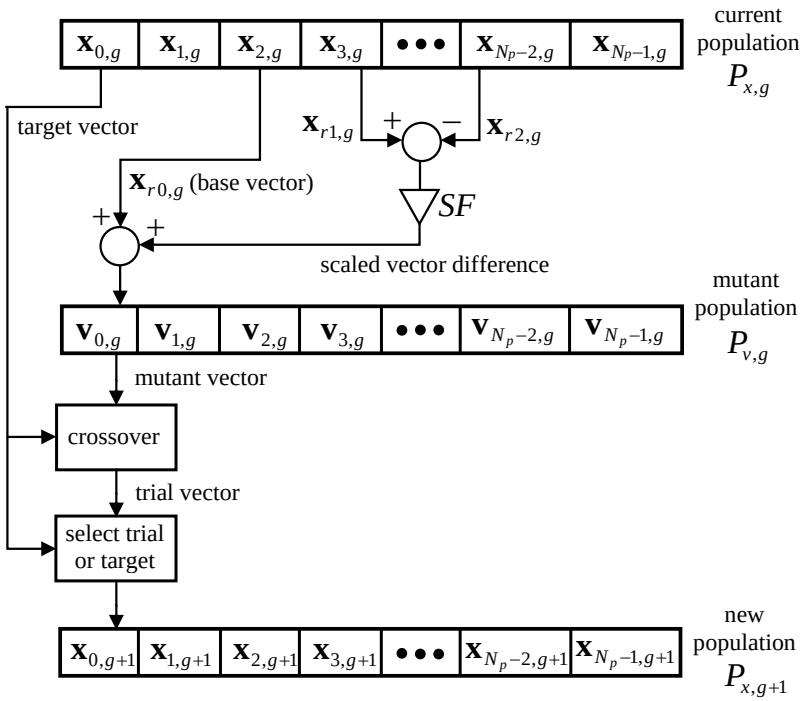

Figure 2.1: Flow diagram of the DE algorithm.

where $I_{X\%,Y}$ represents the saturation current corresponding to the $X\%$ drop of inductance with respect to weak-saturation value L^{high} at given temperature Y. Since L^{high} and L^{low} present a weak temperature sensitivity (see Fig. 1.5), the same values of such parameters have been assumed for T_α and T_β, thus reducing the number of variables to be identified from eight to six parameters. The goal of the DE has been to identify the optimal values of such parameters, providing the best fitting between the experimental inductor current waveforms and the respective wave-shapes reconstructed by means of the generalized algorithm described in Chapter 1. N different case studies have been considered, resulting in N different inductor current waveforms and temperatures. The fitness function F given in (2.7) has been adopted for the DE minimization:

$$F = \sqrt{\sum_{i=1}^{N} \left[\left(\frac{I_{PKsim,i} - I_{PKexp,i}}{I_{PKexp,i}} \right)^2 + \left(\frac{I_{Vsim,i} - I_{Vexp,i}}{I_{Vexp,i}} \right)^2 \right]} \quad (2.7)$$

where $\{I_{PKexp,i}, I_{Vexp,i}\}$ are the experimental peak and valley current values and $\{I_{PKsim,i}, I_{Vsim,i}\}$ are the corresponding simulated values, with $i = 1, ..., N$. The flow diagram of Fig. 2.2 depicts a procedure to evaluate the fitness function F of each individual in the DE population, given the converter operating conditions and experimental data of inductor current $i_L(t)$ and temperature T for

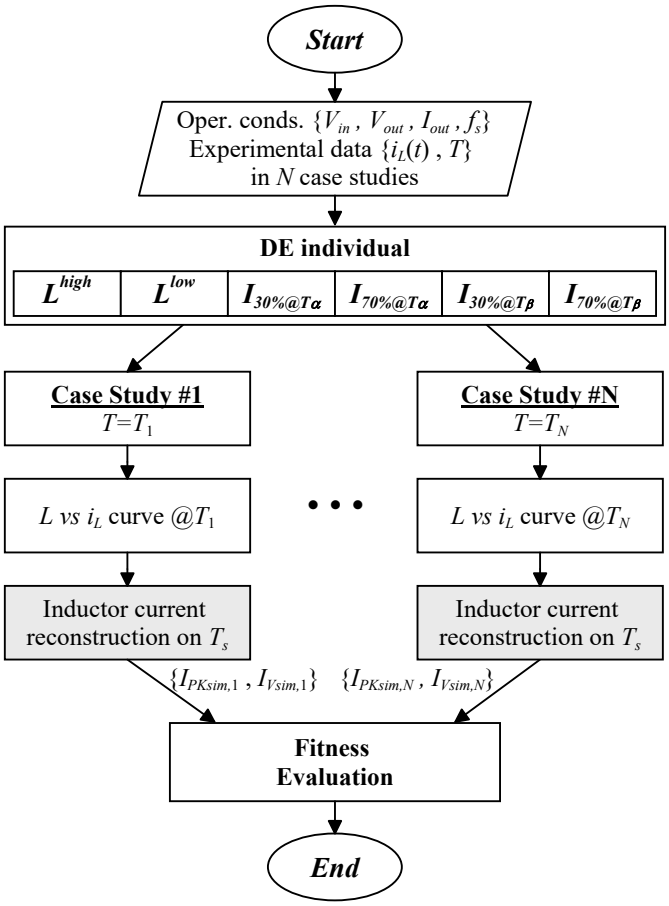

Figure 2.2: Flow diagram for fitness evaluation.

the N analyzed case studies. In particular, for the i-th case study, the L *vs* i_L curve is updated at temperature T_i by using formulas (1.7)-(1.9) and parameters $\{L^{high}, L^{low}, I_{30\%@T_\alpha}, I_{70\%@T_\alpha}, I_{30\%@T_\beta}, I_{70\%@T_\beta}\}$ given by the DE individual. Then, the inductor current wave-shape is reconstructed by means of the algorithm of Fig. 1.12, thus providing $\{I_{PKsim,i}, I_{Vsim,i}\}$ values, which are used to compute the fitness function over the N analyzed case studies.

2.1.3 Case Studies and Discussion

Experimental data, used by the DE to identify the FPIs saturation curves, have been obtained by using the Texas Instruments TPS54160EVM-230 buck converter evaluation board [25], with nominal specifications: V_{in} = 6-36V, V_{out} = 3.3V, $I_{out,max}$ = 1.5A, f_s = 465kHz. Two Coilcraft ferrite core inductors have been considered for the analysis, namely the MSS7341-183 ($L_{nom} = 18\mu H$) and MSS5131-472 ($L_{nom} = 4.7\mu H$), whose main datasheet characteristics are given in Table 2.1. The instrumentation used for the experimental measurements included a LeCroy WaveRunner 44Xi Oscilloscope with LeCroy PP008 passive probes, a Tektronix TCP 305 current probe with Tektronix TCP A300 amplifier, a H&H ZS 1880 Electronic Load and a 0-30V/5A DF 1731SB Dual-Out Linear DC Power Supply, as shown in Fig. 2.3.

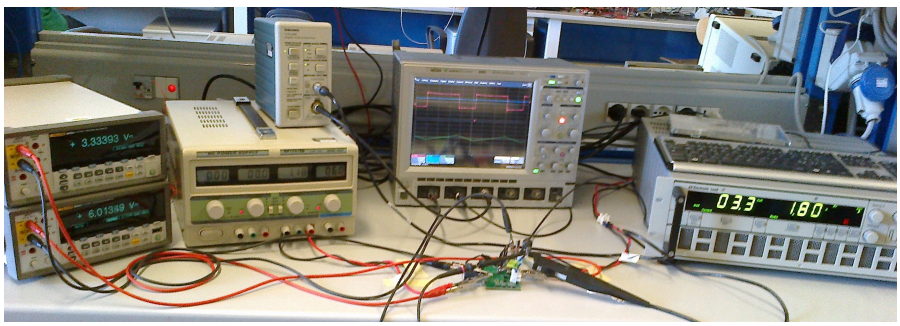

Figure 2.3: Measurement set-up.

Table 2.1: Investigated inductors and their main characteristics

Part Number	Dimensions $[mm^3]$	L $[\mu H]$	DCR $[m\Omega]$	$I_{sat}[A]$ 30% drop	$I_{rms}[A]$ 40°C rise
MSS7341-183	7.3x7.3x4.1	18	75	1.62	2.65
MSS5131-472	5.1x5.1x3.1	4.7	38	1.42	2.50

Table 2.2: Test conditions: $V_{out} = 3.3$V, $f_s = 465$kHz

	MSS7341-183			MSS5131-472		
Case study #	V_{in} $[V]$	I_{out} $[A]$	T $[°C]$	V_{in} $[V]$	I_{out} $[A]$	T $[°C]$
1	6	1.5	28	5	1.0	29
2	6	1.8	30	5	1.3	30
3	6	2.1	32	5	1.6	33
4	12	1.5	29	8	1.0	32
5	12	1.8	31	8	1.3	33
6	12	2.1	34	8	1.6	35

Temperature measurements have been carried out using a Fluke 54 II B dual input digital thermometer (accuracy $0.05\% + 0.3°C$), with a type K thermocouple. For each inductor, the measurements of inductor current and temperature have been performed in $N = 6$ different case studies of the the converter input voltage and output current, listed in Table 2.2. The resulting inductors operating temperatures are also provided, next to the respective test conditions.

MSS7341-183 inductor

For the MSS7341-183 inductor, reference temperatures T_α and T_β, used for L *vs* i_L curves identification, have been fixed at $25°C$ and $50°C$, respectively, thus resulting in the following set of parameters to be identified with the DE: $\{L^{high}, L^{low}, I_{30\%@25°C}, I_{70\%@25°C}, I_{30\%@50°C}, I_{70\%@50°C}\}$. The DE algorithm parameters have been set-up as follows: population size $N_{pop} = 30$ individuals, number of generations $N_{gen} = 100$, scale factor for the DE mutation operator $SF = 0.85$, and crossover probability for the DE crossover operator $C_r = 1$. Five independent DE runs have been performed, starting from different random initial populations, in order to verify the repeatability of the algorithm and identify the optimal discovered solution. The resulting parameters for the MSS7341-183 inductor are shown in Fig. 2.4, corresponding to the fitness function values in the range $F = [0.02631, 0.02910]$. In can be noted that the results are quite repeatable, which means that the DE algorithm converges close to the same solution in all the runs. The optimal solution with the minimum fitness function value (*i.e.*, $F = 0.02631$), obtained during the 5-th DE run, is given in Table 2.3. Fig. 2.5 shows that the simulated saturation curves of the MSS7341-183 part ("sim" subscript), obtained by using model (1.6) and parameters of Table 2.3, provide lower inductance than the datasheet curves declared by the manufacturer ("dat" subscript), especially in the roll-off region. Fig. 2.6 shows the experimental inductor current waveforms (green lines) and the reconstructed wave-shapes obtained by using the DE-based saturation curves (red lines with circle markers), for the six case studies of Table 2.2. For each case study, experimental inductor temperature provided in Table 2.2 has been used to determine the temperature-dependent values of σ and I_L^* of the arctangent model (1.6), adopted during the inductor current reconstruction. The plots highlight an excellent agreement between the experimental and simulated current waveforms, thus validating the proposed DE-based approach for saturation curves identification in SMPS operating conditions.

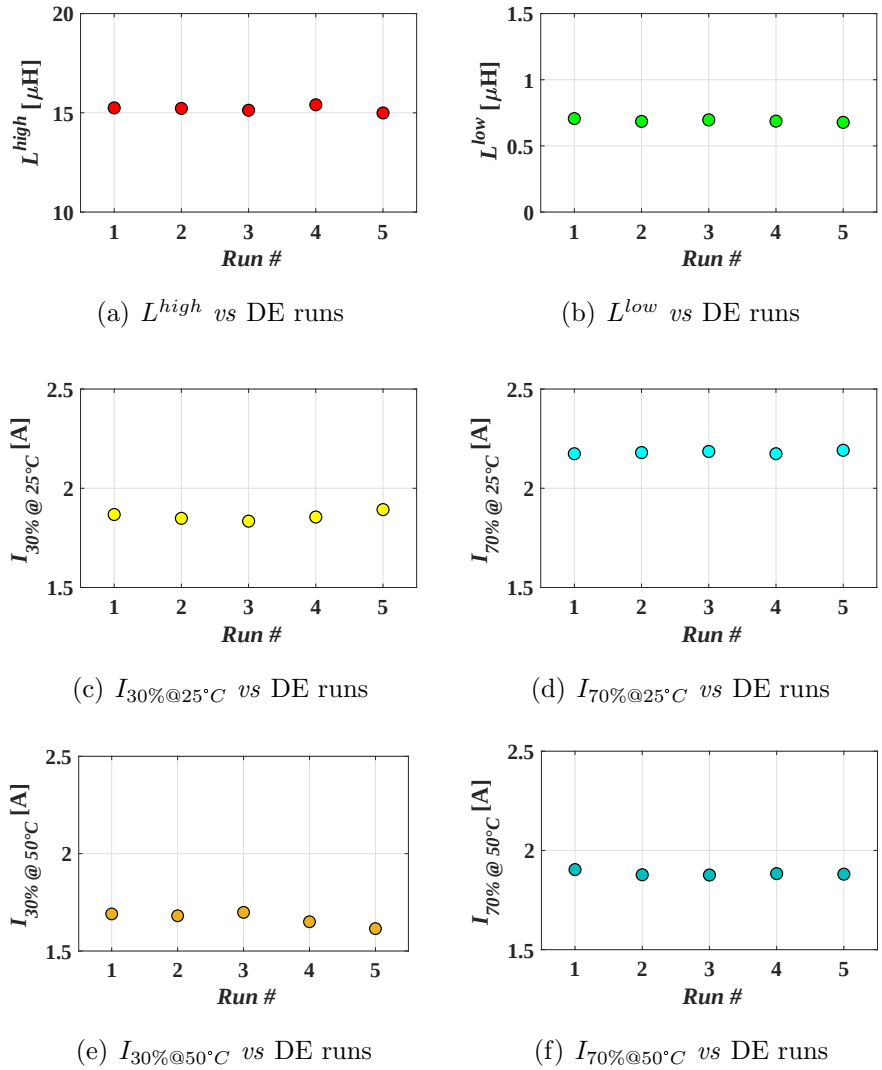

(a) L^{high} *vs* DE runs

(b) L^{low} *vs* DE runs

(c) $I_{30\%@25°C}$ *vs* DE runs

(d) $I_{70\%@25°C}$ *vs* DE runs

(e) $I_{30\%@50°C}$ *vs* DE runs

(f) $I_{70\%@50°C}$ *vs* DE runs

Figure 2.4: L *vs* i_L curve parameters of the MSS7341-183 inductor for five DE runs.

Table 2.3: MSS7341-183 saturation curve parameters.

L^{high} $[\mu H]$	L^{low} $[\mu H]$	$I_{30\%@25^{\circ}C}$ $[A]$	$I_{70\%@25^{\circ}C}$ $[A]$	$I_{30\%@50^{\circ}C}$ $[A]$	$I_{70\%@50^{\circ}C}$ $[A]$
15.0	0.7	1.89	2.19	1.62	1.88

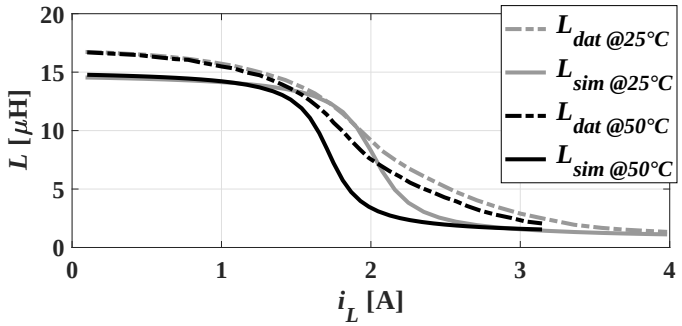

Figure 2.5: Simulated DE-based curves ("sim" subscript) *vs* datasheet curves ("dat" subscript) for MSS7341-183 inductor.

MSS5131-472 inductor

For the MSS5131-472 inductor, reference temperatures T_α and T_β have been fixed at $25^{\circ}C$ and $75^{\circ}C$ respectively, resulting in the following set of parameters to be identified: $\{L^{high},\ L^{low},\ I_{30\%@25^{\circ}C},\ I_{70\%@25^{\circ}C},\ I_{30\%@75^{\circ}C},\ I_{70\%@75^{\circ}C}\}$. The DE algorithm parameters have been set-up as follows: $\{N_{pop} = 100,\ N_{gen} = 100,\ SF = 0.85,\ C_r = 1\}$. Five independent algorithm runs have been performed, and optimal DE solution with the minimum fitness function value (*i.e.*, $F = 0.0434$) has been selected, given in Table 2.4. Fig. 2.7 shows that the simulated saturation curves of the MSS5131-472 part ("sim" subscript), obtained by using model (1.6) and parameters of Table 2.4, provide higher inductance in the weak-saturation region and lower inductance in the roll-off region if compared to the datasheet curves ("dat" subscript).

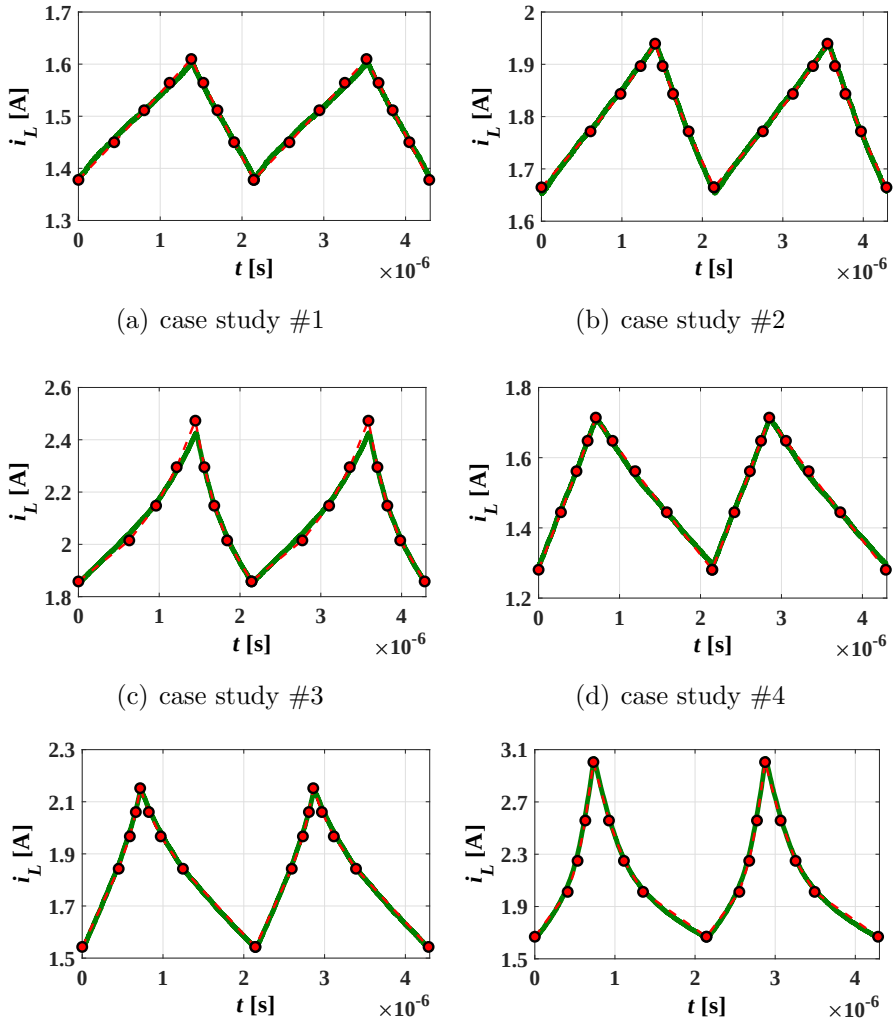

(a) case study #1 (b) case study #2

(c) case study #3 (d) case study #4

(e) case study #5 (f) case study #6

Figure 2.6: MSS7341-183 current waveforms: experimental measurements (green lines) *vs* simulated reconstructions obtained by using DE-based L *vs* i_L curves (red lines with circle markers).

Table 2.4: MSS5131-472 saturation curve parameters.

L^{high} $[\mu H]$	L^{low} $[\mu H]$	$I_{30\%@25^{\circ}C}$ $[A]$	$I_{70\%@25^{\circ}C}$ $[A]$	$I_{30\%@75^{\circ}C}$ $[A]$	$I_{70\%@75^{\circ}C}$ $[A]$
5.7	0.1	1.43	1.87	1.29	1.64

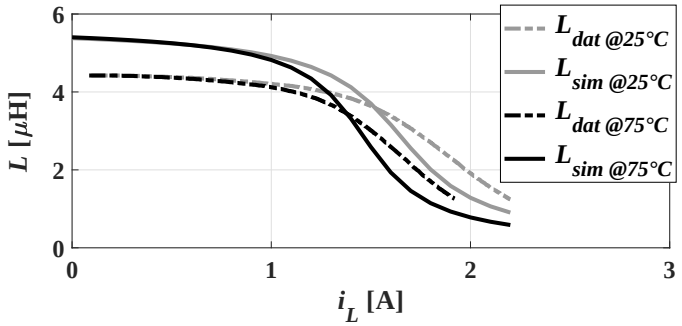

Figure 2.7: Simulated DE-based curves ("sim" subscript) *vs* datasheet curves ("dat" subscript) for MSS5131-472 inductor.

Fig. 2.8 shows the experimental inductor current waveforms (green lines) and reconstructed wave-shapes obtained by using the DE-based saturation curves (red lines with circle markers) in six analyzed case studies. Also in this case, the plots highlight an excellent agreement between experimental and simulated current waveforms. Finally, Fig. 2.9 shows the experimental inductor current waveforms of the two analyzed inductors for case study #6 of Table 2.2, together with the reconstructed current wave-shapes obtained by using the datasheet saturation curves. For both inductors, the predicted peak-to-peak ripple is smaller than the experimental one, since in the current range of interest the datasheet L *vs* i_L curves overestimate the real saturation characteristics. This may determine unreliable prediction of the overall inductor power losses and unreliable inductor selection in the SMPS application under study. The DE-based curves, instead, yield much more realistic current predictions for the same case study (see Fig.s 2.6(f) and 2.8(f)).

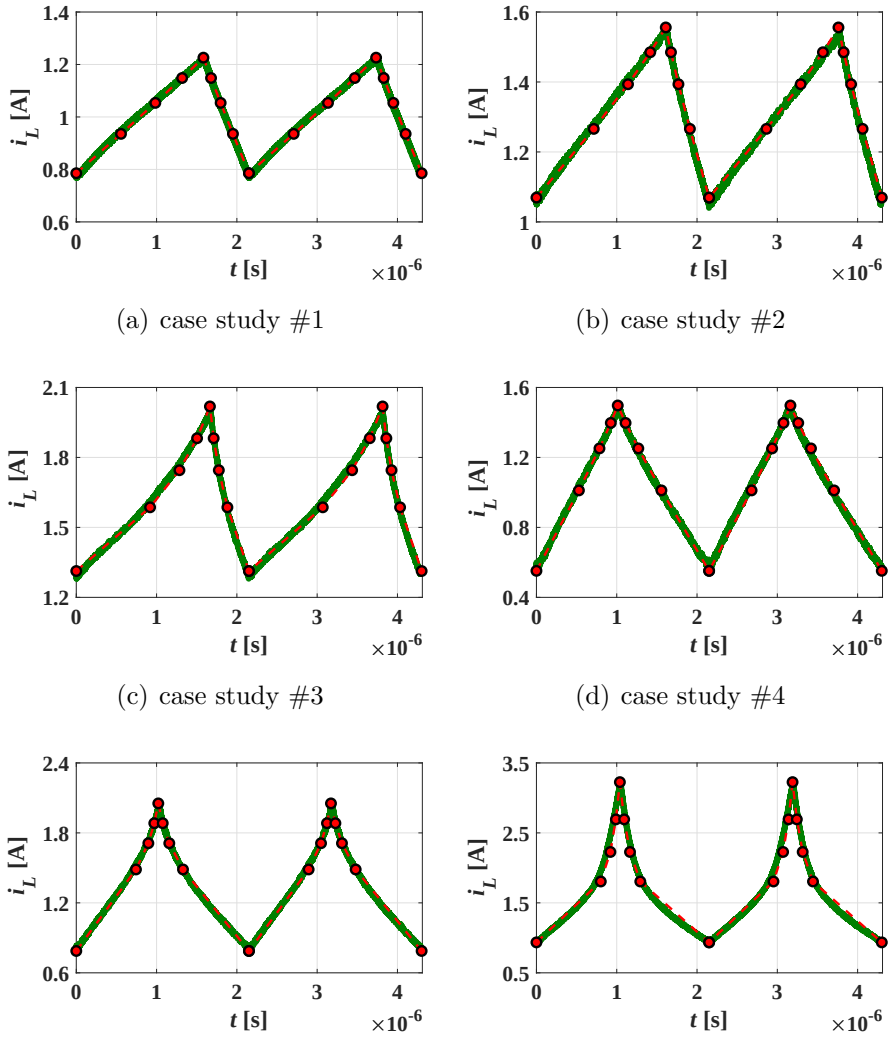

(a) case study #1 (b) case study #2

(c) case study #3 (d) case study #4

(e) case study #5 (f) case study #6

Figure 2.8: MSS5131-472 current waveforms: experimental measurements (green lines) *vs* simulated reconstructions obtained by using DE-based L *vs* i_L curves (red lines with circle markers).

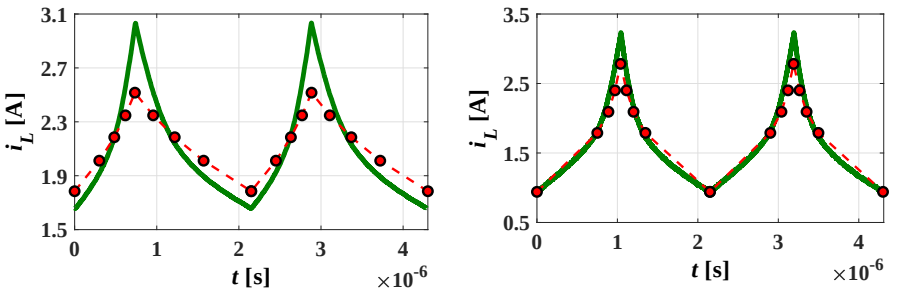

(a) MSS7341-183 (b) MSS5131-472

Figure 2.9: Experimental inductor current waveforms (green lines) *vs* simulated reconstructions obtained by using datasheet L *vs* i_L curves (red lines with circle markers).

2.2 Local and Global Characterization Approaches

This Section discusses the identification of the L *vs* i_L saturation curves by using two dual characterization approaches of FPIs: the *local* approach, aimed at determining local polynomial models valid in small-ripple conditions; the *global* approach, based on a global non-linear model identified in large-ripple conditions.

2.2.1 Local Characterization of FPIs

The shape of the L *vs* i_L curve for FPIs is highly nonlinear. However, if the current during T_s swings over a small interval, the curve can be locally approximated by a linear or quadratic function, as shown in Eq.s (2.8) and (2.9), respectively.

$$L\left[i_L(t)\right] = \alpha + \beta i_L(t) \tag{2.8}$$

$$L\left[i_L(t)\right] = \alpha + \beta i_L(t) + \gamma i_L^2(t) \tag{2.9}$$

Models (2.8) and (2.9) can be used to generate a sequence of local approximations of the L *vs* i_L curve, based on a sequence of contiguous current ripples covering the entire range from the

weak-saturation to the deep-saturation region, as shown in the top and central panels of Fig. 2.10. The increase of the *DC* bias inductor current causes a decrease of the inductance, due to saturation, leading to an increase of the current ripple. Therefore, the inductor operating conditions have to be adjusted by gradually decreasing the volt-seconds imposed by SMPS to the inductor, to prevent the transition to large-amplitude ripples, which would make the local approximation inaccurate. This can be achieved by reducing the voltage V_{Lr} applied to the inductor during the rise-time interval, or the duty-cycle D, or both. The parameters of local models (2.8) and (2.9) can be identified starting from experimental measurements of the inductor voltage and current in small-amplitude current ripple conditions, as discussed hereafter.

2.2.2 Global Characterization of FPIs

Certain conditions of the *DC* current, switching frequency and volt-seconds may result in a large-amplitude inductor current ripple, covering the entire L *vs* i_L curve during each switching period (see the bottom panel of Fig. 2.10). In such a case, the linear and quadratic approximations (2.8) and (2.9) are no more valid, and a global non-linear model should be adopted, which is able to accurately approximate the entire L *vs* i_L curve:

$$L\left[i_L\left(t\right)\right] = L^{low} + \frac{L^{high} - L^{low}}{2}\left\{1 - \frac{2}{\pi}\mathrm{atan}\left\{\sigma\left[i_L\left(t\right) - I_L^*\right]\right\}\right\} \quad (2.10)$$

Let us note that, unlike the original model (1.6) discussed in Section 1.3, in model (2.10) the absolute value of inductor current has been omitted, since only positive current values are considered hereafter for the L *vs* i_L curve identification. Once such curve is determined on a positive current range, it can be symmetrically reconstructed also on a negative current range. The parameters $\{L^{high}, L^{low}, \sigma, I_L^*\}$ of global model (2.10) can be identified starting from experimental measurements of the inductor voltage and current in a large-amplitude current ripple condition, as discussed hereafter.

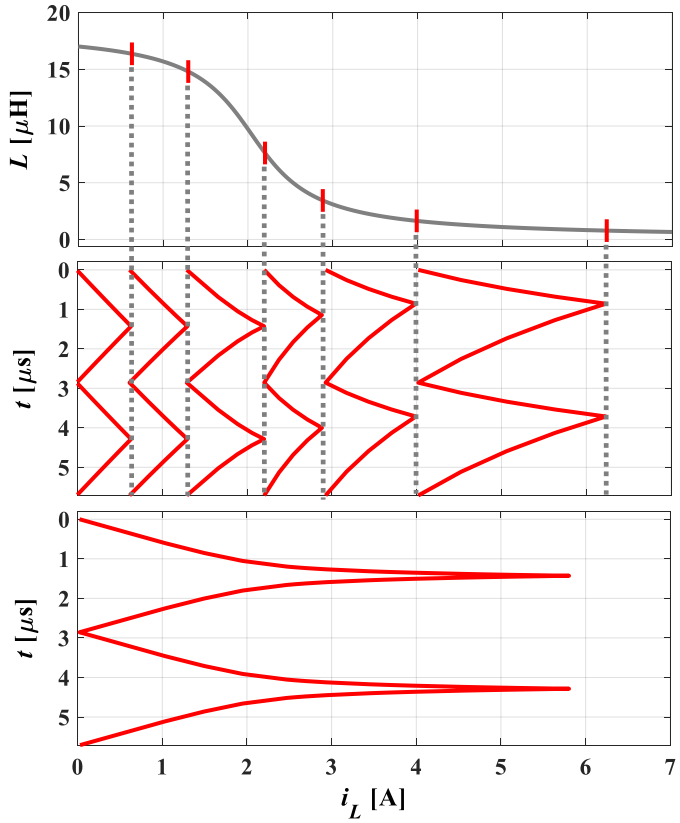

Figure 2.10: Local characterization with small-amplitude ripples (top and central panels) and global characterization with large-amplitude ripple (bottom panel).

2.2.3 Identification of Model Parameters

Linear Model

From (2.8), the instantaneous inductor voltage $v_L(t)$ is related to the current $i_L(t)$ according to (2.11):

$$v_L(t) = \alpha \frac{di_L(t)}{dt} + \beta i_L(t) \frac{di_L(t)}{dt} \tag{2.11}$$

Integrating (2.11) between 0 and $t \in [0, T_s]$ yields (2.12):

$$\int_0^t v_L(\tau)d\tau = \alpha\left[i_L(t) - i_{L0}\right] + \frac{\beta}{2}\left[i_L^2(t) - i_{L0}^2\right] \tag{2.12}$$

By defining $\delta = -\alpha i_{L0} - {}^1\!/_2\beta i_{L0}^2$, (2.12) can be recast as follows:

$$\int_0^t v_L(\tau)d\tau = \alpha i_L(t) + \frac{\beta}{2} i_L^2(t) + \delta \tag{2.13}$$

If the inductor voltage and current waveforms are sampled over the switching period in N time instants t_k, $k = 1, ..., N$, the integral in the left-hand side of (2.13) can be approximated *via* a trapezoidal method, for each t_k:

$$\begin{aligned}\int_0^{t_k} v_L(\tau)d\tau \approx \frac{1}{2}\sum_{i=2}^{k}\left\{\left[v_L(t_{i-1}) + v_L(t_i)\right](t_i - t_{i-1})\right\} = \\ = \alpha i_L(t_k) + \frac{\beta}{2} i_L^2(t_k) + \delta\end{aligned} \tag{2.14}$$

By evaluating (2.14) in the N sampling time instants t_k, $k = 1, ..., N$, the system of N linear equations in three unknowns $\{\alpha, \beta, \delta\}$ is obtained, which can be numerically solved with a Linear Least Squares (LLS) algorithm, to obtain the parameters of the local linear model (2.8). As the L *vs* i_L curve is monotonically decreasing, feasible linear models have to fulfill the constraint $d[L(i_L)]/di_L = \beta \leq 0$.

Quadratic Model

From (2.9), the instantaneous inductor voltage $v_L(t)$ is related to the current $i_L(t)$ according to (2.15):

$$v_L(t) = \alpha\frac{di_L(t)}{dt} + \beta i_L(t)\frac{di_L(t)}{dt} + \gamma i_L^2(t)\frac{di_L(t)}{dt} \tag{2.15}$$

Following the same steps as for the linear model, and assuming $\zeta = -\alpha i_{L0} - {}^1\!/_2\beta i_{L0}^2 - {}^1\!/_3\gamma i_{L0}^3$, we obtain:

$$\int_0^t v_L(\tau)d\tau = \alpha i_L(t) + \frac{\beta}{2} i_L^2(t) + \frac{\gamma}{3} i_L^3(t) + \zeta \tag{2.16}$$

which can be approximated as follows:

$$\int_0^{t_k} v_L(\tau)d\tau \approx \frac{1}{2}\sum_{i=2}^{k}\left\{\left[v_L(t_{i-1})+v_L(t_i)\right](t_i-t_{i-1})\right\} = \\ = \alpha i_L(t_k)+\frac{\beta}{2}i_L^2(t_k)+\frac{\gamma}{3}i_L^3(t_k)+\zeta \tag{2.17}$$

By evaluating (2.17) in the N sampling time instants t_k, $k = 1, ..., N$, the system of N linear equations in four unknowns $\{\alpha, \beta, \gamma, \zeta\}$ is obtained, which can be numerically solved with a LLS algorithm, to obtain the parameters of the local quadratic model (2.9). As the L *vs* i_L curve is monotonically decreasing, feasible quadratic models have to fulfill the constraint $d[L(i_L)]/di_L = \beta + 2\gamma \cdot i_L \leq 0$.

Global Model

From (2.10), the instantaneous inductor voltage $v_L(t)$ is related to the current $i_L(t)$ according to (2.18):

$$v_L(t) = \frac{1}{2}\left(L^{high}+L^{low}\right)\frac{di_L(t)}{dt}+... \\ -\frac{1}{\pi}\left(L^{high}-L^{low}\right)\operatorname{atan}\left\{\sigma\left[i_L(t)-I_L^*\right]\right\}\frac{di_L(t)}{dt} \tag{2.18}$$

Integrating (2.18) between 0 and $t \in [0, T_s]$ yields (2.19):

$$\int_0^t v_L(\tau)d\tau = \frac{1}{2}\left(L^{high}+L^{low}\right)\left[i_L(t)-i_{L0}\right]+... \\ -\frac{1}{\pi}\left(L^{high}-L^{low}\right)\cdot z^+\big|_{i_{L0}}^{i_L(t)} = 0 \tag{2.19}$$

where $z^+\big|_{i_{L0}}^{i_L(t)}$ can be evaluated by using Eq. (1.17a), as follows:

$$z^+\big|_{i_{L0}}^{i_L(t)} = ... \\ \left(i_L(t)-I_L^*\right)\operatorname{atan}\left[\sigma\left(i_L(t)-I_L^*\right)\right]-\frac{\log\left[1+\sigma^2\left(i_L(t)-I_L^*\right)^2\right]}{2\sigma}+... \\ -\left(i_{L0}-I_L^*\right)\operatorname{atan}\left[\sigma\left(i_{L0}-I_L^*\right)\right]+\frac{\log\left[1+\sigma^2\left(i_{L0}-I_L^*\right)^2\right]}{2\sigma} \tag{2.20}$$

By evaluating (2.19) in the N sampling time instants t_k, $k = 1, ..., N$, the system of N nonlinear equations in five unknowns $\{L^{high}, L^{low}, \sigma, I_L^*, i_{L0}\}$ is obtained, which can be numerically solved with a Non-Linear Least Squares (NLLS) algorithm, to obtain the parameters of the global model (2.10).

2.2.4 Experimental Verification

The proposed procedure for the L *vs* i_L curves identification has been applied to the Coilcraft MSS7341-183 inductor. Experimental tests have been carried out by means of the MADMIX system, which is described later on in this study (see Chapter 5). Such automated measurement setup emulates a buck converter and measures the performances of power inductors under hard-switched conditions. Alternatively, the low-cost method for on-line acquisition of the inductor voltage and current waveforms in a given power converter can be adopted [31].

The local and global characterization approaches have been herein tested by means of the MADMIX system. Experimental inductor waveforms have been sampled in N=200 samples over the switching period. A MATLAB implementation of the LLS and NLLS algorithms has been used for parameters identification of each L *vs* i_L model. Hereafter, the obtained results are presented and compared.

Local Linear Models

To reconstruct the L *vs* i_L curve with local linear models, the MSS7341-183 inductor has been tested in a buck converter under the operating conditions listed in Table 2.5, whose last column provides the resulting experimental inductor temperatures. The obtained local linear models are shown in the top panel of Fig. 2.11. In the bottom panel, the experimental inductor currents (green waveforms) are compared to the wave-shapes simulated by using the identified local linear L *vs* i_L models in Simulink (red dashed waveforms). Good predictions of inductor currents have

Table 2.5: Test conditions for FPI local characterization

Case study #	f_s $[kHz]$	V_{in} $[V]$	D $[-]$	I_{out} $[A]$	T_{exp} $[°C]$
1	350	15	0.5	0.32	24.3
2	350	15	0.5	1.00	27.6
3	350	10	0.5	1.60	29.1
4	350	5	0.5	2.15	32.7
5	350	4	0.3	2.80	36.6
6	350	4	0.2	3.80	49.7

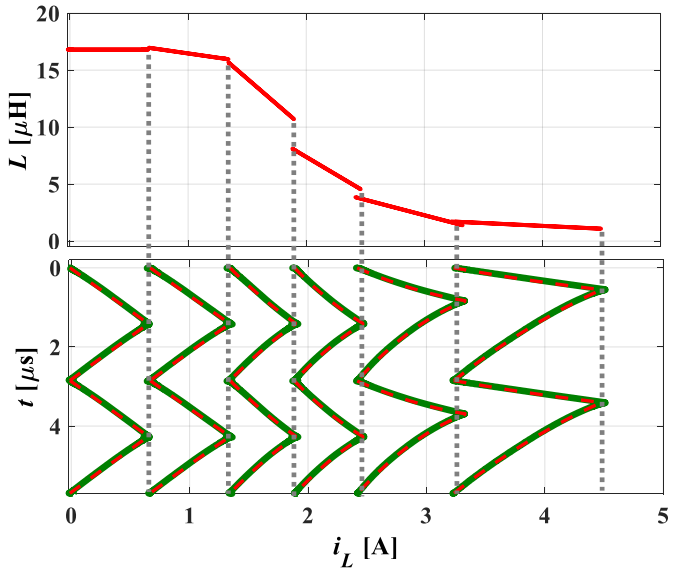

Figure 2.11: Top: identified local linear L *vs* i_L models; bottom: experimental (green) and Simulink (red) current waveforms.

been obtained by using the linear models in all the investigated case studies, going from weak- to deep-saturation region. The values of the model parameters $\{\alpha, \beta\}$ are given in the left part of Table 2.6 (section "linear").

Local Quadratic Models

The MSS7341-183 inductor has been tested under the same operating conditions as before. The resulting quadratic models are shown in the top panel of Fig. 2.12. The quadratic function provides a better modeling of the L *vs* i_L curve in the region where the inductance drop-rate increases, because of the transition from weak to deep saturation. Good predictions of inductor currents are obtained also in this case (see the bottom panel of Fig. 2.12). The values of the model parameters $\{\alpha, \beta, \gamma\}$ are given in the right part of Table 2.6 (section "quadratic").

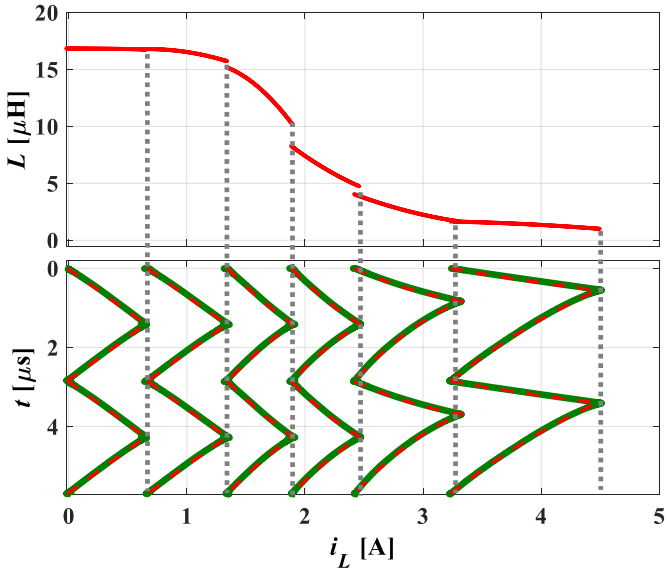

Figure 2.12: Top: identified local quadratic L *vs* i_L models; bottom: experimental (green) and Simulink (red) current waveforms.

Global Model

The MSS7341-183 inductor has been tested under the following conditions: f_s=350kHz, V_{in}=50V, D=0.5, I_{out}=1.1A, resulting in

Table 2.6: Linear and quadratic models' parameters

	linear		quadratic		
Case study #	α $[\mu H]$	β $[\mu H/A]$	α $[\mu H]$	β $[\mu H/A]$	γ $[\mu H/A^2]$
1	16.80	0.00	16.83	-0.01	-0.18
2	17.96	-1.50	15.74	3.13	-2.34
3	27.71	-8.97	5.03	19.32	-8.77
4	19.68	-6.15	32.50	-18.01	2.74
5	10.40	-2.71	20.98	-10.17	1.31
6	3.34	-0.50	-0.13	1.31	-0.24

a large-amplitude current ripple and inductor operating temperature $T_{exp} = 48.7°C$. The upper panel of Fig. 2.13 shows the identified global model, while in the bottom panel the experimental current waveform is compared to the results of the simulation performed in Simulink using the global L *vs* i_L model. The following values of the model parameters have been obtained: $L^{high} = 18.6\mu H$, $L^{low} = 1.28\mu H$, $\sigma = 3.37A^{-1}$, $I_L^* = 1.83$A.

Fig. 2.14 shows a comparison between the local and global models of the MSS7341-183 inductor. The global model corresponds to a fixed inductor temperature of $48.7°C$, whereas local models are associated to different temperatures in the range [24.3, 49.7]$°C$, increasing with the average inductor current (see Table 2.5). In the same figure, the experimental L *vs* i_L curve of the MSS7341-183 inductor is shown, which has been measured by the MADMIX system under large-amplitude current ripple condition ($f_s = 350$kHz, $V_{in} = 50$V, $D = 0.5$, $I_{out} = 1.1$A, $T_{exp} = 48.7°C$). The identified global model is in a good agreement with such experimental curve.

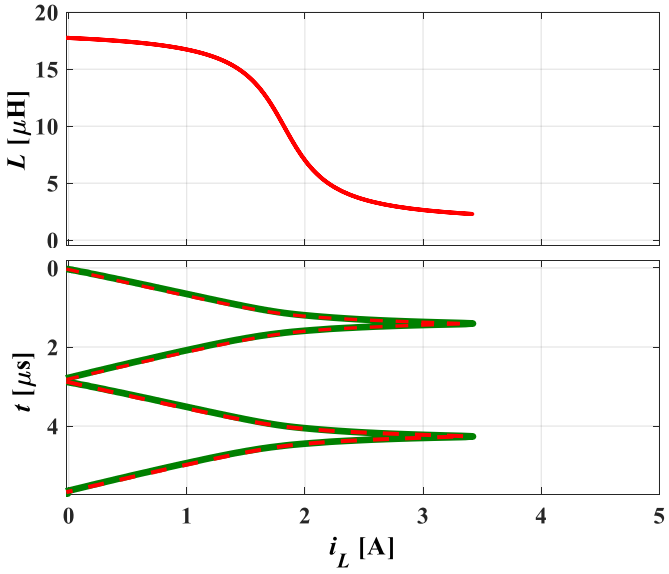

Figure 2.13: Top: identified global L *vs* i_L model; bottom: experimental (green) and Simulink (red) current waveforms.

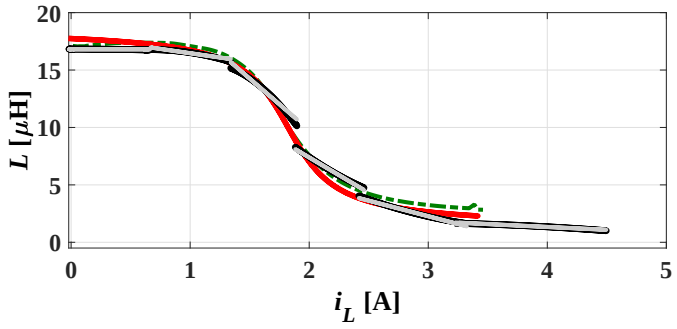

Figure 2.14: Comparison between identified L *vs* i_L models and experimental curve: light gray = linear model, black = quadratic model, red = global model, green = MADMIX curve.

The main outcome of the research activity presented in this Chapter resulted in the publication of the scientific paper:

- G. Di Capua, N. Femia, K. Stoyka, M. Lodi, A. Oliveri, M. Storace, "Ferrite Inductor Models for Switch-Mode Power Supplies Analysis and Design", *14th Int. Conf. on Synthesis, Modeling, Analysis and Simulation Methods and Appl. to Circuit Design (SMACD)*, June 2017.

Chapter 3

Saturation Modeling of Stepped Air-Gap Ferrite Inductors

This chapter discusses saturation behavioral modeling of ferrite inductors with a stepped air-gap. The arctangent-based L *vs* i_L model, proposed in Chapter 1 for fixed air-gap FPIs, is herein extended to a double-arctangent model, accurately describing the saturation characteristic of stepped air-gap inductors. The numerical algorithm for inductor current reconstruction is effectively adopted in combination with a double-arctangent model, in order to reliably predict current wave-shapes of stepped air-gap FPIs operating in saturation.

3.1 FPIs with Stepped Air-Gap

Ferrite inductors with a stepped air-gap are characterized by the presence of two different air-gaps in their magnetic core, as highlighted in Fig. 3.1. The reluctance $\mathcal{R}$ of such a core can be modeled as a parallel of two different reluctances $\mathcal{R}_1$ and $\mathcal{R}_2$, representing the parts of the core with a shorter air-gap length l_{g1} and a longer air-gap length l_{g2}, respectively. As a result, the total inductance

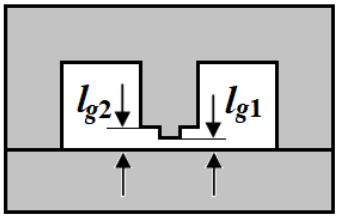

Figure 3.1: Magnetic core with a stepped air-gap.

of the component realized with such a core can be expressed as given in (3.1):

$$L = \frac{n^2}{\mathcal{R}} = \frac{n^2}{\mathcal{R}_1} + \frac{n^2}{\mathcal{R}_2} = L_1 + L_2 \tag{3.1}$$

where n is the inductor winding turn number. Inductances L_1 and L_2 correspond to parts of the core with air-gap lengths l_{g1} and l_{g2}, respectively.

Fig. 3.2 shows a typical curve of the dynamic inductance *versus* current for a stepped air-gap FPI. Such curve presents two knees due to the gradual saturation of the inductances L_1 and L_2. Since L_1 corresponds to the smaller air-gap, its saturation occurs at lower current levels, thus determining the first knee in the L *vs* i_L curve of Fig. 3.2. The second knee is due to the saturation of

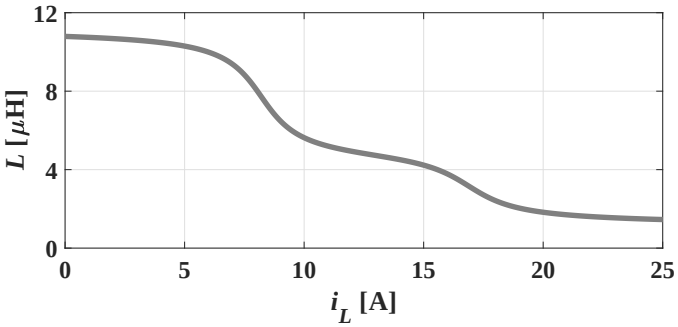

Figure 3.2: Typical L *vs* i_L curve of a FPI with a stepped air-gap.

L_2. As a result, stepped air-gap FPIs have larger inductance at low-current levels (within the first knee of their L *vs* i_L curve), which can help to increase the converter efficiency at light-load [32] [33]. On the other hand, lower inductance between the first and second knee of the saturation curve can help to improve load transient response to/from higher current. In [34] [35], a simplified piecewise constant model has been proposed to describe the L *vs* i_L characteristic of a stepped air-gap ferrite inductor. To accurately represent a real smooth profile of such a curve, an enhanced model has been herein developed, presented in the next Section.

3.2 Inductance *vs* Current Behavioral Model

The L *vs* i_L curve of a stepped air-gap FPI can be analytically described by means of a double-arctangent model, defined as follows:

$$\begin{aligned} L[i_L(t)] &= ... \\ &= \overbrace{L^{low1} + \frac{L^{high1} - L^{low1}}{2}\left\{1 - \frac{2}{\pi}\text{atan}\left\{\sigma_1\left[i_L(t) - I^*_{L1}\right]\right\}\right\}}^{L_1[i_L(t)]} + \\ &+ \underbrace{L^{low2} + \frac{L^{high2} - L^{low2}}{2}\left\{1 - \frac{2}{\pi}\text{atan}\left\{\sigma_2\left[i_L(t) - I^*_{L2}\right]\right\}\right\}}_{L_2[i_L(t)]} \end{aligned} \tag{3.2}$$

where the arctangent-based model (1.6), previously discussed in Chapter 1, is applied twice, to model the inductances L_1 and L_2 as a function of the current $i_L(t)$. Parameters $\{L^{high1}, L^{high2}, L^{low1}, L^{low2}, \sigma_1, \sigma_2, I^*_{L1}, I^*_{L2}\}$ can be determined by applying a curve fitting technique to the experimental L *vs* i_L characteristic of a given inductor. Let us note that, unlike the original model (1.6), in model (3.2) the absolute value of inductor current has been omitted, since only positive current values have been considered for non-linear modeling of stepped air-gap inductors. However, it is

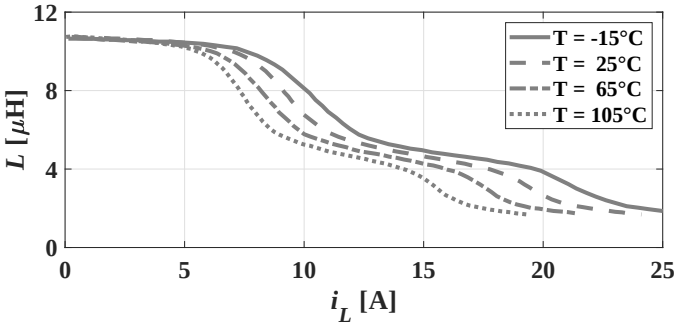

Figure 3.3: Temperature impact on the L *vs* i_L curve of a stepped air-gap FPI.

possible to extend the model and relative numerical algorithm for inductor current reconstruction also to a case including negative current values, similarly to the generalized procedure described in Chapter 1.

Like for fixed air-gap FPIs, the L *vs* i_L curves of stepped air-gap FPIs mostly present a horizontal left-side drift with increasing temperature. Fig. 3.3 shows an example of the temperature impact on the saturation curves for the Coilcraft $10\mu H$ MSS1210-103 inductor. To correctly model such thermal dependence, two experimental L *vs* i_L curves can be used, relative to two different reference temperatures (namely, T_α and T_β). A NLLS technique can be applied to fit each curve by means of the model (3.2) and determine the parameters $\{L^{high\,i}, L^{low\,i}, \sigma_i, I^*_{L\,i}\}$, $i = 1{,}2$, at T_α and T_β. Starting from these values, the thermal coefficients $\{\partial_{high\,i}, \partial_{low\,i}, \partial_{\sigma\,i}, \partial_{I\,i}\}$ can be estimated by using (3.3), for $i = 1{,}2$:

$$\partial_{high\,i} = \frac{L^{high\,i}_{@T_\beta} - L^{high\,i}_{@T_\alpha}}{L^{high\,i}_{@T_\alpha}\,(T_\beta - T_\alpha)}; \quad \partial_{low\,i} = \frac{L^{low\,i}_{@T_\beta} - L^{low\,i}_{@T_\alpha}}{L^{low\,i}_{@T_\alpha}\,(T_\beta - T_\alpha)}; \tag{3.3a}$$

$$\partial_{\sigma\,i} = \frac{\sigma_{i\,@T_\beta} - \sigma_{i\,@T_\alpha}}{\sigma_{i\,@T_\alpha}\,(T_\beta - T_\alpha)}; \quad \partial_{I\,i} = \frac{I^*_{L\,i\,@T_\beta} - I^*_{L\,i\,@T_\alpha}}{I^*_{L\,i\,@T_\alpha}\,(T_\beta - T_\alpha)} \tag{3.3b}$$

Eventually, the thermal dependences of the double-arctangent model parameters can be evaluated as given in (3.4):

$$L^{high\,i}(T) = L^{high\,i}_{@T_\alpha}\left[1 + \partial_{high\,i}(T - T_\alpha)\right] \tag{3.4a}$$
$$L^{low\,i}(T) = L^{low\,i}_{@T_\alpha}\left[1 + \partial_{low\,i}(T - T_\alpha)\right] \tag{3.4b}$$
$$\sigma_i(T) = \sigma_{i\,@T_\alpha}\left[1 + \partial_{\sigma\,i}(T - T_\alpha)\right] \tag{3.4c}$$
$$I^*_{L\,i}(T) = I^*_{L\,i\,@T_\alpha}\left[1 + \partial_{I\,i}(T - T_\alpha)\right] \tag{3.4d}$$

3.3 Inductor Current Reconstruction

From (3.2), the instantaneous inductor voltage $v_L(t)$ is related to the current $i_L(t)$ according to (3.5):

$$\begin{aligned} v_L(t) &= L[i_L\,(t)]\frac{di_L(t)}{dt} = ... \\ &= \left\{L^{low1} + \frac{L^{high1} - L^{low1}}{2}\left\{1 - \tfrac{2}{\pi}\text{atan}\left\{\sigma_1\left[i_L(t) - I^*_{L1}\right]\right\}\right\}\right\}\tfrac{di_L(t)}{dt} + \\ &+ \left\{L^{low2} + \frac{L^{high2} - L^{low2}}{2}\left\{1 - \tfrac{2}{\pi}\text{atan}\left\{\sigma_2\left[i_L(t) - I^*_{L2}\right]\right\}\right\}\right\}\tfrac{di_L(t)}{dt} \end{aligned} \tag{3.5}$$

where v_L represents the inductance voltage drop only. Integrating (3.5) between 0 and $t \in T_r$ (within the rise-time interval) yields (3.6a), while integrating (3.5) between DT_s and $t \in T_f$ (within the fall-time interval) provides (3.6b):

$$\int_0^t v_L(t)dt = V_{Lr} \cdot t = \int_0^t L\left[i_L\,(t)\right]\frac{di_L(t)}{dt}dt \tag{3.6a}$$
$$\int_{DT_s}^t v_L(t)dt = V_{Lf} \cdot (t - DT_s) = \int_{DT_s}^t L\left[i_L\,(t)\right]\frac{di_L(t)}{dt}dt \tag{3.6b}$$

By solving integrals in (3.6a) and (3.6b), two main equations can be obtained, provided in (3.7) and (3.8) respectively:

$$
\begin{aligned}
V_{Lr} \cdot t = & \ldots \\
& = \frac{L^{high1} + L^{low1}}{2} \left[i_{Lr}(t) - i_{L0} \right] - \frac{L^{high1} - L^{low1}}{\pi} \cdot z_1 \big|_{i_{L0}}^{i_{Lr}(t)} + \\
& + \frac{L^{high2} + L^{low2}}{2} \left[i_{Lr}(t) - i_{L0} \right] - \frac{L^{high2} - L^{low2}}{\pi} \cdot z_2 \big|_{i_{L0}}^{i_{Lr}(t)}
\end{aligned}
\tag{3.7}
$$

$$
\begin{aligned}
V_{Lf} \cdot (t - DT_s) = & \ldots \\
& = \frac{L^{high1} + L^{low1}}{2} \left[i_{Lf}(t) - i_{LD} \right] - \frac{L^{high1} - L^{low1}}{\pi} \cdot z_1 \big|_{i_{LD}}^{i_{Lf}(t)} + \\
& + \frac{L^{high2} + L^{low2}}{2} \left[i_{Lf}(t) - i_{LD} \right] - \frac{L^{high2} - L^{low2}}{\pi} \cdot z_2 \big|_{i_{LD}}^{i_{Lf}(t)}
\end{aligned}
\tag{3.8}
$$

where $i_{L0} = i_L(0)$, $i_{LD} = i_L(DT_s)$, $i_{Lr}(t)$ and $i_{Lf}(t)$ are the unknown instantaneous values of the rising and falling inductor currents during T_r and T_f respectively, and z_i (i=1,2) corresponds to the i_L-based indefinite integral given by (3.9):

$$
\begin{aligned}
z_i = z_i(i_L) = & \int \operatorname{atan} \left[\sigma_i \left(i_L - I_{L\,i}^* \right) \right] di_L = \ldots \\
& = \left(i_L - I_{L\,i}^* \right) \operatorname{atan} \left[\sigma_i \left(i_L - I_{L\,i}^* \right) \right] - \frac{\log \left[1 + \sigma_i^2 \left(i_L - I_{L\,i}^* \right)^2 \right]}{2\sigma_i}
\end{aligned}
\tag{3.9}
$$

In (3.7), $z_1(i_L)$ and $z_2(i_L)$ have to be determined between i_{L0} and $i_{Lr}(t)$ during the rise-time interval T_r. Similarly, in (3.8), $z_1(i_L)$ and $z_2(i_L)$ have to be determined between i_{LD} and $i_{Lf}(t)$ during the fall-time interval T_f. As i_{L0} and i_{LD} are not known in advance, guess values have to be used and an iterative procedure adopted, as discussed in Chapter 1. To reconstruct the entire profile of the inductor current waveform, non-linear equations (3.7) and (3.8) have to be numerically solved with respect to $i_{Lr}(t)$ and $i_{Lf}(t)$ in a given number of sampling points over T_r and T_f intervals. The position of such points can be determined by means of the tangent-based algorithm described in detail in Chapter 1 and shown in Fig. 1.9 (in the flow diagrams, replace Eq. (1.14) with Eq. (3.7) and Eq. (1.15) with Eq. (3.8)).

3.4 Simulation Results and Model Validation

The proposed model and relative algorithm for inductor current reconstruction of stepped air-gap FPIs have been adopted to investigate the behavior of three Coilcraft inductors: the MSS1210-103 ($L_{nom} = 10\mu H$), the MSS1210-153 ($L_{nom} = 15\mu H$) and the MSS1210-223 ($L_{nom} = 22\mu H$). The L *vs* i_L curves of these FPIs have been taken from the on-line tool of the manufacturer [17], at two reference temperatures $T_\alpha = 25°C$ and $T_\beta = 105°C$. The NLLS technique has been applied to fit each curve and determine the parameters of model (3.2). For example, the fitted curves obtained for the MSS1210-103 inductor are shown in Fig. 3.4, for $25°C$ (solid blue line) and $105°C$ (solid red line), superimposed to the manufacturer's curves (gray lines). In the same figure, the dashed and dash-dotted lines represent the arctangent functions $L_1\,[i_L(t)]$ and $L_2\,[i_L(t)]$ respectively, modeling the inductances L_1 and L_2 introduced in (3.1). The resulting parameters of model (3.2) are given in Table 3.1 for the three inductors, at two reference temperatures. Starting from such values, thermal coefficients $\{\partial_{high\,i}, \partial_{low\,i}, \partial_{\sigma\,i}, \partial_{I\,i}\}$, $i = 1{,}2$, have been obtained by using (3.3).

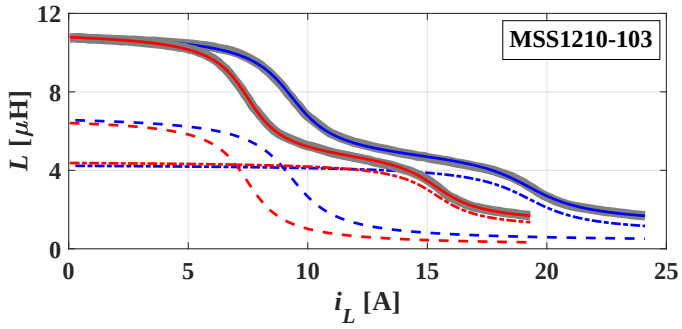

Figure 3.4: Datasheet L *vs* i_L curves (gray) and fitting curves at $25°C$ (blue) and $105°C$ (red) for MSS1210-103 inductor.

Table 3.1: Fitting curve parameters for MSS1210 inductors.

MSS 1210	T $[^\circ C]$	L^{high1} $[\mu H]$	L^{high2} $[\mu H]$	L^{low1} $[\mu H]$	L^{low2} $[\mu H]$	σ_1 $[A^{-1}]$	σ_2 $[A^{-1}]$	I^*_{L1} $[A]$	I^*_{L2} $[A]$
103	25	6.9	4.3	0.4	0.7	0.73	0.54	9.3	19.3
	105	6.8	4.4	0.2	0.9	0.88	0.71	7.5	15.4
153	25	9.6	5.7	0.5	0.4	0.85	0.65	8.1	16.8
	105	9.8	5.4	1.0	0.1	1.10	0.80	6.4	13.3
223	25	13.5	7.8	1.0	0.8	0.93	0.86	7.0	14.3
	105	12.9	8.2	0.6	1.2	1.15	1.09	5.6	11.4

A MATLAB code has been developed to implement the numerical algorithm for inductor current reconstruction of stepped air-gap FPIs. The analysis of the investigated inductors has been performed in six case studies listed in Table 3.2. For each of the case studies #1, #3 and #5, three different operating conditions have been considered (options (a), (b) and (c) in Table 3.2), corresponding to small-amplitude peak-to-peak current ripples covering different regions of the L *vs* i_L curves for the three inductors. Case studies #2, #4 and #6 correspond to large-amplitude peak-to-peak current ripples covering the entire profile of the L *vs* i_L curves. Two different values of inductor temperature have been assumed: $T = 50^\circ C$ for small-amplitude current ripple conditions, and $T = 75^\circ C$ for large-amplitude current ripple conditions. For each device, the relative parameters of the double-arctangent model have been updated at the considered temperature, according to (3.4).

The algorithm for current analysis of stepped air-gap FPIs has been validated by comparison with PSIM simulations. The open-loop buck topology has been adopted for simulations. The inductor has been implemented as a *current-controlled current source*, whose control signal is generated by means of a simplified C-block. At the n-th simulation time instant t_n, the C-block takes as inputs the samples of the inductor voltage $v_L(t_n)$ and current $i_L(t_n)$ and

Table 3.2: Case studies and relevant operating conditions.

MSS 1210	Case studies		T [°C]	Δi_{Lpp} error [%]
103	#1	(a) V_{in} = 36V, I_{out} = 3.0A	50	-0.20
		(b) V_{in} = 24V, I_{out} = 8.0A		-0.14
		(c) V_{in} = 16V, I_{out} = 14.0A		-0.26
	#2	V_{in} = 55V, I_{out} = 8.0A	75	-2.24
153	#3	(a) V_{in} = 36V, I_{out} = 3.0A	50	0.11
		(b) V_{in} = 24V, I_{out} = 8.0A		-0.09
		(c) V_{in} = 16V, I_{out} = 13.0A		-0.17
	#4	V_{in} = 60V, I_{out} = 7.5A	75	-2.70
223	#5	(a) V_{in} = 36V, I_{out} = 2.0A	50	0.02
		(b) V_{in} = 24V, I_{out} = 7.0A		-0.01
		(c) V_{in} = 16V, I_{out} = 11.0A		-0.07
	#6	V_{in} = 65V, I_{out} = 7.0A	75	-1.82

generates a new inductor current sample $i_L(t_{n+1})$ for the next time instant t_{n+1}. Inside the C block, the double-arctangent model parameters are updated according to (3.4) for a given inductor temperature T, and the differential inductance $L\left[i_L(t_n)\right]$ is evaluated according to (3.2). Eventually, a new inductor current sample $i_L(t_{n+1})$ is generated by means of (3.10):

$$i_L(t_{n+1}) = i_L(t_n) + \frac{(t_{n+1} - t_n)v_L(t_n)}{L\left[i_L(t_n)\right]} \tag{3.10}$$

Fig. 3.5 compares the results obtained in MATLAB and PSIM for case studies #1, #3 and #5, relative to the small-amplitude current ripple conditions of the three analyzed inductors. The left-hand side plots compare the inductor current waveforms simulated in PSIM (continuous lines) with those reconstructed in MATLAB (dashed lines with circle markers). The right-hand side plots show the L *vs* i_L curves of the three inductors at 50°C (gray lines) and,

for each curve, the three regions covered by the current ripple (colored lines) in conditions (a), (b) and (c) of the relative case study (see Table 3.2). Fig. 3.6 shows the obtained results for case studies #4, #6 and #8, relative to the large-amplitude current ripple conditions of the three analyzed inductors. The left-hand side plots compare the inductor current waveforms simulated in PSIM (continuous lines) with those reconstructed in MATLAB (dashed lines with circle markers). The right-hand side plots show the L *vs* i_L curves of the three inductors at $75°C$ (gray lines) and the curve regions covered by the current ripple (colored lines). Fig.s 3.5 and 3.6 highlight a very good agreement between the current waveforms simulated in PSIM and reconstructed in MATLAB. The last column of Table 3.2 provides percent errors between the peak-to-peak current ripples obtained in PSIM and MATLAB. Low error values ($\leq$3% in absolute value) confirm the validity of the proposed double-arctangent model and of the relative algorithm for current reconstruction of stepped air-gap ferrite inductors. By using such model and algorithm, it is possible to reliably predict a real magnitude of the inductor peak-to-peak current ripple without performing time-consuming circuit simulations, and effectively exploit the advantages offered by the use of stepped air-gap FPIs operating in saturation.

The main outcome of the research activity presented in this Chapter resulted in the publication of the scientific paper:

- Kateryna Stoyka, Giulia Di Capua, Nicola Femia, "Modeling of Stepped Air-Gap Ferrite Inductors in Switching Power Supplies", *25th IEEE International Conference on Electronics Circuits and Systems (ICECS)*, December 2018.

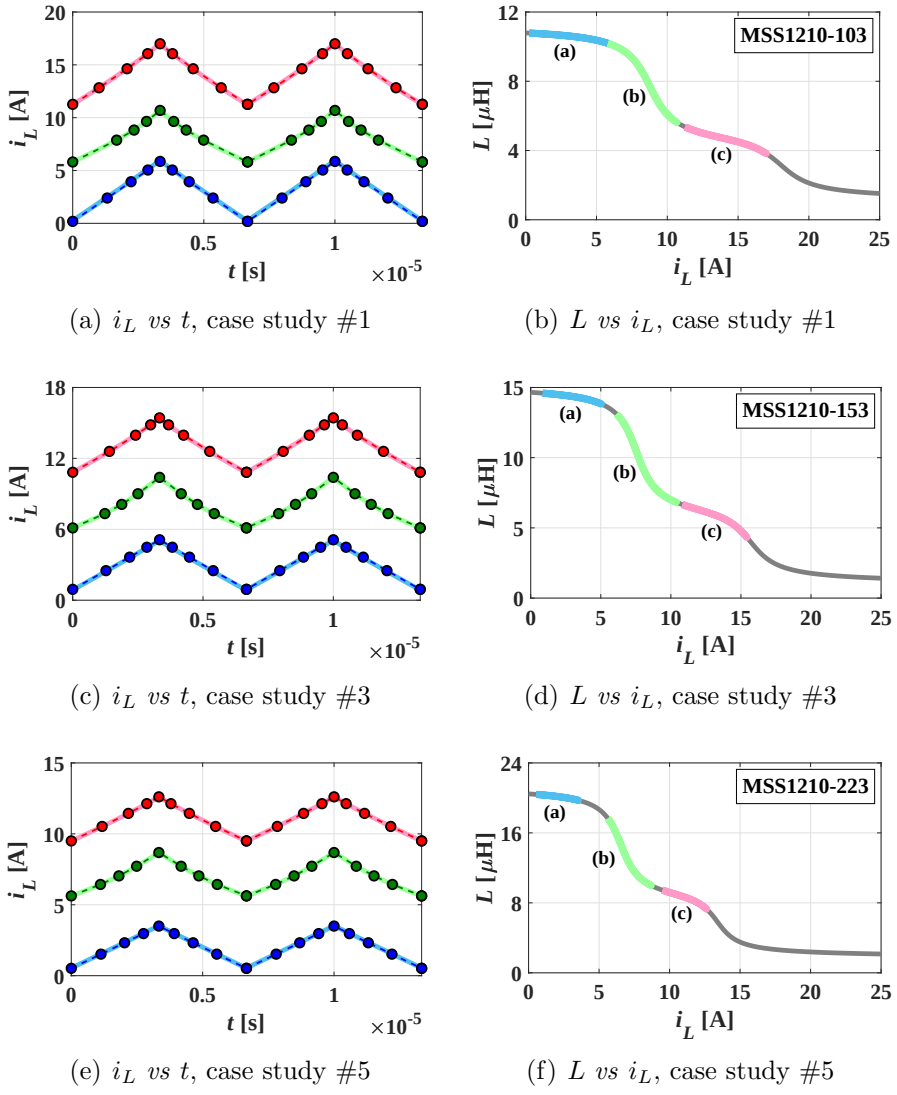

(a) i_L *vs* t, case study #1

(b) L *vs* i_L, case study #1

(c) i_L *vs* t, case study #3

(d) L *vs* i_L, case study #3

(e) i_L *vs* t, case study #5

(f) L *vs* i_L, case study #5

Figure 3.5: Case studies with small-amplitude current ripples. Left: current waveforms simulated in PSIM (continuous lines) and reconstructed in MATLAB (dashed lines with circle markers). Right: inductance *vs* current curves (gray lines) and regions covered by current ripple (colored lines).

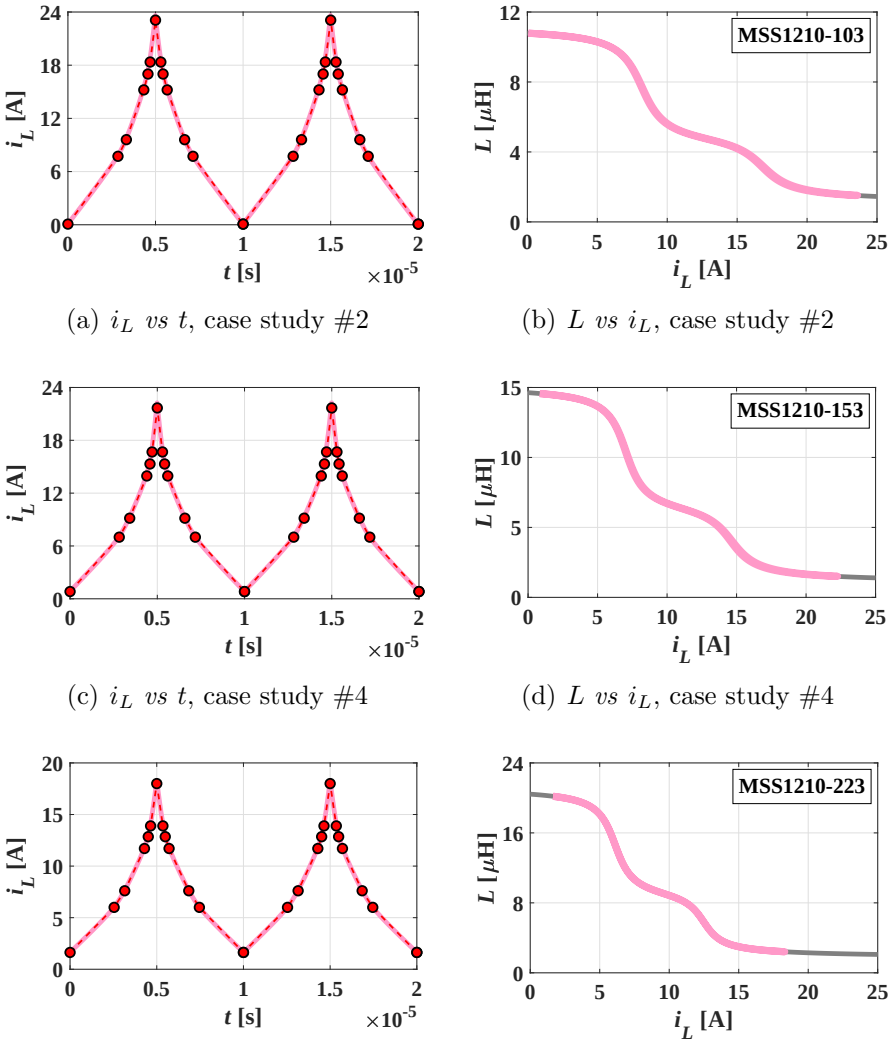

(a) i_L *vs* t, case study #2

(b) L *vs* i_L, case study #2

(c) i_L *vs* t, case study #4

(d) L *vs* i_L, case study #4

(e) i_L *vs* t, case study #6

(f) L *vs* i_L, case study #6

Figure 3.6: Case studies with large-amplitude current ripples. Left: current waveforms simulated in PSIM (continuous lines) and reconstructed in MATLAB (dashed lines with circle markers). Right: inductance *vs* current curves (gray lines) and regions covered by current ripple (colored lines).

Chapter 4

Sustainable Saturation Operation of Ferrite Inductors

This chapter discusses the Sustainable Saturation Operation (SSO) of FPIs in SMPS. A ferrite inductor is considered in SSO if its current ripple, power losses and temperature rise are acceptable and reliable for both the device and the SMPS, despite the inductance drop determined by the core saturation. In the first part of this Chapter, an algorithm is presented which identifies SSO-compliant FPIs with minimum size and volume, given the SMPS specifications about the allowed power losses, temperature rise and peak-to-peak current ripple of the inductor. The second part of this Chapter provides practical design guidelines for quick and straightforward SSO-compliance validation of FPIs, based on a simplified inductance model linearizing the FPI saturation characteristic in the roll-off region.

4.1 FPIs Analysis in SSO

Let us refer to a buck converter with specifications $V_{in} = 5$V, $V_{out} = 3.3$V, $f_s = 465$kHz, and consider a Coilcraft MSS7341-183

inductor of nominal inductance $L_{nom} = 18\mu$H, whose L *vs* i_L characteristic is depicted in the top part of Fig. 4.1. Accordingly, the bottom part of Fig. 4.1 shows the current waveforms of the analyzed inductor relative to three different average current I_L values, such that the inductor peak-to-peak current ripple Δi_{Lpp} falls entirely within the weak-saturation region (red waveform, with I_L = 1A), the roll-off region (green waveform, with I_L = 2A), or the deep-saturation region (blue waveform, with I_L = 3.5A). These waveforms have been simulated by using a generalized numerical algorithm for inductor current reconstruction presented in Chapter 1. For each value of the average current I_L, the operating point swings along the L *vs* i_L curve during the switching period T_s, as highlighted in Fig. 4.1. In particular, the inductor current waveshape is cusp-like in the roll-off region, and its inductance swings over the range from about 3μH to 12μH delimited by current ripple extremes.

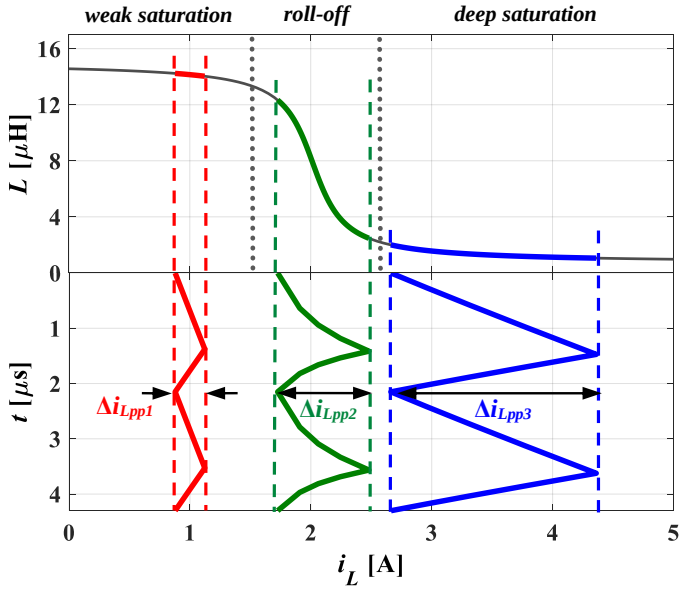

Figure 4.1: L *vs* i_L curve and current waveforms of MSS7341-183 inductor in weak saturation (red), roll-off (green) and deep saturation (blue).

Despite the inductance drop determined by the core saturation, ferrite inductor may be considered in Sustainable Saturation Operation (SSO) if its current ripple, power losses and temperature rise satisfy the acceptability limits and efficiency requirements, for both the device and the SMPS.

4.1.1 SSO-Analysis Algorithm

A generalized numerical algorithm for inductor current reconstruction presented in Chapter 1 can be incorporated into a higher-level algorithm, to validate the SSO-compliant inductor solutions for high-power-density SMPSs. The flow diagram of Fig. 4.2 depicts the SSO-analysis algorithm allowing to determine the inductor current ripple, power losses and operating temperature including saturation effects. Given converter operating conditions $\{V_{in}, V_{out}, I_{out}, f_s\}$ and inductor parameters $\{L^{high}, L^{low}, \sigma, I_L^*\}$, such algorithm evaluates the DC winding resistance $R_{dc}(T)$ and the current values $I_{30\%}(T)$ and $I_{70\%}(T)$ of the L *vs* i_L curve for evolving inductor temperature T. In particular, the resistance $R_{dc}(T)$ is evaluated by means of (4.1):

$$R_{dc}(T) = R_{dc,25^\circ C}\left[1 + \partial_R(T - 25^\circ C)\right] \tag{4.1}$$

where $R_{dc,25^\circ C}$ is the DC winding resistance at $25^\circ C$ and $\partial_R = 3.85e{-}3\,^\circ C^{-1}$ is the copper thermal coefficient. The current values $I_{30\%}(T)$ and $I_{70\%}(T)$ are evaluated according to Eq. (1.9) and used to reconstruct the inductor current wave-shape over the switching period T_s by means of the generalized algorithm given in Fig. 1.12. Based on the resulting current waveform, the peak-to-peak ripple and rms current values are calculated and used to evaluate the inductor total power losses, given as a sum of the winding and core loss contributions. A detailed discussion on the winding and core loss formulas presented in literature is provided in Chapter 5. The SSO-analysis algorithm of Fig. 4.2 evaluates inductor winding losses (P_{wind}) and core losses (P_{core}) by means of formulas (4.2) and (4.3), respectively:

$$P_{wind} = R_{dc}(T) \cdot I_{Lrms}^2 \tag{4.2}$$

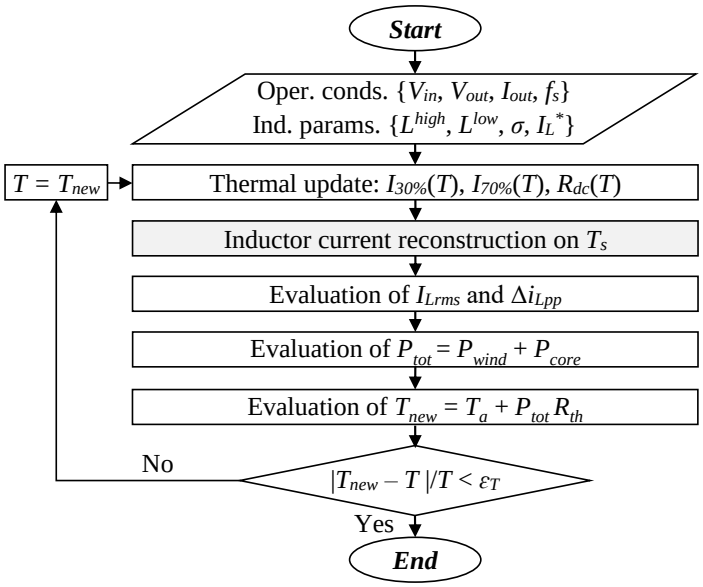

Figure 4.2: SSO-analysis algorithm.

$$P_{core} = K_1 f_s^X (K_2^* \Delta i_{Lpp})^Y \tag{4.3}$$

In formula (4.3), the core loss coefficients K_1, X and Y are typically provided by some power inductors manufacturers, whereas the coefficient K_2^* represents the modified version of the nominal K_2 coefficient declared by the manufacturers for core loss estimation in the weak-saturation region. In particular, K_2^* takes into account the saturation degree of the inductor, as follows:

$$K_2 = \frac{L_{nom}}{2nA_e}, \qquad K_2^* = \frac{L_{eq}}{2nA_e} = K_2 \frac{L_{eq}}{L_{nom}} \tag{4.4}$$

where L_{eq} represents the equivalent inductance of the device, defined as the current-averaged inductance over the peak-to-peak current ripple range, delimited by the valley (I_{vl}) and peak (I_{pk}) current values:

$$L_{eq} = \frac{1}{\Delta i_{Lpp}} \int_{I_{vl}}^{I_{pk}} L(i_L) di_L \tag{4.5}$$

L_{eq} can be estimated *via* a trapezoidal approximation of the integral in (4.5), starting from the N_s inductor current samples (I_k)

and the respective inductance values (L_k) provided by the inductor current reconstruction algorithm, as given by (4.6).

$$L_{eq} \approxeq \frac{1}{\Delta i_{Lpp}} \sum_{k=1}^{N_s-1} \left[\frac{(L_k + L_{k+1})(I_{k+1} - I_k)}{2} \right] \tag{4.6}$$

Eventually, the winding and core loss contributions provided by (4.2) and (4.3) are used by the SSO-analysis algorithm to evaluate the inductor total power losses $P_{tot} = P_{wind} + P_{core}$, and calculate the new value of the inductor operating temperature T_{new}:

$$T_{new} = T_a + P_{tot} R_{th} \tag{4.7}$$

where T_a is the ambient temperature, and R_{th} is the the equivalent thermal resistance of the inductor. A realistic value of R_{th} can be obtained from the temperature rise data $T_\Delta = T - T_a$ (typically, 20°C or 40°C), provided by manufacturers for a given DC inductor current I_{dc}, according to (4.8):

$$R_{th} = T_\Delta / \left(R_{dc} I_{dc}^2 \right) \tag{4.8}$$

According to (4.7), the inductor temperature is iteratively updated and referred to as a convergence parameter for the SSO algorithm termination: if the normalized difference between T_{new} and T is lower than a given tolerance ϵ_T (in this work, ϵ_T=1e-4), the SSO-analysis algorithm is terminated, otherwise the calculations are iterated.

4.1.2 Case Studies and Discussion

To verify the possibility of exploiting the FPIs operation in sustainable and controlled saturation, an investigation has been herein performed regarding a buck converter with specifications V_{in} = 5V, V_{out} = 3.3V, I_{out} = 1.5A, f_s = 465kHz and T_a = 23.5°C. The converter efficiency is defined as follows:

$$\eta = P_{out} / P_{in} \tag{4.9}$$

where $P_{out}=V_{out}I_{out}$ is the output power and $P_{in}=(P_{out}+P_{BUCK})$ is the input power of the converter, P_{BUCK} being the total power dissipated by the entire converter. P_{BUCK} includes both semiconductor and passive devices losses. Accordingly, it results that:

$$P_{BUCK} = P_{out}(1-\eta)/\eta \tag{4.10}$$

Let us assume a minimum efficiency requirement of 85% for the converter. The total power loss budget P_{BUCK} is about 0.87W. Then, for the given case study, the following constraints have been imposed:

- maximum inductor total power losses $P_{tot,MAX}=15\%P_{BUCK}\approx 130mW$;
- maximum inductor current ripple $\Delta i_{Lpp,MAX} = 50\%I_L = 0.75A$;
- minimum equivalent inductance $L_{eq,MIN} = 20\%L_{nom}$ (depends on the specific inductor);
- maximum inductor temperature rise $T_{\Delta,MAX}=10°C$.

Five Coilcraft ferrite inductor families have been considered for the analysis, namely MSS5121, MSS5131, MSS6122, MSS6132 and MSS7341. Their characteristics are summarized in Table 4.1. The maximum current ripple condition allows a minimum inductance value of $4\mu H$ for a given application. Accordingly, three inductors have been selected for each family, with nominal inductance values from $4.7\mu H$ to $7.4\mu H$, taking into account that the solutions to be explored include the possibility of operation in the roll-off region, thus resulting in the reduction of the equivalent inductance with respect to L_{nom}. For each family, the data of the core volume has been provided, normalized with respect to the volume of the smallest family, namely MSS5121, in order to highlight a possible inductor size reduction as a consequence of the use of FPIs in SSO. Each one of the selected inductors can be classified as a feasible solution for the design if its power losses, current ripple, inductance and temperature rise values $x_k = \{P_{tot,k}, \Delta i_{Lpp,k}, L_{eq,k}, T_{\Delta,k}\}$ (with $k = 1, ..., 15$) fulfill all the above constraints, namely:

$$\begin{aligned} X_{feasible} = \{x_k |\, &(P_{tot,k} \leq P_{tot,MAX}) \cap (\Delta i_{Lpp,k} \leq \Delta i_{Lpp,MAX}) \\ &\cap (L_{eq,k} \geq L_{eq,MIN}) \cap (T_{\Delta,k} \leq T_{\Delta,MAX})\} \end{aligned} \tag{4.11}$$

Table 4.1: Investigated inductors and their main characteristics

Family	Dimensions $[mm^3]$	Volume $[mm^3]$	Normal. volume [%]	L $[\mu H]$	$I_{sat}[A]$ 30% drop
MSS5121	5.5x5.1x2.2	57.2	100	4.7	1.66
				5.6	1.54
				6.8	1.38
MSS5131	5.1x5.1x3.1	80.6	141	4.7	1.42
				5.6	1.30
				6.8	1.24
MSS6122	6.1x6.1x2.2	81.9	143	4.7	1.82
				5.6	1.60
				6.8	1.50
MSS6132	6.1x6.1x3.2	119.1	208	4.7	2.84
				5.6	2.74
				6.8	2.30
MSS7341	7.3x7.3x4.1	218.5	382	5.0	3.16
				6.2	2.98
				7.4	2.56

The SSO-analysis algorithm of Fig. 4.2 has been implemented in MATLAB and applied to all the inductors of Table 4.1. On average, three iterations have been sufficient for the algorithm convergence. Fig. 4.3(a)-(d) shows the obtained simulation results, where the analyzed FPIs families have been represented by using different marker colors, with the blue markers corresponding to the smallest-volume cores and the red markers corresponding to the biggest-volume cores. Fig. 4.3(a) shows the inductor total power losses P_{tot} *vs* the nominal inductance L_{nom} of the devices, together with the maximum allowable total power losses $P_{tot,MAX}$ (red dashed line). It can be observed that no feasible solutions are available for the MSS5121 and MSS6122 families. Fig. 4.3(b) depicts the inductor current ripple Δi_{Lpp} normalized with respect to the average inductor current I_L, together with

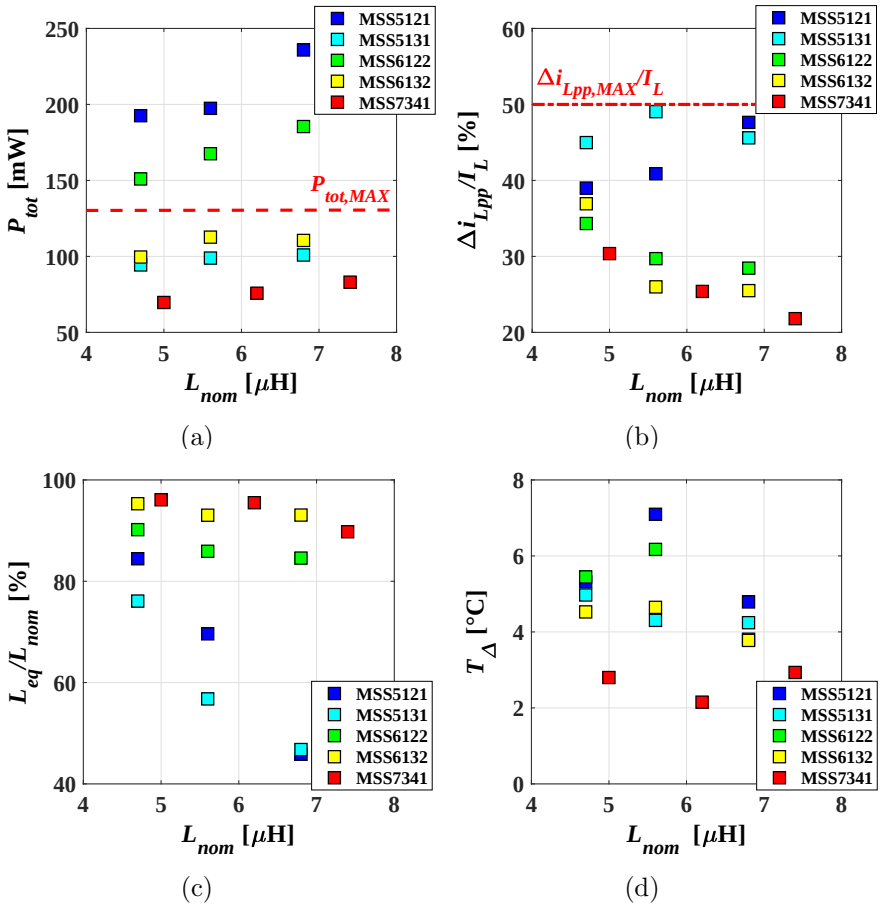

Figure 4.3: Inductor families performances *vs* L_{nom}: (a) total power losses; (b) normalized current ripple; (c) normalized equivalent inductance; (d) temperature rise.

the maximum acceptable normalized current ripple $\Delta i_{Lpp,MAX}/I_L$ (red dashed-dotted line). For the MSS5121 and MSS5131 families (blue and cyan markers, respectively) the current ripple values increase for higher nominal inductances because of their deeper saturation degree. Nevertheless, the maximum allowable ratio $\Delta i_{Lpp,MAX}/I_L$ is satisfied also for such saturated smaller-volume families. Fig. 4.3(c) shows the normalized equivalent inductances L_{eq}/L_{nom}, highlighting that all the parts are working either in the

weak-saturation or in the roll-off region, since their L_{eq} values are all higher than 20% of the respective L_{nom} data. In Fig. 4.3(d) the temperature rise T_{Δ} values are eventually shown. All the considered FPIs present acceptable temperature rise, despite a possible operation in partial saturation.

Some FPIs families do not allow any feasible solution, like the MSS5121 and MSS6122 (see Fig. 4.3(a)). Other families may allow more than one feasible solution. Let us first compare the best performing parts for each family. In particular, among the feasible solutions, those ones characterized by minimum total power losses have been selected as possible optimal solutions for the design, namely the MSS5131-472 ($L_{nom} = 4.7\mu H$), MSS6132-472 ($L_{nom} = 4.7\mu H$) and MSS7341-502 ($L_{nom} = 5\mu H$). Their power losses, volumes, current ripples, equivalent inductances and operating temperatures, determined by means of the SSO-analysis algorithm, are compared in Fig. 4.4. Power losses (square markers) and volumes (upside down triangle markers) are shown in Fig. 4.4(a). The volume of the MSS7341 part is about three times the MSS5131 part volume. As predictable, the smaller-core inductors MSS5131-472 and MSS6132-472 have higher total power losses compared to the biggest-core inductor MSS7341-502. Fig. 4.4(b) shows the inductors normalized current ripples $\Delta i_{Lpp}/I_L$ (triangle markers) and equivalent inductances L_{eq} (circle markers), which are inversely proportional to the current ripple values. Finally, Fig. 4.4(c) shows the normalized equivalent inductances L_{eq}/L_{nom} (facing left triangle markers) and temperatures (diamond markers) for the selected optimal solutions. The smallest-core inductor MSS5131-472 is working within its roll-off region, with the equivalent inductance $L_{eq} \approx 76\% L_{nom}$. The two bigger-core inductors MSS6132-472 and MSS7341-502 are, instead, working in the weak-saturation region, with equivalent inductance values of more than $95\% L_{nom}$. Therefore, between the smaller-core solutions, the smallest-core inductor MSS5131-472 outperforms the bigger-core MSS6132-472 in terms of losses, despite its higher saturation level and ripple. Conversely, the MSS5131-472 has the highest, yet acceptable, operating temperature.

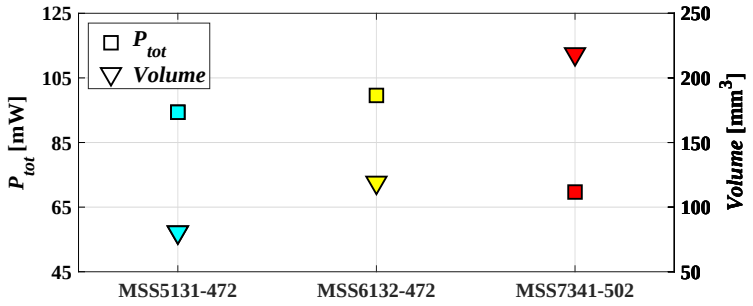

(a)

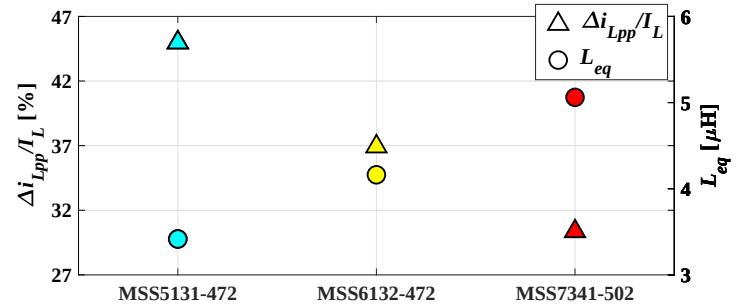

(b)

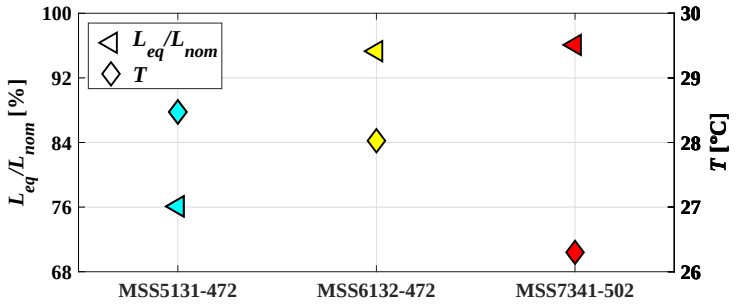

(c)

Figure 4.4: Optimal solutions comparison: (a) total power losses *vs* volume; (b) normalized current ripple *vs* equivalent inductance; (c) normalized equivalent inductance *vs* temperature.

Fig. 4.5(a) shows the simulated current waveforms of the three optimal inductors under the given operating conditions. The MSS-6132-472 and the MSS7341-502 inductors present triangular current wave-shapes, as they are working in the weak-saturation region. The MSS5131-472 inductor, instead, shows a slightly cusp-like current wave-shape due to the partial saturation. Fig. 4.5(b) depicts the L *vs* i_L curves of the selected optimal inductors and the relevant operating regions, highlighted by means of thicker lines. Each curve corresponds to the operating temperature resulting from the SSO-analysis algorithm. Fig. 4.5(b) also highlights that the MSS5131-472 instantaneous inductance swings between about

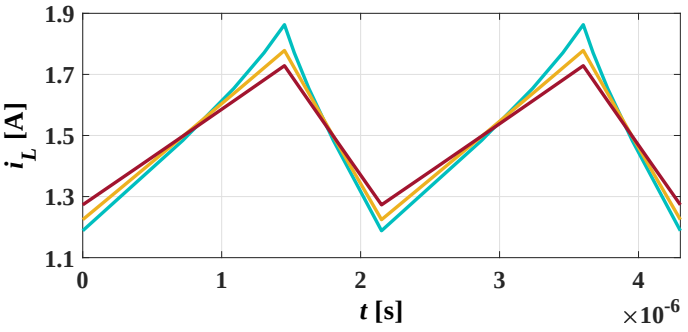

(a)

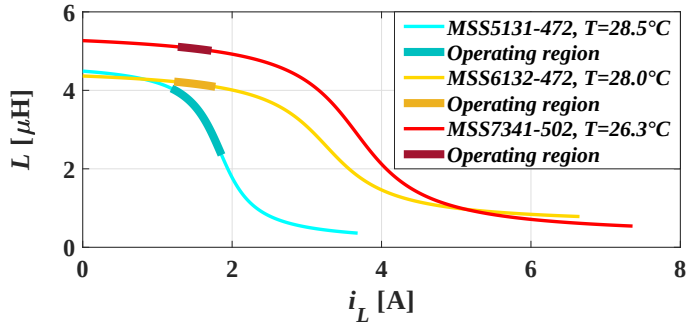

(b)

Figure 4.5: Optimal solutions comparison: (a) inductor current waveforms; (b) inductance *vs* current curves.

$4\mu H$ and $2.4\mu H$ during the switching period. Thus, the inductance drops down to 50% of its nominal value $L_{nom} = 4.7\mu H$, resulting in an equivalent inductance of $3.4\mu H$ (76% of L_{nom}). In conclusion, the smallest-core inductor looks like an optimum trade-off solution in terms of performance and volume.

Let us now explore the other feasible parts of the MSS5131 family, which are characterized by deeper saturation and slightly higher losses (see Fig. 4.3(a),(c)). Fig. 4.6(a) compares the simulated current waveforms for the inductors MSS5131-472 ($L_{nom} = 4.7\mu H$), MSS5131-562 ($L_{nom} = 5.6\mu H$) and MSS5131-682 ($L_{nom} = 6.8\mu H$). The relevant L *vs* i_L curves are shown in Fig. 4.6(b), with

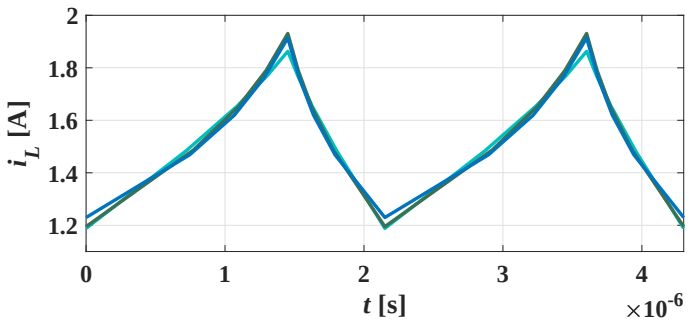

(a)

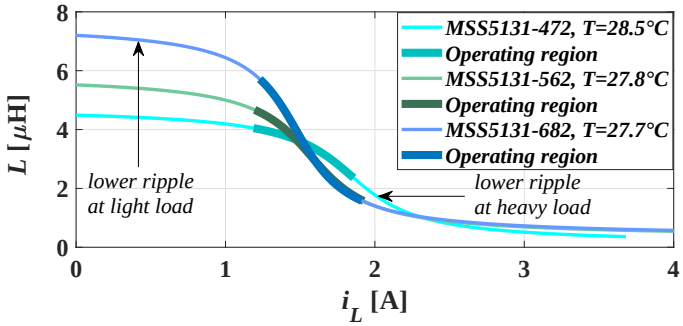

(b)

Figure 4.6: MSS5131 family: (a) inductor current waveforms; (b) inductance *vs* current curves.

the operating regions highlighted by means of thicker lines. The MSS5131-562 inductance varies in the range between $4.7\mu H$ and $1.6\mu H$, whereas the MSS5131-682 inductance varies in the range between $5.7\mu H$ and $1.6\mu H$. Thus, they drop down to 28% and 25% of their nominal values respectively, with a resulting equivalent inductance equal to $3.1\mu H$ (55% of L_{nom}) for MSS5131-562 and $3.4\mu H$ (50% of L_{nom}) for MSS5131-682 (as for MSS5131-472). The peak-to-peak current ripple magnitudes determined by the three parts are nearly the same, as shown in Fig. 4.6(a). The power losses of MSS5131-562 and MSS5131-682 parts are few mW higher than for the MSS5131-472 part (see Fig. 4.3(a)). All these three MSS5131 design solutions are SSO-compliant for the buck converter under study. The MSS5131-682 part can be selected if a higher efficiency at light load is preferred, because of its higher inductance at low current values. Conversely, the MSS5131-472 part is preferable if higher efficiency at heavy load is required.

4.1.3 Experimental Verification

SSO-Analysis Algorithm Validation

The SSO-analysis algorithm results have been validated through experimental tests realized by means of the MADMIX system, described in Chapter 5. Four inductors have been tested, namely the MSS5131-472 (IUT #1), MSS5131-562 (IUT #2), MSS6132-472 (IUT #3) and MSS7341-502 (IUT #4), under the operating conditions provided in Section 4.1.2 (V_{in} = 5V, V_{out} = 3.3V, f_s = 465kHz, $T_a = 23.5°C$), for two different output current values: I_{out} = 1.5A (heavy load) and I_{out} = 0.3A (light load). The resulting winding and core losses of the inductors under test have been evaluated by using formulas (4.2)-(4.3) and FPIs data provided in Table 4.2, such as the nominal and equivalent inductance, the DC winding resistance and core loss coefficients $\{K_1, K_2, X, Y\}$. The experimental results and the SSO-analysis algorithm predictions are summarized in Table 4.3. For all the investigated FPIs, the power loss and temperature rise estimation are in good agreement

Table 4.2: FPIs data for winding and core loss evaluation

IUT #	L_{nom} $[\mu H]$	L_{eq} *@1.5A* $[\mu H]$	L_{eq} *@0.3A* $[\mu H]$	R_{dc} $[m\Omega]$	K_1	K_2	X	Y
1	4.7	3.4	4.4	31.1	8.65e-5	8.18e-1	1.21	2.01
2	5.6	3.1	5.4	34.6	8.65e-5	8.96e-1	1.21	2.01
3	4.7	4.2	4.3	34.8	1.75e-4	5.39e-1	1.21	2.01
4	5.0	5.1	5.2	15.7	2.77e-4	5.89e-1	1.21	2.01

Table 4.3: MADMIX experimental measurements and SSO-analysis algorithm simulation results

$I_{out} = 1.5A$ (*heavy load*)								
IUT #	R_{th} (exp.) $[°C/W]$	P_{core} (sim.) $[mW]$	P_{wind} (sim.) $[mW]$	P_{tot} (sim.) $[mW]$	P_{tot} (exp.) $[mW]$	P_{tot} error $[\%]$	T_Δ (sim.) $[°C]$	T_Δ (exp.) $[°C]$
1	52.7	23.3	71.1	94.4	95.8	-1.5	5.0	5.0
2	43.5	19.7	79.2	98.9	105.7	-6.4	4.6	4.3
3	45.5	20.4	79.2	99.6	101.0	-1.4	4.6	4.5
4	40.2	34.1	35.6	69.7	65.3	6.7	2.6	2.8
$I_{out} = 0.3A$ (*light load*)								
IUT #	R_{th} (exp.) $[°C/W]$	P_{core} (sim.) $[mW]$	P_{wind} (sim.) $[mW]$	P_{tot} (sim.) $[mW]$	P_{tot} (exp.) $[mW]$	P_{tot} error $[\%]$	T_Δ (sim.) $[°C]$	T_Δ (exp.) $[°C]$
1	100.0	23.3	3.5	26.8	23.8	12.6	2.4	2.7
2	93.6	19.7	3.6	23.3	23.4	-0.4	2.2	2.2
3	95.5	20.4	3.9	24.3	25.2	-3.6	1.9	2.3
4	62.6	34.1	1.7	35.8	32.0	11.9	2.0	2.2

with the MADMIX experimental results. In particular, the power loss percent errors are typically lower than 10% in heavy load conditions and 15% in light load conditions. Such errors are within the typical tolerance range of FPIs parameters.

Efficiency Measurements

Additional experimental tests have been realized by using the Texas Instruments TPS54160EVM-230 peak-current-mode control buck board [25], operating with $V_{in} = 5\text{V}$, $V_{out} = 3.3\text{V}$, $I_{out} = 1.5\text{A}$, $f_s = 465\text{kHz}$. The experimental measurements set-up included a LeCroy WaveRunner 44Xi oscilloscope, a Tektronix TCP 305 50A current probe with Tektronix TCP A300 amplifier, a H&H ZS 1880 electronic load 800V/15A/1800W, a TTi EX354RD power supply 300W/2x35V/4A, a Fluke 179 digital multimeter with a type K thermocouple and a Yokogawa WT3000 power analyzer, as shown in Fig. 4.7. Measurements of the inductor current i_L, voltage v_L and temperature T have been performed in heavy load condition ($I_{out} = 1.5\text{A}$) for the four inductors under investigation, namely the MSS5131-472, MSS5131-562, MSS6132-472 and MSS7341-502, at the ambient temperature $T_a = 22.5°C$. For each inductor, the voltage v_L has been obtained by subtracting the voltages v_{Lp} and v_{Lm} measured at the two inductor terminals.

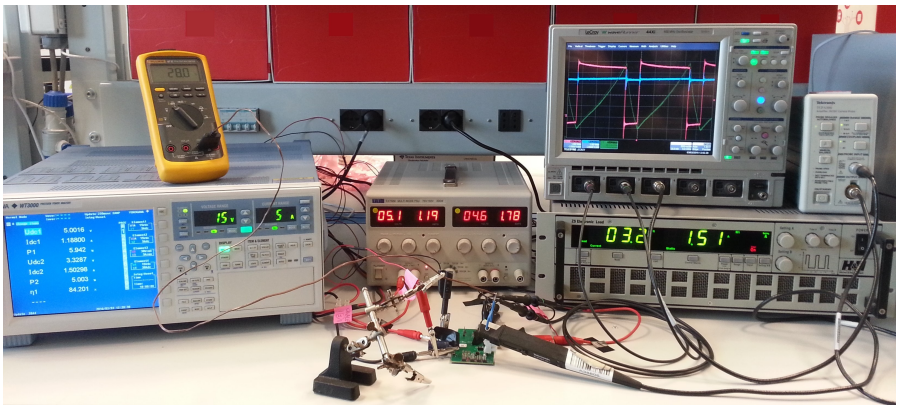

Figure 4.7: Measurement set-up.

Fig. 4.8 shows a summary of measurement results, including experimental inductor waveforms (oscilloscope screenshots) and converter efficiency measurements (power analyzer screenshots). In particular, the experimental current waveforms in Fig. 4.8 correspond to the simulated waveforms for the respective inductors, given in Fig. 4.5(a) and Fig. 4.6(a). The experimental measurements confirm that the MSS5131-472 and MSS5131-562 inductors are SSO-compliant for the given application. Indeed, the peak-current controlled buck regulator ensures a 3.3V output voltage at 1.5A load current, regardless of the inductor saturation (see U_{dc2} and I_{dc2} in the power analyzer screenshots).

Eventually, measurements of the buck converter efficiency have been performed on the entire output current range, from the light load condition (I_{out} = 0.3A) to the high load condition (I_{out} = 1.5A). Fig. 4.9 summarizes the experimental converter efficiency *vs* the load current, with the L *vs* i_L curves relevant to the analyzed FPIs provided in Fig. 4.10. It can be observed that the smallest-core inductors MSS5131-472 and MSS5131-562 determine about 0.7% and 1.2% efficiency decrease at heavy load compared to the biggest-core MSS7341-502 part, due to their higher saturation degree, peak-to-peak current ripple and power loss. However, the MSS5131-562 improves the efficiency at light load, outperforming all the other inductors. Such improvement is due to the fact that the MSS5131-562 part de-saturates at light load current, with the equivalent inductance approaching its nominal value ($5.6\mu H$), thus resulting in lower peak-to-peak current ripple and power loss. As a result, the overall converter efficiency increases. Another inductor has been added to the comparison and included in Fig. 4.9 and Fig. 4.10, namely the MSS5131-332, which has the same size of the other MSS5131 parts and a nominal inductance of $3.3\mu H$, close to the equivalent inductances of the saturated inductors MSS5131-472 ($L_{eq} = 3.4\mu H$) and MSS5131-562 ($L_{eq} = 3.1\mu H$). The MSS5131-332 produces substantial efficiency degradation at light load, without any significant efficiency improvement at heavy load. In fact, the MSS5131-332 has an equivalent inductance of $L_{eq} = 2.7\mu H$ in this application, since the increase of its saturation

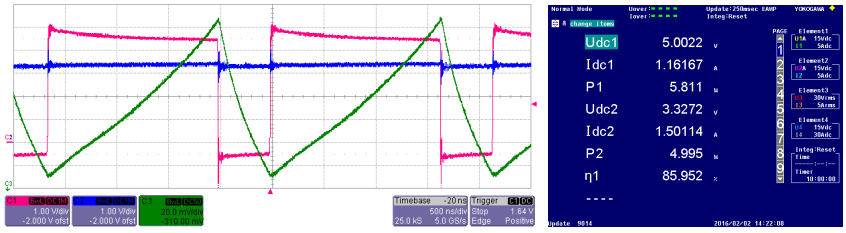

(a) MSS5131-472

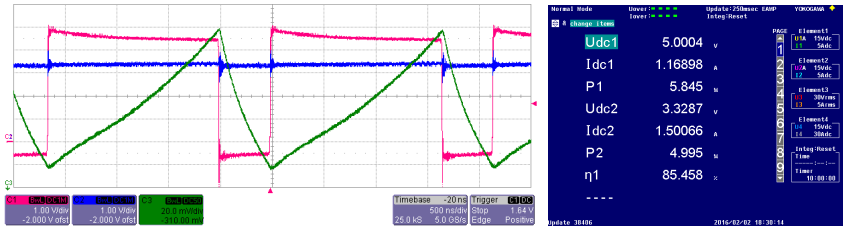

(b) MSS5131-562

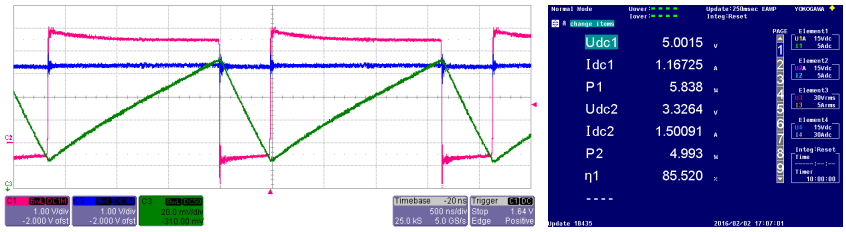

(c) MSS6132-472

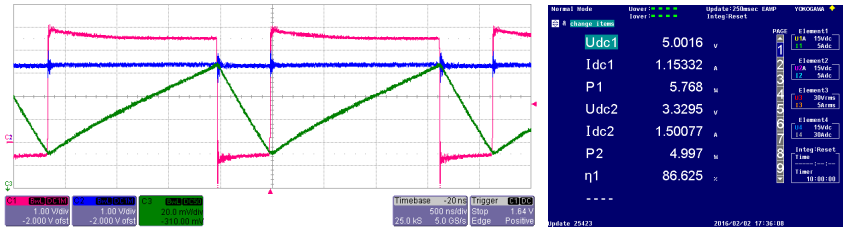

(d) MSS7341-502

Figure 4.8: Left: oscilloscope screenshots with C_1 (magenta) = v_{Lp}, C_2 (blue) = v_{Lm}, C_3 (green) = i_L(x5). Right: power analyzer screenshots with $U_{dc1} = V_{in}$, $I_{dc1} = I_{in}$, $P_1 = P_{in} = V_{in} I_{in}$, $U_{dc2} = V_{out}$, $I_{dc2} = I_{out}$, $P_2 = P_{out} = V_{out} I_{out}$, $\eta_1 = P_{out}/P_{in}$.

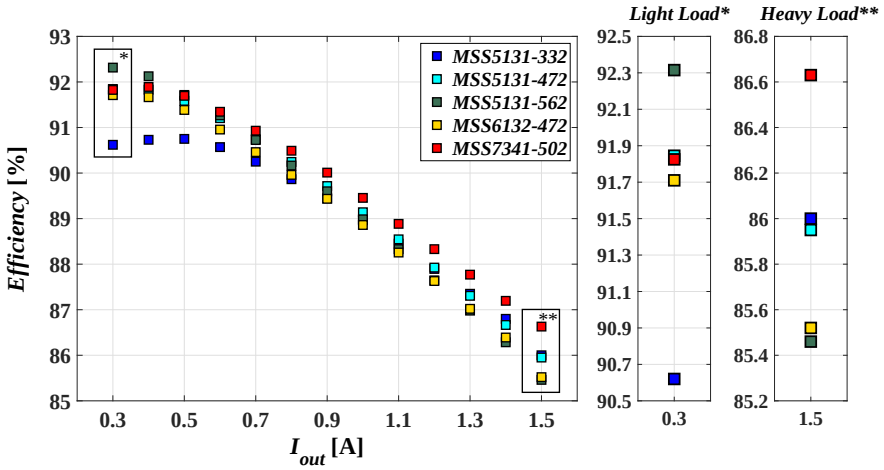

Figure 4.9: Converter efficiency *vs* load current.

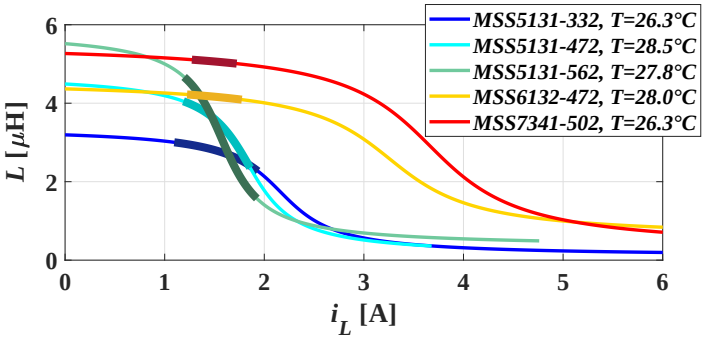

Figure 4.10: L *vs* i_L curves of the analyzed inductors.

current determined by the lower number of turns is not sufficient to keep the inductance at $3.3\mu H$ in the current range of operation. A $3.3\mu H$ inductor with a bigger core is required to keep the inductance within the weak-saturation region.

The SSO-compliant inductor solutions validated in this Section have been identified by means of the previously discussed SSO-analysis algorithm of Fig. 4.2. However, for quicker and simpler selection of FPIs in SSO, an alternative approach can be adopted, not requiring any iterative procedures and based on the linearized model of the L *vs* i_L curve in the roll-off region presented next.

4.2 SSO-Compliance Validation

This Section discusses a method allowing quick and straightforward validation of SSO-compliance for FPIs. A simplified inductance model is proposed linearizing the FPI saturation characteristic in the roll-off region. Based on such a linearized model, an analytical procedure is developed providing practical design guidelines to quickly identify SSO-compliant inductors for given SMPS specifications.

4.2.1 Linearized Inductance Model

The Sustainable Saturation Operation of FPIs can be validated by means of the simplified model linearizing the inductance *vs* current characteristic in the roll-off region, as depicted in Fig. 4.11. The first step is to consider a FPI such that the maximum average inductor current I_L required by the application falls between the saturation current values $I_{10\%}$ and $I_{90\%}$, corresponding to the 10% and 90% drop of inductance with respect to the nominal inductance value L_{nom}. Based on such data, the simplified model linearizing the L *vs* i_L curve in the roll-off region can be considered:

$$L\left[i_L(t)\right] = L_0 - k \cdot i_L(t) \tag{4.12}$$

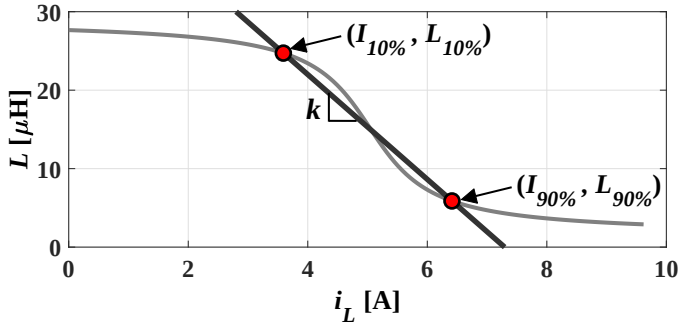

Figure 4.11: L *vs* i_L curve linearization in the roll-off region.

In (4.12) the slope, k, and the y-axis intercept, L_0, of the secant of the L *vs* i_L curve in the roll-off region are given by (4.13):

$$k = \left| \frac{L_{10\%} - L_{90\%}}{I_{10\%} - I_{90\%}} \right| \tag{4.13a}$$

$$L_0 = L_{10\%} + k \cdot I_{10\%} \tag{4.13b}$$

Based on (4.12), the inductor voltage is given by (4.14):

$$v_L(t) = L\left[i_L\left(t\right)\right] \frac{di_L(t)}{dt} = L_0 \frac{di_L(t)}{dt} - k \cdot i_L(t) \frac{di_L(t)}{dt} \tag{4.14}$$

Integrating (4.14) between 0 and t, where 0 is the time instant corresponding to the inductor valley current value I_{vl} and t is a generic time instant within the rise-time interval $T_r = [0, DT_s]$ of the inductor current, yields (4.15):

$$V_{Lr} \cdot t = L_0 \left[i_L(t) - I_{vl}\right] - \frac{k}{2} \left[i_L^2(t) - I_{vl}^2\right] \tag{4.15}$$

Evaluating (4.15) in $t = DT_s$ yields (4.16):

$$\lambda = L_0 \left[I_{pk} - I_{vl}\right] - \frac{k}{2} \left[I_{pk}^2 - I_{vl}^2\right] \tag{4.16}$$

where $\lambda = V_{Lr} DT_s$ is the volt-second product applied to the inductor during the rise-time interval T_r, and I_{pk} is the inductor peak current value in $t = DT_s$. Equation (4.15) can also be integrated and averaged over T_r, resulting in (4.17):

$$\begin{aligned} \frac{\lambda}{2} &= \frac{1}{DT_s} \int_0^{DT_s} V_{Lr} \cdot t dt = ... \\ &= L_0 \left[\frac{1}{DT_s} \int_0^{DT_s} i_L(t) dt - I_{vl}\right] - \frac{k}{2} \left[\frac{1}{DT_s} \int_0^{DT_s} i_L^2(t) dt - I_{vl}^2\right] = \\ &= L_0 \left(I_L - I_{vl}\right) - \frac{k}{2} \left(I_{Lrms}^2 - I_{vl}^2\right) \end{aligned} \tag{4.17}$$

Given the average inductor current I_L and volt-second integral λ, (4.16) and (4.17) represent a system of two equations in

two variables, I_{vl} and I_{pk}, the solution of which yields the prediction of the inductor current ripple in the roll-off region, as $\Delta i_{Lpp} = I_{pk} - I_{vl}$. In particular, let us assume $I_{Lrms} \approx I_L$. This is a good approximation for ripple ratios $\Delta i_{Lpp}/I_L < 1$: it results $I_{Lrms}/I_L = 1.02$ when $\Delta i_{Lpp}/I_L = 0.5$, and $I_{Lrms}/I_L = 1.08$ when $\Delta i_{Lpp}/I_L = 1$. Thus, the solution of equations (4.16) and (4.17) provides the simplified formulas for the evaluation of I_{pk} and I_{vl}, given in (4.18):

$$I_{pk} = \frac{1}{k}\left[L_0 - \sqrt{(L_0 - kI_L)^2 - k\lambda}\right] \tag{4.18a}$$

$$I_{vl} = \frac{1}{k}\left[L_0 - \sqrt{(L_0 - kI_L)^2 + k\lambda}\right] \tag{4.18b}$$

The values of I_{pk} and I_{vl} provided by (4.18) allow to calculate the peak-to-peak current ripple Δi_{Lpp} and the equivalent inductance L_{eq} of the device, defined as the current-averaged inductance over the peak-to-peak current ripple range $[I_{vl}, I_{pk}]$:

$$L_{eq} = \frac{1}{I_{pk} - I_{vl}} \int_{I_{vl}}^{I_{pk}} (L_0 - ki_L)\, di = L_0 - \frac{k}{2}(I_{pk} + I_{vl}) \tag{4.19}$$

which is related to Δi_{Lpp} and λ according to (4.20):

$$L_{eq} = \frac{\lambda}{\Delta i_{Lpp}} \tag{4.20}$$

Equation (4.20) expresses the key concept underlying the use of ferrite inductors in partial saturation: the inductor has to be selected so that its equivalent inductance L_{eq} in the roll-off region is greater than or equal to the inductance needed to obtain a ripple of maximum allowable magnitude $\Delta i_{Lpp,MAX}$, under the applied volt-second product λ. To verify if the inductor current fulfills the constraint $I_{pk} - I_{vl} \leq \Delta i_{Lpp,MAX}$, we can merge (4.18a) and (4.18b), resulting in (4.21):

$$\sqrt{(L_0 - kI_L)^2 + k\lambda} - \sqrt{(L_0 - kI_L)^2 - k\lambda} \leq k\Delta i_{Lpp,MAX} \tag{4.21}$$

Solving (4.21) yields (4.22):

$$L_{av} = L_0 - kI_L \geq \sqrt{\frac{\lambda^2}{\Delta i_{Lpp,MAX}^2} + \frac{\Delta i_{Lpp,MAX}^2}{4} k^2} = L_{av,MIN} \quad (4.22)$$

where L_{av} is the value of the inductance at the average current I_L, and $L_{av,MIN}$ is the minimum value required to comply with the maximum ripple specification. It is worth noting that, when the inductor operates in the roll-off region, it results: $L_{av} > L_{eq} = \lambda/\Delta i_{Lpp}$. Given the average inductor current I_L and the volt-second product λ, the inductor fulfills the maximum ripple constraint $\Delta i_{Lpp} \leq \Delta i_{Lpp,MAX}$ if the parameters k and L_0 of its linearized L *vs* i_L curve in the roll-off region fulfill the constraint (4.22).

Equations (4.18) and (4.22) provide reliable results if the inductor current ripple falls entirely within the roll-off region. Considering that $I_{pk} > I_{vl}$, this happens when the values I_{pk} and I_{vl} predicted with (4.18) jointly fulfill the conditions: $I_{pk} < I_{90\%}$ and $I_{vl} > I_{10\%}$. The relevant inductance values L_{pk} and L_{vl} can be evaluated as:

$$L_{pk} = L_0 - kI_{pk} = \sqrt{L_{av}^2 - k\lambda} \quad (4.23a)$$

$$L_{vl} = L_0 - kI_{vl} = \sqrt{L_{av}^2 + k\lambda} \quad (4.23b)$$

Since $L_{vl} > L_{pk}$, the ripple falls entirely within the roll-off region if the values given by (4.23) jointly satisfy the conditions: $L_{pk} > L_{90\%}$ and $L_{vl} < L_{10\%}$. As a result, the following constraints can be formulated:

$$L_{av,LB} = \sqrt{L_{90\%}^2 + k\lambda} \leq L_{av} \leq \sqrt{L_{10\%}^2 - k\lambda} = L_{av,UB} \quad (4.24)$$

where $L_{av,LB}$ and $L_{av,UB}$ represent the Lower Bound (LB) and the Upper Bound (UB) for L_{av}. Conditions (4.22) and (4.24), if fulfilled, provide quick and effective SSO-compliance assessment for FPIs operating in the roll-off region.

4.2.2 Case Studies and Model Validation

The linearized inductance model (4.12) has been validated over a large set of examples by comparing its results with the predictions of the generalized algorithm for inductor current reconstruction discussed in Chapter 1 and shown in Fig. 1.12. Both methods for current ripple prediction have been applied to four Coilcraft ferrite inductors, namely the MSS1246-223 ($L_{nom} = 22\mu H$), MSS1246-273 ($L_{nom} = 27\mu H$), MSS1260-273 ($L_{nom} = 27\mu H$) and MSS1260-333 ($L_{nom} = 33\mu H$). Their datasheet L *vs* i_L curves, relative to temperature $T = 25°C$, are depicted in Fig. 4.12. For each part, the secant of the respective curve in the roll-off region has been determined, by using the $\{I_{10\%}, L_{10\%}\}$ and $\{I_{90\%}, L_{90\%}\}$ operating points. Such points and relevant parameters of the obtained linearized models are listed in Table 4.4. On their basis, the estimation of inductor current ripple has been performed by means of (4.18), for the operating conditions relative to a buck converter with $V_{in} = 36$V, $V_{out} = 12$V, $f_s = 450$kHz, $\lambda = 7.8$V·s, at two different output current values $I_{out} = I_L = \{4.0, 5.0\}$A. Fig.s 4.13-4.16 show the comparison between the current ripple predictions obtained by using the linearized model (4.12) and the inductor current reconstruction algorithm of Fig. 1.12, where the plots have been denoted as case #1 - case #8. Each plot depicts

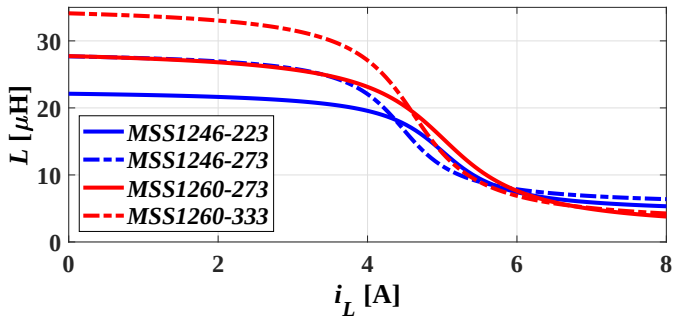

Figure 4.12: Datasheet L *vs* i_L curves of the investigated inductors.

the datasheet L *vs* i_L curve (gray line) and the linearized model for the roll-off region (black line). The portions of the curves covered by the swing of the inductor current ripple during the switching period are also highlighted (green and red portions, respectively).

Table 4.4: Parameters of linearized models for MSS inductors.

Part Number	$L_{10\%}$ $[\mu H]$	$L_{90\%}$ $[\mu H]$	$I_{10\%}$ $[A]$	$I_{90\%}$ $[A]$	L_0 $[\mu H]$	k $[\mu H/A]$
MSS1246-223	20.5	7.9	3.7	5.9	42.1	5.8
MSS1246-273	25.4	9.8	3.3	5.3	51.6	7.9
MSS1260-273	24.7	5.9	3.6	6.4	48.7	6.7
MSS1260-333	30.8	7.2	3.3	5.7	63.3	9.8

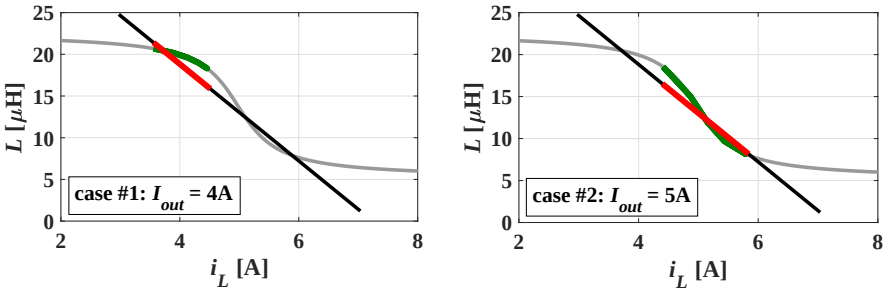

Figure 4.13: Inductor current ripple predictions for MSS1246-223.

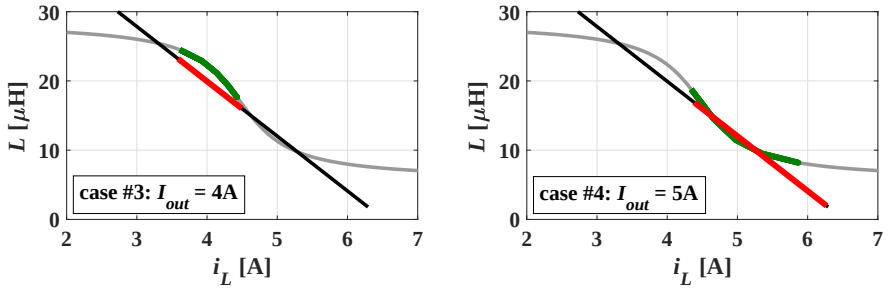

Figure 4.14: Inductor current ripple predictions for MSS1246-273.

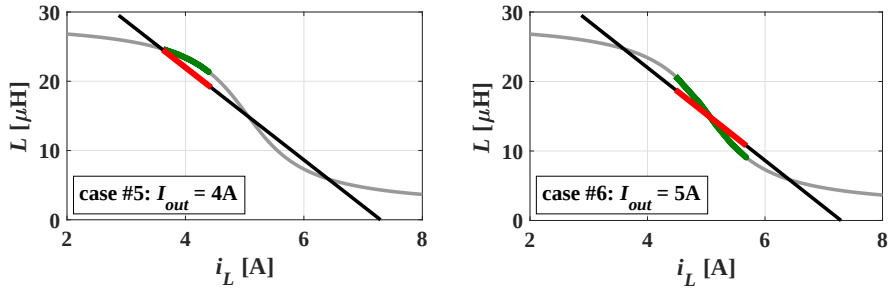

Figure 4.15: Inductor current ripple predictions for MSS1260-273.

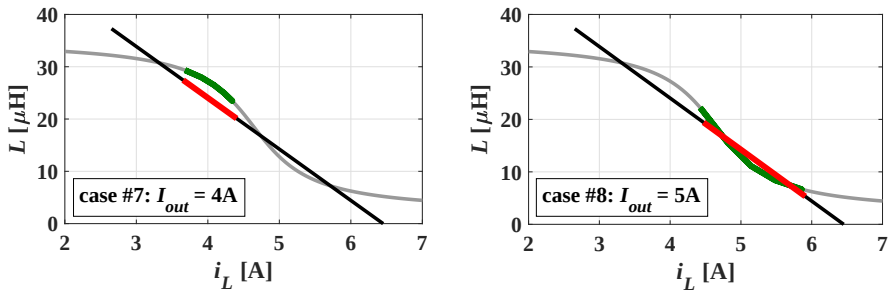

Figure 4.16: Inductor current ripple predictions for MSS1260-333.

The current ripple values obtained by means of the linearized model ($\Delta i_{Lpp,LIN}$) and the arctangent-based model (1.6) fitting the datasheet L *vs* i_L curve ($\Delta i_{Lpp,DAT}$) are summarized in Table 4.5, with the relevant percent error $(\Delta i_{Lpp,LIN} - \Delta i_{Lpp,DAT})/\Delta i_{Lpp,DAT}$. It can be observed that the error is positive for all the considered inductors and case studies. This means that the current ripple obtained with the linearized model overestimates the real ripple. Therefore, the linearized model provides a worst-case prediction of inductor current ripple, which can be used for a conservative choice of inductors adopted to operate in the roll-off region. For the inductors under study, Table 4.5 summarizes the SSO-compliance validation data $\{L_{av}, L_{av,MIN}, L_{av,LB}, L_{av,UB}\}$, obtained by using Eq.s (4.22) and (4.24) and assuming $\Delta i_{Lpp,MAX} = 50\% I_L$. In most of the examined cases, the SSO-compliance conditions are verified,

so that the inductor current ripple satisfies the constraint $\Delta i_{Lpp} \leq \Delta i_{Lpp,MAX}$ and stays entirely within the roll-off region. In some cases, like case #1, case #4 and case #8, the conditions (4.22) and/or (4.24) are not satisfied. Among them, it is possible to discern cases like case #1 and case #8 (see Fig. 4.13 and Fig. 4.16), for which the condition (4.22) is verified, so that the current ripple satisfies the maximum ripple constraint, while the condition (4.24) is slightly violated, which means that the current ripple goes outside the roll-off region and the linearized model may become inaccurate. However, such cases could still be considered SSO-compliant, since the violation of condition (4.24) is very slight. Conversely, for case #4 (see Fig. 4.14) both conditions (4.22) and (4.24) are violated. As a result, the linearized model cannot be used to predict the SSO-compliance, since the inductor current ripple goes far beyond the $I_{90\%}$ saturation current and the model becomes inaccurate.

Table 4.5: Current ripple and SSO-compliance validation data.

Case	$\Delta i_{Lpp,LIN}$	$\Delta i_{Lpp,DAT}$	Error	L_{av}	$L_{av,MIN}$	$L_{av,LB}$	$L_{av,UB}$
	$[A]$	$[A]$	$[\%]$	$[\mu H]$	$[\mu H]$	$[\mu H]$	$[\mu H]$
#1	0.954	0.898	6.2	18.8	10.6	12.9	17.8
#2	1.441	1.378	4.6	13.0	10.2	12.9	17.8
#3	0.906	0.815	11.2	19.9	11.9	15.4	22.5
#4	1.884	1.524	23.6	12.0	12.2	15.4	22.5
#5	0.815	0.764	6.7	22.0	11.1	12.4	22.2
#6	1.203	1.201	0.2	15.3	11.0	12.4	22.2
#7	0.748	0.660	13.3	24.1	13.2	15.1	27.8
#8	1.437	1.434	0.2	14.2	14.2	15.1	27.8

Temperature Impact

In the previous discussion, the L *vs* i_L curves at 25°C have been considered for all the analyzed inductors to predict their inductor current ripple values and provide the SSO-compliance assessment. However, the L *vs* i_L curves drift left-side with increasing temperature, thus resulting in the inductance decrease at a given current of interest. To ensure that an inductor is SSO-compliant despite its possible temperature increase, the analysis should be performed in the worst-case temperature condition. For example, let us assume that the MSS1260-273 inductor is adopted in the application having the same operating conditions of the case #5, for which the inductor temperature does not exceed 75°C. Two L *vs* i_L curves of the part, at 25°C and 75°C, should be considered for the SSO-compliance assessment, by linearization in the respective roll-off regions and evaluation of the resulting current ripple. Fig. 4.17 shows the trace of inductor current ripple estimated at two different temperatures by means of (4.18). As expected, the ripple is bigger at higher temperature (1.0A at 75°C *vs* 0.8A at 25°C). If the worst case ripple satisfies the maximum current ripple constraint (herein, $\Delta i_{Lpp,MAX} = 50\% I_L = 2\text{A}$), the selected inductor can be considered SSO-compliant.

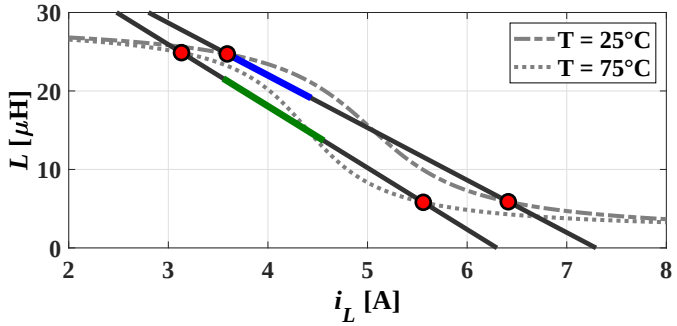

Figure 4.17: L *vs* i_L curves linearization for MSS1260-273 inductor and current ripple predictions at 25°C (blue) and 75°C (green).

Experimental Verification

The linearized model (4.12) has been validated experimentally, by comparing its current ripple prediction with the measured current ripple of the MSS1260-273 part, operating under the same conditions of the previous case study, namely $V_{in} = 36$V, $V_{out} = 12$V, $f_s = 450$kHz, $I_{out} = 4$A. The experimental inductor temperature $T_{exp} = 59°C$ has been measured and used to get the datasheet L *vs* i_L curve of the part relative to T_{exp}. Fig. 4.18 shows the measured current waveform (green) and the current ripple evaluated by using (4.18) (red). The linearized model predicts 0.98A ripple, while the experimental value is 0.89A, which proves the reliability of the proposed SSO-compliance validation method.

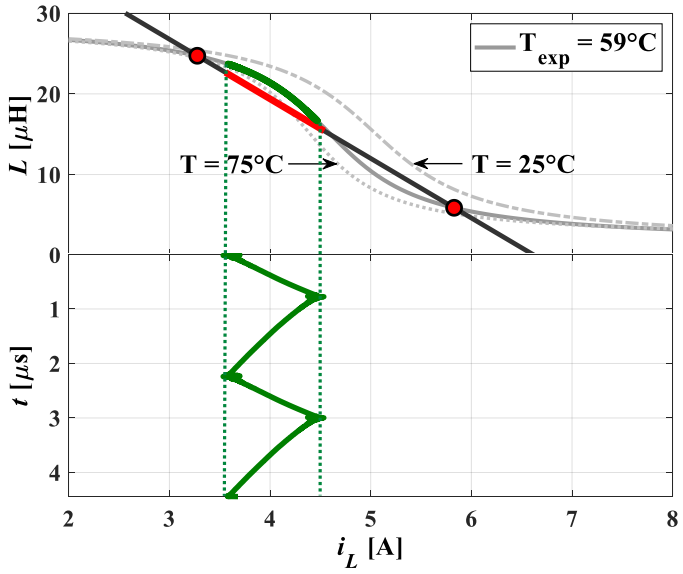

Figure 4.18: L *vs* i_L curve linearization for MSS1260-273 and current ripple prediction (red) *vs* experimental current ripple (green).

Final Remarks

It is worth noting that the core losses of ferrite inductors analyzed in this Chapter have been estimated using the manufacturer's core loss formula (4.3) and relevant coefficients, by modifying the coefficient K_2^* according to the saturation degree of each inductor (see Subsection 4.1.1). In scientific literature, enhanced core loss formulations have been proposed including the *DC* bias dependence and thus taking into account a possible magnetic core saturation. A detailed overview of such models is presented in Chapter 5, and their relevant drawbacks are highlighted. The alternative inductor *AC* loss model is specifically proposed in this dissertation to overcome the limitations of the classical core loss formulas, which can be used in combination with the *DC* loss model to evaluate the inductor total power losses, as discussed in the next Chapter.

The main outcome of the research activity presented in this Chapter resulted in the publication of the scientific papers:

- G. Di Capua, N. Femia, K. Stoyka, "Switching Power Supplies with Ferrite Inductors in Sustainable Saturation Operation", *International Journal of Electrical Power & Energy Systems*, vol. 93, pp. 494-505, Dec. 2017.
- G. Di Capua, N. Femia, K. Stoyka, "Validation of inductors Sustainable-Saturation-Operation in Switching Power Supplies Design," *2017 IEEE International Conference on Industrial Technology (ICIT)*, March 2017.
- Giulia Di Capua, Nicola Femia, Kateryna Stoyka, "Power Magnetics Volume and Weight Reduction in Aerospace Power Supply Units", *17th Workshop on Control and Modeling for Power Electronics (COMPEL)*, June 2016.

Chapter 5

Power Loss Behavioral Modeling of Ferrite Inductors

This chapter discusses power loss behavioral modeling of FPIs in SMPS applications, including the effects of saturation. FPIs total power losses are determined by winding losses and magnetic core losses. However, the core and winding losses cannot be easily measured as separate contributions in SMPS applications. FPIs total power losses can be alternatively evaluated as the sum of a DC term and an AC term. Since the DC losses can be easily estimated from the DC winding resistance and the DC current flowing through the winding, the major challenge still remains how to determine the AC losses of FPIs. The first part of this chapter discusses the modeling of the total power losses for FPIs, followed by the modeling of the sole AC loss contribution. Both approaches are based on the use of a Genetic Programming (GP) algorithm, by means of which the model structure and relevant parameters are identified, starting from a set of experimental power loss data.

5.1 Inductor Power Loss Models: State-of-the-Art

The inductor average total power losses P_{tot} are by definition the mean value of the instant power absorbed by the device over the switching period $T_s = 1/f_s$:

$$P_{tot} = f_s \int_0^{T_s} v_L(t) \cdot i_L(t)\, dt \tag{5.1}$$

where $v_L(t)$ and $i_L(t)$ are the inductor voltage and current waveforms, respectively. Total power losses P_{tot} are determined by magnetic core losses and winding losses, which depend on:

- *core volume and geometry*, characterized by sharp edges and not allowing easy analytical modeling;
- *core materials*, whose characteristics are not disclosed by inductors manufacturers;
- *winding arrangement*, where skin and proximity effects can occur since Litz wires are not usually adopted for commercial parts.

The total power losses P_{tot} can be separated in two contributions in two different ways: winding and core losses (Subsection 5.1.1), or DC and AC losses (Subsection 5.1.2).

5.1.1 Winding and Core Losses

The total inductor power losses can be split as shown in (5.2):

$$P_{tot} = P_{wind} + P_{core} \tag{5.2}$$

Winding losses P_{wind} can be seen as the sum of DC and AC winding losses:

$$P_{wind,dc} = R_{dc} \cdot I_L^2 \tag{5.3}$$

$$P_{wind,ac} = R_{ac} \cdot I_{ac,rms}^2 \tag{5.4}$$

where R_{dc} is the DC winding resistance, R_{ac} is the AC winding resistance including high-frequency effects, I_L and $I_{ac,rms}$ are the average and rms values of the DC and AC inductor current components, respectively. The DC losses can be easily evaluated from the DC winding resistance. The high-frequency winding losses can be predicted by using several methods [36–41], if the winding cross-sectional area and the layers distribution are known. Unfortunately, the manufacturers of commercial components do not disclose winding geometry data. The datasheets only provide the nominal value of R_{dc} resistance, obtained in DC test conditions. Therefore, since the exact R_{ac} resistance value is not available, the use of the R_{dc} resistance value to estimate the high-frequency AC winding losses can result in poor accuracy in the calculation of the total inductor losses.

Core losses P_{core} modeling has been investigated in several studies by considering the separation of hysteresis, eddy-currents and excess loss contributions [42–44]. Unfortunately, the parameters of such models are not easy to obtain, since sophisticated experimental measurements are needed to evaluate separately the different loss terms. The Steinmetz Equation (SE), introduced in [45] and given in (5.5), represents *de facto* the empirical behavioral core loss formula mostly used in SMPS design:

$$P_{core,SE} = C_m f_s^{\alpha} B_{ac}^{\beta} (A_e l_e) \tag{5.5}$$

where f_s is the excitation frequency, B_{ac} is the AC magnetic flux density magnitude, and A_e and l_e are the equivalent cross-sectional area and magnetic path length of the magnetic core. The coefficients C_m, α and β depend on core material, magnetic induction and switching frequency operating range, and are usually given in the datasheets of magnetic cores [46, 47]. Since the peak-to-peak current ripple Δi_{Lpp} is easier to measure than the AC magnetic flux density B_{ac}, the SE can be re-formulated as a function of Δi_{Lpp}:

$$P_{core,SE} = K_1 f_s^X (K_2 \Delta i_{Lpp})^Y \tag{5.6}$$

where the coefficients K_1, K_2, X and Y depend on material and switching frequency range. K_1 also depends on the core volume.

Some power inductors manufacturers adopt the formulation given in (5.6) and provide relevant core loss coefficients [48]. Both models (5.5) and (5.6) are given for sinusoidal operating conditions. More details on how to get coefficients $\{K_1, K_2, X, Y\}$ from coefficients $\{C_m, \alpha, \beta\}$ are provided in Appendix A.

Several papers show how to extend the validity of the SE to non-sinusoidal conditions. In [49–53] enhanced versions of the SE have been proposed, namely the Modified Steinmetz Equation (MSE), the Generalized Steinmetz Equation (GSE), the *improved* Generalized Steinmetz Equation (i-GSE), the Natural Steinmetz Extension (NSE) and the Improved Steinmetz Equation (ISE), valid for both sinusoidal and non-sinusoidal operating conditions and requiring no more parameters than the basic SE. In particular, Appendix A also describes how the i-GSE formula can be used for core loss calculation, given inductor voltage, duty-cycle, frequency and manufacturer's core loss coefficients. However, all these formulations neglect the dependence of core losses on DC bias, thus yielding inaccurate core loss estimation in saturation. In [54], a DC bias-dependent loss map has been created by measuring the dynamic minor loop areas traced on the magnetic flux density B *versus* the magnetic field H (or $B-H$) plane of magnetic material. Minor loop areas, which are proportional to the core losses, have been measured in different conditions of applied DC bias magnetic filed H_{DC}, by fixing the peak-to-peak magnitude of either the magnetic flux density (ΔB) or the magnetic field (ΔH), as shown in Fig. 5.1. It has been experimentally verified that, with increasing bias, core losses may either increase if ΔB value is maintained constant, or decrease if ΔH value is fixed.

Enhanced discussions on magnetic core loss models accounting for DC bias have been specifically proposed. In [55], Muhlethaler *et al.* have presented a study about the influence of premagnetization on magnetic material power losses. However, no analytical formulations have been given to model the SE parameters dependence on DC bias. In [56], Kosai *et al.* have proposed a correction to the SE for operating conditions involving saturation, based on a multiplicative exponential term of the ratio μ_{nom}/μ

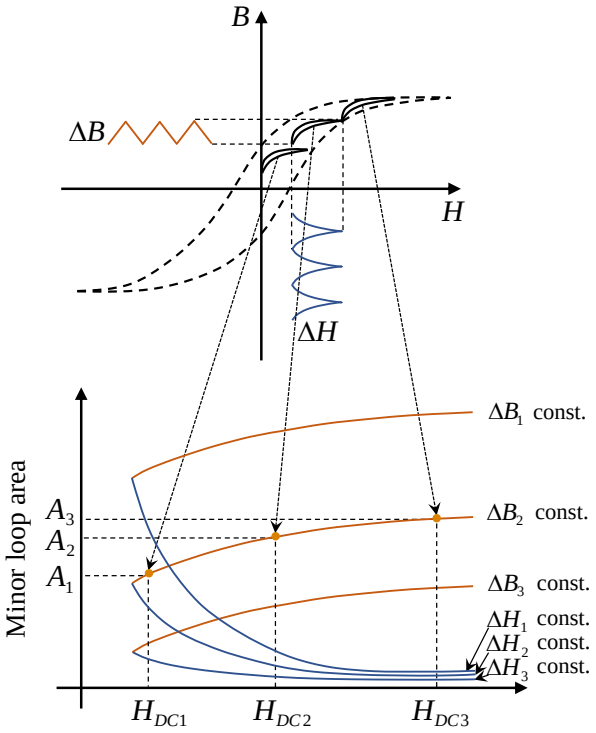

Figure 5.1: Dynamic minor loops and loss map [54].

representing the saturation level of the core material:

$$P_{core} = C_m f_s^{\alpha} B_{ac}^{\beta} (A_e l_e) \cdot \exp\left[a\left(\mu_{nom}/\mu - 1\right)\right] \tag{5.7}$$

where μ_{nom} is the nominal magnetic permeability of material at zero bias, μ is the effective magnetic permeability in saturation, and a is an additional model parameter. However, neither μ_{nom} nor μ are easily measurable quantities for commercial magnetic devices. In [57], a core loss model has been proposed based on the use of a multiplicative bias factor as a function of the *DC* magnetic field H_{DC}. A quadratic term and a square root term of H_{DC} have been introduced to model the *DC* bias dependence for different magnetic materials. In [58], an FEA approach has been proposed to calculate the magnetic core losses and their dis-

tribution for a planar inductor in the presence of DC current. A polynomial curve-fitting model given in (5.8) has been proposed for the calculation of core losses:

$$P_{core} = C_m f_s^{\alpha} B_{ac}^{\beta} (A_e l_e) \cdot \sum_{i=0}^{7} a_i H_{DC}^{i} \tag{5.8}$$

However, only sinusoidal excitations have been analyzed. Finally, in [59] Sokalski *et al.* have suggested that the core loss function obeys the scaling law. On the basis of such assumption, a complicated expression has been proposed, including the DC bias H_{DC} influence on core losses:

$$\begin{aligned} P_{core} = \Delta B^{\beta} \Bigg\{ & \sum_{i=1}^{4} \Gamma_i \left(\frac{f_s}{\Delta B^{\alpha}} \right)^{i(1-x)} + \ldots \\ & + \sum_{i=1}^{2} \left[\Gamma_{i+5} \left(\frac{f_s}{\Delta B^{\alpha}} \right)^{(i+y)(1-x)} \tanh(H_{DC} c_{i+1} - r_{i+1}) \right] \Bigg\} \end{aligned} \tag{5.9}$$

where $\{\Gamma_i, c_i, r_i, \alpha, \beta, x, y\}$ represent the model parameters, and $\Delta B = 2B_{ac}$ is the peak-to-peak AC magnetic flux density magnitude. Compared to (5.7) and (5.8), such formulation can be more accurate yet too complicated for SMPS designers, as it involves a high number of model parameters not provided by magnetic parts manufacturers, and requires magnetic quantities measurements, like the AC magnetic flux density B_{ac} and the DC magnetic field H_{DC}.

The main limitation of core loss models [55–57, 59] lies in the use of the magnetic quantities like magnetic flux density and magnetic field, which are not easy to measure for commercial inductors operated in SMPS. In principle, such quantities can be estimated starting from the inductor voltage and current measurements, if the inductor winding turn number, magnetic path length and cross-sectional area are known. Unfortunately, such data are not disclosed by inductors manufacturers in their datasheets. For this reason, it is impossible to determine the parameters of said models by applying curve fitting techniques to the experimental core losses.

5.1.2 *DC* and *AC* losses

The total inductor power losses can also be split as shown in (5.10):

$$P_{tot} = P_{dc} + P_{ac} \tag{5.10}$$

The *DC* losses P_{dc} depend on the *DC* components of inductor voltage V_L and current I_L, and can be evaluated as given in (5.11):

$$P_{dc} = V_L \cdot I_L = R_{dc} \cdot I_L^2 = P_{wind,dc} \tag{5.11}$$

which corresponds to (5.3). The *AC* losses P_{ac} depend on the *AC* components of the inductor voltage $v_{L,ac}(t)$ and current $i_{L,ac}(t)$, and is given by (5.12):

$$P_{ac} = f_s \int_0^{T_s} v_{L,ac}(t) \cdot i_{L,ac}(t)\, dt = P_{core} + P_{wind,ac} \tag{5.12}$$

where P_{core} corresponds to the magnetic core losses provided in (5.5) and (5.6), and $P_{wind,ac}$ is the *AC* winding loss contribution given in (5.4). This power loss separation (5.10) has the advantage of allowing the direct measurement of the two contributions (5.11) and (5.12), starting from the experimental waveforms of inductor voltage and current. In fact, the *DC* components of the measured waveforms provide the *DC* losses P_{dc} (5.11), while their *AC* components provide the *AC* losses P_{ac} (5.12).

5.2 Loss Measurement Techniques

5.2.1 Core Loss Measurements

Several literature contributions have been presented on core loss measurement techniques for magnetic components [60–66]. In the classical four-wire two-winding method, the core under test is wound as a transformer [60] [61]: excitation is inserted on the core through one winding, and voltage is measured on the other sensing winding, as shown in Figure 5.2. The core losses are then

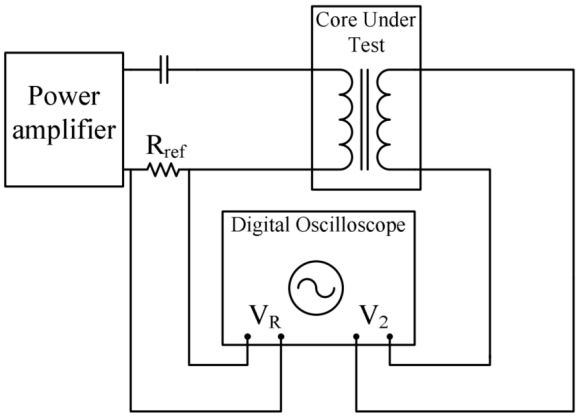

Figure 5.2: Two-winding method for core loss measurements.

evaluated by integrating the product of the voltage on sensing winding and the current through the excitation winding:

$$P_{core} = \frac{1}{T_s R_{ref}} \int_0^{T_s} v_2 v_R dt \tag{5.13}$$

where R_{ref} is the current sensing resistance, and T_s is the period of the excitation frequency. A third winding can be possibly considered to test a given DC pre-magnetization condition [62].

The two-winding methods have no significant drawbacks in principle. They allow to measure the core losses and exclude the winding losses, but are sensitive to phase discrepancy mainly due to current sensing, probe mismatch and oscilloscope time resolution limit. New compensation methods consider capacitive cancellation for core loss measurement at very high frequencies [63] [64]. A capacitor is connected in series with the inductor of the core under test and finely tuned to resonate with it at the test frequency. The core losses can be measured after compensating the parasitic resistances. These compensation methods automatically exclude the losses of the excitation winding and greatly reduce the sensitivity to phase discrepancy. However, in certain conditions, it could be difficult to realize an exact compensation at the

excitation frequency: the value of the cancellation capacitor is quite critical, and a small variation can induce a big measurement error [65]. Lastly, enhanced compensation methods rely on an inductive cancellation approach [66], to further reduce the phase sensitivity problem. It also enables accurate core loss measurement for arbitrary waveform excitation without the requirement to fine-tune the cancellation component value.

All the aforementioned studies usually consider experimental test conditions performed on laboratory magnetic component prototypes, built or modified according to established measurement procedures. In principle, methods like [64] [66] are applicable also for inductor total loss measurement. However, for commercial pre-assembled shielded core power inductors in real-world switching operating conditions, it could be more difficult to separate core and winding losses, mainly because the windings arrangement of commercial inductors can be quite irregular and error sources cannot be prevented or attenuated [65]. Direct measurements of the DC and AC loss contributions for commercial power inductors is definitely more straightforward than the measurement of separate contributions for core and winding losses.

5.2.2 DC and AC Loss Measurements

Separate measurement of the DC and AC loss contributions can be realized by means of the MADMIX system [67] shown in Figure 5.3. Such automated measurement setup is able to measure the performance of power inductors under hard-switched conditions, reproducing exactly a real SMPS operation. In particular, the MADMIX emulates the operation of an open-loop DC-DC buck converter: given the input voltage V_{IN}, the duty-cycle D, the switching frequency f_s and the output current I_{OUT}, the power inductor is subjected to a DC current $I_L = I_{OUT}$, a positive voltage $V_{Lr} = V_{IN}(1-D)$ during the rise-time interval, and a negative voltage $V_{Lf} = -V_{IN}D$ during the fall-time interval. Among all the possible features, the MADMIX allows setting desired SMPS-based operating conditions and makes high-speed measurements of

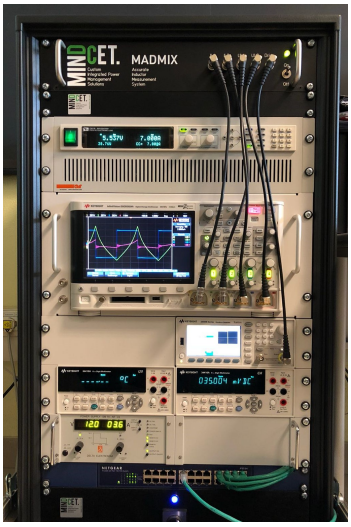

(a)

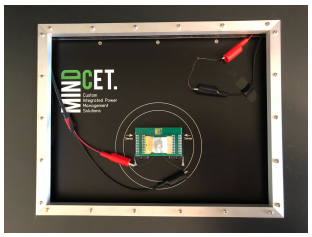

(b)

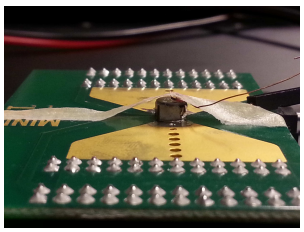

(c)

Figure 5.3: MADMIX: (a) front panel, (b) top panel and (c) device under test

the inductor voltage and current. Moreover, it can perform user-programmed tests over wide operating ranges and collect large series of measurement results, including *DC* and *AC* inductor power losses, evaluated starting from the measured inductor voltage and current waveforms according to (5.11) and (5.12). As an example, voltage and current waveforms of a 10μH Coilcraft MSS1260-103 inductor measured by the MADMIX are shown in Figure 5.4 (a). The datasheet L *vs* i_L curve of the inductor is shown in Figure 5.4 (b). The operating conditions adopted for the test are V_{IN} = 12 V, duty-cycle $D = 0.5$, switching frequency $f_s = 200$ kHz and average load current $I_{out} = 7.25$A, involving the operation in the roll-off region (red portion of the curve given in Figure 5.4(b)). For this test example, the MADMIX measured an average inductance of 4.5 μH, a peak-to-peak current ripple of 3.34 A, *DC* losses of 1.22 W (0.05% standard deviation), *AC* losses of 175mW (1.7% standard deviation), inductor and ambient temperatures of 71°C and 26°C, respectively.

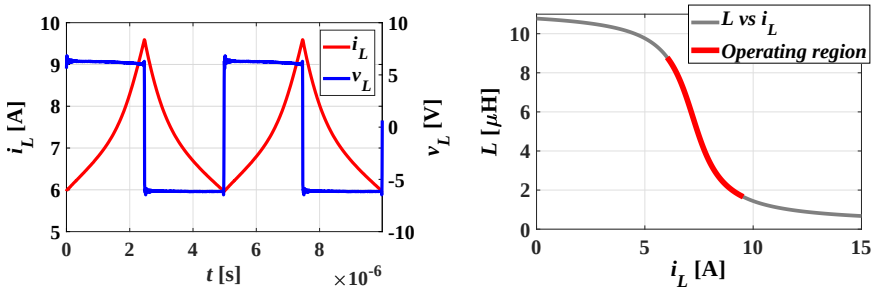

(a) (b)

Figure 5.4: MADMIX-based inductor waveforms: (a) voltage and current; (b) L *vs* i_L curve with relevant operating region

An alternative acquisition method for on-line FPIs characterization has been recently proposed in [31], which is based on sampling of the voltage and current waveforms of power inductor operated in SMPS, and allows for the estimation of the resulting power losses.

5.3 Genetic Programming

Genetic Programming (GP) is an evolutionary algorithm introduced by Koza in [68], able to identify models and functions from observed data. The GP is a population-based algorithm, where the population is composed of models. The GP models are generally represented by means of tree structures, as shown in Figure 5.5. To construct such trees, the GP algorithm makes use of a given set of elementary functions, constant coefficients and independent variables or model inputs. By definition, the group of independent variables and constant coefficients composes the *terminal set*, and the group of elementary functions represents the *non-terminal set* the GP algorithm works with.

Similarly to other evolutionary algorithms, for the GP algorithm the individuals in the initial population are randomly generated. During its evolution, the GP algorithm transforms the

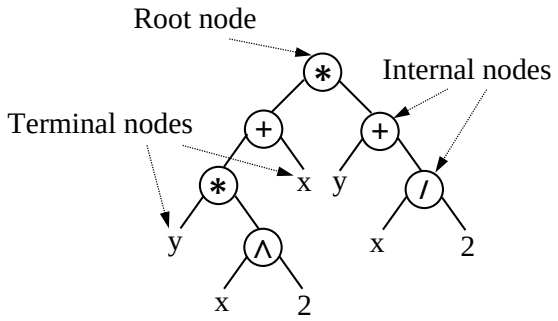

Figure 5.5: Tree representation of a typical GP program

current population of models into a new population of models, by applying classical genetic operators, such as crossover, mutation, elitism, etc. At the end of its evolution, the algorithm finds a model with the best-so-far fitness value.

Genetic operators are applied to individuals that are probabilistically selected based on their fitness. That is, better individuals are more likely to be selected and used for offspring models generation than worse individuals. The most commonly employed method for selecting individuals in GP is the *tournament selection*, for which a fixed number of individuals is randomly chosen from the current population, and the best of them is selected as a parent for offspring generation.

The *crossover* operation consists in the creation of one or two offspring models by recombining randomly chosen parts from two selected parent models. The most commonly used form of crossover is *subtree crossover*. Given two parents, subtree crossover randomly selects a crossover point in each parent tree. Then, it creates the offspring by replacing the subtree rooted at the crossover point in a copy of the first parent with a copy of the subtree rooted at the crossover point in the second parent, as illustrated in Figure 5.6.

The *mutation* operation consists in the creation of one new offspring model by randomly altering a randomly chosen part of one selected parent model. The most commonly used form of mutation is *subtree mutation*, which randomly selects a mutation

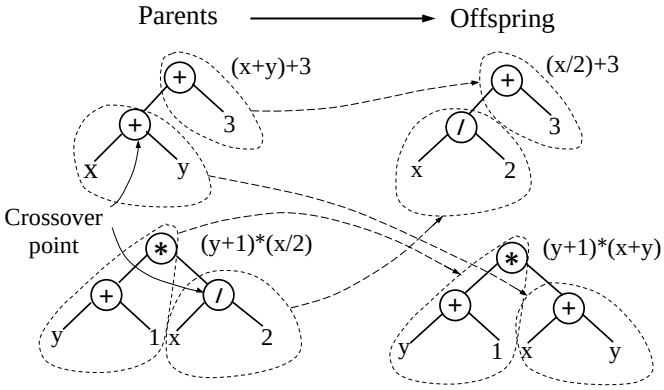

Figure 5.6: Subtree crossover

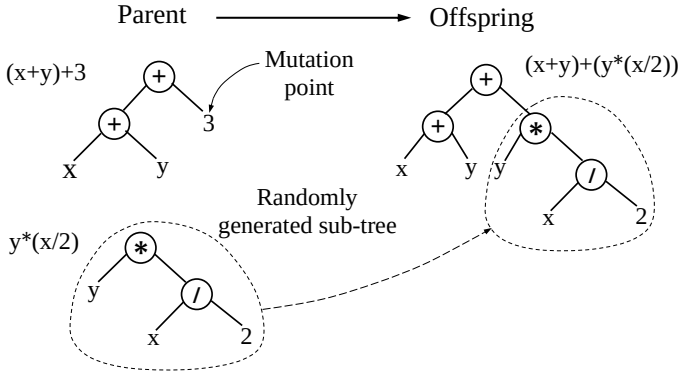

Figure 5.7: Subtree mutation

point in a tree and substitutes the subtree rooted there with a randomly generated subtree, as illustrated in Figure 5.7. Another common form of mutation is *point mutation*, in which a random node is selected and the function stored there is replaced with a different randomly selected function (having the same number of inputs as the original function). The choice of which of the operators described above should be used to create an offspring is probabilistic. Typically, crossover is applied with the highest probability, whereas the mutation rate is usually smaller.

5.4 Behavioral Modeling of Inductor Total Power Losses

This Section discusses an analytical behavioral modeling of the total power losses for FPIs used in SMPS applications, including possible operation of inductors in saturation. The model identification procedure starts from the assumption that the main quantities influencing the inductor total power losses P_{tot} are:

- the rms inductor current I_{Lrms};
- the average inductor current I_L;
- the switching frequency f_s;
- the peak-to-peak inductor current ripple Δi_{Lpp};
- the volt-second product $\lambda = V_{Lr}DT_s$ of the inductor voltage V_{Lr} applied during the rise-time interval $T_r = [0, DT_s]$.

Among such quantities, I_{Lrms} is expected to influence the winding losses, f_s could be present in both winding and core loss terms, and I_L is likely to influence the core losses representing their dependence on the DC bias. The remaining quantities Δi_{Lpp} and λ are expected to have major influence on the core losses, since they determine the dimensions of the minor hysteresis loop area in terms of ΔH and ΔB, respectively. This is particularly important for inductor operation in saturation, as the shape and dimensions of the traced minor hysteresis loop change, thus causing variations in power losses. Under this condition, the magnetic permeability of the material changes, and the relationship existing between Δi_{Lpp} and λ becomes highly non-linear. The quantities $\{f_s, \Delta i_{Lpp}, \lambda, I_L, I_{Lrms}\}$ have been herein used as the input variables of the total loss model to be determined. In principle, such set of input variables can be redundant for the purposes of power loss modeling, since some of the considered quantities could be obtained starting from the others (e.g., I_{Lrms} could be reconstructed from I_L and Δi_{Lpp} values). Whatever choice of input variables is adopted, the GP algorithm will find the main quantities whose influence on the total power losses is dominant with respect to the other quantities.

5.4.1 Identification of Total Power Loss Model by GP

The GP algorithm has been herein adopted to identify a total power loss model generalized for different FPIs, working in a wide range of SMPS operating conditions. In particular, m different Inductors Under Test (IUTs) have been considered for the analysis, with a set of n test conditions for each device. For each *i-th* test condition, a data vector has been created consisting of 5 independent variables $\mathbf{x}_i = (f_{si}, \Delta i_{Lppi}, \lambda_i, I_{Li}, I_{Lrmsi})$, with $i = 1, ..., n$, representing the inputs to the power loss model, and one output variable equal to the experimental total power losses $y_{ij} = P_{tot,exp}(\mathbf{x}_i)$, where $j = 1, ..., m$ indicates the *j-th* analyzed inductor. The resulting $n \times m$ data vectors $(\mathbf{x}_i, y_{ij})$, with $i = 1, ..., n$ and $j = 1, ..., m$, composed a *training* data set $\mathcal{T}$ the GP algorithm works with, shown in Table 5.1.

The GP algorithm has been set to identify a global behavioral model (5.14):

$$P_{tot,bhv} = F\left(f_s, \Delta i_{Lpp}, \lambda, I_L, I_{Lrms}, \mathbf{p}\right) \tag{5.14}$$

such that the value of the function F computed for each test condition $\mathbf{x}_i$ of the training data set $\mathcal{T}$ is as close as possible to the corresponding experimental value y_{ij}, $\forall i \in \{1, ..., n\}$ and $\forall j \in \{1, ..., m\}$. The structure of the behavioral power loss function F in (5.14) is the same for all the analyzed devices, while the coefficients vector $\mathbf{p}$ changes from one inductor to the other.

Table 5.1: Data set $\mathcal{T}$ of the GP algorithm

Test condition	IUT #1	IUT #2	...	IUT #m
$\mathbf{x}_1$	$(\mathbf{x}_1, y_{11})$	$(\mathbf{x}_1, y_{12})$	...	$(\mathbf{x}_1, y_{1m})$
$\mathbf{x}_2$	$(\mathbf{x}_2, y_{21})$	$(\mathbf{x}_2, y_{22})$	...	$(\mathbf{x}_2, y_{2m})$
...	...	...	...	...
$\mathbf{x}_n$	$(\mathbf{x}_n, y_{n1})$	$(\mathbf{x}_n, y_{n2})$	...	$(\mathbf{x}_n, y_{nm})$

To determine the values of the coefficients vector $\mathbf{p}_j$ for the *j-th* device, a Non-Linear Least Squares (NLLS) method has been used. In particular, a Levenberg-Marquardt least square optimization method has been adopted [69]. Such algorithm starts from the model structure provided by the GP algorithm and finds the best coefficients values $\mathbf{p}_j$ for each inductor. The χ-squared error criterion has been applied to the experimental losses y_{ij} and the GP-predicted losses $F(\mathbf{x}_i, \mathbf{p}_j)$ for $i = 1, ..., n$, as given in (5.15):

$$\chi_j^2 = \frac{1}{n} \sum_{i=1}^{n} \Big\{ F(\mathbf{x}_i, \mathbf{p}_j) - y_{ij} \Big\}^2 \tag{5.15}$$

The values of coefficients $\mathbf{p}_j$ for the *j-th* inductor have been determined by minimizing χ_j^2.

Fitness Evaluation

To estimate the global accuracy of the GP-based model over the whole training data set, the Root Mean Square Error ($RMSE$) between the experimental and GP-predicted losses has been estimated by means of (5.16), thus taking into account the χ_j^2 errors relative to the m analyzed inductors:

$$RMSE = \sqrt{\frac{1}{m} \sum_{j=1}^{m} \chi_j^2} \tag{5.16}$$

One common problem with evolving tree-structured individuals is that, as the evolution progresses, the individuals may become complex in structure or length, without any significant reduction of the relevant $RMSE$. To prevent this effect, the following fitness function has been adopted:

$$Fitness = a \cdot RMSE + b \cdot F_{complexity} + c \cdot N_\alpha \tag{5.17}$$

where a, b and c are balancing coefficients of the fitness function, $F_{complexity}$ is the metrics expressing the GP model complexity, and

N_α is the total number of non-linear sub-trees composing a tree-structured program, *i.e.* sub-trees having a non-linear function as a root node. The terms $b \cdot F_{complexity}$ and $c \cdot N_\alpha$ control the model complexity and expansion, thus avoiding not intelligible expressions.

A Single-Objective Optimization (SOO) approach has been herein adopted to discover the total power loss behavioral model $P_{tot,bhv}$ minimizing the $Fitness$ value, thus jointly limiting the model fitting error, complexity and expansion.

Complexity Evaluation

Table 5.2 shows the elements of the terminal and non-terminal sets used by the GP algorithm for models generation. Such elements have been assigned different complexity factors, and on their basis the global complexity $F_{complexity}$ of each constructed GP model has been estimated. Each element of the terminal set has been assigned a unit complexity factor, whereas each element of the non-terminal set has been assigned a complexity factor equal or greater than one.

To quantify the global complexity of each GP model, the term $F_{complexity}$ has been introduced, based on the complexity values given in Table 5.2, and calculated in the following way:

- if a function (non-terminal element) is the argument of another function, the complexity factors of the two functions are multiplied;
- if two functions are multiplied or summed, their complexity factors are summed and subsequently multiplied by the complexity factor of a sum or a product, respectively.

In the first case, a vertical development of the models (*i.e.*, involved functions of functions) is prevented, especially for the functions with great complexity. In the second case, a horizontal development of the models is prevented, *i.e.*, models composed of many simple functions multiplied or summed among them, when a single more complicated function (*e.g.*, exponential or power function) could be sufficient to model the quantity of interest.

Table 5.2: Non-terminal and terminal sets

Non-terminal set		
Description	Expression	Complexity
sum	$f + g$	1.5
multiplication	$f \cdot g$	1.0
division	f/g	1.5
logarithm	$\log(f)$	2.0
natural exp.	$\exp(f)$	2.0
power	f^{α}	2.0
exponential	α^{f}	2.0
square root	$\sqrt{f}$	2.0
reciprocal	$1/f$	1.5
Terminal set		
Description	Expression	Complexity
input	$\mathbf{x} = \{f_s, \Delta i_{Lpp}, \lambda, I_L, I_{Lrms}\}$	1.0
coefficient	p	1.0

GP Settings

Table 5.3 summarizes the adopted GP settings and main parameters values. In order to find the best set-up for the balancing coefficients a, b and c of the *Fitness* function, a preliminary tuning has been executed, based on a maximum complexity threshold. The obtained values of such coefficients are given in Table 5.3.

5.4.2 Case Studies

The discussion is herein referred to power inductors with ferrite magnetic cores. Two inductors have been considered for the investigation: the Coilcraft 18 μH MSS7341-183 (IUT # 1) and 15 μH MSS7341-153 (IUT # 2), both assembled with shielded cores of the same ferrite material, but having different winding turn number. The main characteristics of these FPIs are listed in Table 5.4.

Table 5.3: GP algorithm settings and parameters

Description	Value
Population size	50
Generation number	200
Maximum tree size	50 nodes
Selection operator	tournament
Crossover operator	subtree crossover
Mutation operator	subtree mutation
Elite size	5
Tournament selection size	10
Crossover probability	0.65
Mutation probability	0.30
Direct copy probability	0.05
Fitness coefficients	a = 10 b = 1 c = 5

Table 5.4: Investigated inductors and their main characteristics

Part Number	Dimensions $[mm^3]$	L_{nom} $[\mu H]$	DCR $[m\Omega]$	$I_{sat}[A]$ 30% drop	$I_{rms}[A]$ 40°C rise
MSS7341-183	7.3x7.3x4.1	18	75	1.62	2.65
MSS7341-153	7.3x7.3x4.1	15	55	1.78	3.00

Experimental data of the training data set $\mathfrak{T}$ have been collected by using the MADMIX system described in Subsection 5.2.2. For both IUTs, the operating conditions given in Table 5.5 have been fixed by means of the MADMIX system. All the possible combinations of such values have been tested, resulting in a training data set composed of $n \times m = 378$ experimental data vectors. All the quantities of interest, such as I_L, I_{Lrms}, Δi_{Lpp}, λ and P_{tot}, have been measured for each tested condition. Both

Table 5.5: Training and validation set operating conditions

Quantity	Units	Training set	Validation set
f_s	kHz	$[250, 350, 450]$	$[300, 400, 500]$
V_{IN}	V	$[8, 12, 16]$	$[6, 10, 14]$
D	–	$[0.3, 0.4, 0.5]$	$[0.2, 0.6, 0.7]$
I_{out}	A	$[1.2, 1.4, 1.6, 1.8, 2.0, 2.2, 2.4]$	$[1.2, 1.6, 2.0, 2.4]$

IUTs have been tested in a wide range of inductor current, in order to cover both weak-saturation and roll-off region of the relative L *vs* i_L curves shown in Fig. 5.8, and guarantee power loss characterization also in operating conditions involving saturation. Eventually, to check the GP models predictions capability, a validation set has been created, based on the operating conditions given in Table 5.5.

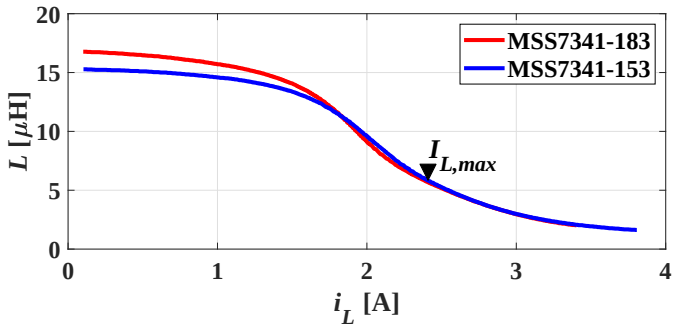

Figure 5.8: Inductors L *vs* i_L curves and maximum tested inductor current $I_{L,max}$

5.4.3 Resulting GP-based Models

The GP-SOO approach has been applied to the composed training data set: 15 independent GP algorithm runs have been executed

to discover the models minimizing the *Fitness* function given in Eq. (5.17) and having the most intelligible expressions. The best GP models − in terms of the $RMSE$ calculated on the validation set − are given in Eqs. (5.18)-(5.20), whose respective $RMSE$ values are of 5.65 mW, 4.40 mW and 4.76 mW. The values of the coefficients $\{p_0, ..., p_5\}$ are shown in Table 5.6 for the two IUTs.

$$P_{tot} = p_0 I_{Lrms}^{p_1} + p_2 f_s \Delta i_{Lpp} \lambda \exp(p_3 I_{Lrms}) \tag{5.18}$$

$$P_{tot} = p_0 I_{Lrms}^{p_1} + f_s (p_2 \Delta i_{Lpp} \lambda + p_3 \lambda^2) I_{Lrms}^{p_4} \tag{5.19}$$

$$P_{tot} = p_0 I_{Lrms}^{p_1} + p_2 f_s \Delta i_{Lpp}^{p_3} I_{Lrms}^{p_4} \lambda^{p_5} \tag{5.20}$$

All the models (5.18)-(5.20) include two loss terms. The first one clearly represents the winding losses. It is approximately proportional to the square of the rms inductor current ($p_1 \approx 2$) through the multiplicative coefficient p_0, representing an estimate of the winding resistance DCR (expressed in mΩ). The second term, instead, represents the core losses. It is proportional to the switching frequency and depends jointly on the inductor current

Table 5.6: GP models coefficients

Coefficients	p_0	p_1	p_2	p_3	p_4	p_5
Model (5.18)						
IUT #1	52.9	2.1	0.084	-0.44	–	–
IUT #2	48.8	1.9	0.095	-0.47	–	–
Model (5.19)						
IUT #1	52.5	2.1	0.029	0.0014	-0.301	–
IUT #2	44.2	2.0	0.018	0.0023	-0.094	–
Model (5.20)						
IUT #1	51.2	2.1	0.033	0.78	-0.45	1.18
IUT #2	44.2	2.0	0.016	0.54	-0.22	1.46

ripple and the volt-second product (expressed in $V\mu s$), as well as on the rms inductor current, representing the DC-bias contribution. It should be noted that both average and rms currents have been used as inputs to the GP algorithm. However, for all the considered case studies, such currents are only slightly different (the average and maximum differences are about 1% and 7%, respectively). This is the reason why the models generated by the GP use I_{Lrms} as bias term, instead of I_L. It is interesting to note that the term containing Δi_{Lpp} and λ is proportional to the hysteresis loop area. As the current increases, the saturation region is approached and the hysteresis loop flattens, thus causing a decrease in the resultant core losses. This phenomenon is modeled through the multiplicative bias term, which decreases with inductor current. In fact, $p_3 < 0$ in Eq. (5.18) and $p_4 < 0$ in Eq. (5.19) and Eq. (5.20). Among the others, model (5.19) has the lowest error on the validation data set. Conversely, model (5.20) has the optimal trade-off between accuracy and complexity, and has been therefore selected as a behavioral total power loss model identified by the GP algorithm:

$$P_{tot,bhv} = p_0 I_{Lrms}^{p_1} + p_2 f_s \Delta i_{Lpp}^{p_3} I_{Lrms}^{p_4} \lambda^{p_5} \tag{5.21}$$

5.4.4 Experimental Validation

The total power losses of the two analyzed inductors have been simulated by computing the model (5.21) on the validation data set given in Table 5.5. Fig.s 5.9(a) and 5.10(a) show the power loss predictions (red circles) for IUT #1 and IUT #2, respectively. Fig.s 5.9(b) and 5.10(b) show the power loss predictions obtained by using classical formulas for winding and core loss evaluation (green circles), such as Eq.s (5.3), (5.4) and (5.6). In the same plots, the relevant experimental total power losses (blue circles) are also shown. All such figures show the total power losses for 108 samples, relative to all the conditions included in the validation dataset and given in the ascending order of the average load current. The coefficients $\{K_1, K_2, X, Y\}$, adopted in classical core loss

formula (5.6), have been estimated by means of the NLLS curve fitting of the experimental AC power losses in weak-saturation region, as discussed in Appendix A. It can be observed that good fittings can still be obtained by using classical approaches, but only at low power loss levels, corresponding to low average current values in weak-saturation region (in Fig.s 5.9(b) and 5.10(b), first 54 samples relative to I_{out}=$\{1.2, 1.6\}$A). As expected, when the saturation is approached, such models don't assure a reliable power loss prediction. Strong overestimation of power losses has been in fact obtained, with predicted losses being about three times the experimental one in the worst-case condition (in Fig.s 5.9(b) and 5.10(b), sample #101). As discussed in [54], if Δi_{Lpp} value is maintained constant, the hysteresis loop area is expected to decrease with increasing current, as well as the resulting core losses. However, formula (5.6) doesn't include the DC bias dependence and thus overestimates the core losses.

The relative percent errors obtained by using the GP-based behavioral model (5.21) and the classical approach based on Eq.s (5.3), (5.4) and (5.6) are eventually shown in Fig.s 5.9(c)-(d) and 5.10(c)-(d) for IUT #1 and IUT #2, respectively. A quite good fitting of power losses is ensured for all the analyzed operating conditions by using the GP-based model. The error is quite small, even if the frequency, the duty-cycle and the input voltage conditions of the adopted validation dataset are different from those of the training dataset used to identify the GP-based model. In particular, the error is limited in a range of about $\pm 5\%$, which is a much better result than the predictions of the classical formulas for winding and core loss estimation, having maximum errors of about 180% and 230% for IUT #1 and IUT #2, respectively. The GP approach results thus in a viable mean to overcome the limitations of the classical SE-based loss formulas, by modeling the inductor saturation and avoiding power loss overestimation.

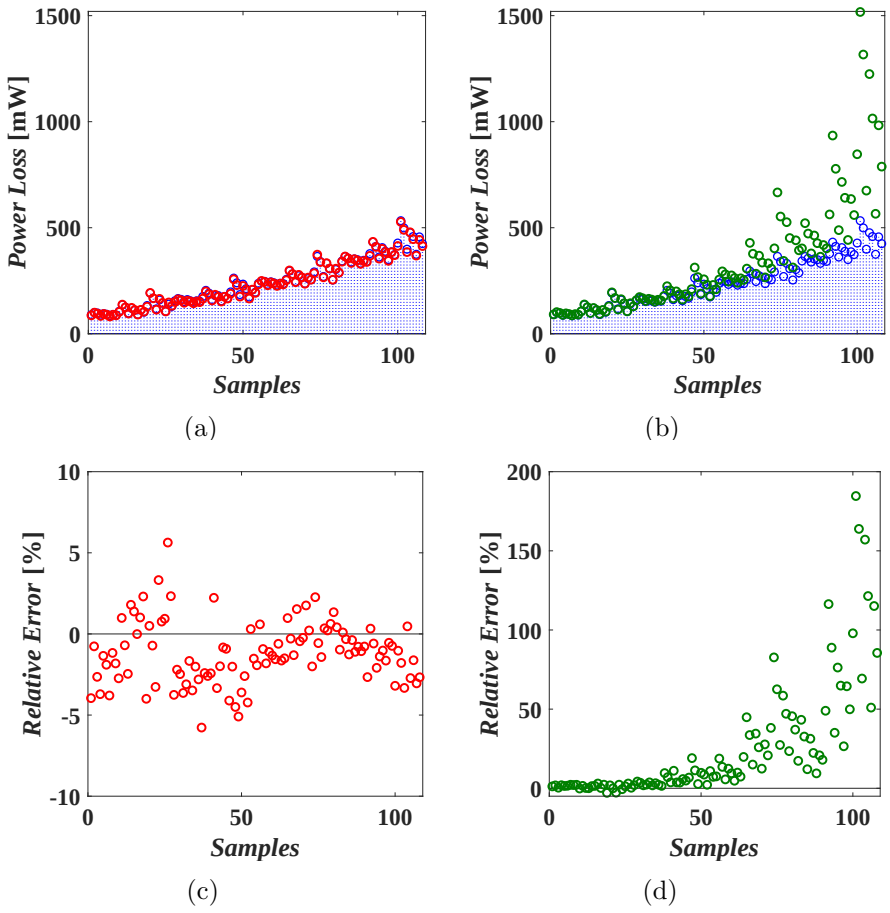

Figure 5.9: Total power losses and relative errors for MSS7341-183. (a) $P_{tot,bhv}$ losses (red) *vs* experimental losses (blue); (b) classical model losses (green) *vs* experimental losses (blue); (c) relative errors of $P_{tot,bhv}$; (d) relative errors of classical model.

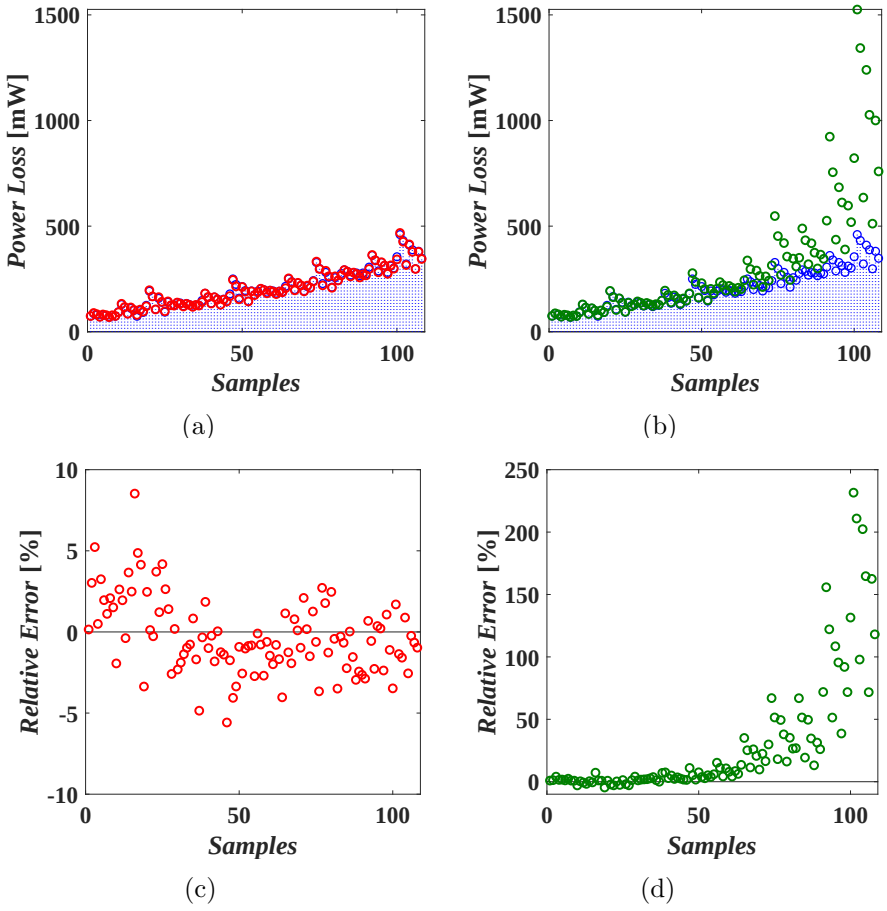

Figure 5.10: Total power losses and relative errors for MSS7341-153. (a) $P_{tot,bhv}$ losses (red) *vs* experimental losses (blue); (b) classical model losses (green) *vs* experimental losses (blue); (c) relative errors of $P_{tot,bhv}$; (d) relative errors of classical model.

5.5 Behavioral Modeling of Inductor *AC* Power Losses

In the previous Section, behavioral modeling of the total power losses for FPIs has been discussed, including both *DC* and *AC* loss contributions. The inductor peak-to-peak current ripple and rms current have been considered as the input variables of the total power loss model, together with the switching frequency, average inductor current and volt-second product. However, while the frequency, the average current (depending on the load) and the volt-second product may be considered as *primary variables* directly imposed by the SMPS operation to the inductor, the peak-to-peak ripple and rms current (depending on the ripple) are rather a *response* of the inductor to the applied primary variables, greatly depending on the saturation degree of the device. Hence, to estimate the inductor total power losses by means of the identified behavioral model (5.21), the inductor peak-to-peak ripple and rms current must be first simulated or measured experimentally, to be subsequently used as the inputs of the loss equation. This could be a limitation during SMPS design phase, when a quick preselection of the feasible saturated FPIs may be needed, without performing experimental tests or simulations based on the use of the enhanced non-linear saturation models of the inductors.

Since the *DC* losses can be easily estimated from the *DC* winding resistance and average inductor current, the major challenge still remains how to model the *AC* losses of FPIs. This Section presents a behavioral modeling of the *AC* power losses for FPIs as a function of the main operating conditions directly imposed by the SMPS application, including possible operation of inductors in saturation. The model identification procedure starts from the following assumptions:

- the *AC* loss equation is expressed as a function of the switching frequency f_s, the average current I_L and the equivalent voltage $V_{eq} = D\,V_{Lr}$ evaluated over the rise-time interval T_r;

- f_s and V_{eq} are the *input variables* of the AC loss equation, whereas I_L is an *input parameter* determining the value of the numeric coefficients of the loss equation.

The use of the equivalent voltage V_{eq} reflects the fact that the inductor AC power losses are only dependent on the volt-seconds applied to it, regardless of the SMPS topology.

5.5.1 Identification of AC Power Loss Model by GP

In this Section, a Multi-Objective Optimization (MOO) approach has been adopted in combination with the GP algorithm, to identify a new AC power loss model for FPIs, offering an optimal trade-off between accuracy and complexity. For a given FPI, a set of m average current conditions I_{Lj} has been considered for the analysis, with $j = 1, ..., m$. For each current value, n couples of frequency and voltage conditions $\mathbf{x}_i = (f_{si}, V_{eqi})$ have been adopted, with $i = 1, ..., n$. For each of the $n \times m$ test conditions, a data vector has been created, including the test values $\mathbf{x}_i$ and the resulting experimental AC power losses $y_{ij} = P_{ac,exp}(f_{si}, V_{eqi}, I_{Lj})$. The resulting *training* data set $\mathfrak{T}$ is shown in Table 5.7.

The GP algorithm has been set to identify a global behavioral model (5.22):

$$P_{ac,bhv} = F\left(f_s, V_{eq}, \mathbf{p}(I_L)\right) \tag{5.22}$$

Table 5.7: Data set $\mathfrak{T}$ of the GP algorithm

Test condition	I_{L1}	I_{L2}	...	I_{Lm}
$\mathbf{x}_1$	$(\mathbf{x}_1, y_{11})$	$(\mathbf{x}_1, y_{12})$	...	$(\mathbf{x}_1, y_{1m})$
$\mathbf{x}_2$	$(\mathbf{x}_2, y_{21})$	$(\mathbf{x}_2, y_{22})$	...	$(\mathbf{x}_2, y_{2m})$
...	...	...	...	...
$\mathbf{x}_n$	$(\mathbf{x}_n, y_{n1})$	$(\mathbf{x}_n, y_{n2})$	...	$(\mathbf{x}_n, y_{nm})$

such that the value of the function F computed for each test condition of the training data set $\mathcal{T}$ is as close as possible to the corresponding experimental value y_{ij}, $\forall i \in \{1, ..., n\}$ and $\forall j \in \{1, ..., m\}$. The structure of the behavioral power loss function F in (5.22) is the same for all the average current conditions, while the coefficients $\mathbf{p}$ are functions of I_L.

To determine the coefficients $\mathbf{p}$ of the GP-based model (5.22) for each average inductor current I_{Lj} $(j = 1, ..., m)$, a NLLS method has been applied to the n experimental data vectors relative to I_{Lj}. In particular, a Levenberg-Marquardt least square optimization method has been adopted [69]. Such algorithm starts from the model structure provided by the GP algorithm and finds the best coefficients values $\mathbf{p}$ for each average current. The χ-squared error criterion has been applied to the experimental losses y_{ij} and the GP-predicted losses $F\left(f_{si}, V_{eqi}, \mathbf{p}\left(I_{Lj}\right)\right)$, as given in (5.23):

$$\chi_j^2 = \frac{1}{n} \sum_{i=1}^{n} \left\{ F\left(f_{si}, V_{eqi}, \mathbf{p}\left(I_{Lj}\right)\right) - y_{ij} \right\}^2 \tag{5.23}$$

The values of coefficients $\mathbf{p}$ for each average current I_{Lj} have been determined by minimizing χ_j^2. Then, the interpolating functions $\mathbf{p}(I_L)$ have been determined, as discussed hereafter.

To estimate the global accuracy of the GP-based model over the whole training data set, the $RMSE$ between the experimental and GP-predicted losses has been estimated by means of (5.24), thus taking into account the χ_j^2 errors relative to the m analyzed average current conditions:

$$RMSE = \sqrt{\frac{1}{m} \sum_{j=1}^{m} \chi_j^2} \tag{5.24}$$

GP Settings

Table 5.8 shows the elements of the terminal and non-terminal sets used by the GP algorithm for models generation. Each element of the terminal set has been assigned a complexity factor equal or lower than one, whereas each element of the non-terminal set has been assigned a complexity factor equal or greater than one. The input variables $\mathbf{x} = \{f_s, V_{eq}\}$ have been assigned a unit complexity factor, except for the multiplication operations between such variables, for which a complexity factor of 0.6 has been attributed to each input, in order to prevent an excessive penalization of quadratic and cubic terms, like f_s^2, V_{eq}^3, $f_s \cdot V_{eq}$, etc. Table 5.9 summarizes the adopted GP settings and main parameters values.

Table 5.8: Non-terminal and terminal sets

Non-terminal set		
Description	Expression	Complexity
sum	$f + g$	1.0
multiplication	$f \cdot g$	1.0
power	f^g	1.5
division	f/g	1.5
logarithm	$\log(f)$	1.5
natural exp.	$\exp(f)$	1.5
power	f^α	1.5
exponential	α^f	1.5
square root	$\sqrt{f}$	1.5
hyperbolic tangent	$\tanh(f)$	1.5
inverse tangent	$\tan^{-1}(f)$	1.5
reciprocal	$1/f$	1.5
Terminal set		
Description	Expression	Complexity
input	$\mathbf{x} = \{f_s, V_{eq}\}$	0.6 (for multiplications) 1.0 (for other operations)
coefficient	p	1.0

Table 5.9: GP algorithm settings and parameters

Description	Value
Population size	500
Generation number	300
Maximum tree size	50 nodes
Selection operator	binary tournament
Crossover operator	subtree crossover
Mutation operator	subtree & node mutation
Crossover probability	0.80
Subtree mutation probability	0.18
Node mutation probability	0.02

GP-MOO Approach

The elements used by the GP algorithm to evaluate and select the AC loss models are:

- the *accuracy*, quantified by means of the global error term $RMSE$, given in Eq. (5.24);
- the *complexity*, quantified by means of the global complexity term $F_{complexity}$, described in Subsection 5.4.1.

An elitist Non-dominated Sorting Genetic Algorithm (NSGA-II) [70] has been used to discover the behavioral power loss model (5.22) offering a trade-off between the $RMSE$ and the $F_{complexity}$ values over the whole training data set. Such well-known MOO approach returns a Pareto front containing the non-dominated solutions present in the population, *i.e.*, the solutions outperforming the other elements of the front in at least one objective, being worse in some other objectives. Herein, $RMSE$ and $F_{complexity}$ have been considered as *objective functions* for minimization by the proposed GP-MOO algorithm. A detailed description of the MOO approach and of the NSGA-II algorithm is provided in Appendix B.

5.5.2 Case Studies

The discussion is herein referred to power inductors with ferrite magnetic core. Inductors of different ferrite materials and core types have been considered for the investigation, with both shielded and unshielded magnetic cores, to obtain a generalized *AC* loss model valid for different FPIs. In particular, four inductors have been analyzed: the Coilcraft MSS1260-103 ($L_{nom} = 10$ μH), MSS1260-473 ($L_{nom} = 47$ μH) and MSS1038-273 ($L_{nom} = 27$ μH), all assembled with shielded cores of same ferrite material, and the Coilcraft DO3316T-103 ($L_{nom} = 10$ μH), assembled with an unshielded core of a different ferrite material. The main datasheet characteristics of these FPIs are listed in Table 5.10. Experimental data of the training data set $\mathfrak{T}$ have been collected by using the MADMIX system described in Subsection 5.2.2. Each component has been tested in a wide range of inductor current, in order to cover both weak-saturation and roll-off region of the relative L *vs* i_L curve and guarantee power loss characterization also in saturation. Maximum inductance de-rating of about 50% with respect to the nominal inductance L_{nom} has been achieved for each inductor. The following subsections discuss the application of the GP-MOO approach to the MSS1260-103 and MSS1260-473 inductors, followed by the validation of the identified *AC* loss model on the MSS1038-273 and DO3316T-103 parts.

Table 5.10: Investigated inductors and their main characteristics

Part Number	Dimensions $[mm^3]$	L_{nom} $[\mu H]$	DCR $[m\Omega]$	$I_{sat}[A]$ 30% drop	$I_{rms}[A]$ 40°C rise
MSS1260-103	12x12x6	10	24	7.40	4.00
MSS1260-473	12x12x6	47	82	3.30	2.50
MSS1038-273	10.2x10x3.8	27	89	2.84	2.35
DO3316T-103	13.2x9.9x6.4	10	34	3.80	3.90

Case Study #1: MSS1260-103 inductor

To assemble the training data set for the MSS1260-103 inductor, the operating conditions given in Table 5.11 have been fixed by means of the MADMIX system. All the possible combinations of such values have been tested, with $m = 13$ average current values and $n = 80$ operating conditions in terms of f_s and $V_{eq} = V_{IN} \times D \times (1 - D)$ for each current, resulting in a training data set composed of $n \times m = 1040$ experimental data vectors. In particular, an inductance de-rating of 50% is obtained at $I_L = 7.25$A.

All the experimental measurements took about 35 hours. Then, the GP-MOO approach has been applied to the composed training data set: 30 independent GP algorithm runs have been executed to verify the repeatability of the obtained models, lasting about 15 hours. Only the non-dominated Pareto-optimal solutions with the repeatability of at least 8 runs have been selected for a futher comparison. Such solutions are shown as blue markers in Figure 5.11. The two objective functions used during the GP-MOO routine – namely, the $RMSE$ evaluated over the training data set and the corresponding global complexity factor $F_{complexity}$ – are shown on the x and y axes, respectively. The solutions at the bottom-right side of this plot are characterized by very simple structures and very high errors with respect to experimental AC losses. Conversely, the solutions at the top-left side of the plot present the lowest errors and most complicated structures.

Table 5.11: Training set operating conditions for MSS1260-103.

Quantity	Units	Values
f_s	kHz	$[200, 300, 400, 500]$
V_{IN}	V	$[6, 8, 10, 12]$
D	–	$[0.2, 0.35, 0.5, 0.65, 0.8]$
I_{out}	A	$[3, 3.5, 4, 4.5, 5, 5.5, 5.75,$ $6, 6.25, 6.5, 6.75, 7, 7.25]$

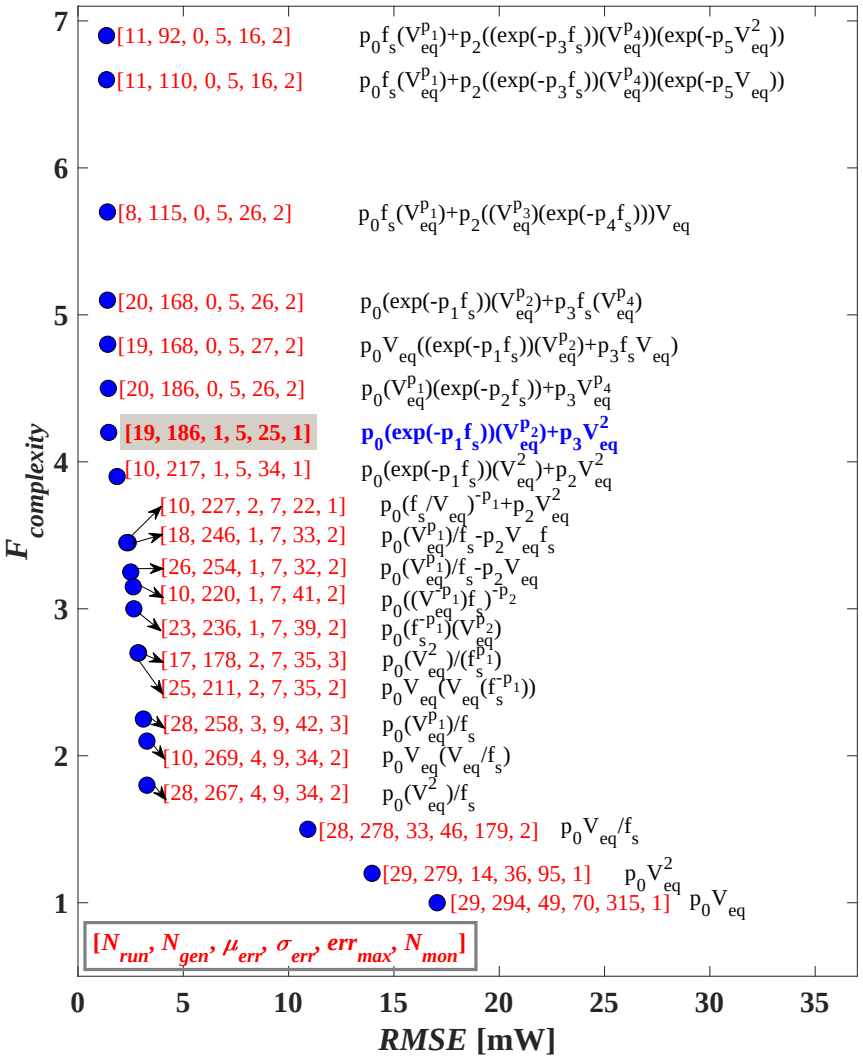

Figure 5.11: Repeatable Pareto-optimal solutions for MSS1260-103 inductor

In order to select an optimal *AC* loss model among all the obtained Pareto-optimal solutions, several metrics have been considered to classify each model:

- N_{run}: number of GP runs during which the algorithm has discovered the model (only models having $N_{run} \geq 8$ are shown in Figure 5.11);
- N_{gen}: average number of generations during which the model exists within the population (averaging done over N_{run});

- μ_{err}: mean value of the percent error distribution of the model over the training data set;
- σ_{err}: standard deviation of the percent error distribution of the model over the training data set;
- err_{max}: maximum percent error of the model over the training data set;
- N_{mon}: average number of intervals over which the model coefficients change their monotonicity with respect to the DC current I_L.

Such metrics are shown in Figure 5.11, next to the respective GP model expressions, from the more complicated ones (at the top of the list) to the simplest ones (at the bottom of the list). Among these solutions, the following model presents an optimal trade-off among all the six metrics:

$$P_{ac,bhv} = p_0 exp\left(-p_1 f_s\right) V_{eq}^{p_2} + p_3 V_{eq}^2 \tag{5.25}$$

where the coefficients $\{p_0, ..., p_3\}$ are the elements of the vector $\mathbf{p}(I_L)$ given in (5.22). The behavioral model (5.25) has a high repeatability ($N_{run} = 19$) and age ($N_{generations} = 186$) and shows excellent performances in terms of the percent fitting errors. It is characterized by a maximum percent error $err_{max} = 25\%$, with a mean percent error $\mu_{err} = 1\%$ and a standard deviation $\sigma_{err} = 5\%$. Only few models outperform the selected one in terms of the maximum percent error. In particular, the two models at the top of Figure 5.11 have lower percent errors ($err_{max} = 16\%$), but a more complicated structure. Also the model described by the metrics values [10, 227, 2, 7, 22, 1] has a lower percent error ($err_{max} = 22\%$), but higher mean percent error and standard deviation ($\mu_{err} = 2\%$, $\sigma_{err} = 7\%$). Moreover, the proposed AC loss model has monotonous coefficients with the DC current ($N_{monotone} = 1$), thus resulting easier to be modeled with any curve fitting algorithm. The coefficients $\{p_0, ..., p_3\}$ of the model (5.25) are shown in Figure 5.12 *vs* the average inductor current I_L, and can be modeled by means of the law (5.26):

$$\mathbf{p}\left(I_L\right) = \mathbf{a}_0 exp\left(\mathbf{a}_1 I_L\right) + \mathbf{a}_2 I_L + \mathbf{a}_3 \tag{5.26}$$

A NLLS algorithm has been used to determine the vector coefficients $\{\mathbf{a}_0, ..., \mathbf{a}_3\}$. The resulting fitting curves of the coefficients $\mathbf{p}$ are shown in Figure 5.12, while the relative vector coefficients $\{\mathbf{a}_0, ..., \mathbf{a}_3\}$ are given in Table 5.12. Figures 5.13 (a)-(f) show the relative percent errors between the predictions of behavioral model

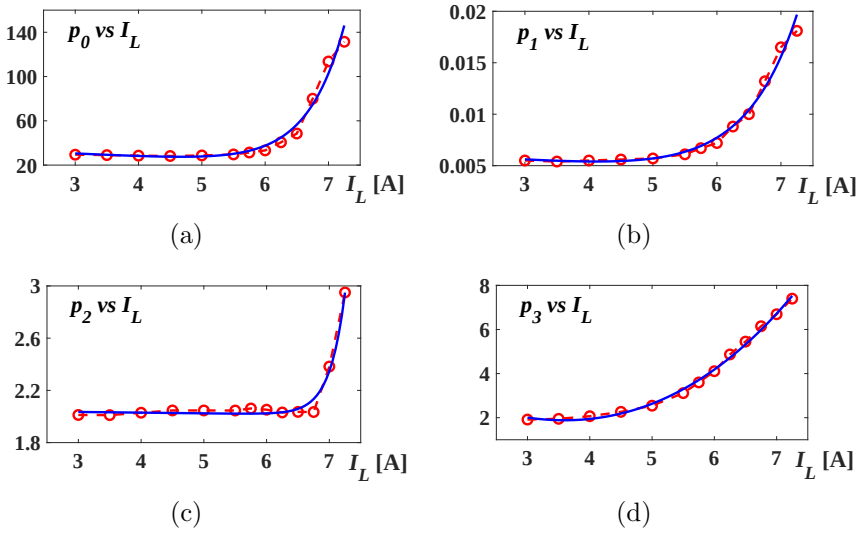

Figure 5.12: Behavioral model coefficients (red) and the relative fitting curves (blue) for MSS1260-103

Table 5.12: Fitting curve parameters of the behavioral model coefficients for MSS1260-103.

MSS1260-103 coefficients	$\mathbf{a_0}$	$\mathbf{a_1}$	$\mathbf{a_2}$	$\mathbf{a_3}$
p_0	5.76E−04	1.70E+00	-2.71E+00	3.86E+01
p_1	2.20E−06	1.23E+00	-4.16E−04	6.78E−03
p_2	9.65E−14	4.12E+00	-5.39E−03	2.05E+00
p_3	2.36E+01	1.36E−01	-5.23E+00	-1.78E+01

(5.25) and the experimental AC losses, for the 6 average current conditions I_L ={3, 4, 5, 6, 7, 7.25}A, selected among the overall 13 current values included in the training data set. The red markers correspond to the errors obtained by using the coefficients $\mathbf{p}$ of the proposed behavioral model, whereas the blue markers depict the errors obtained by using the NLLS fitting curves (5.26) of such coefficients. Each subplot shows the percent errors for 80 samples corresponding to different values of f_s and $V_{eq} = V_{IN} \times D \times (1-D)$, at a fixed I_L value. For all markers, relative power loss error is

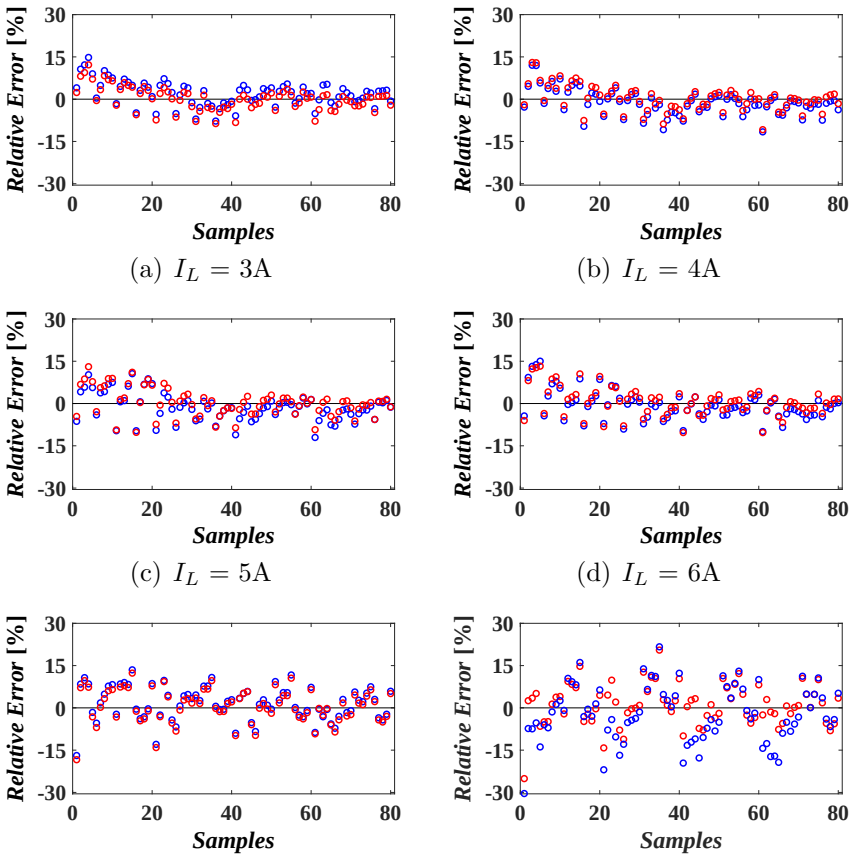

(a) $I_L = 3$A (b) $I_L = 4$A

(c) $I_L = 5$A (d) $I_L = 6$A

(e) $I_L = 7$A (f) $I_L = 7.25$A

Figure 5.13: Errors of $P_{ac,bhv}$ with the model coefficients (red) and the relative fitting curves (blue) for MSS1260-103.

within $\pm 15\%$ in weak-saturation region ($I_L \leq 6A$), and within $\pm 25\%$ in the roll-off region ($I_L > 6A$).

For both weak-saturation and roll-off region, Figures 5.14 (a)-(b) compare the AC loss prediction errors of the proposed model $P_{ac,bhv}$ (red filled markers) with the errors of two benchmark models, evaluated as:

- *benchmark model* 1 = AC winding losses + SE-based core losses (green filled markers);
- *benchmark model* 2 = AC winding losses + i-GSE-based core losses (green empty markers).

The AC winding losses have been evaluated as shown in (5.4), by using measured R_{dc} and $I_{ac,rms}$ values and taking into account the thermal effects on the winding resistance [71]. The SE-based core losses have been evaluated as shown in (5.6). In particular, the core loss coefficients $\{K_1, K_2, X, Y\}$ have been estimated by means of the NLLS curve fitting of the experimental AC power losses in weak-saturation region, as discussed in Appendix A. These same coefficients have also been adopted to evaluate the i-GSE-based core losses according to its reformulated version as a function of

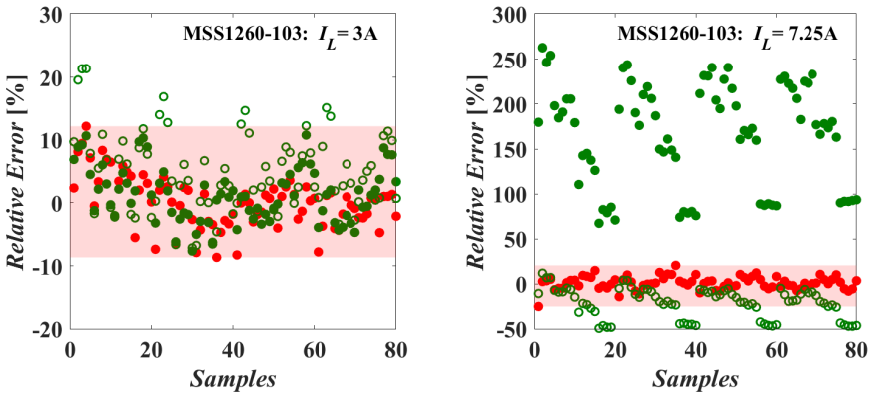

(a) $I_L = 3$A (b) $I_L = 7.25$A

Figure 5.14: Errors of $P_{ac,bhv}$ (red filled) *vs* benchmark model 1 (green filled) *vs* benchmark model 2 (green empty) in weak-saturation (a) and roll-off (b) for MSS1260-103.

the applied inductor voltage, duty-cycle and frequency, and manufacturer's core loss coefficients $\{K_1,K_2,X,Y\}$, discussed in detail in Appendix A. The two benchmark models provide similar results in weak-saturation region (Figure 5.14(a)). On the contrary, in roll-off region the benchmark model 2 underestimates the AC power losses, whereas the benchmark model 1 hugely overestimates it (Figure 5.14(b)). Indeed, none of the two models include the dependence of core losses on DC bias. As discussed in [54], if Δi_{Lpp} value is maintained constant, the hysteresis loop area is expected to decrease with increasing current, as well as the resulting core losses. The benchmark model 1 does not include such core loss correction for DC bias and, as a result, overestimates the AC power losses. Conversely, if ΔB value is kept constant, the hysteresis loop area is expected to increase with the current, as well as the core losses. The benchmark model #2 does not include such DC bias dependence and underestimates the core losses. The results of Figure 5.14 highlight that the proposed behavioral model (5.25) provides reliable AC loss estimation both in weak-saturation and in roll-off region.

Case Study #2: MSS1260-473 inductor

In this second case study, the Coilcraft inductor MSS1260-473 of nominal inductance $L_{nom} = 47\mu$H has been analyzed, having the same magnetic core of MSS1260-103, but different winding turn number. In order to reduce both measurement and execution times needed for the AC loss model identification, such inductor has been tested on the reduced set of 162 operating conditions given in Table 5.13, including $m = 6$ average current values and $n = 27$ operating conditions in terms of f_s and $V_{eq} = V_{IN} \times D \times (1 - D)$ for each current. In particular, an inductance de-rating of about 40% is obtained at $I_L = 3.1$A. The experimental measurements of such a reduced training data set took about 6 hours, whereas the 30 runs of the GP algorithm lasted about 2 hours.

Figure 5.15 shows the identified non-dominated Pareto-optimal solutions having a repeatability of at least 8 runs. The GP-MOO

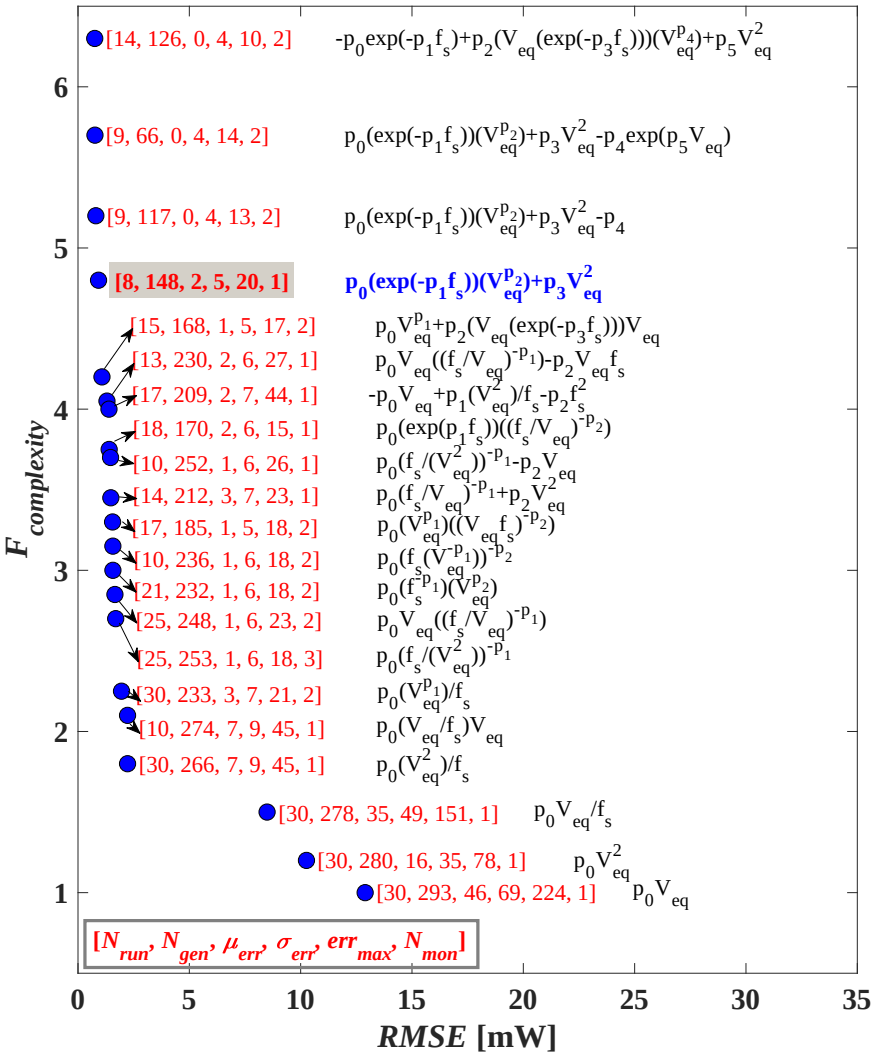

Figure 5.15: Repeatable Pareto-optimal solutions for MSS1260-473 inductor.

algorithm has discovered the model (5.25) also for the MSS1260-473 inductor, even though the dimensions of the training data set have been greatly reduced compared to the MSS1260-103 inductor (case study #1). Such model has a repeatability of 8 runs and persists in the population during 148 generations, presents an average error $\mu_{err} = 2\%$, a standard deviation $\sigma_{err} = 5\%$ and a maximum error $err_{max} = 20\%$ over the training data set, and its parameters are monotonic with the current I_L.

Table 5.13: Training set operating conditions for MSS1260-473.

Quantity	Units	Values
f_s	kHz	$[200, 300, 400]$
V_{IN}	V	$[12, 18, 24]$
D	–	$[0.3, 0.5, 0.7]$
I_{out}	A	$[1, 1.5, 2, 2.5, 2.8, 3.1]$

The coefficients $\mathbf{p}$ of the model (5.25) for the MSS1260-473 inductor are shown in Figure 5.16, together with their NLLS fitting curves. The values of the vector coefficients $\{\mathbf{a}_0, ..., \mathbf{a}_3\}$ of the fitting curves are given in Table 5.14. Figures 5.17 (a)-(b) compare the AC loss prediction errors of the proposed model $P_{ac,bhv}$ with the errors of the two benchmark models, for weak-saturation and roll-off region respectively. Also for the MSS1260-473 inductor,

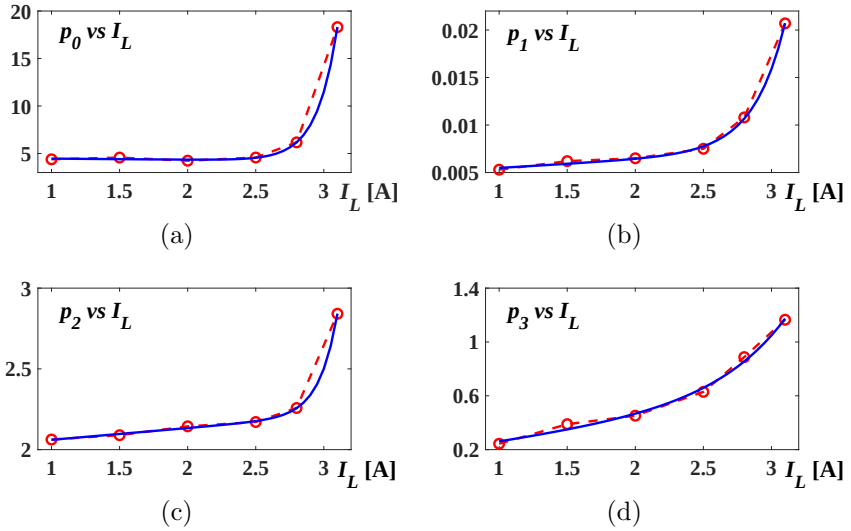

Figure 5.16: Behavioral model coefficients (red) and the relative fitting curves (blue) for MSS1260-473.

the core loss coefficients $\{K_1, K_2, X, Y\}$ have been estimated by means of the NLLS curve fitting of the experimental AC power losses in weak-saturation region, as discussed in Appendix A. As expected, the benchmark model 2 underestimates the AC losses in roll-off region, whereas the benchmark model 1 overestimates it.

Table 5.14: Fitting curves parameters of the behavioral model coefficients for MSS1260-473.

MSS1260-473 coefficients	$\mathbf{a_0}$	$\mathbf{a_1}$	$\mathbf{a_2}$	$\mathbf{a_3}$
p_0	1.63E−08	6.64E+00	-1.15E−01	4.58E+00
p_1	1.89E−08	4.35E+00	8.57E−04	4.62E−03
p_2	4.10E−11	7.57E+00	7.28E−02	1.99E+00
p_3	1.45E−03	1.95E+00	1.44E−01	1.07E−01

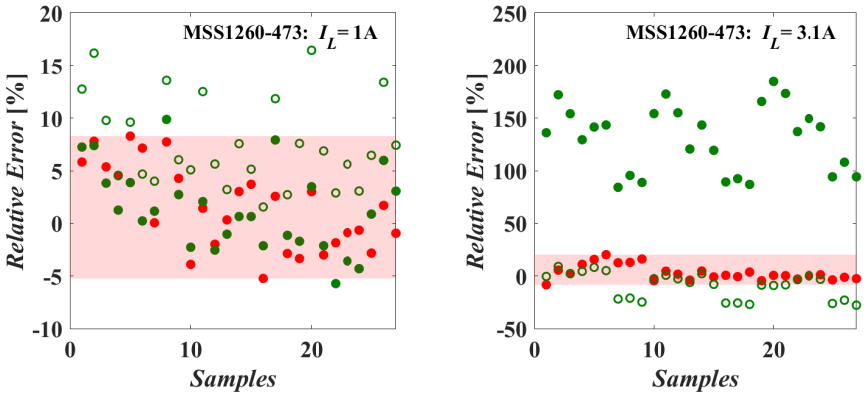

(a) $I_L = 1$A (b) $I_L = 3.1$A

Figure 5.17: Errors of $P_{ac,bhv}$ (red filled) *vs* benchmark model 1 (green filled) *vs* benchmark model 2 (green empty) in weak-saturation (a) and roll-off (b) for MSS1260-473.

Case Study #3: MSS1038-273 inductor

The GP-MOO approach applied in the previous two case studies has led to the same AC power loss model for two inductors of the same family (same magnetic core). In this Section, it is shown that the same model is valid for the devices of a different inductor family. In particular, the inductor MSS1038-273 of nominal inductance $L_{nom} = 27\mu$H has been considered, whose core has the same magnetic material but different size compared to the components of the MSS1260 family (see Table 5.10). The 162 operating conditions given in Table 5.15 have been considered, covering $m = 6$ average current values and $n = 27$ combinations of f_s and $V_{eq} = V_{IN} \times D \times (1 - D)$ for each current. In particular, an inductance de-rating of about 50% is obtained at $I_L = 2.9$A.

The AC loss formula has been kept unchanged for the Coilcraft MSS1038-273 part: in fact, the identification of the power loss model coefficients has been performed starting directly from the model structure (5.25), by applying NLLS algorithm to the training set data of Table 5.15. The resulting coefficients $\mathbf{p}$ are shown in Figure 5.18, together with the NLLS fitting curves (5.26), whose parameters are given in Table 5.16. The proposed behavioral model is characterized by a maximum percent error $err_{max} = 19\%$, with a mean percent error $\mu_{err} = 3\%$ and a standard deviation $\sigma_{err} = 6\%$ over the training data set.

Figures 5.19 (a)-(b) compare the AC loss prediction errors of the model (5.25) with the errors of the two benchmark models, for weak-saturation and roll-off region respectively. The $\{K_1, K_2, X, Y\}$

Table 5.15: Training set operating conditions for MSS1038-273.

Quantity	Units	Values
f_s	kHz	$[200, 300, 400]$
V_{IN}	V	$[8, 12, 16]$
D	–	$[0.3, 0.5, 0.7]$
I_{out}	A	$[0.9, 1.3, 1.7, 2.1, 2.5, 2.9]$

coefficients have been estimated as discussed for the previous case studies. As expected, the behavioral model (5.25) outperforms the two benchmark models, especially in operating conditions involving saturation.

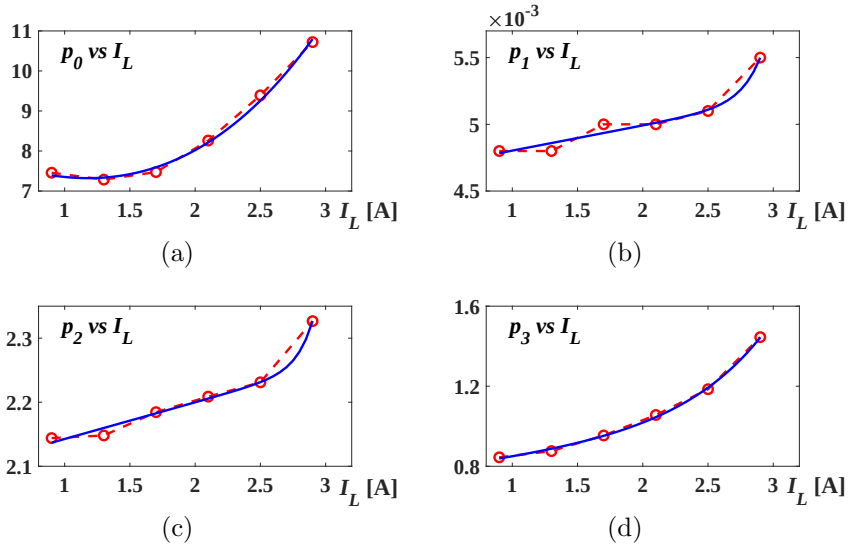

Figure 5.18: Behavioral model coefficients (red) and the relative fitting curves (blue) for MSS1038-273.

Table 5.16: Fitting curves parameters of the behavioral model coefficients for MSS1038-273.

MSS1038-273 coefficients	$\mathbf{a_0}$	$\mathbf{a_1}$	$\mathbf{a_2}$	$\mathbf{a_3}$
p_0	8.45E+00	3.77E−01	-4.96E+00	2.51E−14
p_1	1.75E−12	6.58E+00	1.88E−04	4.61E−03
p_2	4.30E−12	8.13E+00	5.72E−02	2.09E+00
p_3	4.81E−03	1.58E+00	7.85E−02	7.48E−01

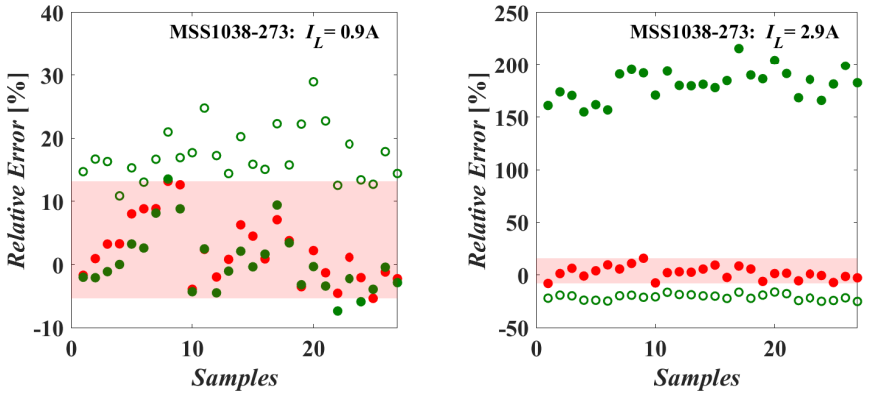

(a) $I_L = 0.9$A (b) $I_L = 2.9$A

Figure 5.19: Errors of $P_{ac,bhv}$ (red filled) *vs* benchmark model 1 (green filled) *vs* benchmark model 2 (green empty) in weak-saturation (a) and roll-off (b) for MSS1038-273.

Case Study #4: DO3316T-103 inductor

In this last case study, it is shown that the findings relevant to the identification of the *AC* power loss model have general validity. In fact, the *AC* power loss model has also been applied to inductors with different ferrite material, dimensions and type of the magnetic core. In particular, the Coilcraft inductor DO3316T-103 (L_{nom} = 10μH) has been considered. This part is assembled with an unshielded core of different ferrite material and size (see Table 5.10). The 405 operating conditions given in Table 5.17 have been considered, covering $m = 9$ average current values and $n = 45$ combinations of f_s and $V_{eq} = V_{IN} \times D \times (1 - D)$ for each current. In particular, an inductance de-rating of about 50% is obtained at $I_L = 4$ A.

The identification of the power loss model coefficients for the Coilcraft DO3316T part started directly from the model structure (5.25). The resulting coefficients $\mathbf{p}$ are shown in Figure 5.20, together with the NLLS fitting curves, whose parameters are given in Table 5.18. The proposed behavioral model is characterized by a maximum percent error $err_{max} = 20\%$, with a mean per-

Table 5.17: Training set operating conditions for DO3316T-103.

Quantity	Units	Values
f_s	kHz	$[300, 400, 500]$
V_{IN}	V	$[8, 10, 12]$
D	–	$[0.2, 0.35, 0.5, 0.65, 0.8]$
I_{out}	A	$[2, 2.25, 2.5, 2.75, 3, 3.25, 3.5, 3.75, 4]$

cent error $\mu_{err} = 1\%$ and a standard deviation $\sigma_{err} = 3\%$ over the training data set. Figures 5.21 (a)-(b) compare the AC loss prediction errors of the proposed model $P_{ac,bhv}$ with the errors of the two benchmark models, for weak-saturation and roll-off region respectively. The $\{K_1, K_2, X, Y\}$ coefficients have been estimated as discussed for the previous case studies. The behavioral model (5.25) outperforms the two benchmark models, especially in operating conditions involving saturation.

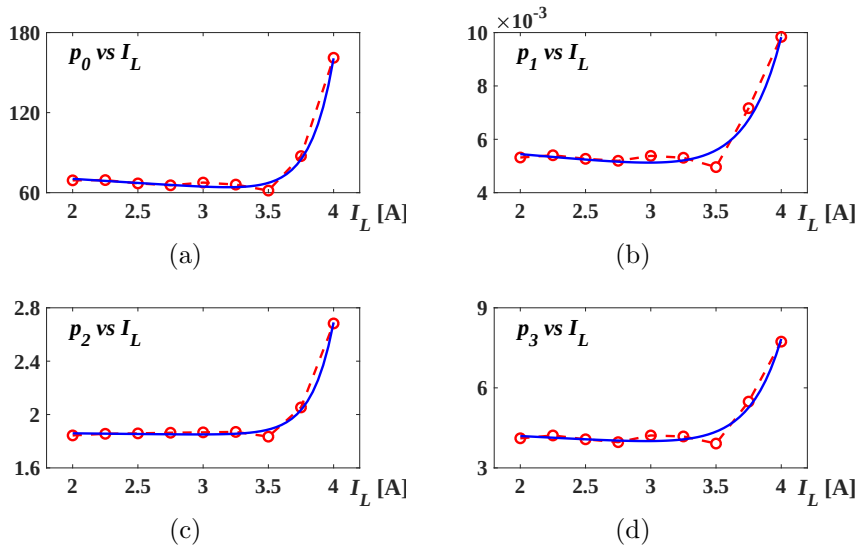

Figure 5.20: Behavioral model coefficients (red) and the relative fitting curves (blue) for DO3316T-103.

Table 5.18: Fitting curves parameters of the behavioral model coefficients for DO3316T-103.

DO3316T-103 coefficients	$\mathbf{a_0}$	$\mathbf{a_1}$	$\mathbf{a_2}$	$\mathbf{a_3}$
p_0	2.00E−08	5.59E+00	-6.21E+00	8.28E+01
p_1	1.61E−09	3.75E+00	-4.39E−04	6.32E−03
p_2	4.09E−11	5.94E+00	-1.04E−02	1.88E+00
p_3	4.33E−07	4.02E+00	-2.63E−01	4.72E+00

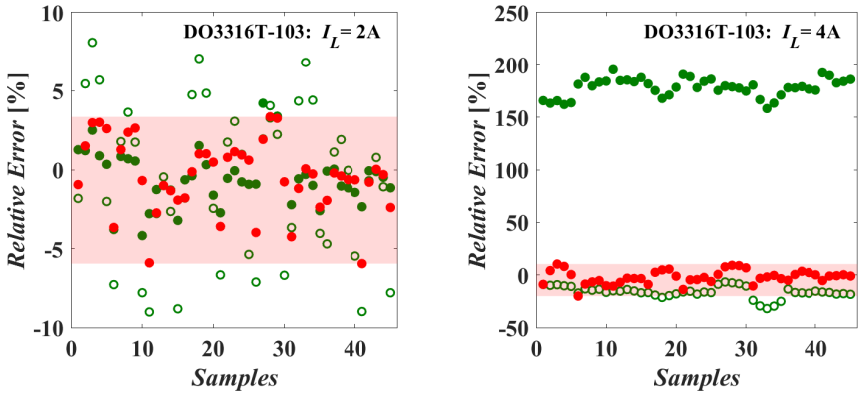

(a) $I_L = 2$A (b) $I_L = 4$A

Figure 5.21: Errors of $P_{ac,bhv}$ (red filled) *vs* benchmark model 1 (green filled) *vs* benchmark model 2 (green empty) in weak-saturation (a) and roll-off (b) for DO3316T-103.

Model Discussion and Final Considerations

The behavioral model (5.25) is the sum of two terms: $p_0 \exp(-p_1 f_s) \cdot \cdot V_{eq}^{p_2}$ and $p_3 V_{eq}^2$. The first term contains a power law dependence on the applied voltage V_{eq}, which reflects the dependence of P_{core} on the magnetic flux density magnitude B_{ac}, V_{eq} being proportional to B_{ac}. The second term contains a square law dependence on the applied voltage V_{eq}, which reflects the dependence of $P_{wind,ac}$ on the

peak-to-peak current ripple magnitude Δi_{Lpp}, V_{eq} being proportional to Δi_{Lpp}. Such result is in agreement with the expected loss trend, since the AC winding losses are proportional to the square of the rms AC current $I_{ac,rms}$, which can be well represented by the square of Δi_{Lpp} in case of triangular or cusp-like inductor current waveform. The proposed model (5.25) also shows an exponential decay of the AC power losses with the increasing switching frequency, which can be explained as follows. For a fixed V_{eq} value, the peak-to-peak current ripple decreases while the frequency increases, resulting in lower $I_{ac,rms}$ value. However, the winding resistance R_{ac} value increases at higher frequency, due to the skin and proximity effects. Thus, the AC winding losses $P_{wind,ac}$ can increase or decrease with the frequency, depending on the winding arrangement. As for the core losses P_{core}, the smaller peak-to-peak current ripple at higher frequencies involves a smaller B_{ac} magnitude and, consequently, a smaller area of the $B-H$ loop, which yields a loss reduction. However, the higher frequency involves that the $B-H$ loop is repeated more frequently, thus causing a consequent loss increase. As a result, the core losses could as increase as decrease with the frequency, depending on the inductor characteristics. For the components analyzed in this study, the model (5.25) reveals that a frequency increase results in an AC power loss decrease.

Both the proposed AC loss model and the adopted benchmark models require experimental measurements data for model coefficients extraction. In particular, the GP-MOO algorithm adopted for the identification of model (5.25) also requires some extra computation time, when the behavioral models are generated for the first time. The amount of this additional time mainly depends on the experimental data used for models identification: the higher the number of the experimental test conditions, the greater the execution time required. However, the major benefit descending from the adoption of the GP-MOO algorithm is that it allows for the identification of a generalized loss model, valid for families of ferrite inductors with different materials and/or core types and size, as proved by the four presented case studies. The identified

model remains unchanged and always valid, independently of the operating conditions the inductor is working in. Conversely, the suggested benchmark models are conservative and can yield inaccurate core loss estimation, especially in operating conditions involving saturation. Once the *AC* loss model has been identified, only the execution time for the curve-fitting NLLS algorithm is needed to extract the model coefficient values. This time is comparable to that one needed for the extraction of any other benchmark models' coefficients. Hence, the computation time of the GP-MOO algorithm execution is the unique extra time contribution for the proposed model.

Temperature Impact

Temperature is an important factor influencing the inductor power losses. The core loss density is sometimes modeled as a polynomial function of temperature in magnetic cores datasheets [46,47]. Unfortunately, few literature studies have investigated the dependence of the core losses on temperature. In [55], Muhlethaler *et al.* have introduced Steinmetz premagnetization graphs providing information about the dependence of the Steinmetz parameters on the *DC* bias for two different temperatures. Herein, the impact of the ambient temperature T_a on the coefficients of the proposed behavioral model (5.25) has been investigated for the MSS1260-473 inductor (case study #2). Experimental measurements of the *AC* power losses have been performed at $T_a = 25°\text{C}$ and $T_a = 37°\text{C}$. The higher ambient temperature has been obtained by incapsulating the inductor into a heated chamber. The TDK B57550G502F 5k$\Omega\pm$1% NTC thermistor has been used for the experimental measurements. For the two ambient temperature conditions, the coefficients of the behavioral model (5.25) have been identified by means of the NLLS technique, as shown in Figure 5.22. It can be observed that, with the temperature increase, all the coefficients decrease in weak-saturation region (at low inductor currents $I_L < 2.5\text{A}$) and increase in roll-off region (beyond 2.5A inductor current). Indeed, while the ambient temperature increases, the

inductance in weak-saturation region typically increases, thus resulting in the lower inductor current ripple and *AC* power losses. In roll-off region, instead, the inductance decreases with the temperature, thus resulting in higher current ripple and losses [72].

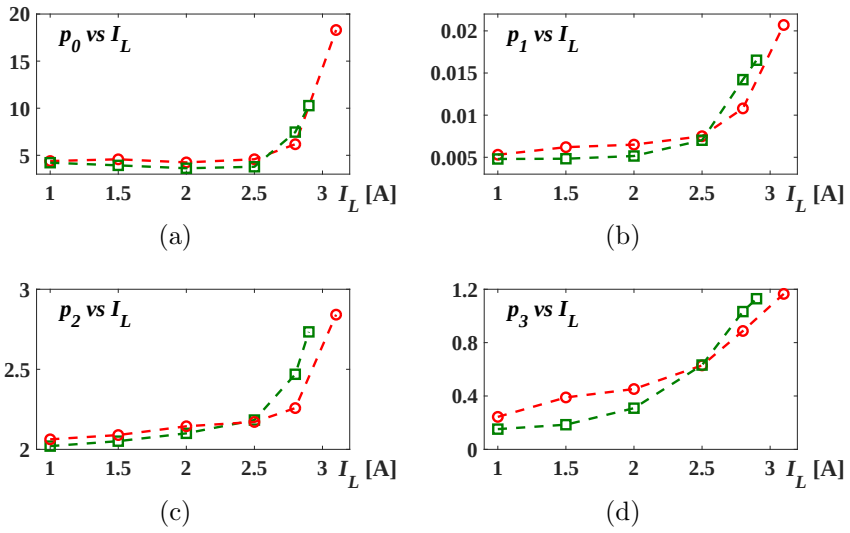

Figure 5.22: Behavioral model coefficients at T_a=25°C (red) and T_a=37°C (green) for MSS1260-473.

The main outcome of the research activity presented in this Chapter resulted in the publication of the scientific papers:

- K. Stoyka, G. Di Capua, N. Femia, "A Novel AC Power Loss Model for Ferrite Power Inductors", *IEEE Trans. on Power Electronics*, vol. 34, no. 3, pp. 2680-2692, March 2019.
- G. Di Capua, N. Femia, K. Stoyka, "Loss Behavioral Modeling for Ferrite Inductors", *15th Int. Conf. on Synthesis, Modeling, Analysis and Simulation Methods and Appl. to Circuit Design (SMACD)*, July 2018.
- G. Di Capua, N. Femia, M. Migliaro, K. Stoyka, "Genetic Programming Approach for Identification of Ferrite Inductors Power Loss Models", *42nd Annual Conf. of IEEE Industrial Electronics Society (IECON)*, October 2016.

Chapter 6

Power-Loss-Dependent Inductance Modeling

This chapter discusses behavioral modeling of the saturation characteristic of FPIs as a function of the inductor total power losses. A novel power-loss-dependent saturation model provides the inductance as a function of the inductor current, parameterized with respect to total power losses. Such model has been identified starting from easily measurable electrical quantities, such as inductor voltage and current, unlike conventional thermal-based modeling approaches requiring information on the core temperature. The proposed approach starts from the assertion that the core temperature is not an *input* variable in the inductor model, but rather an *output*, depending on the ambient temperature, inductor total power losses and equivalent thermal resistance.

6.1 Inductance Model

The buck converter has been herein adopted as a reference case study, but the findings relative to FPIs modeling have general conceptual validity, and can be applied to whatever converter topology. Let $w = [V_{in}, I_{out}, f_s, D]$ be the vector of parameters determining the SMPS operating condition of the power converter. As

the switching period T_s is normally much smaller than the inductor thermal time constant, the inductor operating temperature can be assumed constant during T_s and equal to an average steady-state temperature T:

$$T = T_a + P_{tot} R_{th} \tag{6.1}$$

depending on the ambient temperature T_a, inductor total power losses P_{tot} and equivalent thermal resistance R_{th}. As shown hereinafter, the value of thermal resistance R_{th} under SMPS operating conditions can be determined by means of the experimental data utilized to obtain the proposed power-loss-dependent inductance model.

At a given ambient temperature, the flux linkage Ψ (*i.e.*, magnetic flux linked to all turns) depends on inductor current i_L and temperature T, as shown in Fig. 6.1, where the Ψ *versus* i_L curves at steady-state correspond to different temperatures $T_2 > T_1$. Unfortunately, the core temperature T is not easy to measure. Given the ambient temperature T_a, different SMPS operating conditions generating the same inductor total power losses P_{tot} lead to the same core temperature. Unlike the temperature, P_{tot} can be estimated starting from easily measurable electrical quantities, such as inductor voltage and current. Therefore, the inductor total power losses P_{tot} is considered as input of the proposed saturation model,

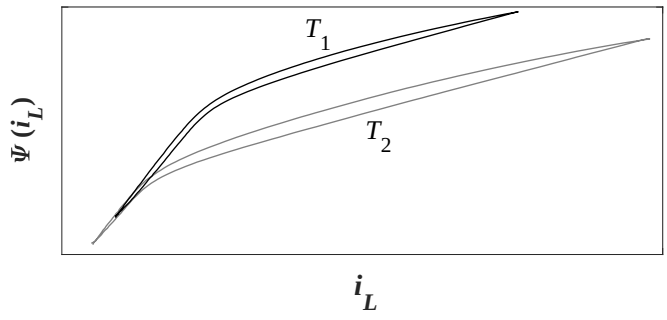

Figure 6.1: Ψ *vs* i_L hysteretic curves measured for the same inductor at two different temperatures $T_2 > T_1$.

instead of temperature T. Accordingly, the inductor voltage v_L is related to the flux linkage Ψ as:

$$v_L(t) = \frac{\partial}{\partial t}\Psi(t, P_{tot}) \tag{6.2}$$

In commercial FPIs, gapped cores determine a flattening of hysteresis loops. For this reason, the hysteresis is not taken into account in the proposed inductance model. At steady-state, Eq. (6.2) can be recast as:

$$v_L(t) = \frac{\partial}{\partial i_L}\Psi(i_L, P_{tot})\frac{di_L}{dt} = L(i_L, P_{tot})\frac{di_L}{dt} \tag{6.3}$$

where $L(i_L, P_{tot}) = \frac{\partial}{\partial i_L}\Psi(i_L, P_{tot})$ is the *dynamic inductance* (in the following, simply referred to as inductance) for the steady-state solution related to w. The plots in Fig. 6.1 show that the slope of $\Psi(i_L)$ is approximately constant for low current values. As i_L increases, the curves exhibit a knee and become again approximately linear, with a lower slope. This behavior is due to magnetic saturation, which is taken into account in the proposed inductance model.

6.2 Power-Loss-Dependent Inductance Model

As described in Section 1.3, the dynamic inductance of FPIs can be modeled by means of an arctangent function of the current i_L. The parameters L^{high}, L^{low}, σ and I_L^* of such a function depend on the inductor temperature T. The experimental L *versus* i_L curves provided by inductors manufacturers at different temperatures highlight a high temperature sensitivity of the parameter I_L^*, whereas L^{high}, L^{low} and σ show a quite weak sensitivity. As an example, Fig. 6.2 shows the experimental curves of the Coilcraft MSS1260-103 inductor for different temperatures [17].

Since inductor temperature and total power losses are linearly related to each other (through Eq. (6.1)), the following power-

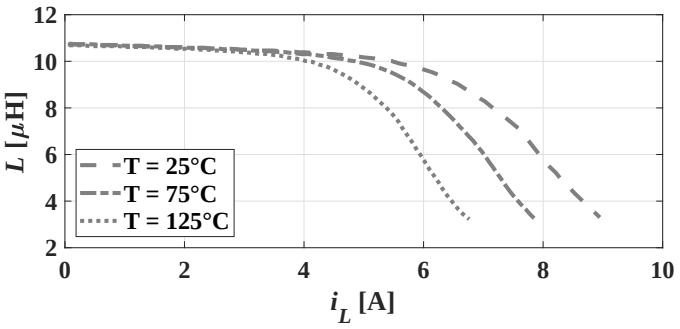

Figure 6.2: L *vs* i_L experimental curves of Coilcraft MSS1260-103 inductor.

loss-dependent saturation model has been herein proposed:

$$L(i_L, P_{tot}) = L^{low}(P_{tot}) + \frac{L^{high}(P_{tot}) - L^{low}(P_{tot})}{2} \times \\ \times \left\{ 1 - \frac{2}{\pi} \text{atan} \left\{ \sigma(P_{tot}) \left[i_L - I_L^*(P_{tot}) \right] \right\} \right\} \tag{6.4}$$

Let us note that, unlike the arctangent model (1.6) discussed in Section 1.3, in model (6.4) the absolute value of inductor current has been omitted, since only positive current values have been considered for power-loss-dependent inductor modeling. Once the L *vs* i_L curve is determined for positive current values, it can be symmetrically reconstructed also for negative current values. The parameters of model (6.4) can be expressed as a function of P_{tot} according to (6.5):

$$\begin{cases} L^{high} = x_1 \\ L^{low} = x_2 \\ \sigma = x_3 \\ I_L^* = x_4 P_{tot} + x_5 \end{cases} \tag{6.5}$$

where $x = [x_1 \; x_2 \; x_3 \; x_4 \; x_5]^T$ is a vector of fitting coefficients to be determined. Given an operating condition w and a time interval

$[t_0, t]$, from (6.3) it follows:

$$\underbrace{\Psi(t_0) + \int_{t_0}^{t} v_L(\tau)d\tau}_{\Psi(t)} = \underbrace{\Psi(t_0) + \int_{i_L(t_0)}^{i_L(t)} L(i'_L, P_{tot})di'_L}_{\hat{\Psi}(i_L(t),P_{tot})} \tag{6.6}$$

where $\Psi(t_0)$ is the flux linkage in $t = t_0$. The experimental flux linkage $\Psi(t)$ in Eq. (6.6) can be computed using the measurements of the inductor voltage, whereas the analytical flux linkage $\hat{\Psi}(i_L(t), P_{tot})$ can be computed by integrating Eq. (6.4), thus obtaining:

$$\begin{aligned}\hat{\Psi}(i_L(t), P_{tot}) &= \Psi(t_0) + \int_{i_L(t_0)}^{i_L(t)} L(i'_L, P_{tot})di'_L = \\ &= \left\{ \frac{L^{high} + L^{low}}{2} i_L + \frac{L^{high} - L^{low}}{2\pi\sigma} \log\left[1 + \sigma^2(i_L - I_L^*)^2\right] + \right. \\ &\quad \left. + \frac{L^{low} - L^{high}}{\pi}(i_L - I_L^*)\text{atan}\left[\sigma(i_L - I_L^*)\right] \right\} \Bigg|_{i_L=i_L(t_0)}^{i_L=i_L(t)}\end{aligned} \tag{6.7}$$

Given K different operating conditions w_k $(k = 1, \ldots, K)$, let $v_{L,k}(t)$, $i_{L,k}(t)$, $\Psi_{L,k}(t)$ and $P_{tot,k}$ be the steady-state inductor voltage, current, flux linkage and power losses related to the k-th operating condition, respectively. If $v_{L,k}$ and $i_{L,k}$ are measured in N time instants t_n $(n = 1, \ldots, N)$, the optimal coefficient vector x^* can be obtained by solving the following nonlinear optimization problem:

$$x^* = \arg\min_x \sum_{k=1}^{K} \sum_{n=1}^{N} \left[\Psi_k(t_n) - \hat{\Psi}(i_{L,k}(t_n), P_{tot,k})\right]^2 \tag{6.8}$$

where $\Psi_k(t_n) = \Psi_k(t_0) + \int_{t_0}^{t_n} v_{L,k}(\tau)d\tau$, $\hat{\Psi}(i_k(t_n), P_{tot,k})$ is given by Eq. (6.7), and the inductance parameters L^{high}, L^{low}, σ and I_L^* are given by Eq. (6.5). The power losses $P_{tot,k}$ can be either measured or estimated by using behavioral models described in Chapter 5. Herein, total inductor power losses have been obtained by summing the *DC* and *AC* loss contributions, estimated by means of Eq.s (5.11) and (5.25), respectively.

6.2.1 Model Implementation

Given a set of experimental measurements, the optimization problem (6.8) can be solved and the resulting optimal vector x^* used to compute the arctangent model parameters (6.5). Then, the inductance $L(i_L, P_{tot})$ can be evaluated for any value of i_L and P_{tot}, through Eq. (6.4). From Eq. (6.3), integrating numerically the ratio $\hat{v}_{L,k}(t)/L(\hat{i}_{L,k}(t), P_{tot,k})$ over the time interval $[t_0, t_n]$ provides the inductor current value $\hat{i}_{L,k}(t_n)$ at the time instant t_n, under the k-th operating condition:

$$\hat{i}_{L,k}(t_n) = \hat{i}_{L,k}(t_0) + \int_{t_0}^{t_n} \frac{\hat{v}_{L,k}(t)}{L(\hat{i}_{L,k}(t), P_{tot,k})} dt \tag{6.9}$$

The estimated initial inductor current $\hat{i}_{L,k}(t_0)$ has been assumed equal to the corresponding experimental initial inductor current $i_{L,k}(t_0)$. The function $\hat{v}_{L,k}(t)$ can be obtained through a piecewise-affine interpolation of samples $v_{L,k}(t_n)$. For the k-th operating condition, the estimated current ripple can be obtained as $\hat{\Delta} i_{Lpp,k} = \max_j \hat{i}_{L,k}(t_j) - \min_j \hat{i}_{L,k}(t_j)$ (for $k = 1, \ldots, K$).

Eventually, the fitting accuracy of the proposed model can be evaluated by means of three percent errors E_k^{Ψ}, E_k^I and E_k^{Δ}, defined as follows:

$$E_k^{\Psi} = 100 \sqrt{\frac{1}{N} \sum_{n=1}^{N} \left[\frac{\Psi_k(t_n) - \hat{\Psi}(i_{L,k}(t_n), P_{tot,k})}{r_k^{\Psi}} \right]^2} \tag{6.10}$$

$$E_k^I = 100 \sqrt{\frac{1}{N} \sum_{n=1}^{N} \left[\frac{i_{L,k}(t_n) - \hat{i}_{L,k}(t_n)}{r_k^I} \right]^2} \tag{6.11}$$

$$E_k^{\Delta} = 100 \frac{|\Delta i_{Lpp,k} - \hat{\Delta} i_{Lpp,k}|}{\Delta i_{Lpp,k}} \tag{6.12}$$

where

$$r_k^{\Psi} = \max_n \Psi_k(t_n) - \min_n \Psi_k(t_n) \tag{6.13}$$

$$r_k^I = \max_n i_{L,k}(t_n) - \min_n i_{L,k}(t_n) \tag{6.14}$$

For each dataset, the errors (6.10)-(6.12) can be calculated over the K operating conditions, and the relevant mean value $\bar{E}^{\{\Psi,I,\Delta\}}$, standard deviation $\sigma^{\{\Psi,I,\Delta\}}$ and maximum value $E_M^{\{\Psi,I,\Delta\}}$ can be subsequently evaluated to characterize the errors distribution.

6.3 Case Studies

The discussion is herein referred to commercial power inductors with different ferrite materials and core types. In particular, two Coilcraft FPIs have been considered: a 10μH shielded MSS1260-103 (IUT #1) and a 10μH unshielded DO3316T-103 (IUT #2). The main characteristics of these inductors are listed in Table 6.1. The coefficients $\{b_0, ..., b_3\}$ of the AC loss model (5.25) for such inductors have been provided in Tables 5.12 and 5.18.

For each inductor, the experimental dataset including inductor current $i_{L,k}(t)$, voltage $v_{L,k}(t)$ and power losses $P_{tot,k}$ $(k = 1, ..., K)$ has been collected by means of the MADMIX system described in Subsection 5.2.2. Two datasets have been constructed for IUT #1 and #2, labeled as $\mathcal{S}_{11}$ and $\mathcal{S}_{12}$ respectively, consisting of $K = 880$ different operating conditions, corresponding to all the combinations of parameters f_s, V_{in}, D and I_{out} listed in the upper part of Table 6.2. For each condition, $N = 200$ samples of voltage and current waveforms have been acquired per period, thus obtaining values $v_{L,k}(t_n)$ and $i_{L,k}(t_n)$, with $n = 1, \ldots, N$, and the total power losses $P_{tot,k}$ have been experimentally measured by the MADMIX system. The experimental datasets covered the following ranges of

Table 6.1: Investigated inductors and their main characteristics

Part Number	Dimensions $[mm^3]$	L $[\mu H]$	DCR $[m\Omega]$	$I_{sat}[A]$ 30% drop	$I_{rms}[A]$ 40°C rise
MSS1260-103	12x12x6	10	24	7.40	4.00
DO3316T-103	13.2x9.9x6.4	10	34	3.80	3.90

Table 6.2: Operating conditions used in datasets $\mathcal{S}_{11}$, $\mathcal{S}_{12}$, $\mathcal{S}_{21}$, $\mathcal{S}_{22}$.

Dataset	$\mathcal{S}_{11}$ (IUT #1)	$\mathcal{S}_{12}$ (IUT #2)
f_s [kHz]	$\{200, 300, 400, 500\}$	$\{200, 300, 400, 500\}$
V_{IN} [V]	$\{6, 8, 10, 12\}$	$\{6, 8, 10, 12\}$
D [−]	$\{0.2, 0.35, 0.5, 0.65, 0.8\}$	$\{0.2, 0.35, 0.5, 0.65, 0.8\}$
I_{out} [A]	$\{3, 3.5, 4, 4.5, 5, 5.5, 6, 6.5, 7, 7.5, 8\}$	$\{2, 2.25, 2.5, 2.75, 3, 3.25, 3.5, 3.75, 4, 4.25, 4.5\}$
Subset	$\mathcal{S}_{21}$ (IUT #1)	$\mathcal{S}_{22}$ (IUT #2)
f_s [kHz]	$\{200, 300\}$	$\{200, 300\}$
V_{IN} [V]	$\{8, 12\}$	$\{8, 12\}$
D [−]	0.5	0.5
I_{out} [A]	$\{5.5, 6, 6.5, 7, 7.5, 8\}$	$\{3.25, 3.5, 3.75, 4, 4.25, 4.5\}$

total power losses $P_{tot,k}$ and peak-to-peak current ripple $\Delta i_{Lpp,k}$:

- IUT #1: $P_{tot,k} \in [0.18,\ 1.89]$W, $\Delta i_{Lpp,k} \in [0.20,\ 6.61]$A;
- IUT #2: $P_{tot,k} \in [0.12,\ 1.52]$W, $\Delta i_{Lpp,k} \in [0.23,\ 6.13]$A.

Two subsets, labeled as $\mathcal{S}_{21}$ and $\mathcal{S}_{22}$, have been then extracted from the original datasets $\mathcal{S}_{11}$ and $\mathcal{S}_{12}$, with the operating conditions given by the $K = 24$ combinations of parameters f_s, V_{in}, D and I_{out} given in the lower part of Table 6.2. These combinations involve the operating conditions with the largest average currents and peak-to-peak current ripples.

The experimental data acquired by the MADMIX system have also been used to evaluate the equivalent thermal resistance R_{th} of the two inductors. The devices surface temperature has been measured during the tests by using a TDK B57550G502F 5kΩ±1% NTC thermistor. Fig. 6.3 shows the plots of experimental temperature rise values $T_\Delta = T - T_a$ as a function of the total power losses P_{tot} (red circle markers), together with linear regression curves (blue lines), whose slopes provide the values of 35°C/W and 43°C/W for the thermal resistances of MSS1260-103 and DO3316T-103, respectively.

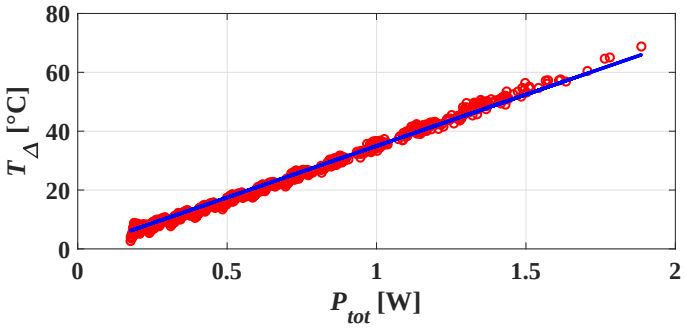

(a)

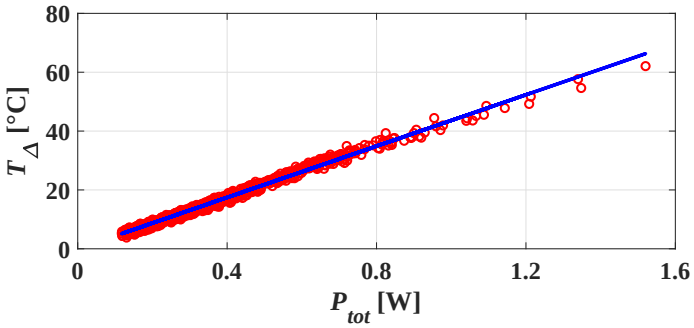

(b)

Figure 6.3: Inductors temperature rise *vs* total power losses (red circles) and relevant linear regression curve (blue line) for IUT #1 (a) and IUT #2 (b).

6.4 Modeling Results

In this Section, the FPIs models obtained with the proposed approach are presented and discussed. The problem (6.8) has been solved on datasets $\mathcal{S}_{11}$ and $\mathcal{S}_{12}$ first (case *a*), and then on subsets $\mathcal{S}_{21}$ and $\mathcal{S}_{22}$ (case *b*). In both cases, the error statistics ($\bar{E}^{\{\Psi,I,\Delta\}}$, $\sigma^{\{\Psi,I,\Delta\}}$ and $E_M^{\{\Psi,I,\Delta\}}$) have been computed on complete datasets $\mathcal{S}_{11}$ and $\mathcal{S}_{12}$. The results are shown in Table 6.3. It can be noticed that the error increase for case *b* is negligible, even if only $K = 24$ operating conditions have been used to train the model. This is

due to the fact that subsets $\mathcal{S}_{21}$ and $\mathcal{S}_{22}$ contain the operating conditions with the largest average currents and peak-to-peak current ripples, *i.e.* the conditions wherein the inductor current spans a wider portion of the arctangent function. This suggests that it is not necessary to employ operating conditions with low current values to achieve a good model fitting. From a practical viewpoint, this means that only a limited set of proper measurements are enough to obtain an accurate model.

The resulting coefficient vectors x^* for IUT #1 and #2 are shown in Table 6.4. The arctangent parameters L^{high}, L^{low}, σ and I_L^* can be obtained by substituting x^* and the measured power

Table 6.3: Statistics of the errors for all performed tests.

IUT #1 (MSS1260-103)			
Dataset	$\bar{E}^{\Psi}[\%]$	$\sigma^{\Psi}[\%]$	$E_M^{\Psi}[\%]$
$\mathcal{S}_{11}$ (case *a*)	1.41	0.29	2.62
$\mathcal{S}_{21}$ (case *b*)	1.42	0.29	2.53
Dataset	$\bar{E}^{I}[\%]$	$\sigma^{I}[\%]$	$E_M^{I}[\%]$
$\mathcal{S}_{11}$ (case *a*)	2.07	0.91	7.65
$\mathcal{S}_{21}$ (case *b*)	2.15	0.92	6.80
Dataset	$\bar{E}^{\Delta}[\%]$	$\sigma^{\Delta}[\%]$	$E_M^{\Delta}[\%]$
$\mathcal{S}_{11}$ (case *a*)	2.60	2.36	17.04
$\mathcal{S}_{21}$ (case *b*)	2.56	2.17	13.36
IUT #2 (DO3316T-103)			
Dataset	$\bar{E}^{\Psi}[\%]$	$\sigma^{\Psi}[\%]$	$E_M^{\Psi}[\%]$
$\mathcal{S}_{12}$ (case *a*)	2.24	0.30	4.20
$\mathcal{S}_{22}$ (case *b*)	2.33	0.33	4.65
Dataset	$\bar{E}^{I}[\%]$	$\sigma^{I}[\%]$	$E_M^{I}[\%]$
$\mathcal{S}_{12}$ (case *a*)	3.44	1.41	11.36
$\mathcal{S}_{22}$ (case *b*)	3.59	1.55	12.13
Dataset	$\bar{E}^{\Delta}[\%]$	$\sigma^{\Delta}[\%]$	$E_M^{\Delta}[\%]$
$\mathcal{S}_{12}$ (case *a*)	3.54	3.49	21.73
$\mathcal{S}_{22}$ (case *b*)	4.02	3.33	20.77

losses $P_{tot,k}$ (corresponding to w_k) in Eq. (6.5). The resulting arctangent functions for the two inductors are shown in Fig. 6.4, for all the 880 operating conditions. The shape of the inductance curve of the two inductors is quite different because of the differ-

Table 6.4: Identified coefficient vectors x^*

IUT	x^*
#1	$[10.48\mu\text{H},\ 1.02\mu\text{H},\ 1.54\text{A}^{-1},\ -1.52\text{AW}^{-1},\ 8.78\text{A}]$
#2	$[8.93\mu\text{H},\ 1.73\mu\text{H},\ 6.94\text{A}^{-1},\ -1.02\text{AW}^{-1},\ 4.48\text{A}]$

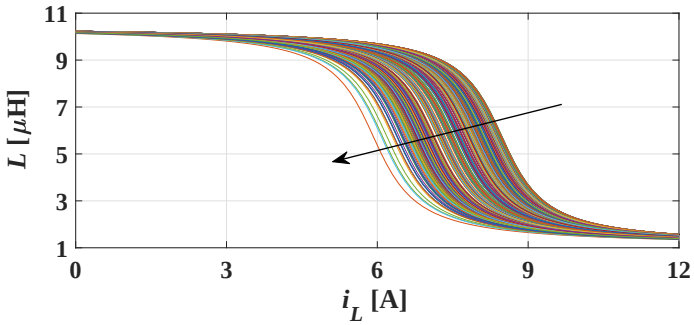

(a)

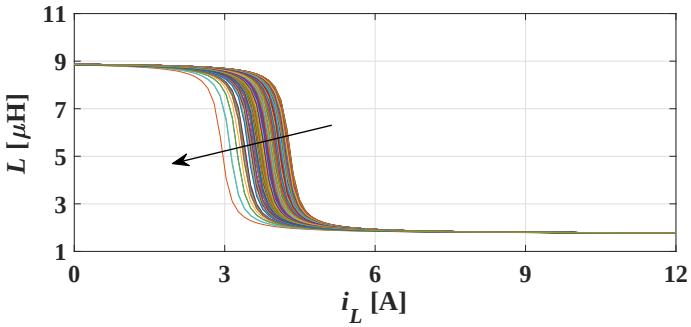

(b)

Figure 6.4: Family of arctangents for IUT #1 (a) and #2 (b). The arrows indicate the increasing direction of P_{tot}.

ent core. It is worth remarking that the L_{nom} value declared in the components datasheet is usually subjected to about 10%-20% uncertainty. For instance, Fig. 6.4(b) points out that the real inductance of DO3316T-103 inductor for low currents is about 9μH, whereas the nominal inductance is 10μH.

Fig. 6.5 shows the experimental flux linkage Ψ *versus* the current i_L (green dashed lines), obtained in the test conditions summarized in Table 6.5 for the two investigated FPIs. Such tests include low and high switching frequency values, as well as low and high output current values. The plots also show the analytical

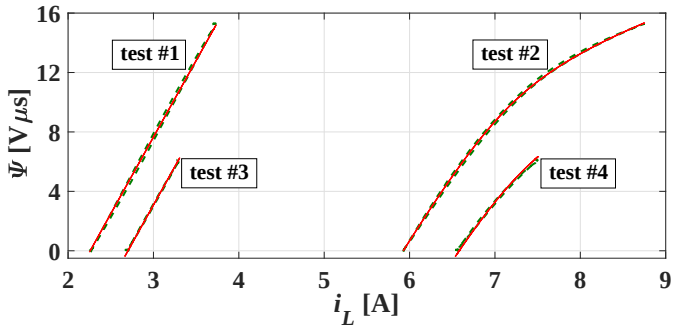

(a)

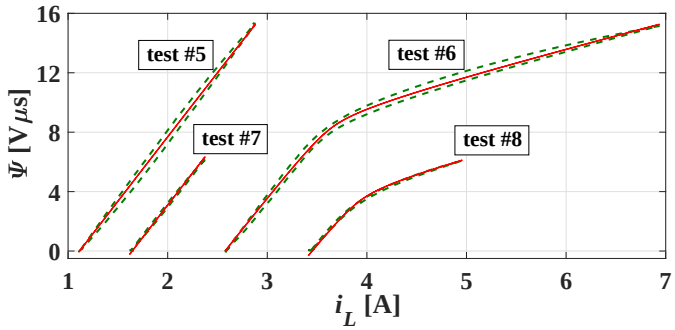

(b)

Figure 6.5: Experimental flux linkage Ψ *vs* i_L (green dashed lines) and analytical flux linkage $\hat{\Psi}$ *vs* i_L (red lines) for IUT #1 (a) and IUT #2 (b).

Table 6.5: Test conditions: $V_{in} = 12$ V, $D = 0.5$

IUT #1 (MSS1260-103)			IUT #2 (DO3316T-103)		
$Test$ #	f_s $[kHz]$	I_{out} $[A]$	$Test$ #	f_s $[kHz]$	I_{out} $[A]$
1	200	3	5	200	2
2	200	7	6	200	4
3	500	3	7	500	2
4	500	7	8	500	4

flux linkage $\hat{\Psi}$ *versus* the current i_L (red lines), obtained by using Eq. (6.7) and the coefficient vectors x^* given in Table 6.4. For both experimental and analytical flux linkage, it has been assumed $\Psi(t_0) = 0$, since the experimental measurements of the flux linkage have not been carried out, and only inductor voltage and current measurements have been instead performed. The analytical flux linkage $\hat{\Psi}$ fits very well the experimental one for all the analyzed tests. It is worth noting that the experimental hysteresis loops are larger for IUT #2 than for IUT #1: this partially justifies the fact that the model accuracy is lower for IUT #2 than for IUT #1 (see Table 6.3).

The errors E_k^{Ψ} *versus* power losses P_{tot} are shown in Fig. 6.6, for the two analyzed inductors. The results highlight that the proposed model provides a good fitting accuracy over a wide range of operating conditions, even by determining the model parameters (6.5) over a limited set of conditions with large average currents and peak-to-peak current ripples.

6.4.1 SMPS Circuit Simulations

The results of circuit simulations obtained in PSIM by using the proposed model have been eventually compared with experimental measurements, in order to validate the accuracy of the inductance modeling approach. The open-loop buck topology has been implemented in PSIM. At operating condition w_k, the zero-order-hold

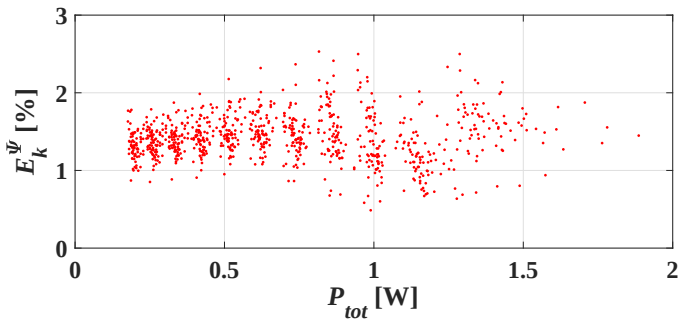

(a)

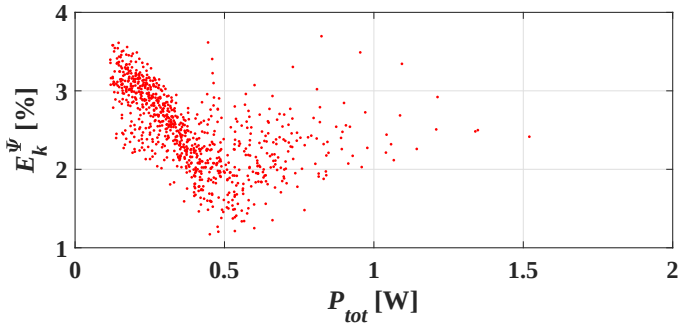

(b)

Figure 6.6: Error E_k^{Ψ} *vs* power losses P_{tot} obtained with the power-loss-dependent inductance model for IUT #1 (a) and IUT #2 (b).

discretization of Eq. (6.9) yields

$$\hat{i}_{L,k}(t_{n+1}) = \hat{i}_{L,k}(t_n) + \frac{(t_{n+1} - t_n)\hat{v}_{L,k}(t_n)}{L(\hat{i}_{L,k}(t_n), P_{tot,k})} \tag{6.15}$$

In particular, the inductor has been implemented in PSIM as a *current-controlled current-source*, whose driving signal is the result of the right-hand-side part of Eq. (6.15), run-time computed by means of a C-block. The inputs to the C-block are:

- the SMPS operating condition $w_k = [V_{in}, I_{out}, f_s, D]$;
- the optimal coefficient vector x^* (listed in Table 6.4);

- the coefficients R_{dc} and $\{b_0, ..., b_3\}$ (listed in Tables 6.1, 5.12 and 5.18);
- the thermal resistance R_{th} (provided in Section 6.3);
- the samples of the simulated inductor voltage $\hat{v}_{L,k}(t_n)$ and current $\hat{\hat{i}}_{L,k}(t_n)$.

The C-block estimates the inductor power losses $\hat{P}_{tot,k}$ through Eq.s (5.11) and (5.25), which is used to compute I_L^* through Eq. (6.5). The inductance is evaluated by means of Eq. (6.4) for $\hat{\hat{i}}_{L,k}(t_n)$ and $\hat{P}_{tot,k}$. Then, the C-block generates the inductor current sample $\hat{\hat{i}}_{L,k}(t_{n+1})$ based on Eq. (6.15). Moreover, the temperature rise $\hat{T}_{\Delta,k}$ is estimated by means of Eq. (6.1), using $\hat{P}_{tot,k}$ and R_{th}.

The tests conditions summarized in Table 6.5 have been adopted in PSIM. The SMPS simulations have been performed with a constant sampling time of 10 ns for both IUT #1 and #2, and validated by comparison with the experimental inductor current waveforms measured by the MADMIX system. For each test, Table 6.6 summarizes the corresponding measured and estimated inductor power losses and temperature rise, and the errors E_k^I, E_k^Δ, E_k^P, E_k^T, where E_k^P and E_k^T are the power losses and temperature rise errors, defined as follows:

$$E_k^P = 100\frac{|\hat{P}_{tot,k} - P_{tot,k}|}{P_{tot,k}} \tag{6.16}$$

$$E_k^T = 100\frac{|\hat{T}_{\Delta,k} - T_{\Delta,k}|}{T_{\Delta,k}} \tag{6.17}$$

For the given operating conditions, the adopted loss model is able to estimate $\hat{P}_{tot,k}$ with the errors E^P lower than 1.1% for IUT #1 and 6% for IUT #2. Also the experimental and estimated temperature rise values are in good agreement, with errors E^T lower than about 11% and 14%, for IUT #1 and #2 respectively. For both inductors, the resulting errors on current E^I and peak-to-peak ripple E^Δ are generally lower than 5% and 10%, respectively. A comparison between the measured inductor current waveforms

Table 6.6: PSIM simulations *vs* experimental data

IUT #1 (MSS1260-103)								
$Test$ #	P_{tot} $[W]$	$\hat{P}_{tot}$ $[W]$	T_Δ $[^\circ C]$	$\hat{T}_\Delta$ $[^\circ C]$	E^P [%]	E^T [%]	E^I [%]	E^Δ [%]
1	0.293	0.296	9.3	10.3	1.1	10.8	2.6	2.5
2	1.103	1.091	38.4	38.2	1.1	0.5	2.9	8.2
3	0.214	0.215	7.4	7.5	0.3	1.4	2.4	0.2
4	1.033	1.031	36.1	36.1	0.3	$\sim$0	3.1	1.6
IUT #2 (DO3316T-103)								
$Test$ #	P_{tot} $[W]$	$\hat{P}_{tot}$ $[W]$	T_Δ $[^\circ C]$	$\hat{T}_\Delta$ $[^\circ C]$	E^P [%]	E^T [%]	E^I [%]	E^Δ [%]
5	0.349	0.341	13.2	14.9	2.1	12.9	3.2	0.4
6	0.920	0.975	37.8	42.5	6.0	12.4	4.6	3.7
7	0.188	0.185	7.1	8.1	1.7	14.1	3.2	5.0
8	0.534	0.527	22.9	23.0	1.3	0.4	3.8	3.4

(green) and PSIM simulations (red) is shown in the left panels of Figs. 6.7 and 6.8. In the right panels of the same figures, the inductance *versus* current curves (gray) and the curve portions covered by the simulations (red) are also plotted. It is worth remarking that operating conditions leading to an inductance decrease higher than 50% (*e.g.*, the case shown in Fig. 6.7(d)) have been considered to highlight the reliability of the modeling approach. In real-world SPMS applications, such extreme conditions are avoided for safety and efficiency reasons.

The main outcome of the research activity presented in this Chapter resulted in the publication of the scientific paper:

- A. Oliveri, G. Di Capua, K. Stoyka, M. Lodi, M. Storace, N. Femia, "A Power-Loss-Dependent Inductance Model for Ferrite-Core Power Inductors in Switch-Mode Power Supplies", *IEEE Transactions on Circuits and Systems I: Regular Papers*, doi: 10.1109/TCSI.2018.2889856.

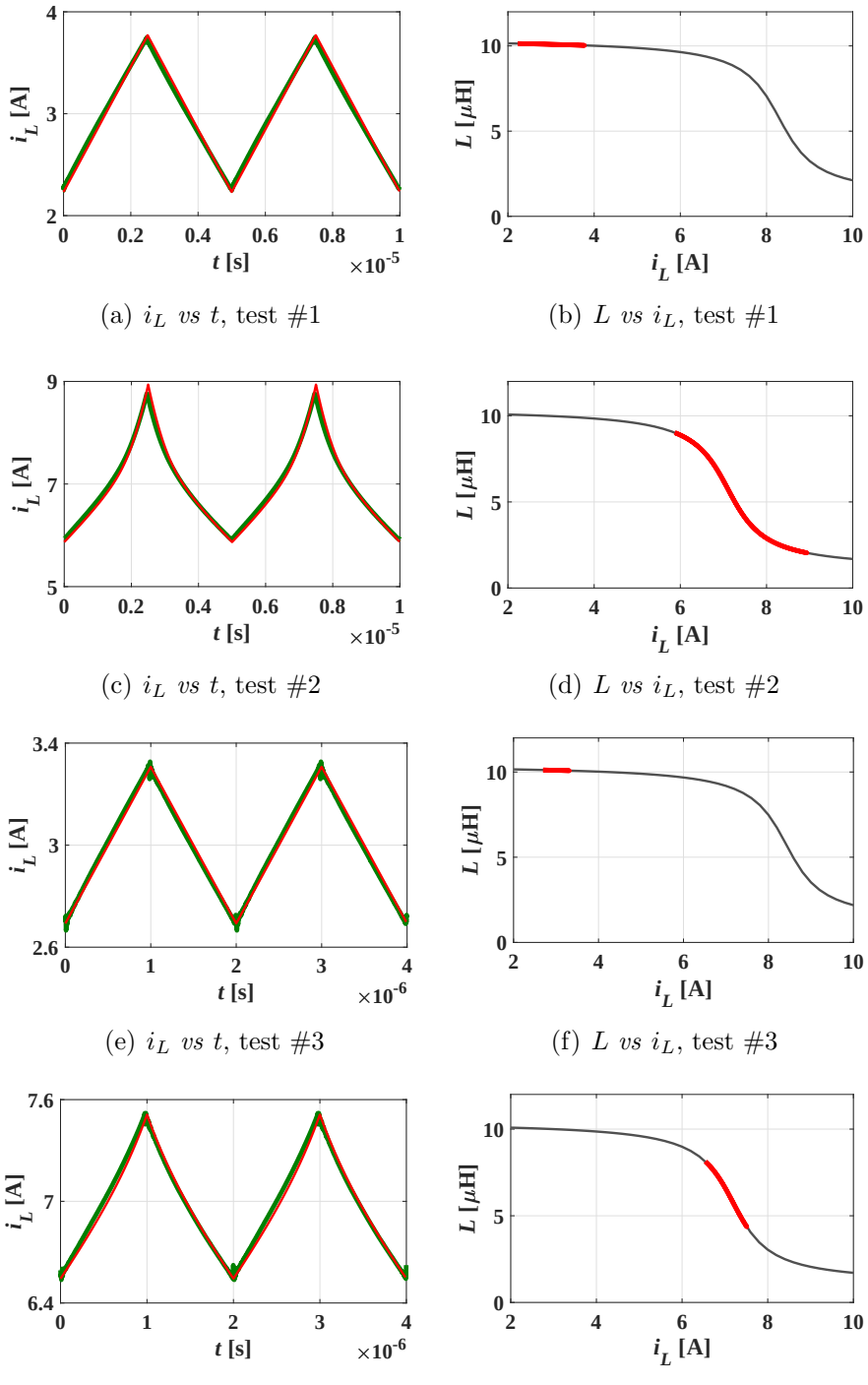

(a) i_L *vs* t, test #1

(b) L *vs* i_L, test #1

(c) i_L *vs* t, test #2

(d) L *vs* i_L, test #2

(e) i_L *vs* t, test #3

(f) L *vs* i_L, test #3

(g) i_L *vs* t, test #4

(h) L *vs* i_L, test #4

Figure 6.7: MSS1260-103 inductor. Left: experimental inductor current waveforms (green) *vs* PSIM simulations (red). Right: simulated inductance *vs* current curves (gray) and regions covered by current ripple (red).

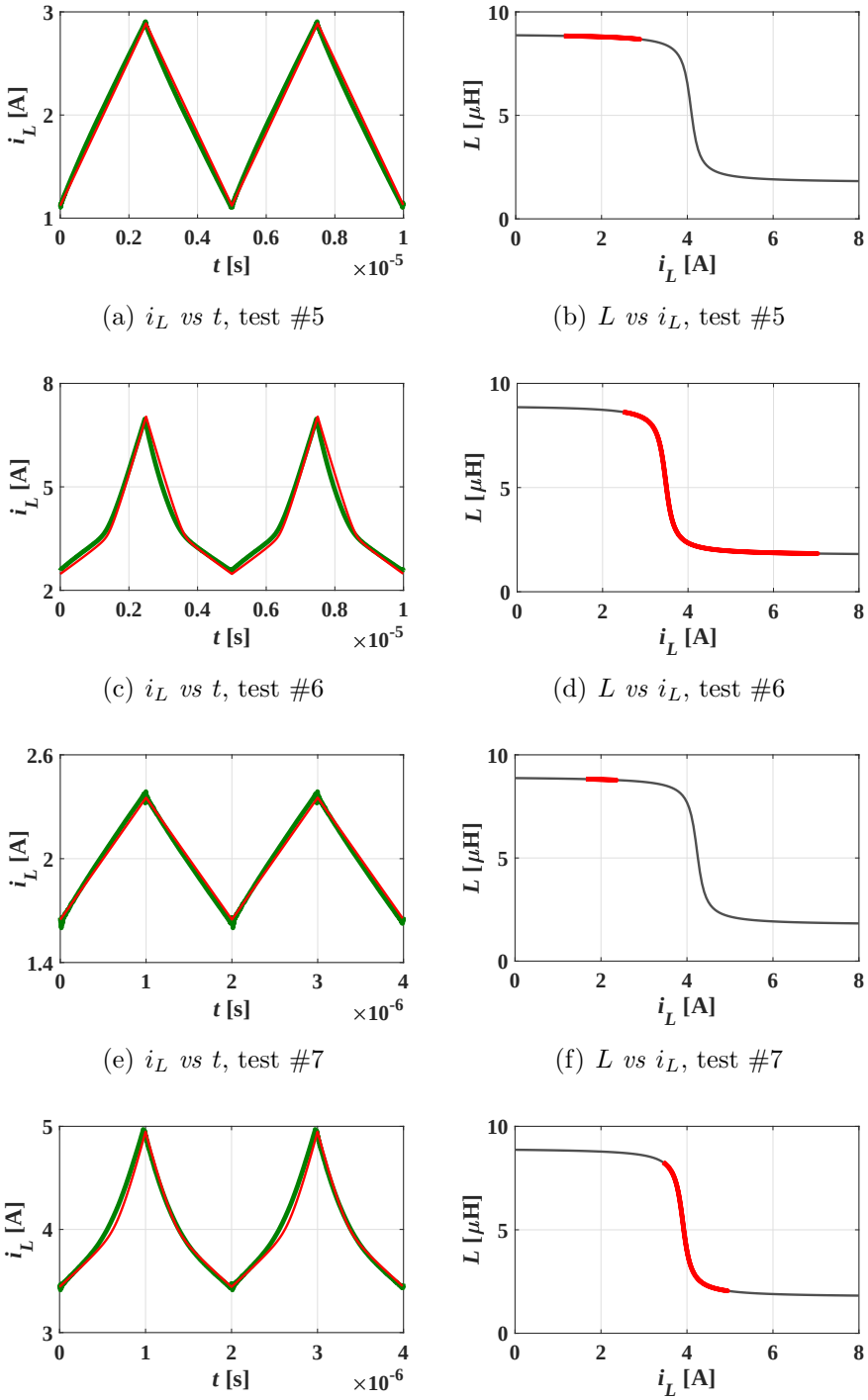

(a) i_L *vs* t, test #5

(b) L *vs* i_L, test #5

(c) i_L *vs* t, test #6

(d) L *vs* i_L, test #6

(e) i_L *vs* t, test #7

(f) L *vs* i_L, test #7

(g) i_L *vs* t, test #8

(h) L *vs* i_L, test #8

Figure 6.8: DO3316T-103 inductor. Left: experimental inductor current waveforms (green) *vs* PSIM simulations (red). Right: simulated inductance *vs* current curves (gray) and regions covered by current ripple (red).

Conclusions and Future Developments

In this dissertation, a variety of numerical techniques and advanced algorithms has been investigated and discussed, with the purpose of bringing innovation in the design of power supply systems, which are pervasive in all the spheres of everyday life. Thanks to the use of such innovative techniques, it is possible to reduce the size of the Switch-Mode Power Supplies (SMPSs) exploiting a smart use of Ferrite Power Inductors (FPIs) in moderate and controlled saturation. In particular, this dissertation has discussed innovative solutions to the problems of the high-power-density SMPS design, including:

a) development of numerical techniques and intelligent algorithms for generation and discovery of behavioral models for saturation and power losses of FPIs used in SMPS applications;

b) development of enhanced numerical algorithms, using the above models, able to reliably predict the FPIs behavior under given SMPS conditions;

c) development of enhanced numerical algorithms able to identify feasible inductor solutions, possibly operating in saturation, allowing to reduce the inductor size and increase the converter power density.

The starting point of this dissertation has been to extend the results of the prior studies which introduced a behavioral *arctangent-*

based model of the inductance *versus* current (L *vs* i_L) characteristic for FPIs and a numerical algorithm for inductor current reconstruction in Continuous Conduction Mode (CCM). In particular, the validity of such model and algorithm has been extended to High Current Ripple (HCR) inductor operation, which may involve negative inductor currents in synchronous-rectification converter topologies and Discontinuous Conduction Mode (DCM) in diode-rectification topologies. The developed generalized saturation model and numerical algorithm are able to reliably reconstruct the inductor saturation characteristic and resulting current wave-shape in whatever operating condition, including saturation, and can be applied to different conduction modes and converter topologies. The saturation arctangent model, valid for FPIs with a fixed air-gap, has also been extended to a *double-arctangent* model, which accurately describes the L *vs* i_L characteristic of FPIs with a stepped air-gap. The inductor current reconstruction algorithm has been adapted to such extended model, to reliably predict the magnitude of inductor current ripple of stepped air-gap inductors.

In order to obtain realistic L *vs* i_L data needed for a reliable inductor current reconstruction in saturation, the Evolutionary Algorithm-based approach for saturation curves identification has been proposed in this dissertation, starting from the experimental measurements of inductor current waveforms and operating temperatures under real SMPS conditions. An alternative approach has also been presented, based on the local and global approximations of the inductor saturation characteristic, obtained under small-amplitude and large-amplitude current ripple conditions, respectively. For both approaches, the identified temperature-dependent L *vs* i_L curves allow achieving much more realistic predictions of the inductor current ripple compared to the predictions obtained with the manufacturers' L *vs* i_L data.

Subsequently, a Sustainable Saturation Operation (SSO) of FPIs has been investigated. The SSO-analysis algorithm has been developed, which identifies SSO-compliant FPIs with minimum size and volume, given the SMPS specifications about the allowed power losses, temperature rise and peak-to-peak current ripple of

the inductor. The experimental results have proved that SSO-compliant inductors allow to increase the SMPS power density while preserving the overall converter efficiency.

Eventually, behavioral models for the total power losses and *AC* power losses of FPIs have been developed by means of a Genetic Programming (GP) algorithm, starting from the experimental inductor power loss measurements performed on a wide range of SMPS operating conditions. The identified GP-based models provide more accurate power loss predictions, especially in saturation, compared to the classical formulas adopted by manufacturers. Based on the identified power loss models, a novel *power-loss-dependent* saturation model has been proposed, providing the inductance as an arctangent function of the current, parameterized with respect to the inductor total power losses. This way, the saturation model does not depend on the inductor temperature, which cannot be considered as a real model input but rather an output, representing the response of the device to given ambient temperature and total power losses.

The developed behavioral models and numerical algorithms have been successfully applied to several commercial FPIs, characterized by different nominal inductances and dimensions, as well as different magnetic materials and core types. The future developments of this dissertation will address:

a) investigation and use of numerical techniques for on-line parameter tuning of the behavioral saturation and loss models, in order to take into account the inductor ageing;

b) investigation of inductor saturation impact on current limiting and control techniques;

c) development of behavioral models and numerical algorithms for the analysis of power inductors realized with different magnetic core materials (e.g., powdered iron, metal alloys) and integrated inductors.

Appendix A

Classical Core Loss Models

A.1 Steinmetz Equation *versus* Manufacturer's Core Loss Formula

According to the SE, average core loss is given by (5.5). According to the manufacturer's core loss formula, average core loss can be expressed as given in (5.6). In order to find the equivalence relations between the Steinmetz coefficients $\{C_m,\ \alpha,\ \beta\}$ and the manufacturer's coefficients $\{K_1,K_2,X,Y\}$, (A.1) and (A.2) can be used:

$$v_L(t) = L[i_L(t)]\frac{di_L(t)}{dt} \tag{A.1}$$

$$v_L(t) = n\frac{d\Phi(t)}{dt} = nA_e\frac{dB(t)}{dt} \tag{A.2}$$

where n is the inductor winding turn number and Φ is the magnetic flux linked to a single winding turn. From the equality of (A.1) and (A.2), it follows:

$$\begin{aligned} &\int_0^{DT_s} L[i_L(t)]\frac{di_L(t)}{dt}dt = \int_0^{DT_s} nA_e\frac{dB(t)}{dt}dt \\ \Rightarrow\quad &\int_{I_{L,min}}^{I_{L,max}} L(i_L)di_L = \int_{B_{min}}^{B_{max}} nA_e dB \end{aligned} \tag{A.3}$$

where $I_{L,min}$ and $I_{L,max}$ are the minimum and the maximum values of the inductor current waveform $i_L(t)$, whereas B_{min} and B_{max} are the minimum and maximum values of the magnetic flux density waveform $B(t)$. In weak saturation, $L(i_L) = L_{nom}$. This condition is normally adopted for core loss modeling by manufacturers. Thus, (A.3) implies (A.4):

$$\begin{aligned} & L_{nom}\Delta i_{Lpp} = 2nA_eB_{ac} \\ \Rightarrow \quad & B_{ac} = \frac{L_{nom}}{2nA_e}\Delta i_{Lpp} = K_2\Delta i_{Lpp} \end{aligned} \tag{A.4}$$

From (5.5), (5.6) and (A.4), the following equivalences can be eventually derived:

$$K_1 = C_mA_el_e, \quad K_2 = \frac{L_{nom}}{2nA_e}, \quad X = \alpha, \quad Y = \beta \tag{A.5}$$

A.1.1 Manufacturer's Formula Coefficients Identification

The coefficients of the manufacturer's core loss formula (5.6) have been herein estimated by means of the NLLS curve fitting of the experimental AC power loss in weak-saturation region, by means of the AC loss model (A.6):

$$P_{ac} = R_{ac} \cdot I_{ac,rms}^2 + K \cdot f_s^X \Delta i_{Lpp}^Y \tag{A.6}$$

where X, Y and $K = K_1K_2^Y$ have been adopted as unknowns during the coefficients identification procedure. The AC winding loss, represented by the first additive term in formula (A.6), has been evaluated by using measured R_{dc} and $I_{ac,rms}$ values. The values of the coefficients $\{K, X, Y\}$, obtained for the inductors investigated in this work, are provided in Table A.1. These same coefficients have also been adopted to evaluate the i-GSE-based core loss of the analyzed devices, as discussed in the following Subsection.

Table A.1: Identified core loss coefficients for analyzed inductors

Part Number	K	X	Y
MSS7341-183	1.14E-03	0.95	2.23
MSS7341-153	1.28E-03	0.93	2.20
MSS1260-103	8.88E-04	0.77	2.02
MSS1260-473	2.19E-03	0.87	2.11
MSS1038-273	3.50E-04	1.17	2.23
DO3316T-103	6.27E-03	0.50	1.91

A.2 *Improved* Generalized Steinmetz Equation (*i*-GSE)

According to the i-GSE [51], the average core loss is given as:

$$P_{core,iGSE} = \frac{1}{T_s}\int_0^{T_s} k_i \left|\frac{dB}{dt}\right|^{\alpha} |\Delta B|^{\beta-\alpha}\,(A_e l_e)\,dt \tag{A.7}$$

where $\Delta B = 2B_{ac}$ and

$$k_i = \frac{C_m}{(2\pi)^{\alpha-1}\int_0^{2\pi} |cos\theta|^{\alpha} 2^{\beta-\alpha} d\theta} \tag{A.8}$$

It can be shown that the integral term in (A.8) can be approximated as:

$$\int_0^{2\pi} |cos\theta|^{\alpha} d\theta \cong 4\left(0.2761 + \frac{1.7061}{\alpha + 1.354}\right) \tag{A.9}$$

The i-GSE can be re-formulated in terms of the applied inductor voltage, duty-cycle, frequency and manufacturer's core loss coefficients $\{K_1, K_2, X, Y\}$. From (A.2), the following relations can be obtained:

$$\Delta B = \int_0^{DT_s} \frac{v_L(t)}{nA_e} dt = \frac{V_{Lr}}{nA_e} DT_s = \frac{2K_2}{L_{nom}} V_{Lr} DT_s \tag{A.10}$$

$$\frac{dB}{dt} = \frac{v_L(t)}{nA_e} = \frac{2K_2}{L_{nom}} v_L(t) \tag{A.11}$$

where V_{Lr} is the constant voltage applied to the inductor during the rise-time interval of the inductor current. Hence, from (A.7), (A.10) and (A.11), we have:

$$P_{core,iGSE} = \frac{k_v}{T_s} \int_0^{T_s} \left| \frac{2K_2 v_L(t)}{L_{nom}} \right|^X \left| \frac{2K_2 V_{Lr} D T_s}{L_{nom}} \right|^{Y-X} dt \tag{A.12}$$

where:

$$k_v = k_i (A_e l_e) = \frac{K_1}{(2\pi)^{X-1} \int_0^{2\pi} |cos\theta|^X 2^{Y-X} d\theta} \tag{A.13}$$

By means of algebra, we obtain:

$$\begin{aligned} P_{core,iGSE} &= f_s k_v \left(\frac{2K_2}{L_{nom}} \right)^Y (V_{Lr} D T_s)^{Y-X} \int_0^{T_s} |v_L(t)|^X dt = \\ &= k_v \left(\frac{2K_2}{L_{nom}} \right)^Y \left(\frac{V_{Lr} D}{f_s} \right)^{Y-X} \left[D |V_{Lr}|^X + (1-D) |V_{Lf}|^X \right] \end{aligned} \tag{A.14}$$

where V_{Lf} is the constant voltages applied to the inductor during the fall-time interval of the inductor current. In such reformulation, the i-GSE jointly depends on the applied inductor voltages, duty-cycle and frequency, and manufacturer's core loss coefficients $\{K_1, K_2, X, Y\}$.

If the coefficients $\{K, X, Y\}$ are instead available (e.g., from the identification procedure described in the previous Section), the i-GSE can be alternatively formulated as follows:

$$\begin{aligned} P_{core,iGSE} &= f_s k_v^* \left(\frac{2}{L_{nom}} \right)^Y (V_{Lr} D T_s)^{Y-X} \int_0^{T_s} |v_L(t)|^X dt = \\ &= k_v^* \left(\frac{2}{L_{nom}} \right)^Y \left(\frac{V_{Lr} D}{f_s} \right)^{Y-X} \left[D |V_{Lr}|^X + (1-D) |V_{Lf}|^X \right] \end{aligned} \tag{A.15}$$

where:

$$k_v^* = k_v \cdot K_2^Y = \frac{K}{(2\pi)^{X-1} \int_0^{2\pi} |cos\theta|^X 2^{Y-X} d\theta} \tag{A.16}$$

Appendix B

Multi-Objective Optimization

This Appendix provides a theoretical description of the multi-objective optimization technique adopted in this dissertation for the inductor power loss behavioral modeling. Said technique is out of the scope of this study and only its main theoretical aspects are herein discussed for the sake of completeness and Reader's convenience.

B.1 Multi-Objective Optimization Problem (MOOP)

A Multi-Objective Optimization Problem (MOOP) has a number of objective functions which are to be maximized or minimized. Moreover, the MOOP usually contains a number of constraints, such as equality and inequality constraints and variable bounds, which must be satisfied by any feasible solution [73]. In general, the multi-objective optimization problem can be formulated as given in (B.1).

$$\begin{aligned} &\text{Minimize/Maximize} && f_m(\mathbf{x}), && m = 1, 2, ..., M; \\ &\text{subject to} && \begin{cases} g_j(\mathbf{x}) \geq 0, & j = 1, 2, ..., J; \\ h_k(\mathbf{x}) = 0, & k = 1, 2, ..., K; \\ x_i^{LB} \leq x_i \leq x_i^{UB}, & i = 1, 2, ..., n. \end{cases} \end{aligned} \tag{B.1}$$

A solution $\mathbf{x}$ is a vector of n decision variables: $\mathbf{x} = [x_1, x_2, ..., x_n]^T$. The last set of constraints in (B.1) are called variable bounds, restricting each decision variable x_i value to be comprised between a Lower Bound (LB), namely x_i^{LB}, and an Upper Bound (UB), namely x_i^{UB}. These bounds delimit a *decision variable space* $\mathcal{D}$, or simply the decision space. If any solution $\mathbf{x}$ satisfies all constraints and variable bounds, it is known as a *feasible solution*. The set of all feasible solutions is called the *feasible region* $\mathcal{S}$, sometimes referred to as simply the search space. The formulation (B.1) considers M objective functions which can be either minimized or maximized: $\mathrm{f}(\mathbf{x}) = [f_1(\mathbf{x}), f_2(\mathbf{x}), ..., f_M(\mathbf{x})]^T$. In the context of optimization, a maximization problem can be converted into a minimization one by multiplying the objective function by -1.

B.2 Pareto-Optimal Front

Let us consider a MOOP with two objectives which are to be minimized (*Objective* 1 and *Objective* 2). Any two solutions can be taken from the feasible objective space and compared. For some pairs of solutions, it can be observed that one solution is better than the other in both objective. For certain other pairs, it can be observed that one solution is better than the other in one objective, but is worse in the second objective. Hence, none of these two solutions can be said to outperform the other with respect to both objectives. When this happens between two solutions, they are called *non-dominated* solutions. Fig. B.1 is drawn with many such solutions and four of these solutions (marked A to D) are highlighted. For clarity, all the non-dominated solutions are joined

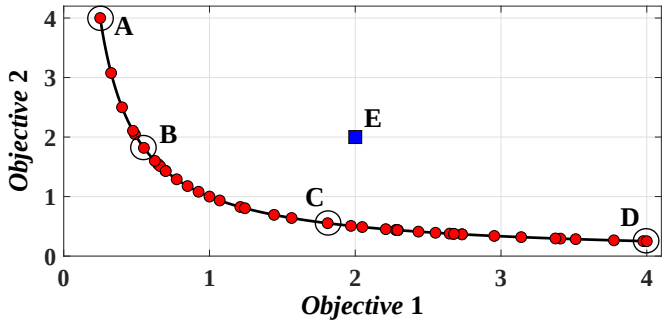

Figure B.1: Pareto-optimal front.

with a curve in the figure. All the solutions lying on this curve are called *Pareto-optimal* solutions, while the curve itself is known as a *Pareto-optimal front*. For problems where all objectives are to be minimized, this front lies in the bottom-left corner of the search space.

It is worth noting that the feasible objective space not only contains Pareto-optimal solutions, but also solutions that are not optimal. For instance, comparing solution E of Fig. B.1 with solution C, it can be observed that the latter outperforms the solution E in both objectives. When this happens, solution E is said to be *dominated* by solution C. There exist many such solutions in the search space, which can be dominated by at least one solution from the Pareto-optimal set. On the other hand, comparing solutions D and E, it can be observed that solution D is better in the second objective but is worse in the first objective compared to solution E. Thus, in the absence of solutions A, B, C, and any other non-dominated solution, one would be tempted to put solution E in the same group with solution D. However, the presence of solution C establishes the fact that solutions C and D are non-dominated with respect to each other, while solution E is dominated solution. Thus, the non-dominated set must be collectively compared with any solution $\mathbf{x}$ for establishing whether the latter solution belongs to the non-dominated set or not. Specifically, the following two conditions must be true for a non-dominated set P_1:

1. Any two solutions of P_1 must be non-dominated with respect to each other.
2. Any solution not belonging to P_1 is dominated by at least one member of P_1.

So far, for simplicity, a two-objective optimization problem has been considered (*Objective* 1 and *Objective* 2 to be minimized). In the case of MOOP the concept of domination can be expressed as follows: a solution $\mathbf{x}^{(1)}$ is said to dominate the other solution $\mathbf{x}^{(2)}$ if both conditions 1 and 2 are true:

1. The solution $\mathbf{x}^{(1)}$ is no worse than $\mathbf{x}^{(2)}$ in all objectives.
2. The solution $\mathbf{x}^{(1)}$ is strictly better than $\mathbf{x}^{(2)}$ in at least one objective.

In the presence of multiple Pareto-optimal solutions, it is difficult to prefer one solution over the other without any further information about the problem. Accordingly, all Pareto-optimal solutions are equally important to the user. Hence it is important to find as many Pareto-optimal solutions as possible. Thus, it is possible to define two goals in a multi-objective optimization:

1. To find a set of solutions as close as possible to the Pareto-optimal front.
2. To find a set of solutions as *diverse* as possible. In addition to being converged close to the Pareto-optimal front, they must also be sparsely spaced in the Pareto-optimal region. Only with a diverse set of solutions, can one be assured of having a good set of trade-off solutions among objectives.

B.3 Non-Dominated Sorting of a Population

B.3.1 Finding a Non-Dominated Set

In the context of the multi-objective optimization, many approaches have been suggested for finding the non-dominated set from a given

population of solutions. Although many approaches are possible, they would usually have different computational complexities. The most computationally efficient method is presented next.

As a first step, the population is sorted according to the descending order of importance to the first objective function value. Thereafter, the population is recursively halved as top (T) and bottom (B) subpopulations. Knowing that the top-half of the population is better in terms of the first objective function, the bottom-half is then checked for domination with the top-half. The solutions of B that are not dominated by any member of T are combined with members of T to form a merged population. The merging and the domination check starts with the innermost case (when there is only one member left in either T or B in recursive divisions of the population) and then proceeds in the bottom-up fashion. This approach can be divided in two steps:

1. The initial population is sorted according to the descending order of importance in the first objective function and renamed as P of size N.
2. Recursion function: if the size of P is one, the function returns P as the output (it is not possible to halve it anymore in T and B). Otherwise, the function halves the population in T and B parts (where T is better than B with respect to the first objective function, thanks to the sorting performed at step 1) and recalls the recursive function applied to T and B population parts. As a result, only non-dominated solutions of T and B are returned as the outputs of the recursive function. Now, if the i-th non-dominated solution of B is not dominated by any non dominated-solution of T, the function creates a merged set $M = T \cup \{i\}$. This check is then repeated for each non-dominated solution of B. In the end, the function returns the merged set M as its output.

B.3.2 Non-Dominated Sorting

Most evolutionary multi-objective optimization algorithms require us to find only the best non-dominated front in a population.

These algorithms classify the population into two sets — the non-dominated set and the remaining dominated set. However, there exist some algorithms which require the entire population to be classified into various non-domination levels. In such algorithms, the population needs to be sorted according to an ascending level of non-domination. The best non-dominated solutions are called non-dominated solutions of *Level* 1. In order to find solutions for the next level of non-domination, there is a simple procedure which is usually followed. Once the best non-dominated set is identified, it is temporarily disregarded from the population. The non-dominated solutions of the remaining population are then found and called non-dominated solutions of *Level* 2. In order to find the non-dominated solutions of *Level* 3, all non-dominated solutions of *Level* 1 and 2 are disregarded and new non-dominated solutions are found. This procedure is continued until all population members are classified into a non-domination level.

In order to illustrate a non-dominated sorting of a population, the case of two objective minimization problem will be referred to once again (see Fig. B.1). So far only Pareto-optimal front has been considered (that drawn in the figure), which contains only the best non-dominated solutions, those of *Level* 1 of the non-dominated sorting. In Fig. B.2, together with the *Level* 1 solutions, the other non-domination levels are shown (*Level* 2 and *Level* 3).

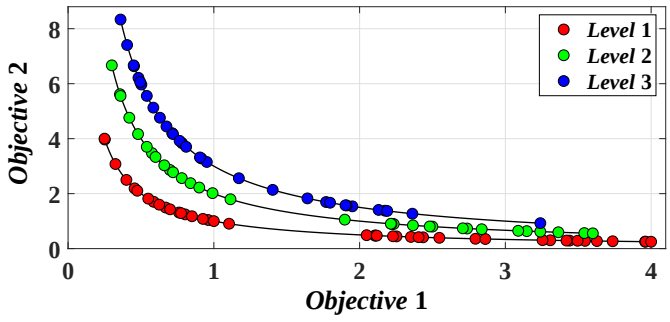

Figure B.2: Non-dominated sorting of a population.

B.4 Elitist Non-Dominated Sorting Genetic Algorithm

An elitist Non-Dominated Sorting Genetic Algorithm (or NSGA-II) is the most popular MOO algorithm proposed by Kalyanmoy Deb in 2000. In NSGA-II, initially, a random population P_0 of size N is created. The population is sorted into different non-domination levels. Each solution is assigned a fitness equal to its non-domination rank (non-domination level), thus assuming minimization of the fitness function. Binary tournament selection, recombination and mutation operators are used to create an offspring population Q_0 of size N. In particular, a *crowded tournament selection operator* is adopted to determine the best individuals to become parents for offspring generation. Such operator compares two randomly selected solutions, i and j, and returns the winner of the tournament on the basis of two attributes, such as a non-domination rank (r) and a local crowding distance (d, defined next) of a solution in the population. A solution i wins a tournament with a solution j if any of the following conditions is true:

1. Solution i has a better rank, that is, $r_i < r_j$.

2. The two solutions have the same rank but solution i has a better crowding distance than solution j, that is, $r_i = r_j$ and $d_i > d_j$.

The crowding distance d_i of a solution i is a measure of the search space around i which is not occupied by any other solution in the population. In particular, d_i is evaluated as the average distance of two neighboring solutions on the either side of solution i along each of the objectives. In Fig. B.3, the crowding distance of the i-th solution is the average side-length of the cuboid (shown by a dashed box) formed by using the nearest neighbors as vertices. As to the boundary solutions at the front extremes, their crowding distance is assumed to be infinite.

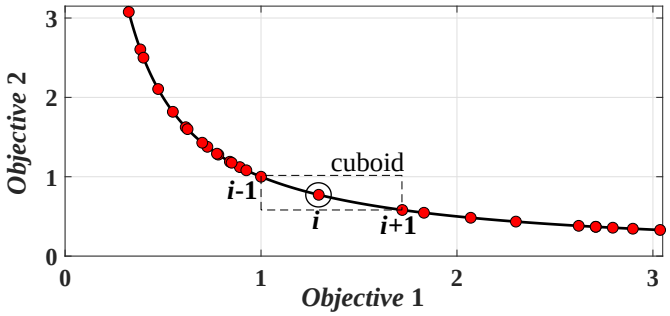

Figure B.3: Crowding distance for i-th solution.

B.4.1 NSGA-II Procedure

At each t-th generation of NSGA-II, once the offspring population Q_t is created by using the parent population P_t (by means of selection, crossover and mutation operators described earlier), the two populations are combined together to form R_t of size $2N$. Then, a non-dominated sorting is used to classify the entire population R_t. Once the non-dominated sorting is over, the new population is filled by solutions of different non-dominated fronts, one at a time. The filling starts with the best non-dominated front and continues with solutions of the second non-dominated front, followed by the third non-dominated front, and so on. Since the overall population size of R_t is $2N$, not all fronts can be accommodated in N slots available in the new population. All fronts which could not be accommodated are simply deleted. When the last allowed front is being considered, there may exist more solutions in the last front than the remaining slots in the new population. This scenario is illustrated in Fig. B.4. Instead of arbitrarily discarding some members from the last front, the strategy is usually adopted to choose those members of the last front which reside in the least crowded region in that front. Such strategy does not affect the proceedings of the algorithms much in the early stages of evolution. This is because, early on, there exist many fronts in the combined population. It is likely that solutions of many good non-dominated fronts are already included in the new population,

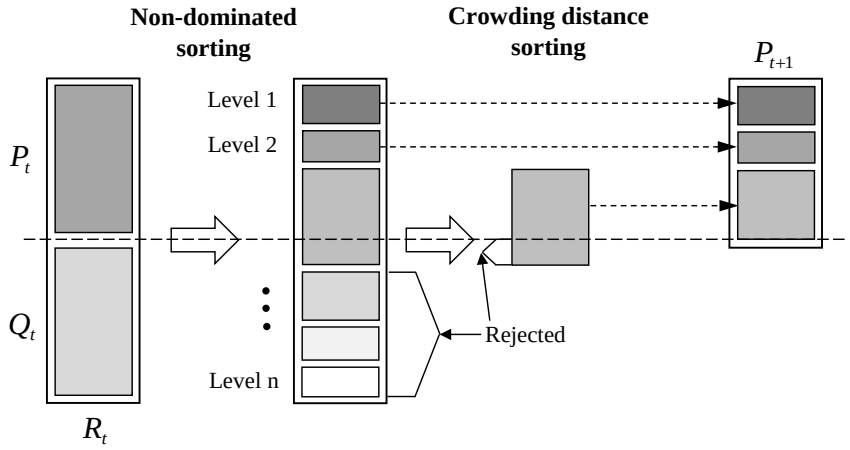

Figure B.4: Schematic of the NSGA-II procedure [73].

before they add up to N. It then hardly matters which solution is included to fill up the population. However, during the latter stages of the evolution, it is likely that most solutions in the population lie in the best non-dominated front. It is also likely that in the combined population R_t of size N, the number of solutions in the first non-dominated front exceeds N. The above algorithm then ensures that a diverse set of solutions will be chosen from this set. When the entire population converges to the Pareto-optimal front, the continuation of this algorithm will ensure a better spread among the solutions.

Summary of Publications

[1] G. Di Capua, N. Femia, K. Stoyka, "An Improved Algorithm for the Analysis of Partially Saturated Ferrite Inductors in Switching Power Supplies", *13th International Conference on Synthesis, Modeling, Analysis and Simulation Methods and Applications to Circuit Design (SMACD 2016)*, Lisbon (Portugal), June 2016.

[2] Giulia Di Capua, Nicola Femia, Kateryna Stoyka, "Power Magnetics Volume and Weight Reduction in Aerospace Power Supply Units", *17th Workshop on Control and Modeling for Power Electronics (COMPEL 2016)*, Trondheim (Norway), June 2016.

[3] G. Di Capua, N. Femia, M. Migliaro, K. Stoyka, "Genetic Programming Approach for Identification of Ferrite Inductors Power Loss Models", *42nd Annual Conference of IEEE Industrial Electronics Society (IECON 2016)*, Florence (Italy), October 2016.

[4] G. Di Capua, N. Femia, M. Migliaro, A. Rizzo, O. Sacco, D. Sannino, K. Stoyka, V. Vaiano, "Photocatalytic Reactor with Multiphase Digital Control of Luminous Radiation", *18th IEEE International Conference on Industrial Technology (ICIT 2017)*, Toronto (Canada), March 2017.

[5] G. Di Capua, N. Femia, K. Stoyka, "Validation of Inductors Sustainable-Saturation-Operation in Switching Power Supplies Design", *18th IEEE International Conference on In-*

dustrial Technology (ICIT 2017), Toronto (Canada), March 2017.

[6] K. Stoyka, N. Femia, G. Di Capua, "Optimizing Power Converters with Partially Saturated Inductors by Evolutionary Algorithms", *2017 14th International Conference on Synthesis, Modeling, Analysis and Simulation Methods and Applications to Circuit Design (SMACD 2017)*, Giardini Naxos (Italy), June 2017.

[7] G. Di Capua, N. Femia, K. Stoyka, M. Lodi, A. Oliveri, M. Storace, "Ferrite Inductor Models for Switch-Mode Power Supplies Analysis and Design", *2017 14th International Conference on Synthesis, Modeling, Analysis and Simulation Methods and Applications to Circuit Design (SMACD 2017)*, Giardini Naxos (Italy), June 2017.

[8] G. Di Capua, N. Femia, K. Stoyka, "A Generalized Numerical Method for Ferrite Inductors Analysis in High Current Ripple Operation", *Integration, the VLSI Journal*, vol. 54, pp. 473-484, June 2017.

[9] G. Di Capua, N. Femia, M. Migliaro, O. Sacco, D. Sannino, K. Stoyka, V. Vaiano, "Intensification of a Flat-Plate Photocatalytic Reactor Performances by Innovative Visible Light Modulation Techniques: A Proof of Concept", *Chemical Engineering and Processing: Process Intensification*, vol. 118, pp. 117-123, August 2017.

[10] G. Di Capua, N. Femia, K. Stoyka, "Switching Power Supplies with Ferrite Inductors in Sustainable Saturation Operation", *International Journal of Electrical Power & Energy Systems*, vol. 93, pp. 494-505, December 2017.

[11] K. Stoyka, G. Di Capua, N. Femia, "A Novel AC Power Loss Model for Ferrite Power Inductors", *IEEE Transactions on Power Electronics*, vol. 34, no. 3, pp. 2680-2692, March 2019.

[12] G. Di Capua, N. Femia, K. Stoyka, "Loss Behavioral Modeling for Ferrite Inductors", *15th International Conference on Synthesis, Modeling, Analysis and Simulation Methods and Applications to Circuit Design (SMACD 2018)*, Prague (Czech Republic), July 2018.

[13] K. Stoyka, R. A. Pessinatti Ohashi, N. Femia, "Behavioral Switching Loss Modeling of Inverter Modules", *15th International Conference on Synthesis, Modeling, Analysis and Simulation Methods and Applications to Circuit Design (SMACD 2018)*, Prague (Czech Republic), July 2018.

[14] Kateryna Stoyka, Giulia Di Capua, Nicola Femia, "Modeling of Stepped Air-Gap Ferrite Inductors in Switching Power Supplies", *25th IEEE International Conference on Electronics Circuits and Systems (ICECS 2018)*, Bordeaux (France), December 2018.

[15] A. Oliveri, G. Di Capua, K. Stoyka, M. Lodi, M. Storace, N. Femia, "A Power-Loss-Dependent Inductance Model for Ferrite-Core Power Inductors in Switch-Mode Power Supplies", *IEEE Transactions on Circuits and Systems I: Regular Papers*, January 2019, doi: 10.1109/TCSI.2018.2889856.

Bibliography

[1] J. Muhlethaler, J. W. Kolar, A. Ecklebe, "Loss Modeling of Inductive Components Employed in Power Electronic Systems," in *8th International Conference on Power Electronics - ECCE Asia*, May 2011, pp. 945–952.

[2] N. J. Schade, *Core Losses in Composite Inductors*, Vishay Intertechnology, Inc., 2016, online.

[3] L. Crane, *Ferrite and Powder Core Materials for Power Inductors*, Coilcraft, Inc., 2006, online.

[4] *Power Inductors and Peak Current Handling Capability*, Renco Electronics, Inc., 2016, online.

[5] He Li-Gao, Wu Jian, "Selection of the Current Ripple Ratio of Converters and Optimal Design of Output Inductor," in *2010 5th IEEE Conference on Industrial Electronics and Applications*, June 2010, pp. 1163–1167.

[6] K. Kuebrich, T. Duerbaum, A. Stadler, K. Schetters, "Influence of Nonlinear Magnetic Inductance in Passive Mains Harmonic Reduction Circuits," in *2005 Twentieth Annual IEEE Applied Power Electronics Conference and Exposition (APEC)*, vol. 2, March 2005, pp. 1170–1175.

[7] R. B. Perpina, M. R. Lumbreras, A. C. Roca, G. V. Quesada, "Real Time Parameter and Models Determination in Saturated Inductors Submitted to Non-Sinusoidal Excitations,"

in *2009 13th European Conference on Power Electronics and Applications*, September 2009, pp. 1–9.

[8] R. A. Salas, J. Pleite, "Simulation of the Saturation and Air-Gap Effects in a POT Ferrite Core With a 2-D Finite Element Model," *IEEE Transactions on Magnetics*, vol. 47, no. 10, pp. 4135–4138, October 2011.

[9] A. V. Radun, "Development of Dynamic Magnetic Circuit Models Including Iron Saturation and Losses," *IEEE Transactions on Magnetics*, vol. 50, no. 5, pp. 1–10, May 2014.

[10] W. H. Wolfle, W. G. Hurley, "Quasi-Active Power Factor Correction with a Variable Inductive Filter: Theory, Design and Practice," *IEEE Transactions on Power Electronics*, vol. 18, no. 1, pp. 248–255, January 2003.

[11] C. Wilhelm, D. Kranzer, B. Burger, "Development of a Highly Compact and Efficient Solar Inverter with Silicon Carbide Transistors," in *2010 6th International Conference on Integrated Power Electronics Systems (CIPS)*, March 2010, pp. 1–6.

[12] A. Stadler, T. Stolzke, C. Gulden, "Nonlinear Power Inductors for Large Current Crest Factors," in *2012 European Power Conversion Intelligent Motion Conference (PCIM)*, May 2012, pp. 1548–1553.

[13] L. Milner, G.A. Rincon-Mora, "Small Saturating Inductors for More Compact Switching Power Supplies," *IEEJ Trans. on Electrical and Electronic Engineering*, vol. 7, no. 1, pp. 69–73, January 2012.

[14] I. Stevanovic, S. Skibin, M. Masti, M. Laitinen, "Behavioral Modeling of Chokes for EMI Simulations in Power Electronics," *IEEE Transactions on Power Electronics*, vol. 28, no. 2, pp. 695–705, February 2013.

[15] D. C. Jiles, D. L. Atherton, "Theory of Ferromagnetic Hysteresis (Invited)," *Journal of Applied Physics*, vol. 55, no. 6, pp. 2115–2120, 1984.

[16] I. D. Mayergoyz, G. Friedman, "Generalized Preisach Model of Hysteresis," *IEEE Transactions on Magnetics*, vol. 24, no. 1, pp. 212–217, January 1988.

[17] *Power Inductor Analysis and Comparison Tool*, Coilcraft, Inc., online.

[18] *REDEXPERT*, Wurth Elektronik, online.

[19] *Selection Assistant of TDK components*, TDK, online.

[20] G. Di Capua, N. Femia, "A Novel Method to Predict the Real Operation of Ferrite Inductors With Moderate Saturation in Switching Power Supply Applications," *IEEE Transactions on Power Electronics*, vol. 31, no. 3, pp. 2456–2464, March 2016.

[21] B. Cougo, H. Schneider, T. Meynard, "High Current Ripple for Power Density and Efficiency Improvement in Wide Bandgap Transistor-Based Buck Converters," *IEEE Transactions on Power Electronics*, vol. 30, no. 8, pp. 4489–4504, August 2015.

[22] A. Van Den Bossche, V. C. Valchev, *Inductors and Transformers for Power Electronics*, ser. Electrical Engineering. Taylor & Francis Group, 2005.

[23] E.C. Snelling, *Soft ferrites: Properties and Applications*. Butterworths, 1988.

[24] S. Maniktala, *Switching Power Supplies A - Z*. Elsevier Science, 2012.

[25] *TPS54160EVM-230 - User's Guide*, Texas Instruments, September 2008.

[26] *TPS55340EVM-017 Evaluation Module - User's Guide*, Texas Instruments, July 2012.

[27] *LM5122EVM-1PH Evaluation Module - User's Guide*, Texas Instruments, August 2013.

[28] Y. Ao, H. Chi, "Experimental Study on Differential Evolution Strategies," in *2009 WRI Global Congress on Intelligent Systems*, vol. 2, May 2009, pp. 19–24.

[29] K. V. Price, R. N. Storn, J. A. Lampinen, *Differential Evolution: A Practical Approach to Global Optimization*, ser. Natural Computing Series. Springer, 2005.

[30] G. Di Capua, N. Femia, K. Stoyka, "Differential Evolution Algorithm-based Identification of Ferrite Core Inductors Saturation Curves," in *IEEE 13th International Conference on Industrial Informatics (INDIN)*, July 2015, pp. 1636–1641.

[31] M. Lodi, A. Oliveri, M. Storace, "Low-Cost Acquisition Method for On-Line Inductor Characterization in Switched Power Converters," in *14th Int. Conf. on Synthesis, Modeling, Analysis and Simulation Methods and Appl. to Circuit Design (SMACD)*, June 2017.

[32] J. Sun, M. Xu, Y. Ren, F. C. Lee, "Light-Load Efficiency Improvement for Buck Voltage Regulators," *IEEE Transactions on Power Electronics*, vol. 24, no. 3, pp. 742–751, March 2009.

[33] P. Mantzanas, M. Barwig, D. Kuebrich, T. Duerbaum, "Efficiency Improvement of a Flyback Converter by Employing a Stepped Air-Gap Transformer," in *2016 18th European Conference on Power Electronics and Applications (EPE'16 ECCE Europe)*, September 2016, pp. 1–10.

[34] W. Wolfle, W. G. Hurley, S. Arnold, "Power Factor Correction for AC-DC Converters with Cost Effective Inductive Filtering," in *2000 IEEE 31st Annual Power Elec-*

tronics Specialists Conference. Conference Proceedings (Cat. No.00CH37018), vol. 1, June 2000, pp. 332–337.

[35] E. Stenglein, D. Kuebrich, M. Albach, "Prediction of the Non-Linear Behavior of a Stepped Air Gap Inductor," in *2016 IEEE 17th Workshop on Control and Modeling for Power Electronics (COMPEL)*, June 2016, pp. 1–6.

[36] P. L. Dowell, "Effects of Eddy Currents in Transformer Windings," *Proceedings of the Institution of Electrical Engineers*, vol. 113, no. 8, pp. 1387–1394, August 1966.

[37] J. P. Vandelac, P. D. Ziogas, "A Novel Approach for Minimizing High-Frequency Transformer Copper Losses," *IEEE Transactions on Power Electronics*, vol. 3, no. 3, pp. 266–277, July 1988.

[38] J. A. Ferreira, "Improved Analytical Modeling of Conductive Losses in Magnetic Components," *IEEE Transactions on Power Electronics*, vol. 9, no. 1, pp. 127–131, January 1994.

[39] C. R. Sullivan, "Computationally Efficient Winding Loss Calculation with Multiple Windings, Arbitrary Waveforms, and Two-Dimensional or Three-Dimensional Field Geometry," *IEEE Transactions on Power Electronics*, vol. 16, no. 1, pp. 142–150, January 2001.

[40] J. Hu, C. R. Sullivan, "AC Resistance of Planar Power Inductors and the Quasidistributed Gap Technique," *IEEE Transactions on Power Electronics*, vol. 16, no. 4, pp. 558–567, July 2001.

[41] A. Reatti, M. K. Kazimierczuk, "Comparison of Various Methods for Calculating the AC Resistance of Inductors," *IEEE Transactions on Magnetics*, vol. 38, no. 3, pp. 1512–1518, May 2002.

[42] M. Sippola, R. E. Sepponen, "Accurate Prediction of High-Frequency Power-Transformer Losses and Temperature Rise,"

IEEE Transactions on Power Electronics, vol. 17, no. 5, pp. 835–847, September 2002.

[43] W. A. Roshen, "A Practical, Accurate and Very General Core Loss Model for Nonsinusoidal Waveforms," *IEEE Transactions on Power Electronics*, vol. 22, no. 1, pp. 30–40, January 2007.

[44] T. Hatakeyama, K. Onda, "Core Loss Estimation of Various Materials Magnetized with the Symmetrical/Asymmetrical Rectangular Voltage," *IEEE Transactions on Power Electronics*, vol. 29, no. 12, pp. 6628–6635, December 2014.

[45] C. P. Steinmetz, "On the Law of Hysteresis," *Proceedings of the IEEE*, vol. 72, no. 2, pp. 197–221, February 1984.

[46] *Curve Fit Equations for Ferrite Materials*, Magnetics, Inc., 1999, online.

[47] *Design of Planar Power Transformers*, Ferroxcube, 1997, online.

[48] *P1172 datasheet*, Pulse Electronics, 2007, online.

[49] J. Reinert, A. Brockmeyer, R. W. A. A. De Doncker, "Calculation of Losses in Ferro- and Ferrimagnetic Materials Based on the Modified Steinmetz Equation," *IEEE Transactions on Industry Applications*, vol. 37, no. 4, pp. 1055–1061, July 2001.

[50] J. Li, T. Abdallah, C. R. Sullivan, "Improved Calculation of Core Loss with Nonsinusoidal Waveforms," in *2001 IEEE Thirty-Sixth IAS Annual Meeting Industry Applications Conference*, vol. 4, September 2001, pp. 2203–2210.

[51] K. Venkatachalam, C. R. Sullivan, T. Abdallah, H. Tacca, "Accurate Prediction of Ferrite Core Loss with Nonsinusoidal Waveforms Using Only Steinmetz Parameters," in *2002 IEEE Workshop on Computers in Power Electronics*, June 2002, pp. 36–41.

[52] A. Van den Bossche, V. Cekov Vaichev, G. Bogomilov Georgiev, "Measurement and Loss Model of Ferrites with Non-Sinusoidal Waveforms," in *2004 IEEE 35th Annual Power Electronics Specialists Conference (PESC)*, vol. 6, June 2004, pp. 4814–4818.

[53] S. Barg, K. Ammous, H. Mejbri, A. Ammous, "An Improved Empirical Formulation for Magnetic Core Losses Estimation Under Nonsinusoidal Induction," *IEEE Transactions on Power Electronics*, vol. 32, no. 3, pp. 2146–2154, March 2017.

[54] K. Terashima, K. Wada, T. Shimizu, T. Nakazawa, K. Ishii, Y. Hayashi, "Evaluation of the Iron Loss of an Inductor Based on Dynamic Minor Characteristics," in *2007 European Conference on Power Electronics and Applications*, September 2007, pp. 1–8.

[55] J. W. Kolar, J. Muhlethaler, J. Biela, A. Ecklebe, "Core Losses Under the DC Bias Condition Based on Steinmetz Parameters," *IEEE Transactions on Power Electronics*, vol. 27, no. 2, pp. 953–963, Feb. 2012.

[56] H. Kosai, Z. Turgut, J. Scofield, "Experimental Investigation of DC-Bias Related Core Losses in a Boost Inductor," *IEEE Transactions on Magnetics*, vol. 49, no. 7, pp. 4168–4171, July 2013.

[57] M. Mu, *High Frequency Magnetic Core Loss Study*, Ph.D. dissertation, Department of Electrical Engineering, Virginia Tech., Blacksburg, VA, USA, 2013.

[58] M. Mu, F. Zheng, Q. Li, F. C. Lee, "Finite Element Analysis of Inductor Core Loss Under DC Bias Conditions," *IEEE Transactions on Power Electronics*, vol. 28, no. 9, pp. 4414–4421, September 2013.

[59] A. Ruszczyk, K. Sokalski, J. Szczyglows, "Scaling in Modeling of Core Losses in Soft Magnetic Materials Exposed to

Nonsinusoidal Flux Waveforms and DC Bias," in *21st Soft Magnetic Materials Conference*, August 2013.

[60] V. J. Thottuvelil, T. G. Wilson, H. A. Owen, "High-Frequency Measurement Techniques for Magnetic Cores," *IEEE Transactions on Power Electronics*, vol. 5, no. 1, pp. 41–53, January 1990.

[61] A. Brockmeyer, "Experimental Evaluation of the Influence of DC-Premagnetization on the Properties of Power Electronic Ferrites," in *1996 Eleventh Annual IEEE Applied Power Electronics Conference and Exposition (APEC)*, March 1996, pp. 454–460.

[62] M. Mu, Y. Su, Q. Li, F. C. Lee, "Magnetic Characterization of Low Temperature Co-Fired Ceramic (LTCC) Ferrite Materials for High Frequency Power Converters," in *2011 IEEE Energy Conversion Congress and Exposition*, September 2011, pp. 2133–2138.

[63] Y. Han, G. Cheung, A. Li, C. R. Sullivan, D. J. Perreault, "Evaluation of Magnetic Materials for Very High Frequency Power Applications," *IEEE Transactions on Power Electronics*, vol. 27, no. 1, pp. 425–435, January 2012.

[64] M. Mu, Q. Li, D. J. Gilham, F. C. Lee, K. D. T. Ngo, "New Core Loss Measurement Method for High-Frequency Magnetic Materials," *IEEE Transactions on Power Electronics*, vol. 29, no. 8, pp. 4374–4381, August 2014.

[65] M. Mu and F. C. Lee and Q. Li and D. Gilham and K. D. T. Ngo, "A High Frequency Core Loss Measurement Method for Arbitrary Excitations," in *2011 Twenty-Sixth Annual IEEE Applied Power Electronics Conference and Exposition (APEC)*, March 2011, pp. 157–162.

[66] D. Hou, M. Mu, F. C. Lee, Q. Li, "New High-Frequency Core Loss Measurement Method With Partial Cancellation

Concept," *IEEE Transactions on Power Electronics*, vol. 32, no. 4, pp. 2987–2994, April 2017.

[67] M. Wens, J. Thone, "MADMIX: The Standard for Measuring SMPS Inductors," *Bodo's Power Systems*, pp. 52–54, April 2015.

[68] J. R. Koza, *Genetic Programming: On the Programming of Computers by Means of Natural Selection.* Cambridge, MA, USA: MIT Press, 1992.

[69] W. H. Press, S. A. Teukolsky, W. T. Vetterling, B. P. Flannery, *Numerical Recipes in C (2nd Ed.): The Art of Scientific Computing.* New York, NY, USA: Cambridge University Press, 1992.

[70] K. Deb, A. Pratap, S. Agarwal, T. Meyarivan, "A Fast and Elitist Multiobjective Genetic Algorithm: NSGA-II," *IEEE Transactions on Evolutionary Computation*, vol. 6, no. 2, pp. 182–197, April 2002.

[71] G. Di Capua, N. Femia, K. Stoyka, "Switching Power Supplies with Ferrite Inductors in Sustainable Saturation Operation," *International Journal of Electrical Power and Energy Systems*, vol. 93, no. Supplement C, pp. 494–505, December 2017.

[72] *Power Choke Coils for Automotive Applications*, Panasonic Industry Europe. [Online]. Available: https://eu.industrial.panasonic.com/node/2539/powerchoke-coils-automotive-applications

[73] K. Deb, *Multi-Objective Optimization Using Evolutionary Algorithms.* New York, NY, USA: John Wiley & Sons, Inc., 2001.